Stress Intensity Factors of the Edge Interfacial Cracks for Arbitrary Material Combinations

By

Xin Lan / 09584102

A dissertation submitted in partial fulfillment

of the requirements for the degree of

Doctor of Engineering

Department of Mechanical Engineering

Kyushu Institute of Technology

June 2012

I dedicate this dissertation to my parents because of all the wonderful things they do for me and supporting me all the way.

ACKNOWLEDGMENTS

My deepest gratitude goes first and foremost to my dissertation supervisor, Professor **Nao-Aki Noda**, who introduced me to the field of interface mechanics. He has been endowing me detailed direction and dedicating academic help along the process of producing this dissertation. Without his consistent and illuminating instruction, this dissertation could not have reached its present form. I am also deeply grateful to Prof. **Kazuhiro Oda**, for his detailed and constructive suggestions and comments, and for his important support throughout this work. In addition, my gratitude should direct to Dr. **Yasushi Takase**, who has been supporting and helping me throughout my doctoral program. He made me so easy to study and work in the lab of *Fracture Mechanics and Elasticity* of Kyushu institute of technology. I would also like to thank my collaborators: Dr. **Yu Zhang**, Mr. **Kengo Michinaka** (master) and Mr. **Ken-Tarou Takaisi** (master), for their contributions to this work.

I would like to express my special gratitude to my doctoral committee members, Prof. **Kenji Matsuda**, Prof. **Kenji Kousa**, Prof. **Tooru Kawabe** and Dr. **Yoshikazu Sano** for their valuable suggestions and advice on my research. Their supports throughout my doctoral program, and constructive comments and suggestions during my doctoral dissertation work have provided a good basis for the present work.

My first advisor, Prof. **Yong Cheng**, introduced me to the field of power machinery and engineering in 2005, when I first worked as a master student in his lab. He was the one who drew my attention to the beautiful world of scientific research. I would like to appreciate his innovative thinking, his ability to constantly concentrate on the most crucial aspects of a problem. All of this makes me benefit a lot and contributes to my future work.

I also extend my gratitude to Prof. **Weiquan Feng**, who has been both a good friend and an advisor. I am grateful to him for sharing with me his enthusiasm about science and his wisdom. I learn a lot from all the exciting and funny discussions we have had over the years. His support and career advice made me benefit so much.

My gratitude also goes to all my friends (too many to list, but you know who you are ☺), who have been supporting me all the time. Thanks for proving friendships that I need.

There are no words to express my gratitude to my parents, Mr. **Chunchang Lan** and Mrs. **Aiqing Yu**. They have always been there for me, giving me their unconditional love and supporting me in all my decisions. They have been a source of energy for me.

Finally, the financial support of **MONBUKAGUSHO** scholarship of the Japanese government, which made it possible for the successful completion of the research work, is gratefully acknowledged.

ABSTRACT

Singular stress fields exist around the areas of the edge interface corners for two materials which are bonded together. And the presence of cracks affects the performances of a structure, and consequently causes a through-thickness crack which eventually results in the failure. The stress intensity factor is used to predict the stress state and the stable crack growth in fracture mechanics. Therefore, researches concerning the stress intensity factors of the edge interface cracks are the main focus of this research.

The crack tip stress method based on FEM was improved to be able to solve the interface crack problems more efficiently. And a post-processing technology of linear extrapolation was proposed to improve the computational accuracy. Then, the improved crack tip stress method was applied to treat various edge interface crack problems.

In this research, the stress intensity factors were computed for the whole range of material combinations and relative crack lengths. And the double logarithmic relationships between the stress intensity factors and the relative crack lengths were demonstrated for various material combinations. Then, approximate formulae of the stress intensity factors for arbitrary material combinations were given by fitting the computed results, for the single-edge cracked bonded dissimilar half-planes and shallow single edge-cracked bonded finite strips subjected to tensile and bending loading conditions. Furthermore, the contour map variations of the stress intensity factors in the whole material combinations space were demonstrated for a series of relative crack lengths. The maximum and minimum stress intensity factors were also obtained for various crack lengths.

The single and double edge interface cracks were compared for the whole range of combination of materials and relative crack lengths. It was found that the stress intensity factors of a double-edge interface crack may possibly be larger than those of a single-edge interface crack for some specific material combinations and relative crack lengths. In addition, the stress intensity factors should be compared in three different zones according to the relative crack lengths.

Finally, the variations of the stress intensity factors of the adhesive joints for various thicknesses of adhesive layers were also demonstrated for various material combinations. Specifically, the three-layered adhesive joints composed of Si (IC chip), resin and FR-4.5(substrate) which are widely used in the chip scale packaging (CSP) technology were investigated. And the effects of the thickness of the adhesive layers for CSP were also discussed in this research.

任意の材料組み合わせを考慮した縁界面き裂の応力拡大係数に関する研究

【論文の要旨】

複合材料や接着構造は工業界に広く使用されているが，異種材料を接合すると，それぞれの材料の変形能や熱膨張率の相違により，界面端部に応力とひずみの集中が生じ，しばしば破壊を引き起こす．このため，界面き裂の解析は古くから破壊力学分野における重要な研究テーマとなっている．たとえば通常の均質材中のき裂では，同一長さ同一荷重を受ける内部き裂に対して，縁き裂が，√2×1.1215 倍危険側の応力拡大係数（無限小き裂の厳しさ）となることが知られている．しかし，界面き裂の場合には，このような内部き裂と縁き裂の厳しさの違いなど，基本的問題がいまだ明らかとなっていない．

本論文では，異種材料の接合端部では，き裂がない場合でも，多くの場合に特異性が生じることにまず注目している．そして，その界面端部の特異場の中に生じた界面き裂の特異応力場の強さを，二重の特異応力場を考慮することによって解析し，その解を任意の材料組み合わせに対して与えている．

本論文は，全７章から構成されている．

まず，第１章では，本研究の背景として，界面の力学を電子実装の評価等に応用した関連分野の研究をまとめている．特に，接着端部並びに，縁界面き裂の解析が，特定の材料組合せに限定されていることや，き裂長さの影響に関する研究が不十分であることを指摘している．そして，界面強度の定量的な予測技術の確立を目的に，任意の材料組合せにおける界面縁き裂の応力拡大係数の解析を研究する必要性を説明している．

第２章では有限要素法解析によるき裂先端節点における応力値に注目して，基準解との比をとることにより応力拡大係数を決定する第ゼロ節点法を考察している．まず，縁き裂が浅い場合には，報告されているように厳密解の得られている基準問題と未知問題を同時に解析することで，有限要素寸法の誤差を打消すことが可能となり，き裂要素寸法に無関係に高精度の応力拡大係数が得られることを確認している．しかし，縁き裂が深い場合には，要素寸法の影響が表れることを指摘し，その影響を詳細に調べている．その結果，どのような要素寸法を用いて解析し，要素寸法が無限小となる場合を外挿によって求めればよいかを明らかにしている．また，

この方法により，すべてのき裂の長さで精度よい結果が得られることを指摘するとともに，極端に細かい要素を用いずに，外挿による方法を用いることで解析時間も節約できることも説明している．

第３章では前章に述べた方法を用いて，き裂長さが無限小に相当する，接合半無限板が引張りと曲げ荷重を受ける問題を取り扱っている．具体的には，まず接合有限板中の縁界面き裂を解析して，き裂長さが小さい場合を調べた結果，き裂長さと応力拡大係数の関係が両対数グラフ上で直線関係となることを見出している．そして，その理由が，（１）き裂が存在しない完全接着界面端部近傍で，材料組み合わせにより界面の応力が無限大，有限値，ゼロに近づく領域が存在すること，（２）その領域内に縁界面き裂がその応力場の影響を受けて存在しているためであることを説明している．

第４章では縁界面き裂を有する接合有限板が引張荷重と面内曲げ荷重を受ける問題をすべてのき裂長さに対して考察している．特に，前章で扱った接合端部の特異応力領域内に，微小な界面縁き裂が存在する場合に関して，その応力拡大係数の漸近解を求めている．接合端部の特異応力領域外の界面縁き裂に対しては，あらゆる材料組合せに対して，応力拡大係数の値がどのように変化するか，どのような材料組み合わせで最大値と最小値を与えるかを説明している．

第５章では接合有限板の両側に界面縁き裂がある問題を取り扱っている．まず接合板の両端部の特異応力領域内に微小な両側界面縁き裂がある場合に，応力拡大係数の漸近解を求めている．次に，片側き裂と両側き裂の結果を比較検討している．均質材では，片側き裂の応力拡大係数が常に同じ長さの両側き裂の応力拡大係数より大きい．しかし，接合板では両側き裂の干渉効果が大きいため，き裂長さによっては，大小関係が逆転する場合があること等を明らかにしている．

第６章では，接着剤で接合された３層構造からなる接着接合板が引張りを受ける場合の界面縁き裂の応力拡大係数について，接着層厚さと材料組合せを変化させて議論している．電子デバイスの高密度パッケージを想定した材料の組み合わせを中心に，接着層の厚さが界面縁き裂の応力拡大係数に与える影響について考察している．また，界面強度は接着層が薄いほうが強いという実験結果が，接合端部に生じた微小き裂に注目したモデルから説明できることを示している．

第７章では本研究で得られた主要な結論をまとめている．

TABLE OF CONTENTS

LIST OF TABLES

LIST OF FIGURES

NOMENCLATURE

ENF	End Notch Flexure
LEFM	linear elastic fracture mechanics
SIF	stress intensity factor
SIFs	stress intensity factors
a	length of the edge interface crack
C_I, C_{II}	constants depending upon material combinations and loading types
e	minimum element size of FE model
E_m	Young's modulus of material m
$f_{ij}(\theta)$	angular functions
$f_I(\theta)$	trigonometric function
F_I, F_{II}	dimensionless SIFs at the crack tip of an interface crack
$F_{I,\mathrm{hom}o}$	normalized SIF for homogenous crack
G_m	shear modulus of material m
H	intensity of stress singularity
K	stress intensity factors
$K_I + iK_{II}$	complex stress intensity factors of interface cracks
K_σ	intensity of stress singularity
$K^{e=0}$	extrapolated SIF
K^{e1} , K^{e2}	SIFs computed by FE meshes with the minimum element sizes e_1, e_2
L,W	length and width of the bonded strip
M	bending load
NL	number of refined layers
P	tensile load
r	radial distance from the crack tip
t	adhesive thickness
T, S	tensile and shear stresses applied to the reference problem
W	width of the bonded strip
α, β	Dundurs' material composite parameters
ε	bi-elastic constant
θ	angle from the interface
θ_1, θ_2	angles of traction-free edges intersect the interface
κ_m	Kolosov constant of material m
λ	order of the stress singularity
σ_y, τ_{xy}	normal and shear stress components near the crack tip
σ_{yy}	normal stress component ahead of the crack tip

$\sigma^{*}_{y0,FEM}, \tau^{*}_{xy0,FEM}$	FE stresses at the crack tip of the reference problem
$\sigma_{y0,FEM}, \tau_{xy0,FEM}$	FE stresses at the crack tip of the target unknown problem
ν_m	Poisson's ratio of material m
(r,θ)	polar coordinates centered at the interface corner o

1 CHAPTER

Introduction

1.1 Research Backgrounds

Modern technology has led to the employing of composites and bonded structures/multiple layers in automotive and aerospace industries as well as in microelectronics packaging. The significant size and weight reduction offered by the chip scale packages (CSP) makes it ideal for the use in mobile devices like cell phones, laptops, palmtops, and digital cameras. The advantages offered by CSP include smaller size (reduced footprint and thickness), lesser weight, relatively easier assembly process, lower over-all production costs and improvement in electrical performance.

Fig.1 demonstrated a wire-bonded µBGA® ball grid array chip scale packaging solution [1]. A typical chip scale packaging process starts with the mounting of the die on the interposer using epoxy. The die is then wire-bonded to the interposer using gold or aluminum wires. Plastic encapsulation then follows to protect the die and wires, usually by transfer molding. After encapsulation, solder balls are attached to the bottom side of the interposer. Finally, the parts are singulated from the leadframe.

As can be seen from Fig. 1.1, quite a lot interfaces exist inside the CSP assemblies. Stress concentration happens along the interfaces due to the discontinuous of material property and geometric configuration. And cyclic pressure and temperature as well as humidity will increase the speed of delamination. Therefore, there is an increasing concern

that the CSP assemblies may not meet the mechanical and the thermal cycling reliability requirements. In Fig. 1.2, the cross-section image reveals delamination after the 3× JEDEC 260°C reflow test. Delamination initiates at the interface between the underfill and the flux residue, and then propagated along the solder mask [2]. Fig. 1.3a and b illustrate the solder die attach/silicon die interface with and without delamination respectively. And this delamination would imply a critical failure in applications requiring high thermal and electrical conductivity [3]. Therefore, Reliability evaluations based on fracture mechanics on the interface problems of CSP win quite a lot of attentions.

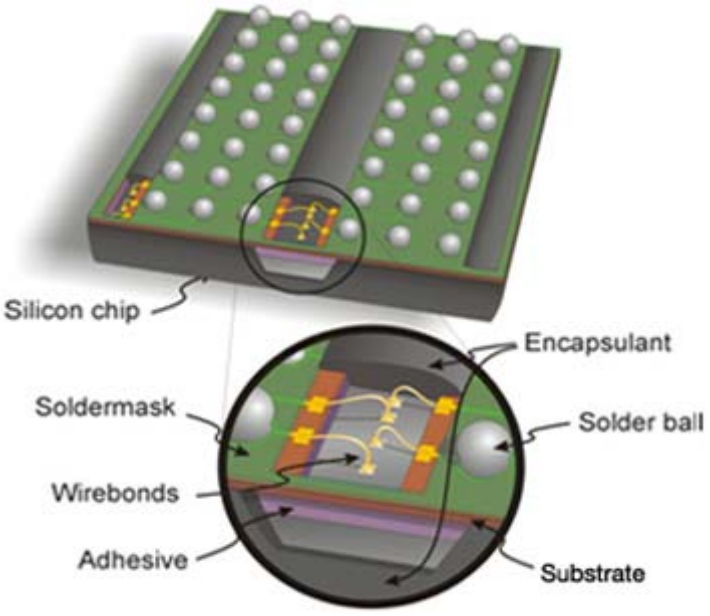

Fig. 1.1 Demonstration of wire-bonded µBGA® ball grid array chip scale packaging solution (CSP) (Ref. [1])

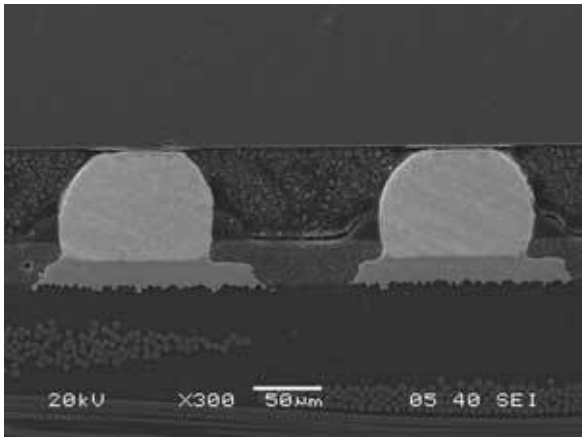

Fig. 1.2 Underfill delamination at the board level (Ref. [2])

(a)

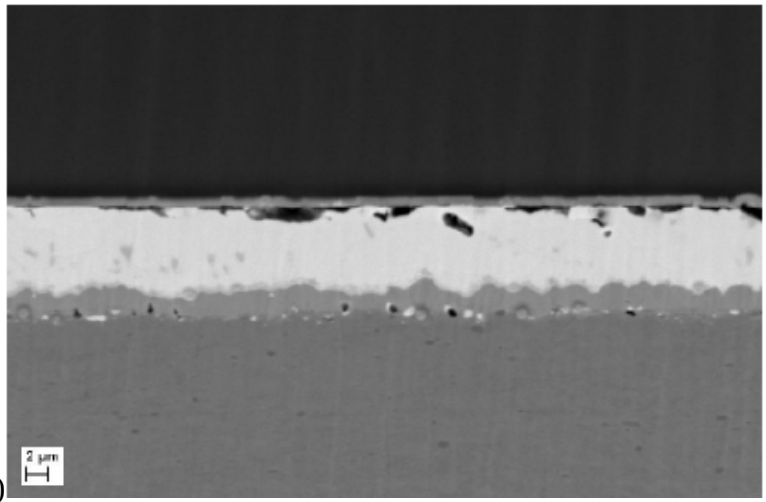

(b)

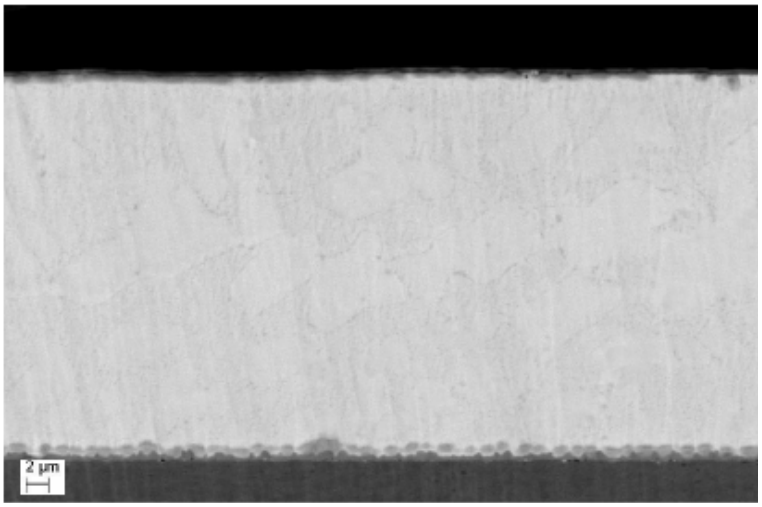

Fig. 1.3 Typical SEM image of (a) 10 μm die attach with delamination and (b) 34 μm die attach without delamination (Ref. [3])

For elastic fracture mechanics concepts to an interface crack between dissimilar materials, Williams [4] was the first to determine the characteristic oscillating stress singularity at the crack tip in the elastic interfacial crack problem. Then, elastic solutions around the interface crack tip to specific problems were discussed by Erdogan [5,6], England [7], and Rice and Sih [8]. Bogy [9] revealed that the stresses at the interface corner approach to infinity (stress singularity) in elastic bi-material planes. This qualitatively explained why the failures of the bonded structures mostly initiate from the interface corner in the engineering. However, the oscillation phenomenon (say, the oscillations of stresses and the overlap of crack surfaces/ the oscillations of displacements) were observed in the vicinity of a crack tip in the aforementioned solutions which lead to controversies base on the physical properties of the actual materials for practical purposes. Therefore, quite a lot modified solutions to the interface cracks free of contradictions (*material may not overlap, normal tractions must be compressive in the contact zone*) were proposed [10] by considering the contact of crack surfaces. Specifically, Comninou [11,12], Atkinson [13] and Mak [14] proposed formulations of the interface cracks with crack surfaces contacting around the interface crack tip to eliminate the contradictions. Comninou [11,12] also pointed out that one of the contact zones is much larger than the other because the interface is also subjected to some shear loading. Based on Comninou's pioneering work, Dundurs and Gautesen [15] assumed that the crack is fully open at the end which leads to the oscillatory singularity (*disregarded the short contact zone*), and analyzed the situation at the end of the crack with the large contact zone. Then they found that the results predicted by the modified solutions coincide with those by the classical elastic solutions out of the interpenetration zone for the small scale contact zones. Finite element solutions for a small strain isotropic J_2-deformation plastic theory were obtained by Shih and Asaro [16,17]. They found that the interpenetration zone predicted by the

elastic solutions can be treated as a small scale nonlinearity. In any case, the actual situation is somewhat more optimistic than that suggested by the elasticity treatment. And the stress fields around the crack tip can be predicted by the linear elasticity solutions of comparable magnitude under small scale yielding conditions. Zywicz and Parks [18] also analyzed the small-scale yielding plastic zone around an interface crack tip. In 1988, Rice [19] re-examined the elastic fracture mechanics concepts for interfacial cracks and discussed the classical type of definitions of SIFs associated with interface cracks. Hutchinson and Suo [20] reviewed the application of the Stress intensity factor (SIF) to the mixed mode fracture of an interface crack. They found that the contradictions (*crack faces overlap and the oscillations of the stresses*) vanish in the elastic-plastic fields of an interface crack. Ichikawa [21] found that good agreement turns out for the classical elastic solutions and modified solutions within the extreme vicinity of an interface crack tip. From now on, the elastic fracture mechanics concepts are proved to be able used for estimating the fracture of an interface crack. And there has been a resurgence of interest in the elastic interface crack problems. Then quite a lot fracture criterions [22-28] have been proposed regarding the interface cracks.

1.2 Research Purposes

Fatigue cracks are normally observed around the areas of discontinuities and edge corners due to the high bending and residual stresses. The presence of cracks affects the performances of a structure, and consequently causes a through thickness crack which eventually results in the failure. For the bi-material systems, high stress singularity exists around the interface corner which leads to the initiation of edge interface cracks. In addition, in linear elastic fracture mechanics, the SIF is used to predict the stress state and

the stable crack growth caused by the remote load. Therefore, the analysis of the SIFs for edge interface cracks is fundamental to our understanding of the failure and fatigue of the bi-material/multi-layer systems. An exhaustive investigation on the stress intensity factors (SIFs) will contribute to a better understanding of the initiation and propagation of the interfacial cracks.

Let's consider a butt joint which is composed of two elastic materials, and the geometrical configuration is characterized by the angles θ_1 and θ_2 which the traction-free surfaces of the two elastic materials make with the interface. Many studies have considered the evaluation of the order of stress singularity $\lambda-1$ for various geometries and different combinations of materials [29-34]. Those researches were the pioneering works which qualitatively explained why edge interface cracks are normally observed from the free edge corner of the multi-layer systems. Then the computing of the intensity of stress singularity K_σ also acquires a fair mount of attentions. Reedy and Guess [35] have determined the magnitude of the intensity of stress singularity for a thin elastic layer sandwiched between two rigid substrates. Akisanya and Fleck [36] applied the contour integral to evaluate H-field at the free-edge of a long bi-material strip subjected to uniform tension. Xu et al. [37] proposed numerical methods to determine the multiple stress singularities and the related stress intensity coefficients. However, as widely known, it is not easy to determine the SIFs for the interface cracks due to the multiple singularities (including the oscillatory stress singularities), so literatures concerning the evaluation of stress intensity factors of interfacial cracks appeared later. Till recently, various numerical methods [38-50] have been reported to determine the SIFs of an interface crack. Specifically, the crack tip stress method [49] has been reported to be able to determine the SIFs of the interface cracks using FE method with a high accuracy.

In the aforementioned studies, none has considered the SIFs of the interface cracks for

arbitrary combination of materials. In this research, the study objects will be concentrated into several types of edge interface cracks in various bi-material systems subjected to tensile and bending loading conditions. And the crack tip stress method base on FEM proposed by Oda [49] will be reexamined by considering the robustness and convergence study. Highly accurate determination of SIFs for edge interface cracks based on FEM will be demonstrated by investigating the effects of FE model density and element sizes. Then, the SIFs for various edge interface cracks will be computed for the whole range of material combinations and crack lengths using the improved crack tip stress method. In addition, the effect of material combinations and relative crack lengths on the SIFs of various edge interface cracks will also be the main interest.

1.3 Overview of Chapters

Singular stress fields exist around the areas of the edge interface corners for two materials bonded together. This is the reason why fatigue cracks are normally observed from the edge corner. It was supposed that FE method was not suitable for the singular problems since the stresses approach infinity at the crack tip. However, Nishitani [51] proposed a novel numerical method based on FEM to evalute the SIF of a cracked homogenous strip. The computational accuracy is guaranteed by using the reference problems with highly accurate analytical solutions. This method is denoted as “crack tip stress method”. In 2009, Oda [49] successfully extended this method into the interface crack problems. Accurate results can be obtained by introducing a suitable shearing loading for the reference problem. However, considerable errors exist for some specific crack problems (Say, deep edge interface crack problems). The author of the current paper will re-examine the effect of the FE model density and the minimum element size, and

propose a post-processing technology of linear extrapolation to improve the accuracy. Then, the SIFs of various edge interface cracks will be investigated for arbitrary material combinations and crack lengths by using the improved “crack tip stress method”. In addition, the effect of material combinations and relative crack lengths on SIFs of various edge interface cracks will be discussed.

The paper is composed of total 7 chapters and organized as follows.

Chapter 1 introduces the application of composites and bonded structures/multiple layers in microelectronics packaging. After reviewing the issues of the linear elastic fracture mechanics on interface problems, Chapter 1 introduces the study object of this paper. Various types of edge interface crack problems need to be investigated because edge interface cracks are normally observed in the actual application. Specifically, according to the author’s best knowledge, little published literatures concentrate the discussions on the SIFs for arbitrary combination of materials. Therefore, the SIFs of various edge interface cracks for arbitrary material combinations are chosen as the main interest of this research.

Chapter 2 introduces the crack tip stress method proposed by Oda, which is based on the concept introduced by Teranishi and Nishitani [51]. The limitations of the method are demonstrated and investigated by pursuing a convergence study. A post-processing technique of linear extrapolation is proposed to improve the computational accuracy. The new technique reduces the computational cost significantly since very refined meshes around the crack tip are no longer necessary. The accuracy and efficiency of the improved crack tip stress method are demonstrated by comparing the SIFs of several numerical examples with published data. In addition, the general procedure and precautions of the improved crack tip method are also discussed in this chapter.

Chapter 3 In this chapter the SIFs at the crack tip of a bi-material bonded semi-infinite plate are investigated for arbitrary combination of materials. To obtain the

asymptotic solutions of the SIFs, the double logarithmic relationships between the SIF and the crack size are demonstrated with varying material combinations. Then, an approximate formula of the SIFs at the crack tip for the bonded dissimilar half-planes under arbitrary combination of materials is given by fitting the computed results.

Chapter 4 restricts the discussion to the SIFs of the bi-material bonded finite strips subjected to tensile and bending loading conditions. The effect of material combinations and relative crack lengths to the SIFs are investigated. The formula for SIFs of the very shallow edge interface cracks in bi-material butt joints subjected to tension and bending loads are proposed. Furthermore, the contour map variations of the SIFs in the whole $\alpha - \beta$ space are demonstrated for a series of relative crack lengths. The maximum and minimum SIFs are also obtained for various crack lengths.

Chapter 5 is devoted to the double-edge interface cracks. The effect of the relative crack lengths and material mismatch parameters are of special interest in this chapter. The SIFs for the single and double edge interface cracks will be compared for the whole range of combination of materials ($0 \le \alpha \le 0.95, -0.2 \le \beta \le 0.45$) and relative crack lengths ($0 \le a/W \le 0.9$). It is found that the SIFs of a double edge interface crack may be possibly larger than those of a single edge interface crack for some specific combination of materials and relative crack lengths. In addition, the transverse extent of the bonded strip should be divided into three different zones according to the dominance effect of the free edge singularity.

Chapter 6 introduces the SIFs of the adhesive joints for various material combinations. In this chapter the SIFs are computed for both the left and right region in the $\alpha - \beta$ space since no symmetry of the SIFs exists any more for the adhesive joints. The variations of the SIFs for various thicknesses of adhesive layer are also demonstrated. In addition, the three-layered adhesive joints composed by Si (IC chip), resin and FR-4.5(substrate) which are widely used in the chip size packaging (CSP) technology are

also investigated. The SIFs for various relative crack lengths and interlayer thicknesses are computed using the improved crack tip stress method. Furthermore, the effect of interlayer thickness on the SIFs are also discussed for CSP in this chapter.

Chapter 7 gives an overview of the main conclusions and achievements in this paper.

1.4 References of Chapter 1

[1] Tessera Technologies (no date),µBGA® Chip Scale Packaging Solution [online] Available from http://www.tessera.com/technologies/microelectronics/semiconductor packaging/CSP/Pages/ubga-wire.aspx [Accessed 4th Jan 2012]

[2]Zhao, R., Ji, Q., Carson, G., Todd, M. and Shi, G., 2007, Flux and underfill compatibility in a lead-free environment. [online] Available from http://www.electroiq.com/articles/ap/print/volume-16/issue-6/features/the-back-end-process/flux-and-underfill-compatibility-in-a-lead-free-environment.html [Accessed 4th Jan 2012]

[3]Hu, G.J., Luan, J.E., Braton, X., B. and Tay, A.A.O., Analysis of interfacial delamination in IC packaging: Use stress or fracture mechanics.

[4] Williams, M.L., The stress around a fault or crack in dissimilar media. Bull. Seismol. Soc. America, 1959; 49: 199-208

[5] Erdogan, F., Stress distribution in non-homogeneous elastic plane with cracks. Trans. ASME., Series E, J. Appl. Mech., 1963; 30:232-236.

[6] Erdogan, F., Stress distribution in bonded dissimilar materials with cracks. Trans. ASME., Series E, J. Appl. Mech., 1965;32:403-410.

[7] England, A.H., A crack between dissimilar media. Trans. ASME., Series E, J. Appl. Mech., 1965;32:400-402.

[8] Rice, J.R. and Sih, G.C., Plane problems of cracks in dissimilar media. Trans. ASME., Series E, J. Appl. Mech., 1965;32:418-423.

[9] Bogy, D.B, Edge bonded dissimilar orthogonal elastic wedges under normal and shear loadings. J. Appl Mech., 1966; 35: 146-154.

[10] Comninou, M., The interface crack. Trans. ASME., Series E, J. Appl. Mech., 1977;44:631-636.

[11] Comninou, M., Interface crack with friction in the contact zone. Trans. ASME., Series E, J. Appl. Mech., 1977;44:780-781.

[12] Comninou, M., The interface crack in a combined tension-compression and shear field.

J. Appl Mech., 1979; 46: 345-352.

[13] Atkinson, C., The interface crack with a contact zone. Int. J. Fract., 1982;18:161-177.

[14] Mak, A.F., Keer, L.M., Chen, S.H. and Lewis, J.L., A no-slip interface crack. Trans. ASME., Series E, J. Appl. Mech., 1980;47:347-350.

[15] Dundurs. J. and Gautesen, A.K., An opportunistic analysis of the interface crack. Int. J. Fract., 1988; 36: 151-159.

[16] Shih, C.F. and Asaro, R.J., Elastic-plastic analysis of cracks in bi-material interface. J. Appl Mech., 1988,55: 299-316.

[17] Shih, C.F. and Asaro, R.J., Elastic-plastic and asymptotic fields of interface cracks. Int. J. Fract., 1990;42:101-116.

[18] Zywicz, E. and Parks, D.M., Elastic yield zone around an interfacial crack tip. Trans. ASME., Series E, J. Appl. Mech., 1989;56:577-584.

[19] Rice, J.R., Elastic fracture mechanics concepts for interface cracks. J. Appl Mech., 1988, 55: 98-103.

[20] Hutchinson, J.W. and Suo, Z., Mixed mode cracking in layered materials. Advances in Appl. Mech., 1992;29:64-187.

[21] Ichikawa, M., A critical analysis of interface crack models and a quantitative comparison of the classical solution with the modified solution of an interface crack. Trans. JSME., Series A, 1991;57(538):1346-1350.

[22] Mulville, D.R. and Mast, P.W., Strain energy release rate for interfacial cracks between dissimilar media. Eng. Fract. Mech., 1976; 8: 555-565.

[23] Charalambides, P.G., Lund, J., Evans, A.G. and McMeeking, R.M., A test specimen for determining the fracture resistance of biomaterial interfaces. Trans. ASME., Series E, J. Appl. Mech., 1989; 56: 77-82.

[24] O'Dowd, N.P., Shih, C.F. and Stout, M.G., Test geometries for measuring interfacial fracture toughness. Int. J. Solids Struct., 1992; 29(5): 571-589.

[25] Yuuki, R., Liu, J.Q., Xu, J.Q., Ohira, T. and Ono, T., Mixed mode fracture criteria for an interface crack. Eng. Fract. Mech.. 1994, 47(3): 367-377.

[26] Xu, L. and Tippur, H.V., Fracture parameters for interfacial cracks : an experimental-finite element study of crack tip fields and crack initiation toughness. Int. J. Fract., 1995; 71: 345-363.

[27] Bowen, J.M. and Knauss, W.G., An experimental study of interfacial crack kinking. Experimental Mechanics, 1993; 33(1): 37-43.

[28] Ikeda, T.R., Miyazaki N.Y., and Soda, T.H., Mixed mode fracture criterion of interface crack between dissimilar materials, 1998; 59(6): 725-735.

[29] Williams, M.L., Stress singularities resulting from various boundary conditions in angular corners of plates in extension. J. Appl. Mech., 1952;19:526–8.

[30] Bogy, D.B., Two edge-bonded elastic wedges of different materials and wedges angles

under surface tractions. J. Appl. Mech., 1971;38:377–86.
[31] Bogy, D.B., Wang KC. Stress singularities at interface corners in bonded dissimilar isotropic elastic materials. Int J. Solids Struct, 1971;7:993–1005.
[32] Hein, V.L., Erdogan, F. Stress singularities in a two-material wedge. Int J. Fract. Mech., 1971;7:317–330.
[33] Dempsey, J.P., Sinclair, G.B., On the stress singularities in the plane elasticity of the composite wedge. J. Elast., 1979;9:373–91.
[34] van Vroonhoven, J.C.W., Stress singularities in bi-material wedges with adhesion and delamination. Fatigue & Fract Engng Mat. & Struct, 1992; 15:157-171.
[35] E.D. REEDY, JR. and GUESS, T.R., Composite to metal tubular lap joints: strength and fatigue resistance. Int J. Fract., 1993; 63: 351-367.
[36] Akisanya, A.R. and Fleck, N.A., Interfacial cracking from the free edge of a long bimaterial strip. Int J. Solids Structures, 1997; 34:1645-1665.
[37] Xu, J.Q., Liu, Y.H., Wang, X.G., Numerical methods for the determination of multiple stress singularities and related stress intensity coefficients. Engng Fract Mech., 1999;63:775-790.
[38] Wu, Y.L., A new method for evaluation of stress intensities for interface cracks. Engng Fract Mech., 1994;48:755-61.
[39] Yuuki, R., Cho, S.B.. Efficient boundary element analysis of stress intensity factors for interface cracks in dissimilar materials. Eng Fract Mech., 1989;34:179-188.
[40] Miyazaki, N., Ikeda, T., Soda, T. and Munakata, T., Stress intensity factor analysis of interface crack using boundary element method—Application of contour-integral method. Engng Fract Mech., 1993; 45(5): 599-610.
[41]Yang, X.X., Kuang, Z.B., Contour integral method for stress intensity factors of interface crack. Int J. Fract., 1996;78:299-313.
[42] Dong, Y.X., Wang, Z.M., Wang, B., On the computation of stress intensity factors for interfacial cracks using quarter point boundary elements. Engng Fract Mech., 1997;57:335-342.
[43] Qian, W. and Sun, C. T., Calculation of stress intensity factors for interlaminar cracks in composite laminates. Compos Sci Technol., 1997;57(6): 637-650.
[44] Shbeeb, N. I. and Binienda, W. K., Analysis of an interface crack for a functionally graded strip sandwiched between two homogeneous layers of finite thickness. Engng Fract Mech., 1999;64(6): 693-720.
[45] Matsumto, T., Tanaka, M. and Obara, R., Computation of stress intensity factors of interface cracks based on interaction energy release rates and BEM sensitivity analysis. Engng Fract Mech., 2000;65(6): 683-702.
[46] Huang, H. and Kardomateas, G.A., Mixed-mode stress intensity factors for cracks located at or parallel to the interface in bimaterial half planes. Int J. Solids and Struct.,

2001; 38(21): 3719-3734.
[47] Xuan, Z.C., Feng, Z.S. and Gao, D.Y., Computing lower and upper bounds on stress intensity factors in bimaterials. Int J. Non-Linear Mech., 2007;42(2): 336-341.
[48] Liu Y.H., Wu, Z.G., Liang, Y.C., Liu, X.M., Numerical methods for determination of stress intensity factors of singular stress field. Engng Fract Mech., 2008;75:4793-4803.
[49] Oda, K., Kamisugi, K. and Noda, N.A., Analysis of stress intensity factor for interface cracks based on proportional method. Trans JSME, Series A., 2009; 75(752):476-482.
[50] Panta, M., Singh, I.V. and Mishraa, B.K., Evaluation of mixed mode stress intensity factors for interface cracks using EFGM. Appl Math Model., 2011;35(7): 3443-3459.
[51] Nisitani, H., Teranisi, T. and Fukuyama, K., Stress intensity factor analysis of a biomaterial plate based on the crack tip stress method. Trans. JSME., Series A, 2009;75:467-482.

2 CHAPTER The improved crack tip stress method for interface cracks and post-processing technique

2.1 Introduction

In linear elastic fracture mechanics, the SIF is used to predict the stress state and the stable crack growth caused by the remote load. Therefore, quite a lot research has been devoted to the analysis of SIFs of the interface crack problems. Till recently, many researchers have tried to develop procedures to compute the generalized SIFs for interface cracks by using analytical or numerical methods. Just mention a few of those procedures, Yuuki and Cho [1] determined the SIFs of several interface crack problems by the boundary element method. Miyazakia et al. [2] presented the M1-integral method (an extended J-integral method) for SIF analyses of two-dimensional bimaterial interface crack problems, using the results obtained from the boundary element method. Wu [3] presented for calculating the SIFs at the tip of an interface crack based on an evaluation of the J-integral by the virtual crack extension method. Yang and Kuang [4] established a path independent contour integral method for the SIFs of the interface crack. Dong et al. [5] proposed procedures for SIF computation using traction singular quarter-point boundary elements. Qian and Sun [6] proposed an alternative and efficient method based on near-tip crack surface displacement ratio to obtain the SIFs of the inter-laminar cracks in composite laminates. Shbeeb and Binienda [7] formulated the singular integral equations with Cauchy kernels for the interface crack problem of a composite layer that consists of a

homogeneous substrate, coating and a nonhomogeneous functionally graded interphase. Then, mixed-mode SIFs and strain energy release rates were calculated. Matsumto et al. [8] evaluated the SIFs of bimaterial interface cracks based on the interaction energy release rates. Huang and Kardomateas [9] proposed a method for obtaining the mixed-mode SIFs for bimaterial interface cracks or cracks parallel to the bimaterial interface in half-plane configurations. The dislocation solutions in two different bimaterial half planes are presented, and then they were applied to calculate the mixed mode SIFs of cracks either at the interface or parallel to the interface. Ou [10] computed the singularities and near-tip field intensity factors of piezoelectric interface cracks in metal/piezoelectric bimaterials via Stroh's theory. Xuan et al. [11] presented a finite element approach for finding complementary bounds of SIFs in bimaterials. The SIF is formulated as an explicit computable linear function of displacements by means of the two-point extrapolation method. Liu [12] et al. developed a simple and effective numerical method to calculate the SIFs for an interface crack with one or two singularities. Treifi et al. [13, 14] computed the SIFs for different configurations of cracked/notched plates subjected to in-plane shear and bending loading conditions by the fractal-like finite element method. Panta et al. [15] demonstrated the implementation of element free Galerkin method for the stress analysis of structures having cracks at the interface of two dissimilar materials.

In this research, the numerical method proposed by Oda [16], which is based on the concept of crack tip stress method introduce by Teranishi and Nisitani [17], will be re-examined and improved for solving several crack problems. The crack tip stress method was initially proposed to determine the SIFs of the cracked homogenous plates, by using the ratio of crack-tip stresses between the reference and target unknown problems. Then, in 2009, Oda [16] extended the crack tip method to analyze the SIFs of interface crack problems by making the singular terms the same for the reference and target unknown

problems. This pioneering work provides a convenient manner to obtain the SIFs of interface crack problems by using FE method. However, recently it is found that the method sometimes does not provide reliable results for some specific crack lengths (say, the relative crack length $a/W > 0.4$ for the edge interface cracks). Therefore, the limitations of the crack tip stress method regarding the interface crack problems will be demonstrated and investigated by pursuing a convergence study in this research. A post-processing technique of linear extrapolation will be proposed to improve the computational accuracy. The new technique reduces the computational cost significantly since very refined meshes around the crack tip are no longer necessary. The accuracy and efficiency of the improved proportional method will be demonstrated by comparing the SIF results of several numerical examples with published data. In addition, the general procedure and precautions of the improved proportional method will also be discussed in this paper.

2.2 Numerical analysis method

2.2.1 The physical background of the crack tip stress method

Nisitani et al. were the first [17] to propose a numerical method, which is named after the *crack tip stress method*, using the FE stress values to compute the SIF of a cracked homogenous plate. According to the theory of linear-elastic fracture mechanics (LEFM), mode I SIF near the crack tip in a homogenous plate is defined by the following equation.

$$\sigma_{yy}(r,\theta) \to \frac{K_I}{\sqrt{2\pi r}} f_I(\theta) \quad (r \to 0) \tag{2.1}$$

Here, K_I is the mode I SIF, σ_{yy} is the normal stress component ahead of the crack tip, $f_I(\theta)$ is trigonometric function to be derived analytically. Specifically, when $\theta = 0$, Eq.(2.1) becomes

$$\sigma_y(r) \to \frac{K_I}{\sqrt{2\pi r}}, \quad \sigma_y = \sigma_{yy}\big|_{\theta=0} \quad (r \to 0) \tag{2.2}$$

Rearranging Eq.(2.2) gives $K_I/\sigma_y \to \sqrt{2\pi r}$ $(r \to 0)$. For a given point at $\theta = 0$ with a distance from the crack tip $r = r_0$, $K_I/\sigma_y = \sqrt{2\pi r_0}$ is constant and a following relationship can be deduced theoretically for two different crack problems A and B.

$$\left[K_I^*/\sigma_y^*\right]_A = \left[K_I/\sigma_y\right]_B \tag{2.3}$$

Assuming the SIF for problem A is analytically given in advance, while that for problem B is yet to be solved. Problem A is denoted as the reference problem and problem B is denoted as the target unknown problem. Here, the superscript * is introduced to indicate the values of the reference problem A for notational convenience. Although the values of σ_y^*, σ_y in Eq.(2.3) for the singular problems cannot be computed by FE analysis accurately, the ratio of σ_y^*/σ_y can be given without any difficulty. This is because the error for the two problems A and B are nearly the same if the same FE meshes are used for the two problems A and B.

$$\frac{\left[K_I\right]_B}{\left[K_I^*\right]_A} = \frac{\left[\sigma_y\right]_B}{\left[\sigma_y^*\right]_A} = \frac{\left[\sigma_{y,FEM}\right]_B}{\left[\sigma_{y,FEM}^*\right]_A} \quad \text{although} \quad \left[\sigma_y\right]_B \neq \left[\sigma_{y,FEM}\right]_B \tag{2.4a}$$

It has been reported by Nisitani et al. [17] the stress distributions computed by FEM are almost the same under the same loading conditions of $K_I = const$ for various crack problems, independent of the crack lengths. Then the SIF for problem B (the given unknown problem) can be accurately determined using Eq.(2.4b). It should be noted that

the same FE mesh grids have to be used in the singular region near the crack tip to compute σ_y^*, σ_y for problems A and B.

$$\left[K_I\right]_B = \frac{\left[\sigma_{y,FEM}\right]_B}{\left[\sigma^*_{y,FEM}\right]_A}\left[K_I^*\right]_A \tag{2.4b}$$

2.2.2 Formulation for the interface crack problems

The method discussed in Section 2.2.1 can not be used directly into solving the interface crack problems since oscillatory singularity is observed along the interface. Oda et al. [16] extended this method to the interface crack problems by creating the same singular stress fields for the reference and target unknown problems. A definition of the SIFs for an interface crack in bonded dissimilar materials was proposed by Erdogan (1965). The stress distributions along the interface are defined as shown in Eq. (2.5).

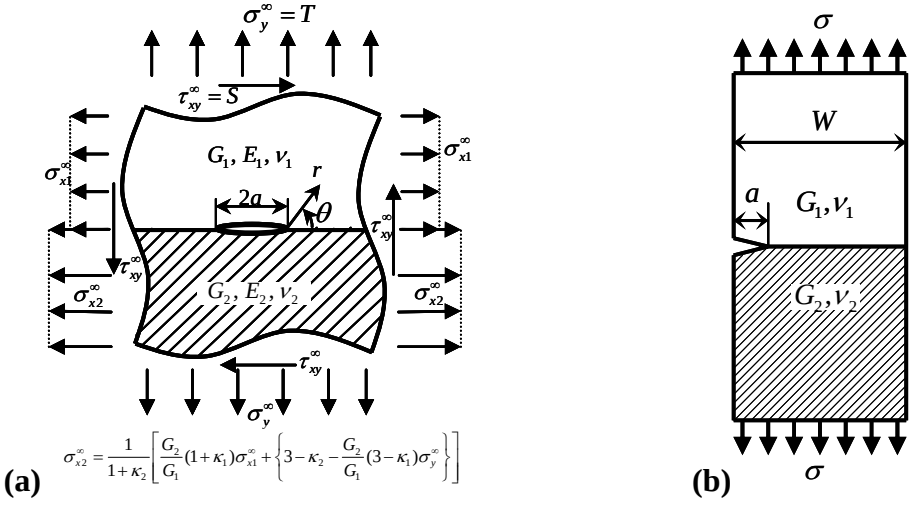

Fig. 2.1 Demonstration of (a) the reference problem (problem C) and (b) a given unknown problem (problem D)

$$\sigma_y + i\tau_{xy} = \frac{K_I + iK_{II}}{\sqrt{2\pi r}}\left(\frac{r}{2a}\right)^{i\varepsilon}, r \to 0 \tag{2.5}$$

Here, σ_y, τ_{xy} denote the stress components near the crack tip, r is the radial distance from the crack tip, and ε is the bi-elastic constant given by:

$$\varepsilon = \frac{1}{2\pi}\ln\left[\left(\frac{\kappa_1}{G_1}+\frac{1}{G_2}\right)/\left(\frac{\kappa_2}{G_2}+\frac{1}{G_1}\right)\right] \tag{2.6}$$

$$\kappa_m = \begin{cases} 3-4\nu_m \ (plane \quad strain) \\ 3-\nu_m/1+\nu_m \ (plane \quad stress) \end{cases}, \quad (m=1,2) \tag{2.7}$$

where $G_m\,(m=1,2)$, $\nu_m\,(m=1,2)$ and $\kappa_m\,(m=1,2)$ are the shear moduli, Poisson's ratios and Kolosov constant of either respective materials. The real and imaginary parts of the oscillatory SIFs $K_I + iK_{II}$ in Eq.(2.5) may be separated as

$$K_I = \lim_{r\to 0}\sqrt{2\pi r}\,\sigma_y\left(\cos Q + \frac{\tau_{xy}}{\sigma_y}\sin Q\right) \tag{2.8}$$

$$K_{II} = \lim_{r\to 0}\sqrt{2\pi r}\,\tau_{xy}\left(\cos Q - \frac{\sigma_y}{\tau_{xy}}\sin Q\right) \tag{2.9}$$

and

$$Q = \varepsilon\ln\left(\frac{r}{2a}\right) \tag{2.10}$$

Similarly, let's consider two different interface crack problems C and D shown in Fig. 2.1 with the same crack lengths $a = a_0$ and the same combination of materials $\varepsilon = \varepsilon_0$, assuming the SIFs of problem C are given in advance and those for problem D are yet to be solved. Problem C is termed the reference problem whose values are marked with *, and problem D is termed the given unknown problem. Examining the points with the same

radial distances $r = r_0$ for the two problems C and D, then gives $\left[Q^*\right]_C = [Q]_D = \varepsilon_0 \ln(\frac{r_0}{2a_0})$. Recall Eq.(2.8) and (2.9), a proportional relationship given in Eq.(2.11) is established if and only if Eq.(2.12) can be satisfied,

$$\frac{\left[K_I\right]_D}{\left[K_I^*\right]_C} = \frac{\left[\sigma_y\right]_D}{\left[\sigma_y^*\right]_C} = \frac{\left[\sigma_{y,FEM}\right]_D}{\left[\sigma_{y,FEM}^*\right]_C}, \frac{\left[K_{II}\right]_D}{\left[K_{II}^*\right]_C} = \frac{\left[\tau_{xy}\right]_D}{\left[\tau_{xy}^*\right]_C} = \frac{\left[\tau_{xy,FEM}\right]_D}{\left[\tau_{xy,FEM}^*\right]_C} \tag{2.11}$$

$$\left[\frac{\tau_{xy}^*}{\sigma_y^*}\right]_C = \left[\frac{\tau_{xy}}{\sigma_y}\right]_D \tag{2.12}$$

Then the SIFs of the given unknown problem (problem D) can be computed using Eq.(2.13) in a similar manner as discussed in Section 2.2.1. The condition of Eq.(2.12) can be satisfied by choosing a suitable external load for the reference problem. The detailed information about how to make the condition Eq.(2.12) satisfied by using FEM will be discussed in section 2.2.3.

$$\begin{aligned}
[K_I]_D &= \frac{[\sigma_y]_D}{[\sigma_y^*]_C}[K_I^*]_C = \frac{[\sigma_{y,FEM}]_D}{[\sigma_{y,FEM}^*]_C}[K_I^*]_C \\
[K_{II}]_D &= \frac{[\tau_{xy}]_D}{[\tau_{xy}^*]_C}[K_{II}^*]_C = \frac{[\tau_{xy,FEM}]_D}{[\tau_{xy,FEM}^*]_C}[K_{II}^*]_C
\end{aligned} \tag{2.13}$$

2.2.3 The determination of the reference problem and its external load

In this method, a crack along the interface of two bonded dissimilar half-planes subjected to tension and shear as shown in Fig. 2.1a is treated as the reference problem. The analytical solution of the SIFs at the crack tip for the reference problem takes the form

$$K_I^* + iK_{II}^* = (\sigma_y^\infty + i\tau_{xy}^\infty)\sqrt{\pi a}(1+2i\varepsilon) \tag{2.14}$$

where $\sigma_y^\infty, \tau_{xy}^\infty$ are the remote uniform tension and shear applied to the bonded dissimilar half-planes.

Using the principle of superposition, the stress components of the reference problem subjected to remote tension and shear $\sigma_y^\infty, \tau_{xy}^\infty$ can be expressed by using the values of that subjected to pure unit tension $\sigma_y^\infty = 1, \tau_{xy}^\infty = 0$ and pure unit shear $\sigma_y^\infty = 0, \tau_{xy}^\infty = 1$. Let $\sigma_{y0,FEM}{}^*, \tau_{xy0,FEM}{}^*$, $\sigma_{y0,FEM}^{\sigma_y^\infty=1,\tau_{xy}^\infty=0}{}^*, \tau_{xy0,FEM}^{\sigma_y^\infty=1,\tau_{xy}^\infty=0}{}^*$ and $\sigma_{y0,FEM}^{\sigma_y^\infty=0,\tau_{xy}^\infty=1}{}^*, \tau_{xy0,FEM}^{\sigma_y^\infty=0,\tau_{xy}^\infty=1}{}^*$ denote the stress components at the crack tip of the reference problem subjected to combined remote tension and shear $\sigma_y^\infty, \tau_{xy}^\infty$, pure unit tension $\sigma_y^\infty = 1, \tau_{xy}^\infty = 0$ and pure unit shear $\sigma_y^\infty = 0, \tau_{xy}^\infty = 1$, respectively. Then $\sigma_{y0,FEM}{}^*, \tau_{xy0,FEM}{}^*$ take the following form

$$\sigma_{y0,FEM}{}^* = \sigma_{y0,FEM}^{\sigma_y^\infty=1,\tau_{xy}^\infty=0}{}^* \times \sigma_y^\infty + \sigma_{y0,FEM}^{\sigma_y^\infty=0,\tau_{xy}^\infty=1}{}^* \times \tau_{xy}^\infty \tag{2.15}$$

$$\tau_{xy0,FEM}{}^* = \tau_{xy0,FEM}^{\sigma_y^\infty=1,\tau_{xy}^\infty=0}{}^* \times \sigma_y^\infty + \tau_{xy0,FEM}^{\sigma_y^\infty=0,\tau_{xy}^\infty=1}{}^* \times \tau_{xy}^\infty \tag{2.16}$$

Recall Eq.(2.12), the FE stress components at the crack tip for the problems C and D behave

$$\left[\frac{\tau_{xy0,FEM}{}^*}{\sigma_{y0,FEM}{}^*}\right]_C = \left[\frac{\tau_{xy0,FEM}}{\sigma_{y0,FEM}}\right]_D \tag{2.17}$$

where, the superscript 0 stands for the node at the crack tip. Inserting Eq.(2.15), (2.16) into Eq.(2.17) gives the solution of $\tau_{xy}^\infty / \sigma_y^\infty$ needed for determining the external loads applied to the reference problem.

$$\frac{\tau_{xy}^\infty}{\sigma_y^\infty} = \frac{\sigma_{y0,FEM}^{\sigma_y^\infty=1,\tau_{xy}^\infty=0}{}^* \times \tau_{xy0,FEM} - \tau_{xy0,FEM}^{\sigma_y^\infty=1,\tau_{xy}^\infty=0}{}^* \times \sigma_{y0,FEM}}{\tau_{xy0,FEM}^{\sigma_y^\infty=0,\tau_{xy}^\infty=1}{}^* \times \sigma_{y0,FEM} - \sigma_{y0,FEM}^{\sigma_y^\infty=0,\tau_{xy}^\infty=1}{}^* \times \tau_{xy0,FEM}} \tag{2.18}$$

Let $\sigma_y^{\infty}=1$ so that τ_{xy}^{∞} can be determined. Inserting $\sigma_y^{\infty}=1,\tau_{xy}^{\infty}$ into Eq.(2.14) gives the values of the oscillatory SIFs for the reference problem (problem C). Finally, the SIFs for the given unknown problem (problem D) can be yielded using the proportional relationship as given in Eq.(2.19).

$$[K_I]_D=\frac{[\sigma_{y0,FEM}]_D}{[\sigma^*_{y0,FEM}]_C}[K_I^*]_C,\quad [K_{II}]_D=\frac{[\tau_{xy0,FEM}]_D}{[\tau^*_{xy0,FEM}]_C}[K_{II}^*]_C \tag{2.19}$$

Specially, when both materials for a bonded structure are identical, all the imaginary terms in the discussion vanish. Thus, the current method is also applicable to the homogenous crack problems.

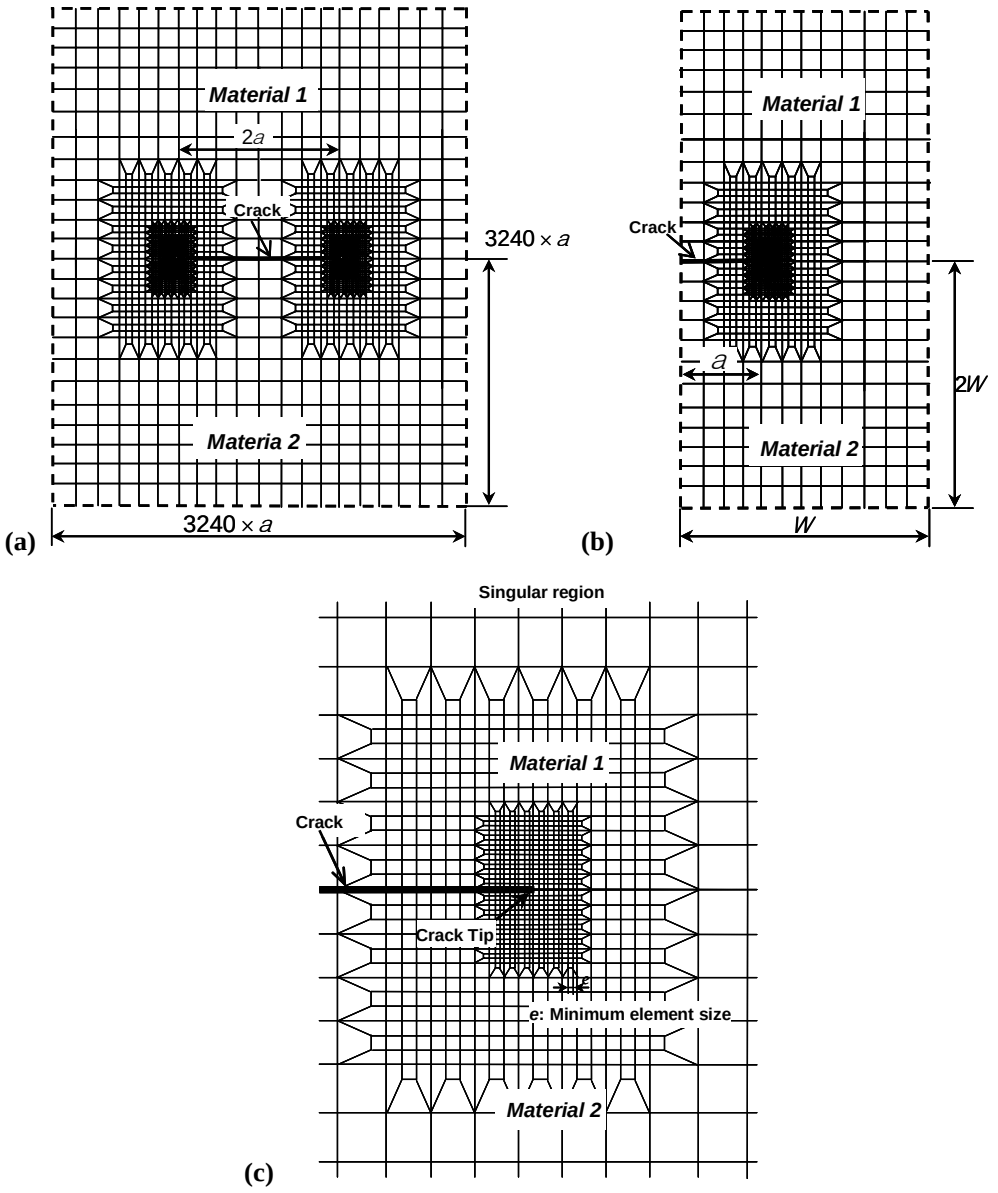

Fig. 2.2 FE model geometric configurations for (a) the reference problem and (b) the target unknown problem (c) the FE mesh in the singular region used for the analysis

2.3 Post-processing technique of linear extrapolation and numerical verification

In this study, the efficiency and accuracy of the crack tip stress method mentioned above are demonstrated by pursuing a convergence study. The effects of the minimum element size e and the number of refined layers NL in FE analysis will be investigated and depicted through several numerical examples.

2.3.1 Specifications and configurations of the FE models

The MSC.MARC 2007 r1 [19] finite element analysis package is used to compute the stress components in this research. Fig. 2.2a shows the FE model geometric configurations for the reference problem shown in Fig. 2.1a. The crack length for the dissimilar bonded half-planes shown in Fig.2a (the reference problem) is set to $2a = 20mm$ in this research. It should be noted that the FE stress components at the crack tip for the reference problem converge as the width of the model is larger than 1500 times the crack length a [16]. Then a plate width of $W = 1620 \times 2a = 32400mm$ and a length of $L = 2W = 64800mm$ are used to model the reference problem ($L = 2W, W/a = 1620$). Fig. 2.2b shows the FE model geometric configurations for the single-edge cracked bonded strip shown in Fig. 2.1b (an example for the target unknown problem). The crack length for the target unknown problem is fixed to a=10mm which is the same as the half crack length of the reference problem. The width of the bonded strip W varies from $a/W = 0.1 \sim 0.9$, the length L is assumed to be much greater than the width W ($L = 2W$ is assumed in the FE model). Furthermore, the minimum element size e of the FE models are kept the same for the reference and given unknown problems.

The singular regions around the crack tip of both the reference and the target unknown problems are well refined in a self-similar manner. Fig. 2.2c shows the FE mesh type in the singular region. The singular region is refined with increasing the number of layers and the element size for each inferior layer is one third of the superior one. The meshes shown in Fig. 2.2a and b are made of eight-node quadrilateral elements in plane stress or plane strain condition. Furthermore, the meshes for the reference and target unknown problems are kept the same to make sure a high computational accuracy of $\left[\tau_{xy}^{*}/\sigma_{y}^{*}\right]_{C} = \left[\tau_{xy}/\sigma_{y}\right]_{D}$. It should be noted that although highly accurate stress components

σ_y, τ_{xy} near the crack tip can't be obtained for the two problems by FE analysis, the ratios of τ_{xy}/σ_y are fairly accurate since the same FE mesh sizes and model density are assumed in the computation.

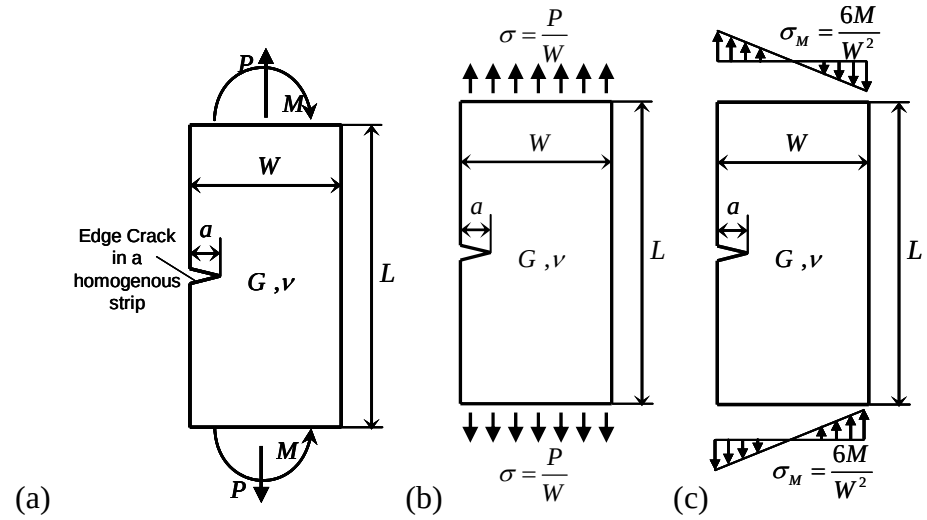

Fig. 2.3 (a) a single-edge-cracked homogenous strip subjected to tension and bending loading conditions , tensions at the top and bottom boundaries to counter the (b) tensile and (c) the bending loading conditions

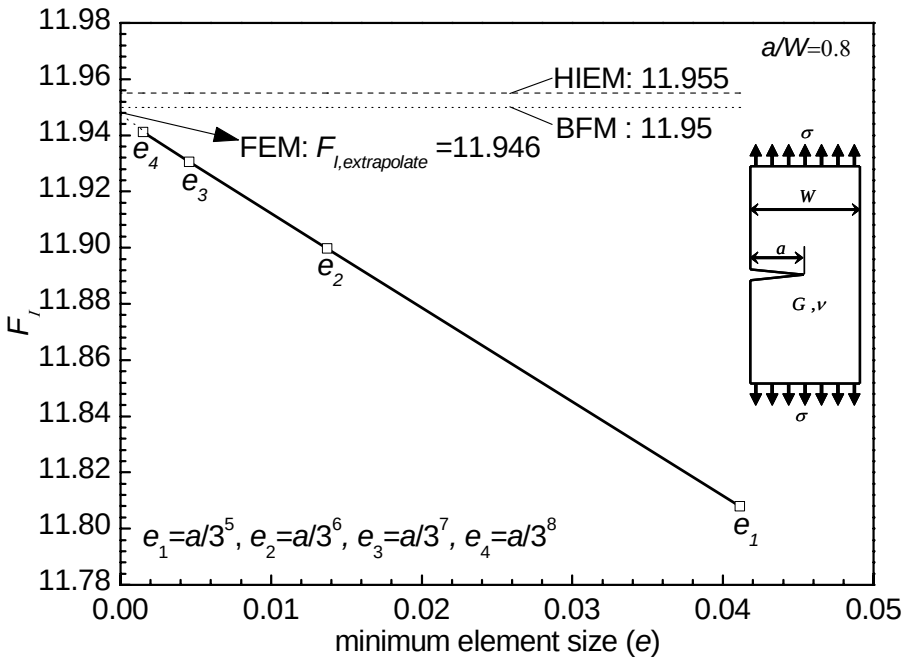

(a)

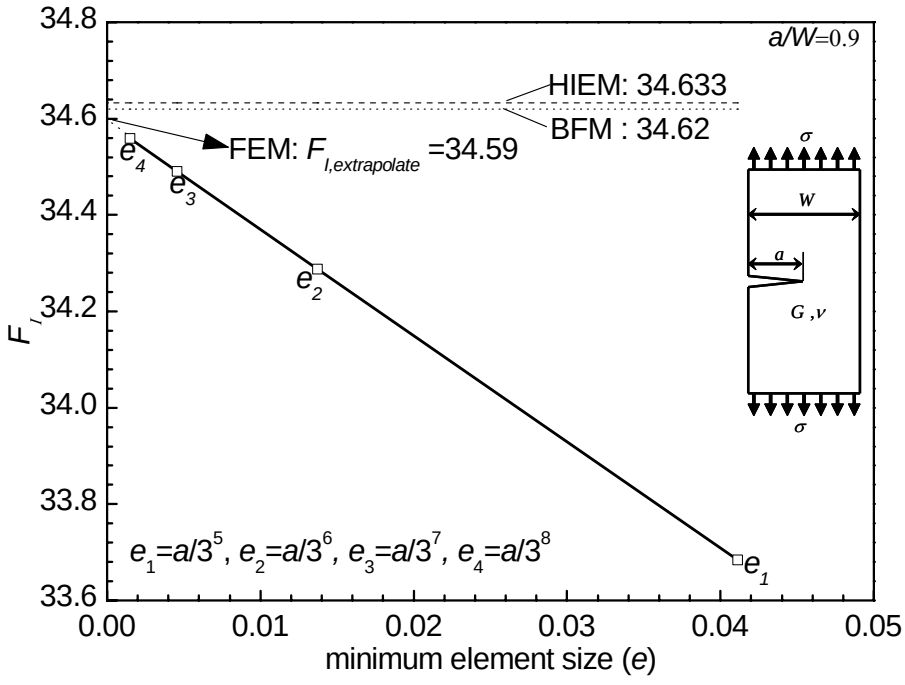

(b)

Fig. 2.4 Extrapolation of normalized SIFs $F_I = K_I / \sigma\sqrt{\pi a}$ for a homogenous strip subjected to (a)(b) tensile and (c)(d) bending loads (Continue)

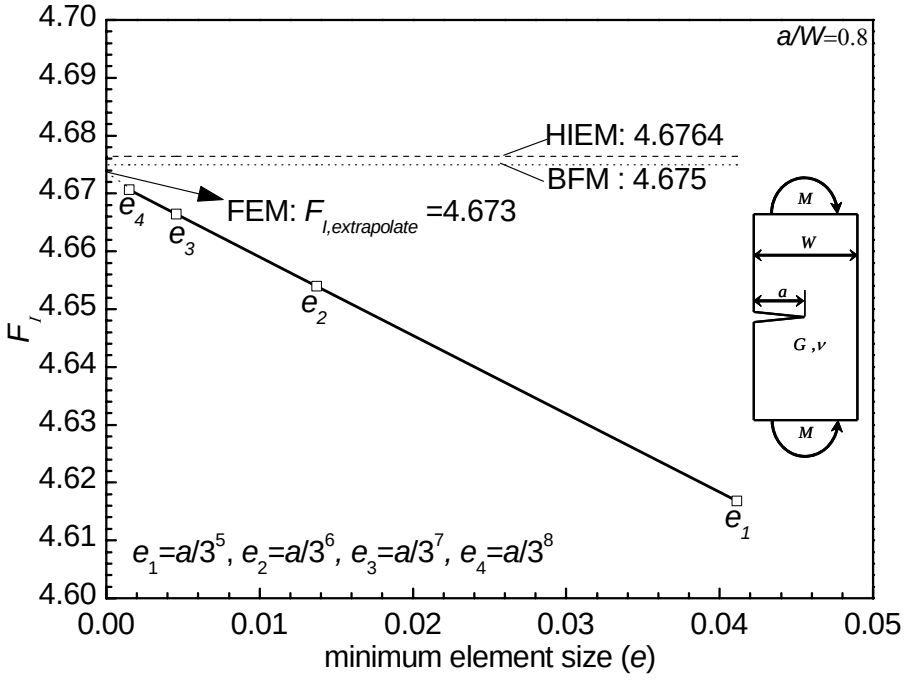

(c)

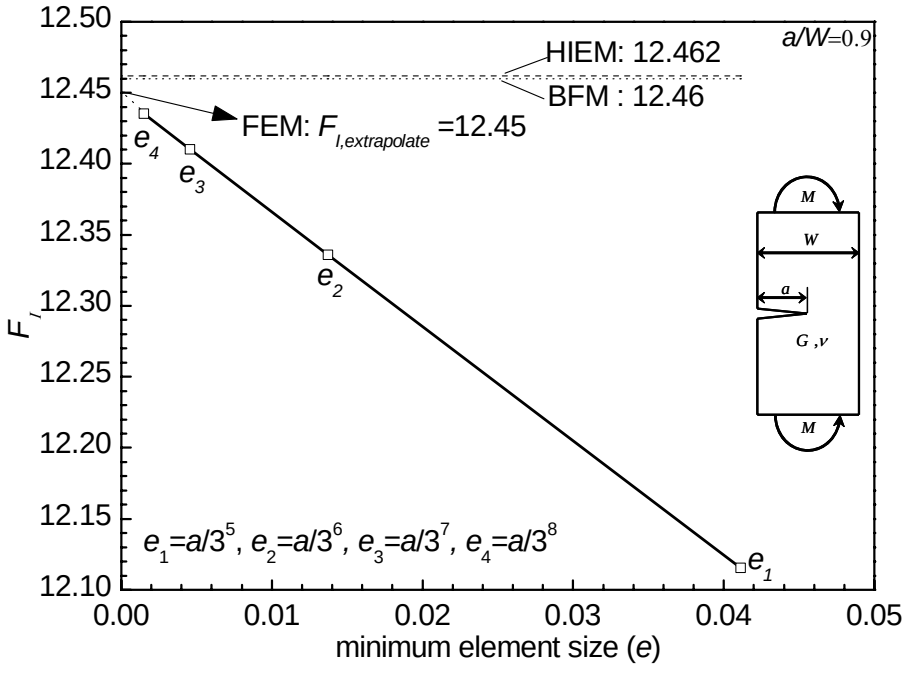

(d)

Fig. 2.4 Extrapolation of normalized SIFs $F_I = K_I/\sigma\sqrt{\pi a}$ for a homogenous strip subjected to (a)(b) tensile and (c)(d) bending loads

Table 2.1 Mode I SIFs $K_I/\sigma\sqrt{\pi a}$ of a single edge cracked homogenous strip shown in Fig. 2.3a for various relative crack lengths and different minimum element sizes

a/W	Uniform tension				In-plane bending			
	Case 1	Case 2	Case 3	Case 4	Case 1	Case 2	Case 3	Case 4
	e=a/243	*e=a*/729	*e=a*/2187	*e=a*/6561	*e=a*/243	*e=a*/729	*e=a*/2187	*e=a*/6561
0.1	1.1883	1.1886	1.1887	1.1887	1.0447	1.0450	1.0451	1.0452
0.2	1.3659	1.3665	1.3667	1.3668	1.0536	1.0541	1.0543	1.0544
0.3	1.6576	1.6588	1.6593	1.6594	1.1222	1.1232	1.1235	1.1237
0.4	2.1073	2.1098	2.1106	2.1109	1.2578	1.2596	1.2601	1.2603
0.5	2.8159	2.8210	2.8228	2.8234	1.4921	1.4951	1.4961	1.4965
0.6	4.0141	4.0253	4.0291	4.0304	1.9042	1.9100	1.9119	1.9126
0.7	6.3093	6.3374	6.3468	6.3500	2.7046	2.7173	2.7216	2.7231
0.8	11.8078	11.8997	11.9306	11.9410	4.6168	4.6539	4.6664	4.6706
0.9	33.6838	34.2870	34.4904	34.5588	12.1154	12.3359	12.4102	12.4352

Table 2.2 Normalized SIF $K_I/\sigma\sqrt{\pi a}$ computed by linear extrapolation for Fig. 2.3a

$\frac{a}{W}$	Uniform tension				In-plane bending			
	Present	Original	Kaya-Erdogan (1987) [20]	Noda et al. (1992) [21]	Present	Original	Kaya-Erdogan (1987) [20]	Noda et al. (1992) [21]
0.1	1.189	1.188	1.1892	1.189	1.045	1.044	1.0472	1.046
0.2	1.367	1.366	1.3673	1.367	1.054	1.054	1.0553	1.054
0.3	1.659	1.658	1.6599	1.659	1.124	1.122	1.1241	1.123
0.4	2.111	(2.107)	2.1114	2.111	1.260	(1.258)	1.2606	1.259
0.5	2.824	(2.816)	2.8246	2.823	1.497	(1.492)	1.4972	1.495
0.6	4.031	(4.014)	4.0332	4.032	1.913	(1.904)	1.9140	1.913
0.7	6.352	(6.309)	6.3549	6.355	2.724	(2.705)	2.7252	2.725
0.8	11.946	(11.808)	11.955	11.95	4.673	(4.617)	4.6764	4.675
0.9	34.593	(33.6834)	34.633	34.62	12.448	(12.115)	12.462	12.46

2.3.2 Convergence study for the single-edge-cracked homogenous strip

A single edge-cracked homogenous strip subjected to tensile and bending loads as shown in Fig. 2.3a is analyzed for various crack sizes (for a range of $a/W = 0.1 \sim 0.9$). Fig. 2.3b and c show the tension applied at the top and the bottom boundaries to counter the tensile load and bending moment applied to the plate shown in Fig. 2.3a, respectively.

In order to investigate the effects of the minimum element size e and FE model density on the SIFs, four pairs of models (a pair of model is composed by one reference problem and one target unknown problem with the same model densities) with different minimum element sizes are tested to carry out the convergence study. The mesh pattern, model density and minimum element size for each pair of models are fixed the same. Namely, the minimum element size for each pair of models is $a/3^5, a/3^6, a/3^7, a/3^8$ which corresponding to the total number of mesh layers $NL = 9,10,11,12$, respectively.

The results computed from different pairs of models are presented in Table 2.1. It can be seen from this table that the minimum element size (number of refined layers NL) has a significant effect on the accuracy especially when the crack length is considerably deep, say when $a/W \geq 0.4$. This effect becomes particularly prominent as the crack length increases. The SIFs for the extremely deep crack cases ($a/W = 0.8, 0.9$) are plotted against the minimum element size in Fig. 2.4. The accurete results obtained by the body force method (BFM) and the hypersingular equation method (HIEM) are plotted in dashed lines. It can be seen that increasing the number of refined layers (NL) can significantly improve the accuracy, however, this will lead to dramatic increase in the number of FE elements, and consequently the computational cost. Fig. 2.4 also demonstrates that accurate results can be obtained using linear extrapolation of SIFs from meshes with different minimum element sizes. Specifically, when increasing the number of refined layers $NL \to \infty$, the minimum element size $e \to 0$. Hence, the accurate SIFs for $NL \to \infty$ can be computed using the following equation.

$$K_{accu} = K^{e=0} = \left(e_2 K^{e1} - e_1 K^{e2}\right) \Big/ \left(e_2 - e_1\right), \quad e_1 \neq e_2 \leq a / 243 \tag{2.20}$$

Where $K^{e=0}$ is the extrapolated SIF, and K^{e1} K^{e2} are the SIFs computed by two different meshes with the minimum element sizes e_1, e_2 respectively. The values of SIFs computed by the present method are tabulated and compared to those predicted by

Kaya-Erdogan [20] and Noda et al. [21] in Table 2.2. It can be seen that the extrapolated results and those of Kaya-Erdogan [20] and Noda et al. [21] are in very good agreement, and their accuracy is much better than the original method [16].

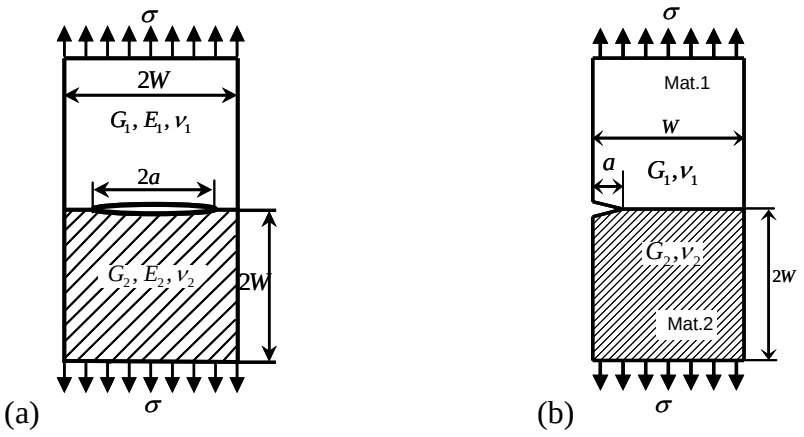

Fig. 2.5 (a) a central-cracked and (b) an edge-cracked dissimilar bonded strip subjected to uniform tension

2.2.3 Convergence study for central and single-edge interface crack problems

Two-dimensional plane-stress problems of central and single-edge interface crack problems are analyzed for various crack lengths. The problems are demonstrated in Fig. 2.5a and b, respectively. The FE models are built in a similar manner as depicted in Section 2.3.1. Fig. 2.6 shows the results for a central cracked bonded strip with a relative crack length of $a/W = 0.8$. The elastic parameters in Fig. 2.6 are restricted to $E_1/E_2 = 4, \nu_1 = \nu_2 = 0.3$. As can be seen from Fig. 2.6, extrapolation is not necessary for the central crack case since the results converge asymptotically with increasing the number of refined layers around the singular region when $NL \geq 9$. The SIF values for others material combinations are tabulated in Table 2.3 together with those predicted by other researchers. As shown in the table, the improved crack tip stress method results almost coincide with those of the original one [16],

and they are in very good agreement with those of Yuuki and Cho [1] and Miyazaki et al. [2]. Therefore, the post-processing technique of extrapolation is not necessary for the central interface crack case. And accurate results can be obtained by using meshes with minimum element size smaller than $a/729$.

The SIFs for the edge cracked dissimilar bonded strip $a/W = 0.7, 0.8$ are plotted and compared with those of Yuuki and Cho [1] and Miyazaki et al. [2] in Fig. 2.7. The elastic parameters in Fig. 2.7 are also restricted to $E_1/E_2 = 4, \nu_1 = \nu_2 = 0.3$. The data of Yuuki and Cho [1] and Miyazaki et al. [2] are plotted in dashed lines. From this figure, it can be seen that the normalized SIF $K_I/\sigma\sqrt{\pi a}$ also behave linear relationship with the minimum element size. Good results can be obtained by using linear extrapolation without adding too more refined layers. Here, it should be noted that the exact values for $K_{II}/\sigma\sqrt{\pi a}$ should also be computed through linear extrapolation although a simple linear behavior is not observed for this case. For the not deep crack case, post-processing of extrapolation is also necessary since the effect of minimum element size e to the SIFs is dominated by the bi-material elastic properties. This means the original method may also include un-ignored errors for the not deep crack case. In this study, models with the minimum element size $e = a/3^6, a/3^7$ are recommended since they have the best compromise between accuracy and computational cost. The normalized SIFs for other material combinations are tabulated in Table 2.4 together with those of Yuuki and Cho [1] and Miyazaki et al. [2]. Table 2.4 illustrates that the SIF values computed by the current method are in very good agreement with those predicted by Yuuki and Cho [1] and Miyazaki et al. [2]. Furthermore, the results computed by the current method are much better than those predicted by the original method [16], especially for the deep crack cases. The results computed by the original method [16] for the deep crack case are given in parentheses in Table 2.4. Therefore, the current method can get accurate SIFs without using high model density (say, the total

number of layers is $NL = 10,11$ in this research), and it has a faster convergence speed than other numerical methods.

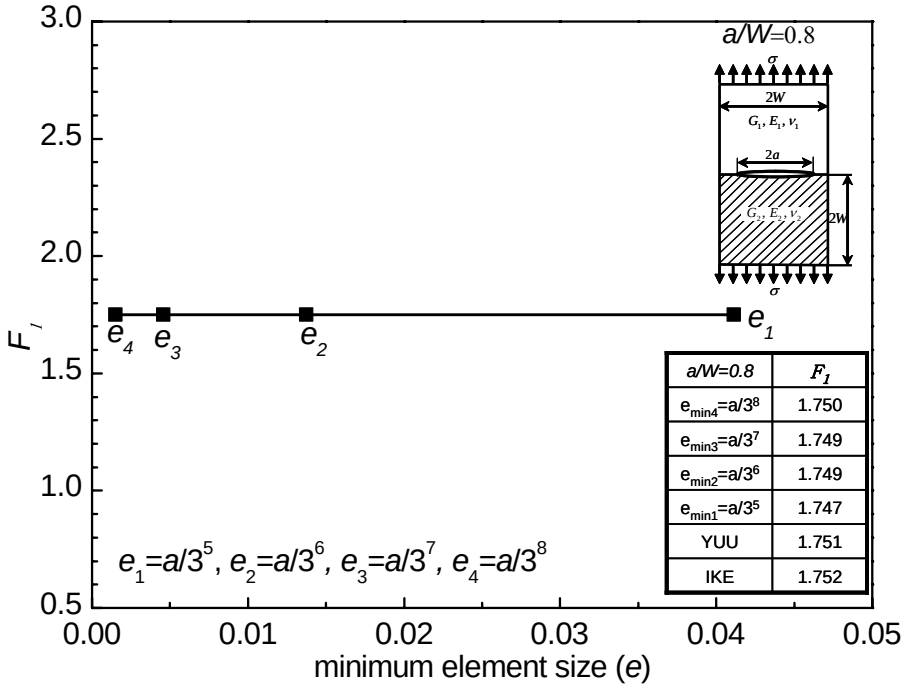

a/W=0.8	F_1
$e_{min4}=a/3^8$	1.750
$e_{min3}=a/3^7$	1.749
$e_{min2}=a/3^6$	1.749
$e_{min1}=a/3^5$	1.747
YUU	1.751
IKE	1.752

(a)

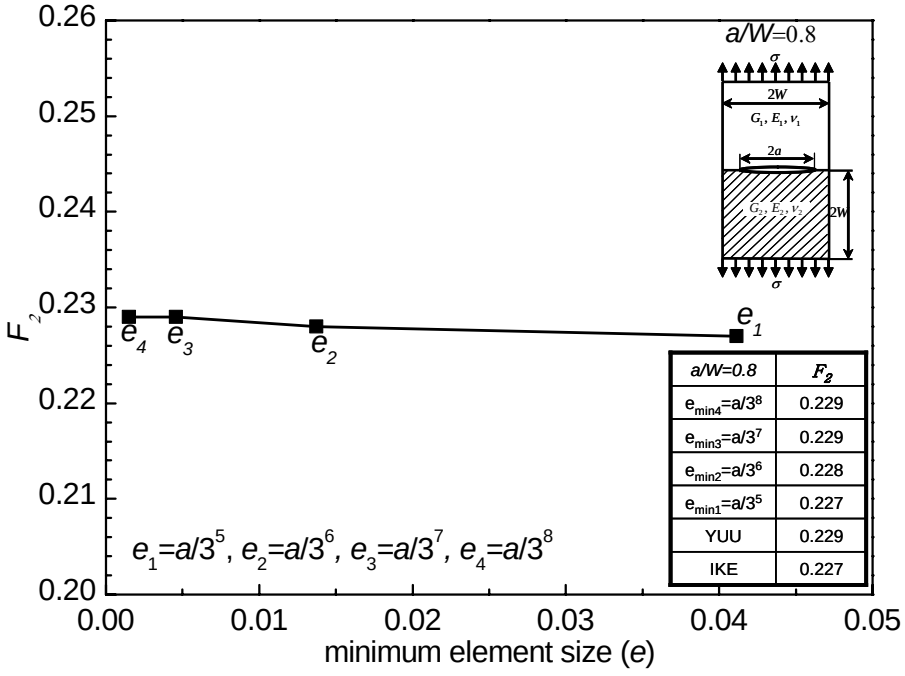

a/W=0.8	F_2
$e_{min4}=a/3^8$	0.229
$e_{min3}=a/3^7$	0.229
$e_{min2}=a/3^6$	0.228
$e_{min1}=a/3^5$	0.227
YUU	0.229
IKE	0.227

(b)

Fig. 2.6 Variations of normalized SIFs $F_1 = K_1/\sigma\sqrt{\pi a}, |F_2| = |K_2|/\sigma\sqrt{\pi a}$ with minimum element size e of FE models for a bi-material bonded strip

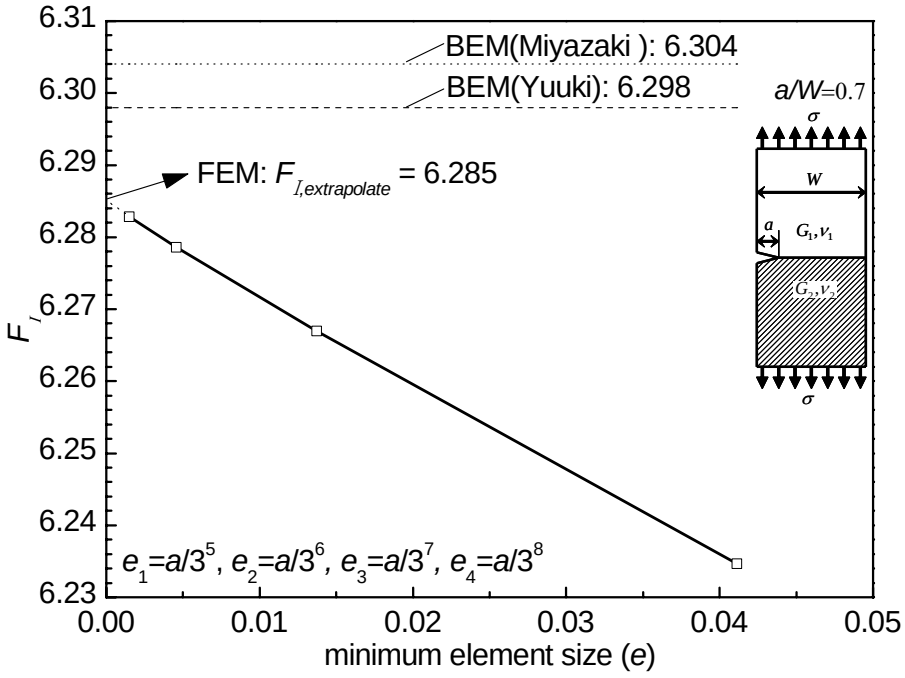

(a)

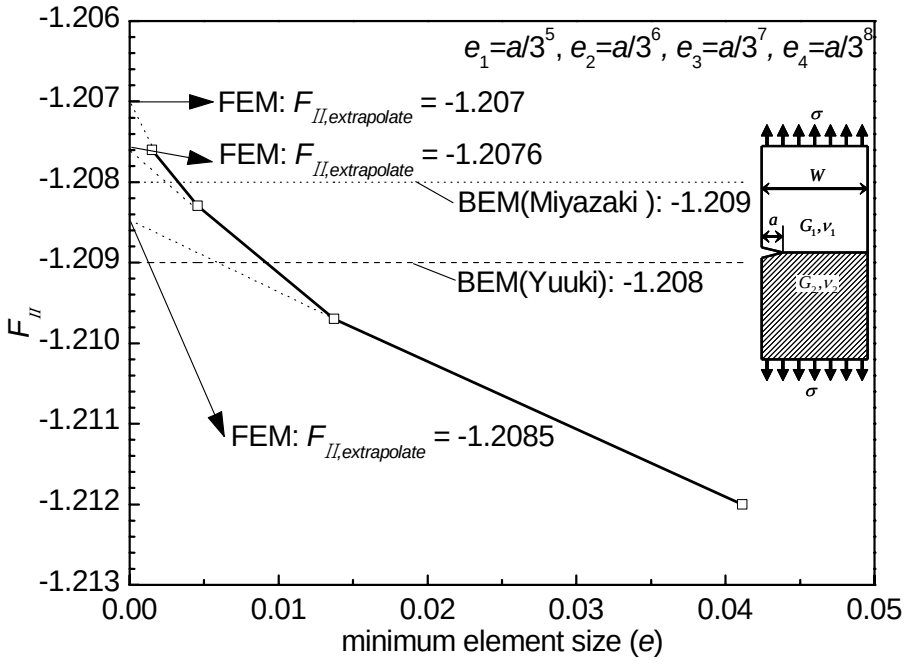

(b)

Fig. 2.7 Variations of normalized SIFs $F_1 = K_1/\sigma\sqrt{\pi a}, F_2 = K_2/\sigma\sqrt{\pi a}$ with the minimum element size e for a bonded strip (a) (b) $a/W = 0.7$ and (c) (d) $a/W = 0.8$ subjected to uniform tension. (Continue)

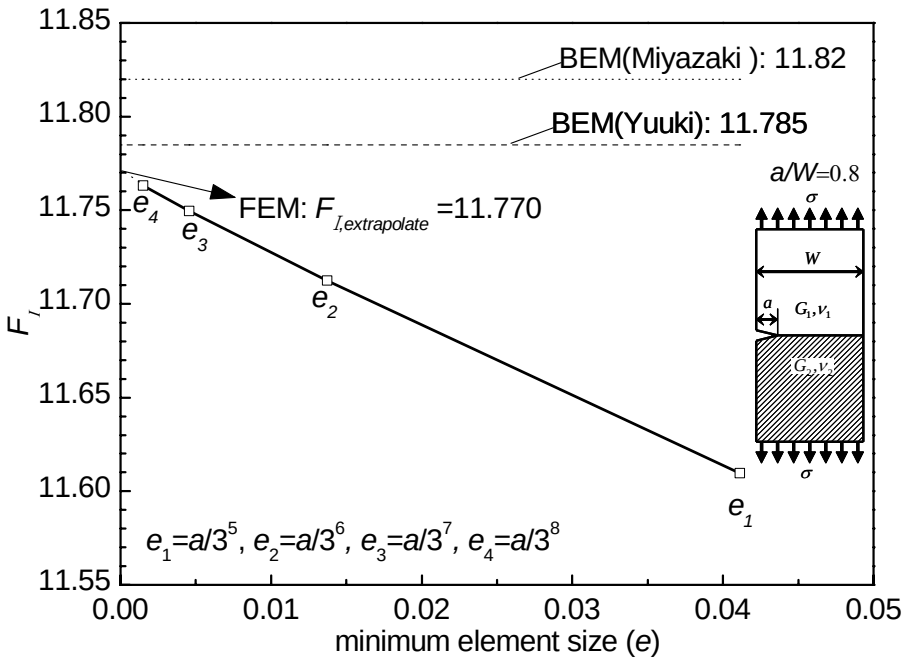

(c)

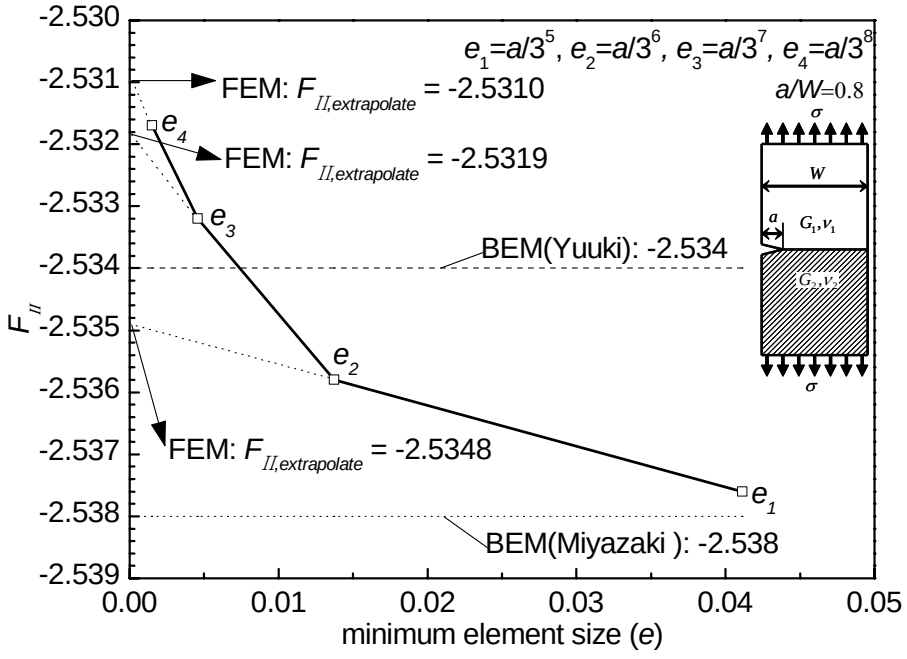

(d)

Fig. 2.7 Variations of normalized SIFs $F_1 = K_1/\sigma\sqrt{\pi a}, F_2 = K_2/\sigma\sqrt{\pi a}$ with the minimum element size e for a bonded strip (a) (b) $a/W = 0.7$ and (c) (d) $a/W = 0.8$ subjected to uniform tension.

Table 2.3 Normalized SIFs for central interface crack ($\nu_1 = \nu_2 = 0.3$,Plane stress)

		$K_I/\sigma\sqrt{\pi a}$				$K_{II}/\sigma\sqrt{\pi a}$			
E_2/E_1	a/W	Present	Oda et al. (2010)	Yuuki-Cho (1989)	Miyazaki et al. (1993)	Present	Oda et al. (2010)	Yuuki-Cho (1989)	Miyazaki et al. (1993)
2	0.1	1.001	1.001	0.996	1.001	-0.072	-0.072	-0.072	-0.072
	0.2	1.019	1.019	1.019	1.020	-0.071	-0.071	-0.071	-0.071
	0.3	1.052	1.052	1.053	1.053	-0.071	-0.071	-0.072	-0.071
	0.4	1.103	1.103	1.104	1.104	-0.073	-0.073	-0.073	-0.073
	0.5	1.179	1.179	1.180	1.181	-0.078	-0.077	-0.078	-0.077
	0.6	1.294	(1.293)	1.294	1.296	-0.086	(-0.086)	-0.085	-0.085
	0.7	1.475	(1.474)	1.477	1.478	-0.101	(-0.101)	-0.100	-0.100
	0.8	1.796	(1.793)	1.798	1.799	-0.132	(-0.131)	-0.131	-0.131
	0.9	2.542	(2.532)	-	-	-0.215	(-0.213)	-	-
4	0.1	0.987	0.987	0.983	0.987	-0.129	-0.129	-0.129	-0.129
	0.2	1.006	1.006	1.005	1.006	-0.127	-0.127	-0.127	-0.127
	0.3	1.038	1.038	1.038	1.031	-0.127	-0.127	-0.127	-0.127
	0.4	1.088	1.088	1.088	1.089	-0.130	-0.130	-0.131	-0.130
	0.5	1.161	1.161	1.162	1.163	-0.138	-0.137	-0.137	-0.137
	0.6	1.271	(1.271)	1.272	1.273	-0.151	(-0.151)	-0.151	-0.150
	0.7	1.445	(1.443)	1.445	1.446	-0.177	(-0.176)	-0.176	-0.176
	0.8	1.750	(1.747)	1.751	1.752	-0.229	(-0.227)	-0.229	-0.227
	0.9	2.457	(2.448)	-	-	-0.370	(-0.365)	-	-
10	0.1	0.968	0.967	0.963	0.968	-0.175	-0.175	-0.173	-0.174
	0.2	0.986	0.986	0.985	0.986	-0.172	-0.172	-0.170	-0.171
	0.3	1.018	1.018	1.018	1.018	-0.171	-0.171	-0.171	-0.170
	0.4	1.065	1.065	1.065	1.066	-0.174	-0.174	-0.174	-0.173
	0.5	1.135	1.134	1.134	1.136	-0.183	-0.182	-0.183	-0.182
	0.6	1.238	(1.238)	1.238	1.239	-0.199	(-0.199)	-0.199	-0.198
	0.7	1.400	(1.399)	1.400	1.402	-0.231	(-0.230)	-0.230	-0.229
	0.8	1.684	(1.682)	1.684	1.686	-0.295	(-0.293)	-0.295	-0.293
	0.9	2.338	(2.333)	-	-	-0.470	(-0.463)	-	-
100	0.1	0.946	0.945	0.940	0.946	-0.206	-0.207	-0.205	-0.206
	0.2	0.964	0.964	0.962	0.964	-0.202	-0.202	-0.201	-0.201
	0.3	0.995	0.996	0.994	0.994	-0.201	-0.200	-0.201	-0.200
	0.4	1.039	1.039	1.038	1.039	-0.203	-0.204	-0.203	-0.203
	0.5	1.105	1.104	1.104	1.104	-0.212	-0.212	-0.211	-0.210
	0.6	1.200	(1.200)	1.201	1.201	-0.229	(-0.229)	-0.228	-0.228
	0.7	1.350	(1.349)	1.349	1.351	-0.262	(-0.261)	-0.260	-0.260
	0.8	1.610	(1.610)	1.610	1.612	-0.329	(-0.327)	-0.328	-0.327
	0.9	2.210	(2.209)	-	-	-0.517	(-0.508)	-	-

Table 2.4 Normalized SIFs for edge interface cracks
($v_1 = v_2 = 0.3$, Plane stress)

		$K_I/\sigma\sqrt{\pi a}$				$K_{II}/\sigma\sqrt{\pi a}$			
E_2/E_1	a/W	Present	Oda et al. (2010)	Yuuki-Cho (1989)	Miyazaki et al. (1993)	Present	Oda et al. (2010)	Yuuki-Cho (1989)	Miyazaki et al. (1993)
2	0.1	1.195	1.193	1.188	1.195	-0.129	-0.129	-0.128	-0.129
	0.2	1.367	1.365	1.366	1.368	-0.137	-0.137	-0.137	-0.137
	0.3	1.658	1.653	1.657	1.659	-0.158	-0.158	-0.157	-0.158
	0.4	2.108	2.101	2.108	2.110	-0.198	-0.198	-0.198	-0.198
	0.5	2.818	2.790	2.820	2.882	-0.267	-0.316	-0.268	-0.267
	0.6	4.021	(4.003)	4.024	4.031	-0.396	(-0.398)	-0.398	-0.397
	0.7	6.331	(6.286)	6.348	6.353	-0.670	(-0.673)	-0.673	-0.670
	0.8	11.892	(11.747)	11.930	11.950	-1.406	(-1.411)	-1.407	-1.410
	0.9	34.330	(33.394)	-	-	-4.891	(-4.871)	-	-
4	0.1	1.209	1.207	1.201	1.209	-0.239	-0.240	-0.238	-0.239
	0.2	1.368	1.365	1.387	1.368	-0.251	-0.251	-0.254	-0.250
	0.3	1.653	1.644	1.653	1.654	-0.288	-0.286	-0.288	-0.288
	0.4	2.100	2.093	2.100	2.101	-0.359	-0.359	-0.359	-0.359
	0.5	2.805	2.791	2.807	2.807	-0.484	-0.484	-0.483	-0.483
	0.6	3.998	(3.977)	4.000	4.006	-0.716	(-0.718)	-0.701	-0.716
	0.7	6.284	(6.235)	6.298	6.304	-1.208	(-1.212)	-1.209	-1.208
	0.8	11.768	(11.610)	11.785	11.820	-2.532	(-2.538)	-2.534	-2.538
	0.9	33.735	(32.741)	-	-	-8.797	(-8.742)	-	-
10	0.1	1.229	1.228	1.220	1.229	-0.340	-0.341	-0.338	-0.340
	0.2	1.369	1.367	1.367	1.369	-0.349	-0.350	-0.349	-0.349
	0.3	1.648	1.643	1.646	1.648	-0.399	-0.400	-0.398	-0.399
	0.4	2.089	2.082	2.088	2.090	-0.495	-0.495	-0.495	-0.494
	0.5	2.787	2.772	2.788	2.789	-0.664	-0.663	-0.664	0.663
	0.6	3.967	(3.944)	3.966	3.974	-0.979	(-0.981)	-0.980	-0.978
	0.7	6.224	(6.168)	6.229	6.241	-1.648	(-1.652)	-1.651	-1.648
	0.8	11.611	(11.436)	11.590	11.660	-3.450	(-3.451)	-3.454	-3.456
	0.9	32.984	(31.921)	-	-	-11.968	(-11.858)	-	-
100	0.1	1.252	1.251	-	1.251	-0.425	-0.426	-	-0.424
	0.2	1.370	1.368	-	1.370	-0.428	-0.429	-	-0.428
	0.3	1.642	1.637	-	1.642	-0.485	-0.486	-	-0.485
	0.4	2.078	2.070	-	2.078	-0.598	-0.597	-	-0.597
	0.5	2.770	2.754	-	2.770	-0.799	-0.797	-	-0.797
	0.6	3.937	(3.912)	-	3.940	-1.173	(-1.175)	-	-1.172
	0.7	6.165	(6.104)	-	6.177	-1.972	(-1.973)	-	-1.969
	0.8	11.459	(11.270)	-	11.500	-4.121	(-4.114)	-	-4.124
	0.9	32.267	(31.146)	-	-	-14.277	(-14.106)	-	-

2.3.4 Examples of axisymmetrical crack problems in a cylindrical bar

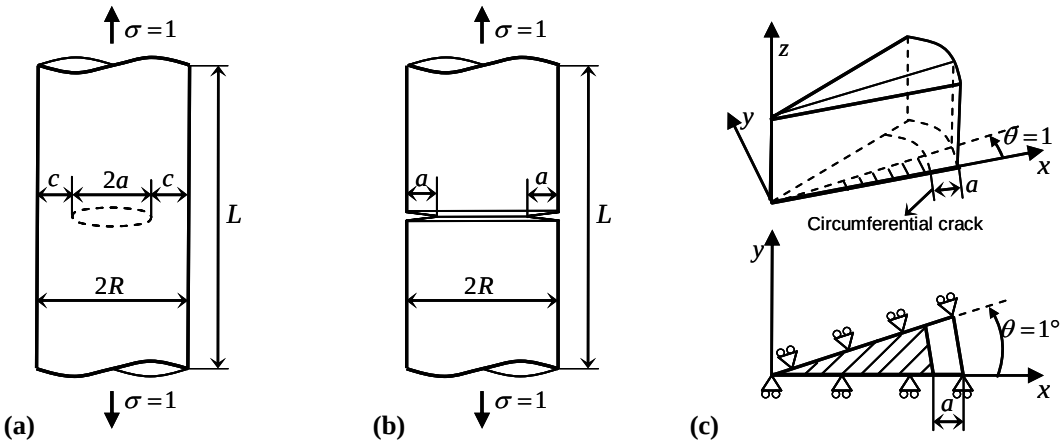

Fig. 2.8 (a) a penny-shaped crack and (b) a circumferential surface crack in a cylindrical bar under tension (c) 3-D FE mesh geometry of circumferential crack

Table 2.5 Normalized stress intensity factors $K_I/\sigma\sqrt{\pi a}$ of a single circumferential crack in a round bar

a/R	Penny-shaped crack			Circumferential surface crack		
	Axisy model	3-D model	Ref [26]	Axisy model	3-D model	Ref[27]
0.1	0.6369	0.6369	0.6369	1.1811	1.1825	1.180
0.2	0.6393	0.6394	0.6396	1.2620	1.2616	1.261
0.3	0.6462	0.6462	0.6468	1.3930	1.3928	1.393
0.4	0.6600	0.6600	0.6616	1.6017	1.6016	1.602
0.5	0.6855	0.6856	0.6881	1.9388	1.9387	1.940
0.6	0.7294	0.7294	0.7335	2.5142	2.5142	2.516
0.7	0.8067	0.8067	0.8123	3.6153	3.6152	3.618
0.8	0.9551	0.9552	0.9613	6.2381	6.2382	6.243
0.9	1.3218	1.3217	1.3251	16.6569	16.6566	16.67

The applicable possibility of treating the axisymmetrical crack problems by using the improved crack tip stress method is discussed in this section. Requirements of the mesh patterns are further investigated and discussed. Similarly, the 8-node quadrilateral element in plane strain condition is used to build the reference problem as discussed in section 2.3.1.

And two different mesh types as the 8-node axisymmetric solid element and eight-node hexahedral solid element are used to mesh the penny-shaped and circumferential surface crack problems as shown in Fig. 2.8a and b, respectively. The 2D axisymmetric model is refined in a similar way as shown in Fig. 2.2c, and the 3D FE model and its boundary conditions are demonstrated in Fig. 2.8c. A convergence study for the normalized SIFs with the minimum element sizes for the axisymmetrical crack problems under deep crack case $a/R = 0.9$ is shown in Fig. 2.9. It can be seen from Fig. 2.9 that linear extrapolation should be used for both the penny-shaped and circumferential crack problems. The normalized SIFs for penny-shaped and circumferential cracks as well as those of Benthem [22] and Nishitani [23] are tabulated and compared in Table 2.5, respectively. It can be seen from this table that the normalized SIFs computed by axisymmetric models coincide with thosed predicted by 3-D solid models. Furthermore, the SIF values predicted by the current method for the penny-shaped crack and circumferential surface crack are in good agreement with those of Benthem[22] and Nishitani [23], respectively. This means the current method is also useful for the axisymmetrical crack problems. And the computational accuracy of the improved proportional method is independent with the FE element types for the reference and target unknown problems.

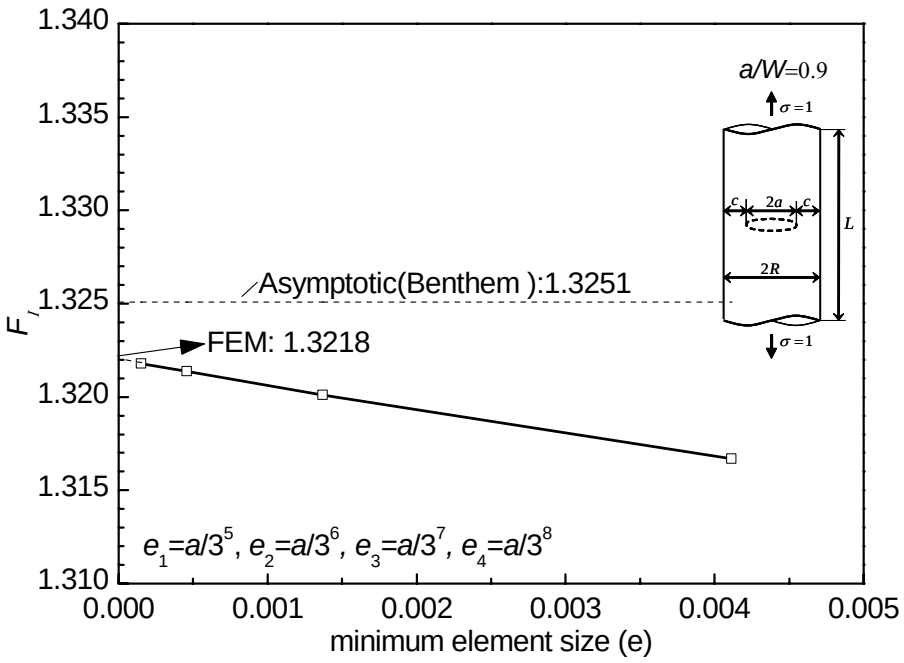

(a)

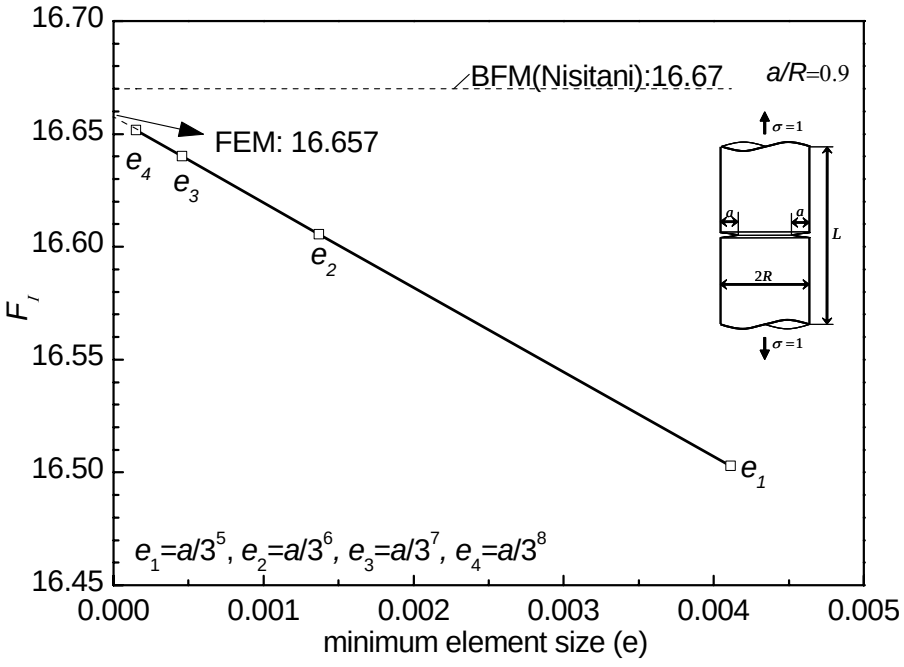

(b)

Fig. 2.9 Extrapolation of normalized SIFs $F_I = K_I / \sigma\sqrt{\pi a}$

Table 2.6 Normalized SIFs for single-edge interface cracks a/W=0.1 computed by different element types (υ 1= υ 2=0.3, Plane Stress)

	E_2/E_1	Reference Tension		Reference Bending		Unknown Tension		Final SIF results		
		σ_y	τ_{xy}	σ_y	τ_{xy}	σ_y	τ_{xy}	$\tau\infty$	F_I	F_{II}
4node	1	20.6855	6.0E-10	0	11.7483	24.5812	0	0	1.1883	0
	2	20.0492	-2.5977	4.8652	11.4294	24.1942	-2.6533	0.0333	1.1941	0.1292
	3	19.2508	-3.8644	7.2250	11.0285	23.7075	-3.9971	0.0505	1.2017	0.1971
	4	18.6162	-4.6060	8.5995	10.7092	23.3198	-4.8142	0.0611	1.2082	0.2398
	10	16.8208	-6.1570	11.447	9.8026	22.2191	-6.6430	0.0853	1.2285	0.3406
	100	15.1168	-7.2287	13.383	8.9377	21.1701	-8.0673	0.1046	1.2512	0.4258
8node	1	26.4101	0	-4.3E-09	17.0392	31.4000	0	0	1.1889	0
	2	25.4466	-4.2596	6.7703	16.4782	30.7417	-4.4474	0.0331	1.1946	0.129
	3	24.2415	-6.3314	10.025	15.7714	29.9139	-6.6975	0.0502	1.2021	0.1967
	4	23.2868	-7.5411	11.906	15.2074	29.2543	-8.0639	0.0607	1.2084	0.2393
	10	20.6003	-10.056	15.744	13.6007	27.3803	-11.114	0.0847	1.2285	0.3399
	100	18.0715	-11.772	18.286	12.0613	25.5920	-13.479	0.1039	1.2511	0.4248

2.4 Effect of element types on the SIFs

The computational accuracy is greatly kept by the current method based on the concept of proportion. Errors of the FE stress components are eliminated to the largest extent in the proportional process in computing SIFs. However, effects of the variations on the element types on the SIFs have not been revealed yet. Therefore, a test was performed to verify the robustness of the method on element types. Various types of elements are available for the FE meshes. For the singular problems, it is suggested that the 8-node quadrilateral element (second order) can catch the stress concentration better than the 4-node quadrilateral element (linear). Two-dimensional plane-stress problem of a single-edge interface crack problem a/W=0.1 is analyzed by using the linear and second order elements for various material combinations. The material properties of the bonded

strip are $E_2/E_1 = 1,2,3,4,10,100, \nu_1 = \nu_2 = 0.3$. The FE models are built in a similar manner as depicted in Section 2.3.1. The FE stress components and SIFs computed from the two types of elements are tabulated in Table 2.6. As can been seen from this table, although the FE stress components computed by the two types of elements are totally different, and the second order element can catch the stress concentration better than the linear element; the final SIFs values are almost the same. The SIFs computed by linear and second order models coincide with each other by 4 digits. This means the current method is firmly robust and independent of the element types.

2.5 Conclusions

The limitations of the use of the crack tip stess method was demonstrated and investigated by pursuing a convergence study. Then, a post-processing technique of extrapolation was proposed to get the high-precision SIFs of interface crack problems by using the Finite Element Method. The accuracy and robustness of the improved proportional method were tested via several numerical examples. The computational accuracy was greatly improved comparing with the original one. Furthermore, the FE modeling requirements as well as the general procedure and precautions were also depicted as follows:

1. The crack length (half length) and material combinations of the target unknown problem and the reference problem should be kept the same. Furthermore, FE element sizes in each refined layer around the singular region should also be made the same for the reference and target unknown problems.

2. The element types of FE meshes are not necessarily the same for the reference and target unknown problems. For example, in this research, the FE model of the reference problem

is made of two dimensional quadrilateral element, but that of the target unknown problem can be made of other types of elements. Say, the axisymmetrical solid element and hexahedral solid element in Section 2.3.4. However, it should be noted that the model density and minimum element size for the two problems should be the same.

3. The post-processing technique of linear extrapolation should be employed in the analysis. Models with the minimum element size of $e = a/3^6, a/3^7$ are recommended to get the best compromise between accuracy and computational cost.

2.6 References of Chapter 2

[1] Yuuki, R., Cho, S.B., Efficient boundary element analysis of stress intensity factors for interface cracks in dissimilar materials. Eng Frac Mech., 1989;34:179-188.

[2] Miyazaki, N., Ikeda, T., Soda, T. and Munakata, T., Stress intensity factor analysis of interface crack using boundary element method—Application of contour-integral method. Engng Fract Mech., 1993; 45(5): 599-610.

[3] Wu, Y.L. A new method for evaluation of stress intensities for interface cracks. Engng Fract Mech., 1994;48:755-61.

[4] Yang, X.X., Kuang, Z.B., Contour integral method for stress intensity factors of interface crack. Int J. Fract., 1996;78:299-313.

[5] Dong, Y.X., Wang, Z.M., Wang, B., On the computation of stress intensity factors for interfacial cracks using quarter point boundary elements. Engng Fract Mech., 1997;57:335-342.

[6] Qian, W. and Sun, C. T., Calculation of stress intensity factors for interlaminar cracks in composite laminates. Compos Sci Technol. 1997;57(6): 637-650.

[7] Shbeeb, N. I. and Binienda, W. K., Analysis of an interface crack for a functionally graded strip sandwiched between two homogeneous layers of finite thickness. Engng Fract Mech.1999;64(6): 693-720.

[8] Matsumto, T., Tanaka, M. and Obara, R., Computation of stress intensity factors of interface cracks based on interaction energy release rates and BEM sensitivity analysis. Engng Fract Mech., 2000;65(6): 683-702.

[9] Huang, H. and Kardomateas, G. A., Mixed-mode stress intensity factors for cracks located at or parallel to the interface in bimaterial half planes. Int J Solids and Struct. 2001;

38(21): 3719-3734.
[10] Ou, Z.C. and Chen, Y.H., Near-tip stress fields and intensity factors for an interface crack in metal/piezoelectric bimaterials. Int J Engng Sci. 2004;42(13-14):1407-1438.
[11] Xuan, Z.C., Feng, Z.S. and Gao, D.Y., Computing lower and upper bounds on stress intensity factors in bimaterials. Int J Non-Linear Mech., 2007;42(2): 336-341.
[12] Liu, Y.H., Wu, Z.G., Liang, Y.C., Liu, X.M., Numerical methods for determination of stress intensity factors of singular stress field. Engng Fract Mech., 2008;75:4793-4803.
[13] Treifi, M., Oyadiji, S.O., Tsang, D.K.L., Computations of modes I and II stress intensity factors of sharp notched plates under in-plane shear and bending loading by the fractal-like finite element method. Int J Solids Struct., 2008;45:6468-84.
[14] Treifi, M., Oyadiji, S.O., Tsang, D.K.L., Computations of the stress intensity factors of double-edge and centre V-notched plates under tension and anti-plane shear by the fractal-like finite element method. Engng Fract Mech., 2009;76:2091-2108.
[15] Panta, M., Singh, I.V. and Mishraa, B.K., Evaluation of mixed mode stress intensity factors for interface cracks using EFGM. Appl Math Model., 2011;35(7): 3443-3459.
[16] Oda, K. Kamisugi, K. and Noda, N.A., Analysis of stress intensity factor for interface cracks based on proportional method, Trans JSME., Series A, 2009; 75(752):476-482.
[17] Teranishi, T. and Nisitani, H. Determination of highly accurate values of stress intensity factor in a plate of arbitrary form by FEM, Trans JSME, Series A, 1999;65(635):16-21,.
[18] Erdogan, F., Stress distribution in bonded dissimilar materials with cracks. Trans ASME, J. Appl. mech., 1965;32: 403-410.
[19] MSC Marc 2007 r1. MSC Marc 2007r1 User's Guide, 2007. MSC.Software Corp., California, USA.
[20] Kaya, A.C., Erdogan, F., On the solution of integral equations with strongly singular kernels. Quarterly of Applied Mathematics. 1987; 45(1):105-122.
[21] Noda, N.A., Araki, K., Erdogan, F., Stress intensity factors in two bonded elastic layers with a single edge crack under various loading conditions. Int. J. Frac. 1992;57:101-126.
[22] Benthem, J.P. and Koiter, W.T., Mechanics of fracture 1, Method of analysis and solutions of crack problems, edited by G.C.Sih, Noordhoff International publishing leyden 1973:131-178.
[23] Nisitani, H. and Noda, N.A., Proc. Int. Conf. Appl. Frac Mech. Mater Struct., 1984:519-523.

3 CHAPTER

Stress intensity factors of the edge cracked bonded half-planes

3.1 Introductions

Quiet a lot interface crack problems have been treated previously, and various numerical methods have been reported to determine the SIFs of an interface crack till recently. However, several fundamental questions are still unsettled for interface cracks. For example, the equivalent condition is well-known for the SIFs between the central and edge cracks in homogenous wide plate in Fig. 3.1a, b. Say, the SIF of Fig. 3.1b is equivalent to $\sqrt{2} \times 1.1215$ times that of Fig. 3.1a when the two crack lengths are the same as $2a = a'$. On the other hand, the similar equivalent condition has not been revealed yet for the central and edge interface cracks in the bonded dissimilar wide plates. In our previous studies, therefore, the central interface cracks in a dissimilar bonded plane in Fig. 3.1c have been treated for arbitrary material combinations [1, 2]. In this study an edge interface crack in bonded dissimilar half-planes will be considered as shown in Fig. 3.1d, which is the most fundamental counterpart problem for the central interface crack.

In this chapter the SIFs at the crack tip in a bi-material bonded half-planes as shown in Fig. 3.1d will be investigated for arbitrary combination of materials. Then, finally an approximate formula for a shallow edge interface crack for arbitrary combination of materials and relative crack size will be given by fitting the computed results.

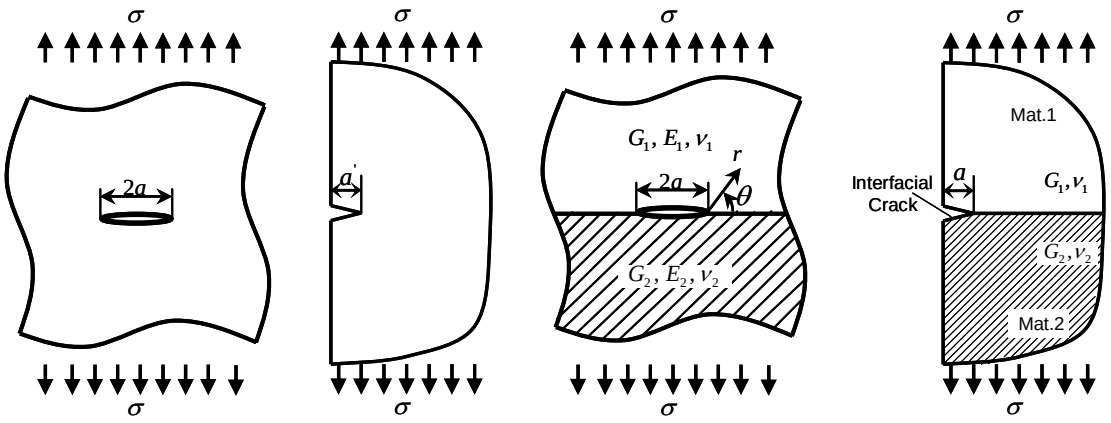

(a) $K_I = \sigma\sqrt{\pi a}$ (b) $K_I = 1.1215\sigma\sqrt{\pi a}$ (c) $K_I, K_{II} = ?$ (d) $K_I, K_{II} = ?$

Fig. 3.1 (a) Central cracked and (b) edge cracked homogenous wide plate (c) central cracked and (d) edge cracked dissimilar bonded wide plate

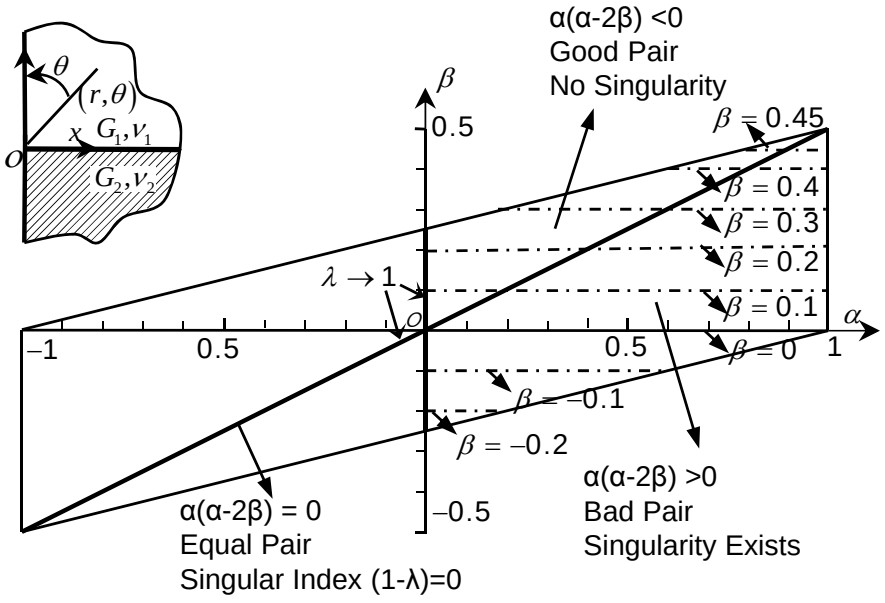

Fig. 3.2 $\alpha - \beta$ space for the Dundurs' material composite parameters

3.2 Dundurs' material composite parameters and typical material combinations

Consider the bi-material half-planes shown in Fig. 3.1d. It is composed of two elastic,

isotropic and homogeneous semi-infinite plates that are perfectly bonded along the interface. The material above the interface is termed material 1, and the material below is termed material 2. In 1969, Dundurs showed that the stress distribution in such a body depends on only two combinations of the elastic constants. All the possible values of the composite parameters (α,β) are constrained in a parallelogram in the $\alpha-\beta$ plane shown in Fig. 3.2. The four elastic parameters G_1,ν_1 and G_2,ν_2 for Fig. 3.1d determine an unique point in the $\alpha-\beta$ plane, but one point in the $\alpha-\beta$ plane may correspond to an infinite number of material combinations. In addition, the SIFs shown in Fig. 3.1d are only determined by (α,β), and they are point symmetrical about the origin of the coordinates for the $\alpha-\beta$ plane. According to the singularity near the interface corner of a perfectly bonded strip, the composite parameters (α,β) in the $\alpha-\beta$ space may be divided into three groups. Say, Good pair for $\alpha(\alpha-2\beta)<0$, equal pair for $\alpha(\alpha-2\beta)=0$ and bad pair for $\alpha(\alpha-2\beta)>0$. The SIFs for the aforementioned problem in plane strain or plane stress are only determined on the two elastic mismatch parameters α and β [3]. Here, the Dundurs' material composite parameters are defined as

$$\alpha=\frac{G_1(\kappa_2+1)-G_2(\kappa_1+1)}{G_1(\kappa_2+1)+G_2(\kappa_1+1)} \tag{3.1}$$

$$\beta=\frac{G_1(\kappa_2-1)-G_2(\kappa_1-1)}{G_1(\kappa_2+1)+G_2(\kappa_1+1)} \tag{3.2}$$

where the subscripts denote material 1 or 2, $G_m=E_m/2(1+\nu_m),(m=1,2)$, G_m, E_m and ν_m denote shear modulus, Young's modulus and Poisson's ratio for material m, respectively. $\kappa_m=(3-\nu_m)/(1+\nu_m)$ for plane stress and $\kappa_m=(3-4\nu_m)$ for plane strain. In this chapter, only the SIFs for $\alpha\geq 0$ in $\alpha-\beta$ space will be investigated since switching material 1 and 2 ($mat1\Leftrightarrow mat2$) will only reverse the signs of α and β ($(\alpha,\beta)\Leftrightarrow(-\alpha,-\beta)$).

The SIFs for the whole range of material combinations in the $\alpha-\beta$ space as shown

in Fig. 3.2 are our main research interests. And those for the typical engineering materials will also be discussed. The Stresses at the crack tip of an edge interface crack are given by

$$\sigma_y + i\tau_{xy} = \frac{1}{\sqrt{2\pi r}}\left(K_I + i \cdot K_{II}\right)\left(\frac{r}{2a}\right)^{i\varepsilon} \tag{3.3}$$

Where the oscillatory index ε (which is also denoted as bi-elastic constant) takes the form

$$\varepsilon = \frac{1}{2\pi}\ln\frac{\kappa_1/G_1 + 1/G_2}{\kappa_2/G_2 + 1/G_1} = \frac{1}{2\pi}\ln\left(\frac{1-\beta}{1+\beta}\right) \tag{3.4}$$

Fixing β to constants reflects the bonded strips behave the same characteristic oscillating properties, since the oscillatory index ε depends only upon the Dundurs' material composite parameter β. So, the SIFs are evaluated for various α $(0 < \alpha < 1)$ by fixing β to constants $\beta = -0.2, -0.1, 0, 0.1, 0.2, 0.3, 0.4, 0.45$ as shown in Fig. 3.2. In addition, switching material 1 and 2 for the bonded strips shown in Fig. 3.1d only reverses the signs of Dundurs' material composite parameters (α, β), therefore, we restrict our discussion to material combinations in the right part of the $\alpha - \beta$ plane ($\alpha > 0$) shown in Fig. 3.2.

Suga et al. [4] investigated the (α, β) values for typical engineering materials. The results computed by Suga are given in Fig. 3.3 where β is plotted against α. From this figure, the typical (α, β) values are concentrated along the $\beta = \alpha/4$ line in the $\alpha - \beta$ space, and scattered distributed in a narrow band between $\beta = \alpha/4 - 0.1$ and $\beta = \alpha/4 + 0.1$ lines. In addition, the α values may arrange over the whole possible region of $0 < \alpha < 1$, and β values are between -0.05 and 0.24.

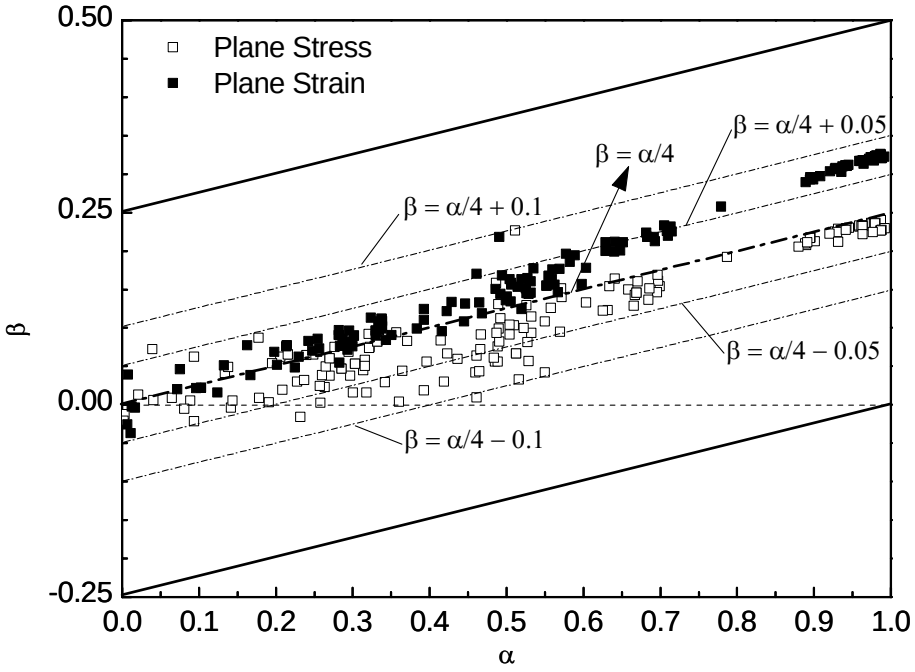

Fig. 3.3 $\alpha-\beta$ space for typical engineering materials (Suga,1988, Ref. [4])

3.3 Stress intensity factors of the edge cracked bonded half-planes subjected to tensile and bending loading conditions

The normalized SIFs at the crack tip of the edge interface crack in bi-material bonded strips are systematically investigated by varying the relative crack lengths a/W, as well as the material elastic parameters α and β. Here, we restrict our discussion to material combinations with fixed β. The double logarithmic distributions are shown in Fig. 3.4-3.11 for the normalized SIFs $F_I = K_I/\sigma\sqrt{\pi a}, F_{II} = K_{II}/\sigma\sqrt{\pi a}$ of $\beta = -0.2, -0.1, 0, 0.1, 0.2, 0.3, 0.4, 0.45$, respectively. From those figures, it is found that the double logarithmic distributions behave linearity when $a/W < 0.01$ and differ within about 5% at $a/W < 0.05$.

After examining every material combination it is seen that the plus and minus of the

slope for each curve varies depending on the sign of $\alpha(\alpha-2\beta)$. Specifically, the slope for each line is positive when $\alpha(\alpha-2\beta)<0$, zero when $\alpha(\alpha-2\beta)=0$ and is negative when $\alpha(\alpha-2\beta)>0$. Furthermore the slope equals the order of stress singularity for a perfectly bi-material strip. It physically means the existence of stress singularity around the interface corner. For example, free-edge singularity exists when the slope is negative and vanishes when it is positive. In particular, uniform stress distribution appears when the slope is 0. As an example, the distributions of the composite parameters for different types of materials are plotted in Fig. A.1 [5] of the appendix. Thus, it can also be deduced for the limiting case, the values of $F_I = K_I/\sigma\sqrt{\pi a}, F_{II} = K_{II}/\sigma\sqrt{\pi a}$ for the bonded semi-infinite plate ($a/W \to 0$) take the form:

$$\begin{aligned} &\alpha(\alpha-2\beta)>0: \quad F_I, F_{II} \to \infty \\ &\alpha(\alpha-2\beta)=0: \quad F_I, F_{II} \to \textit{finite} \\ &\alpha(\alpha-2\beta)<0: \quad F_I, F_{II} \to 0 \end{aligned} \tag{3.5}$$

Although when $\alpha(\alpha-2\beta)>0$, $F_I \to \infty, F_{II} \to \infty$ as $a/W \to 0$, actual crack extension along the interface may be controlled by the stress intensity factors K_I, K_{II} instead of F_I, F_{II}. In order to simulate the crack extension it is important to consider how the values of K_I, K_{II} change depending on the crack length. The double logarithmic distributions of the general SIFs K_I and K_{II} at the crack tip are plotted in Fig. 3.12. Linearity within the zone of the free-edge singularity can also be found from this figure. Here, it should be noted that all the SIFs increase monotonically with increasing relative crack lengths a/W for all the material combinations. Since F_I, F_{II} sometimes go to infinity, one may misunderstand that K_I, K_{II} also approach infinity as $a/W \to 0$. However, as shown in Fig. 3.12, K_I, K_{II} always approach zero independent of material combinations as $a/W \to 0$.

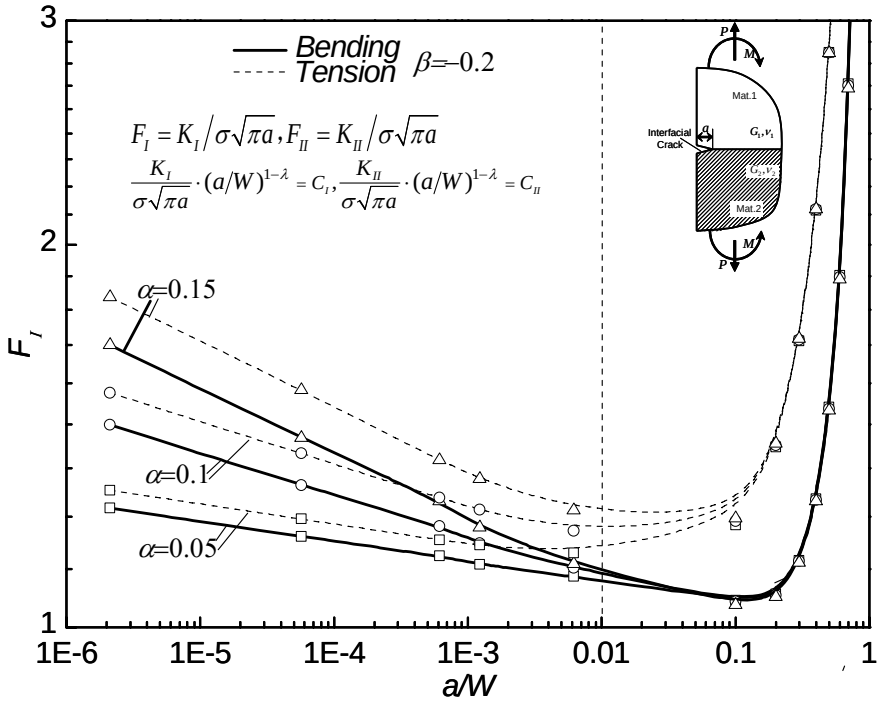

(a)

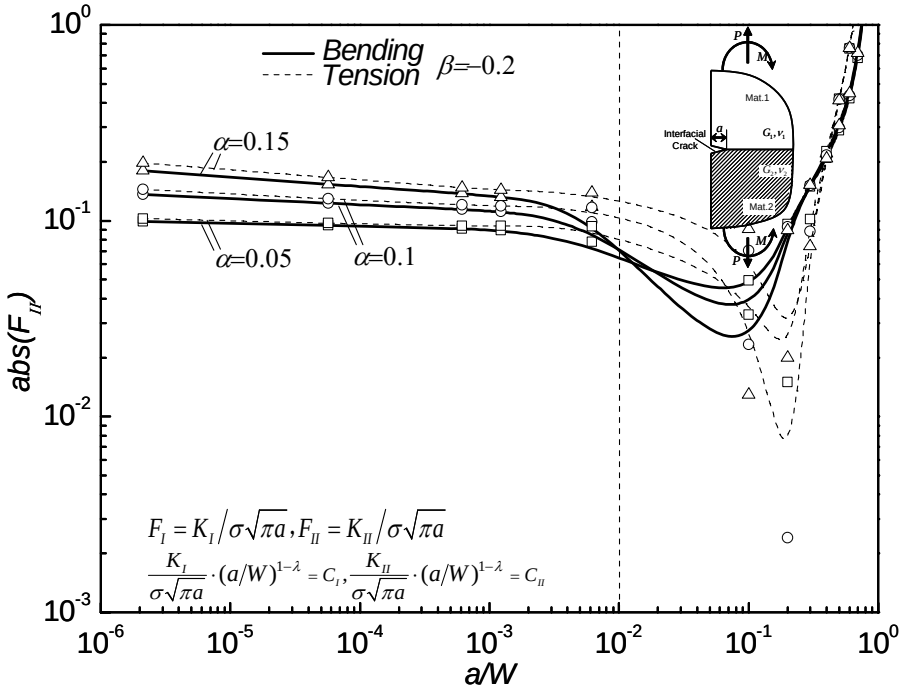

(b)

Fig. 3.4 Double logarithmic distributions of (a) F_I and (b) $abs(F_{II})$ for $\beta = -0.2$

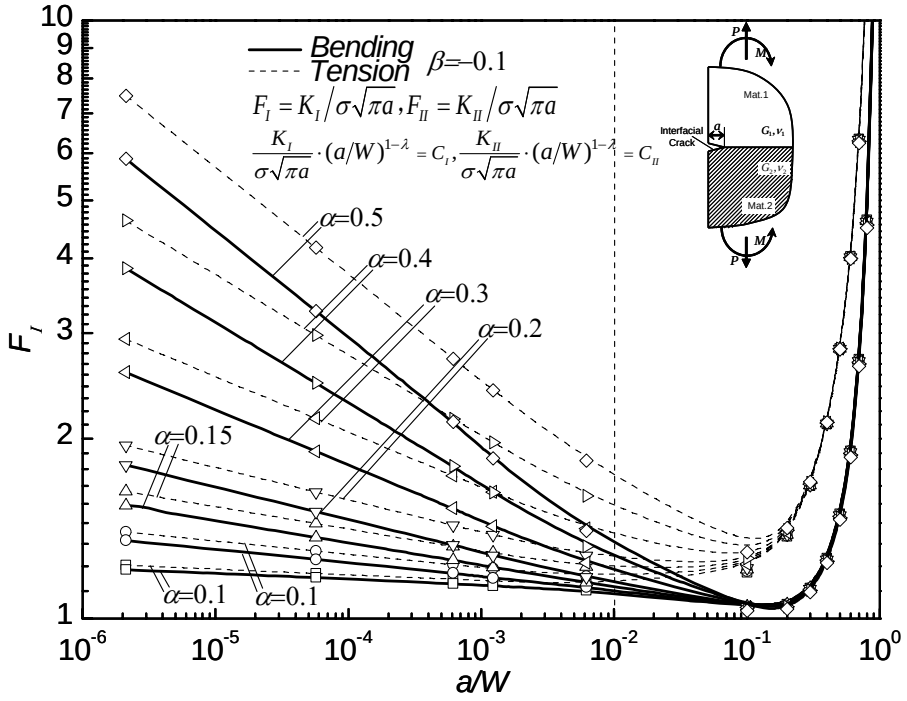

(a)

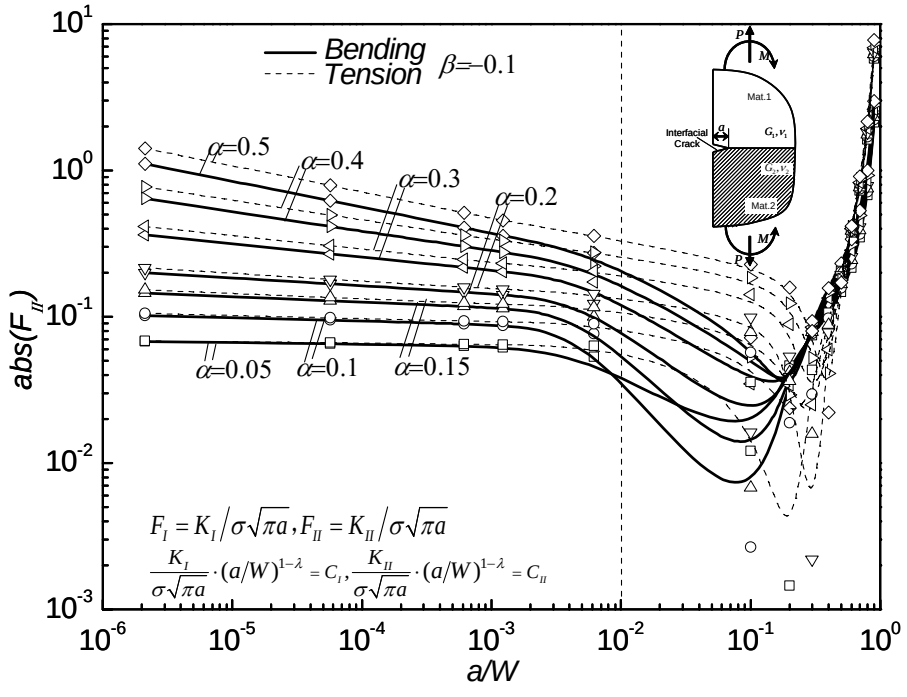

(b)

Fig. 3.5 Double logarithmic distributions of (a) F_I and (b) $abs(F_{II})$ for $\beta = -0.1$

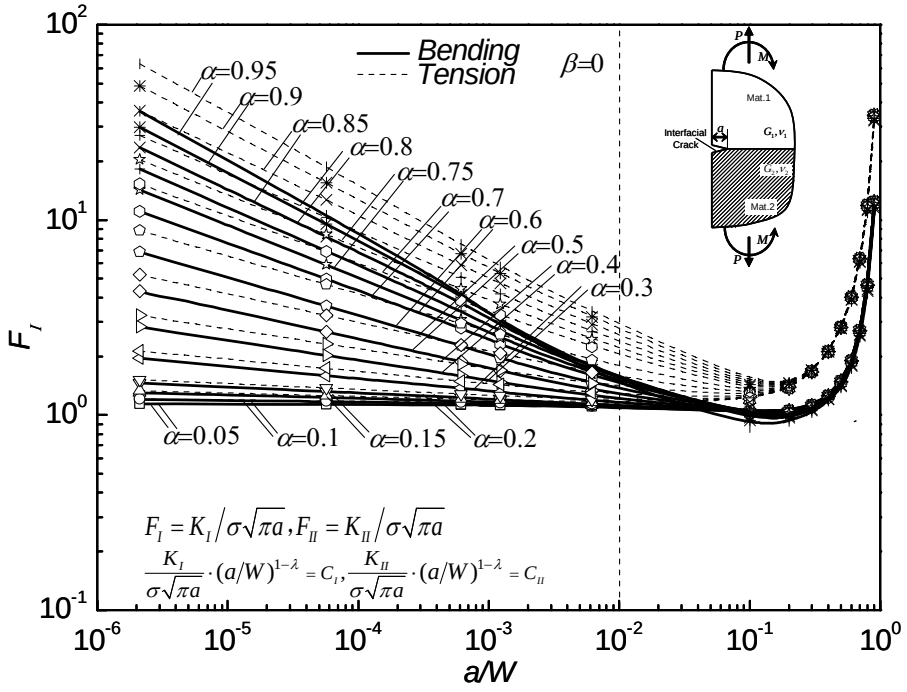

(a)

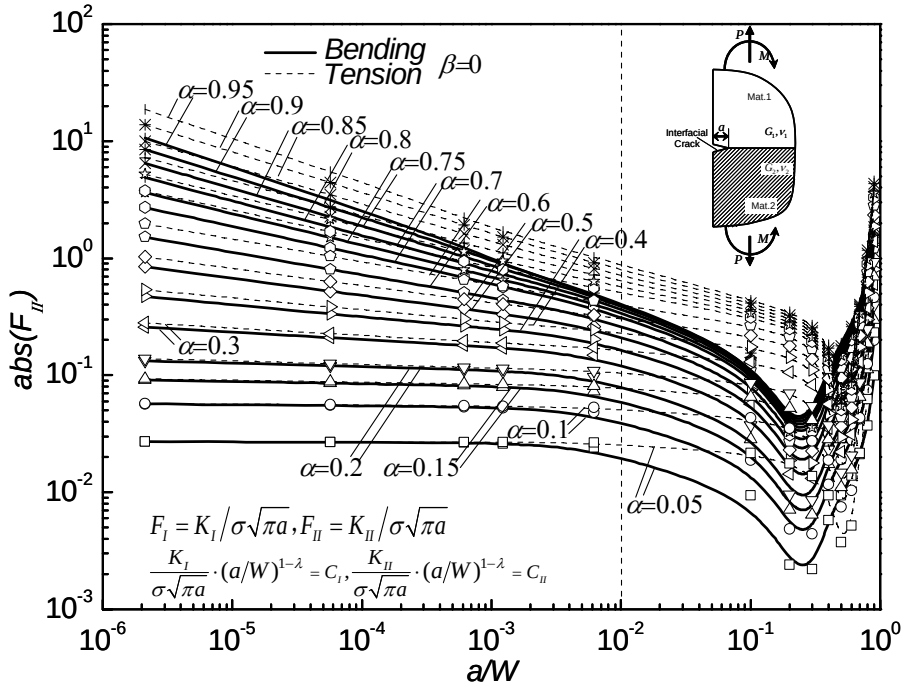

(b)

Fig. 3.6 Double logarithmic distributions of (a) F_I and (b) $abs(F_{II})$ for $\beta = 0$

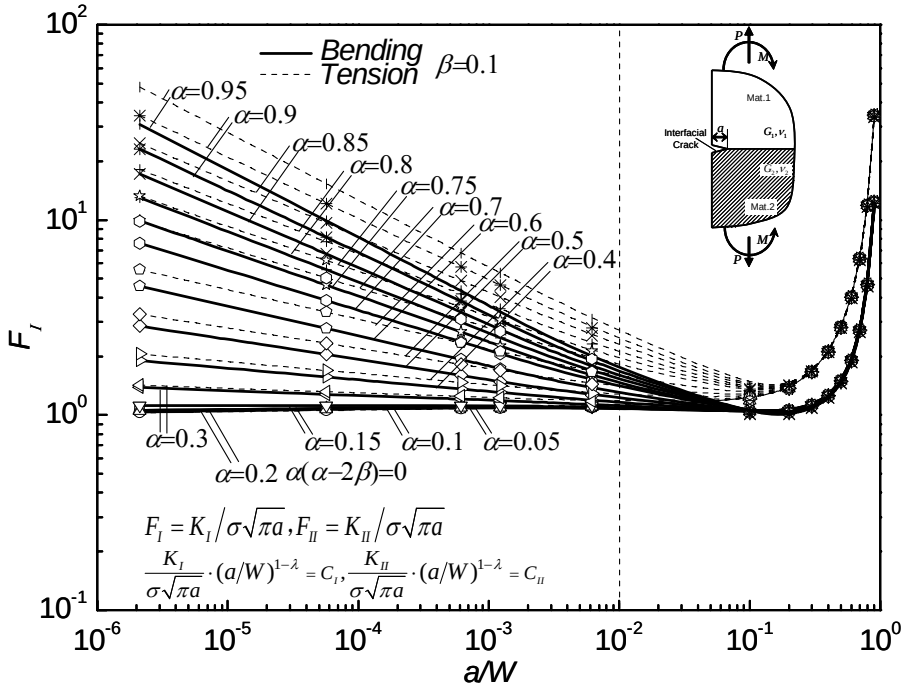

(a)

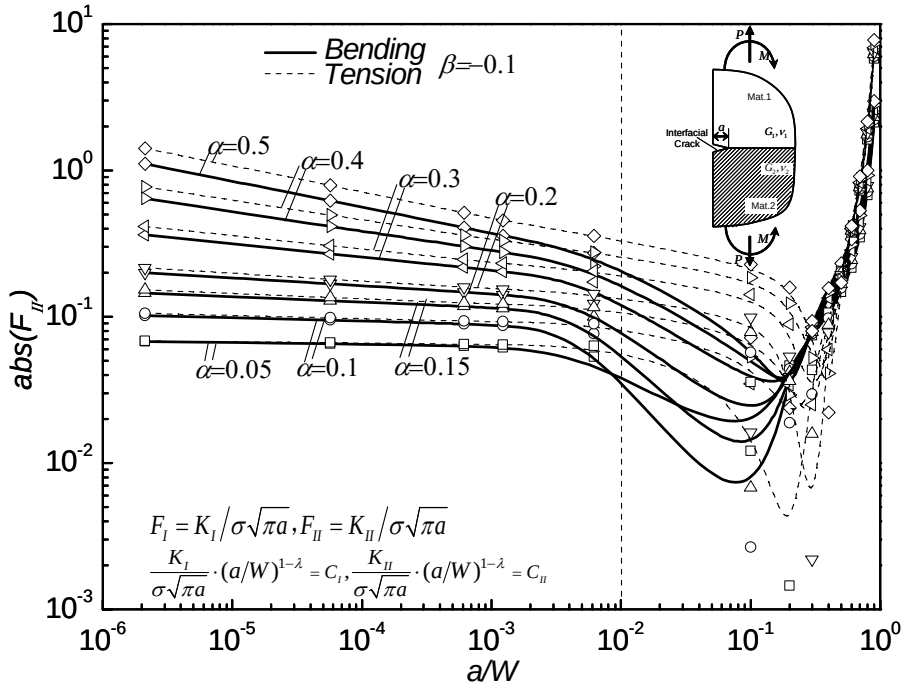

(b)

Fig. 3.7 Double logarithmic distributions of (a) F_I and (b) $abs(F_{II})$ for $\beta = 0.1$

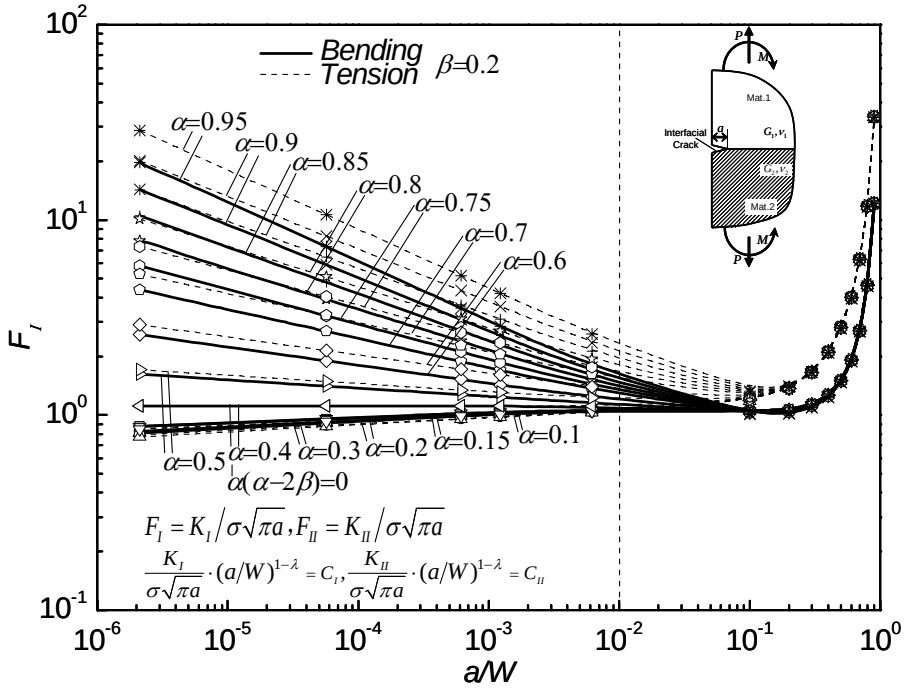

(a)

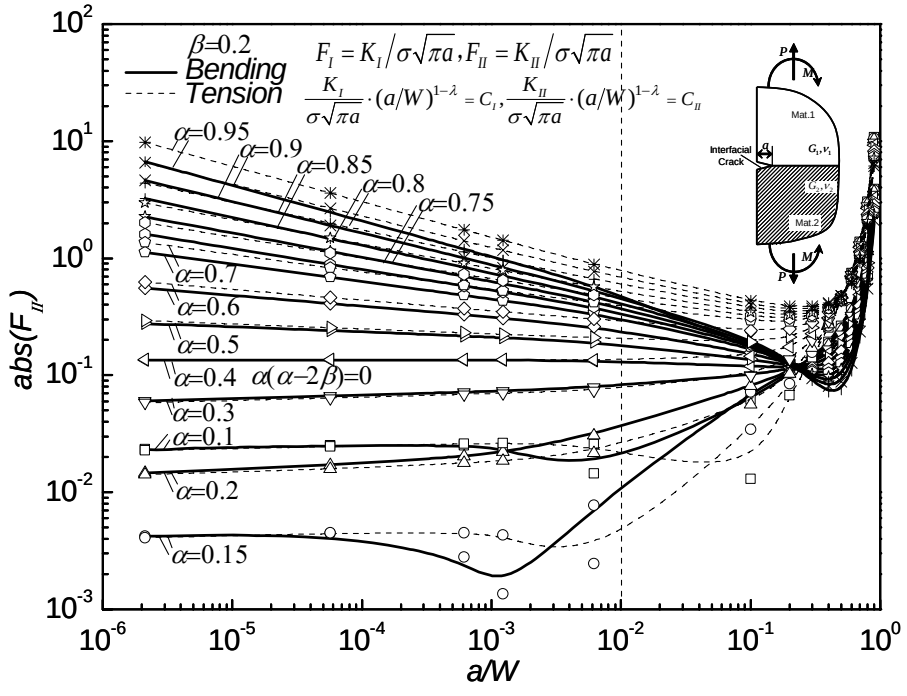

(b)

Fig. 3.8 Double logarithmic distributions of (a) F_I and (b) $abs(F_{II})$ for $\beta = 0.2$

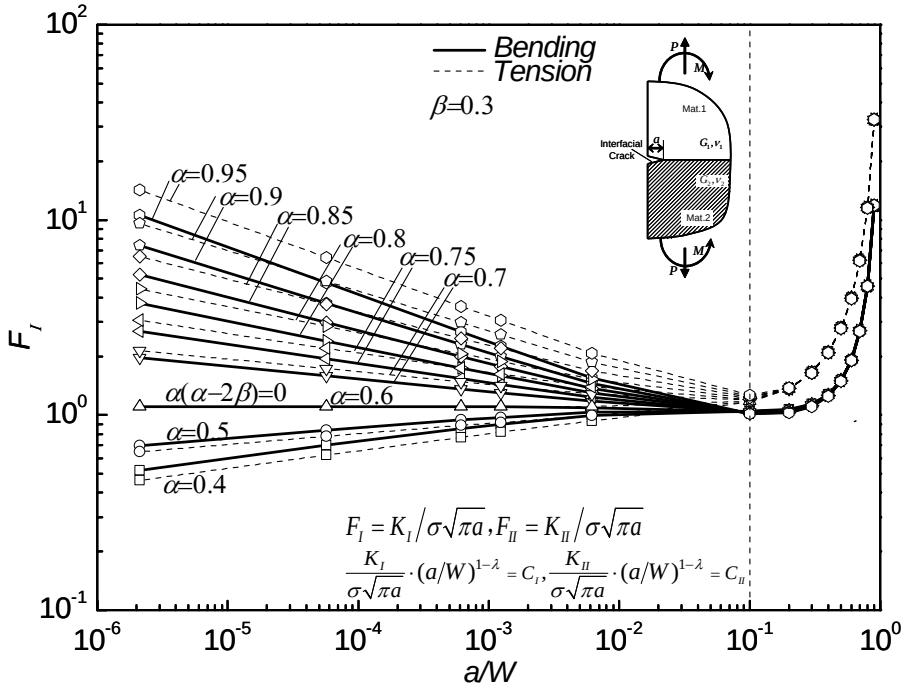

(a)

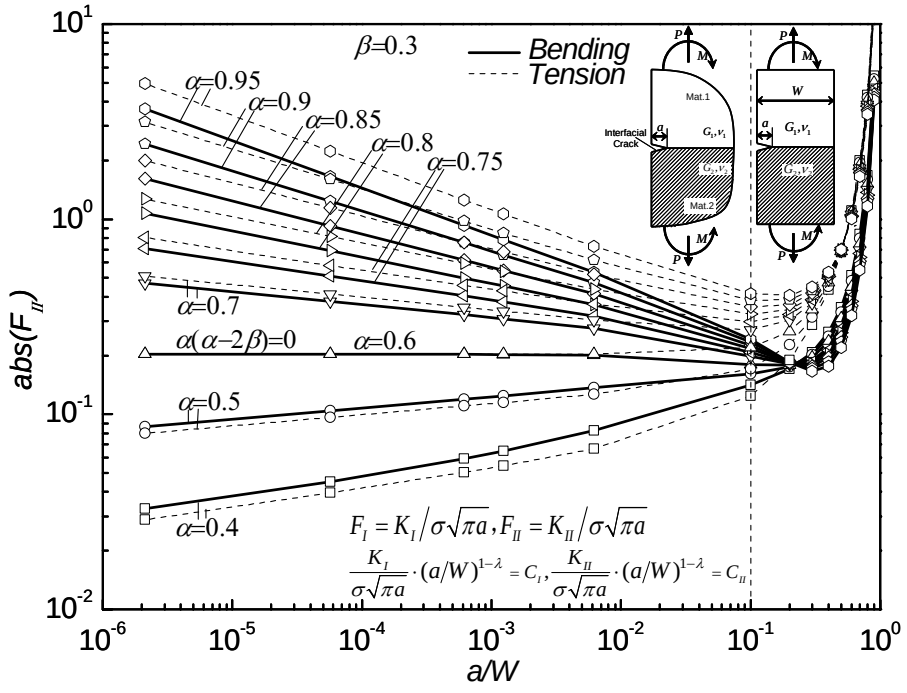

(b)

Fig. 3.9 Double logarithmic distributions of (a) F_I and (b) $abs(F_{II})$ for $\beta = 0.3$

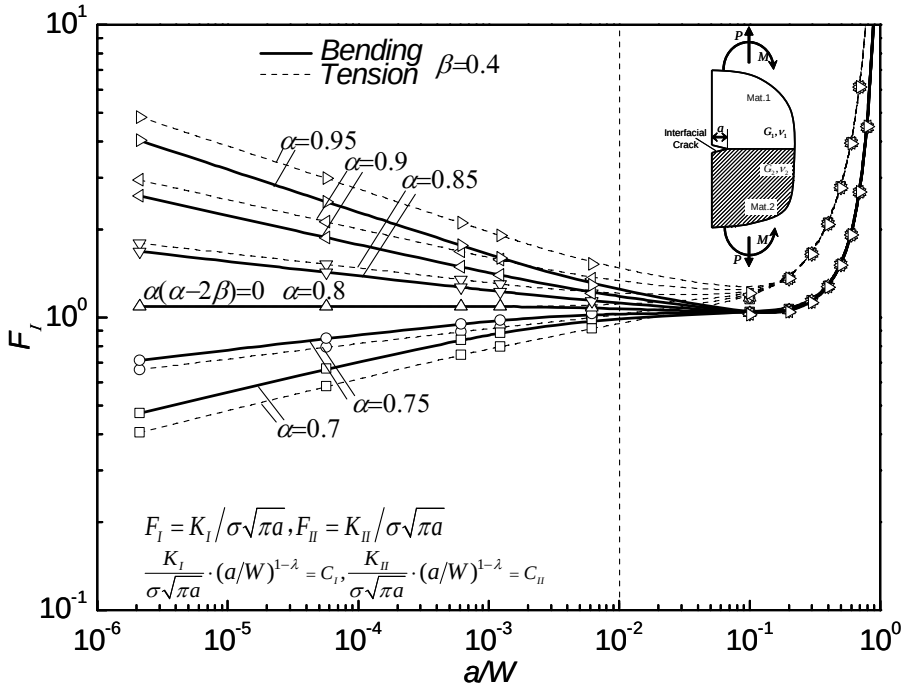

(a)

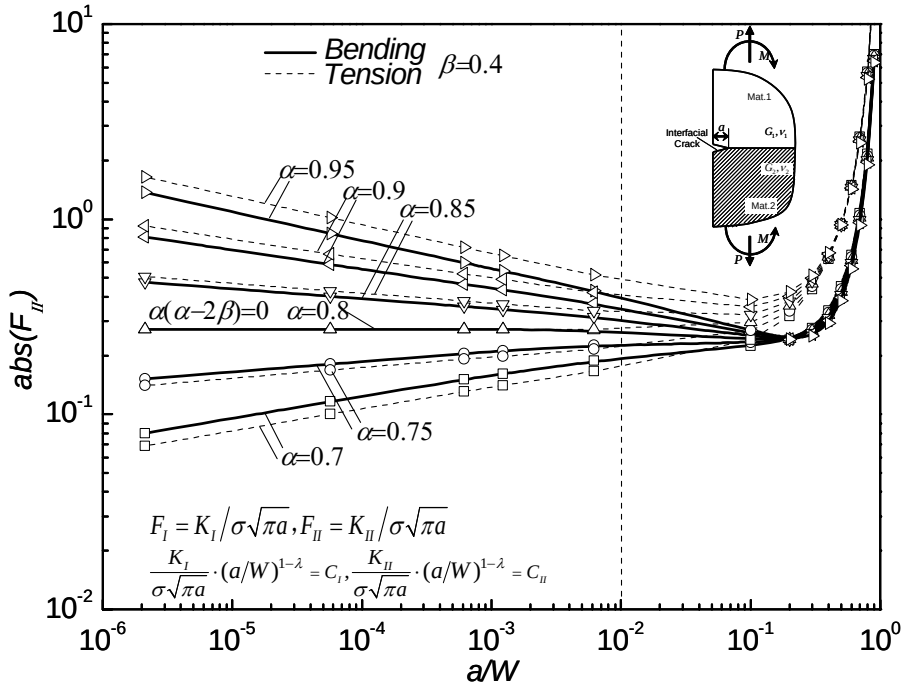

(b)

Fig. 3.10 Double logarithmic distributions of (a) F_I and (b) $abs(F_{II})$ for $\beta = 0.4$

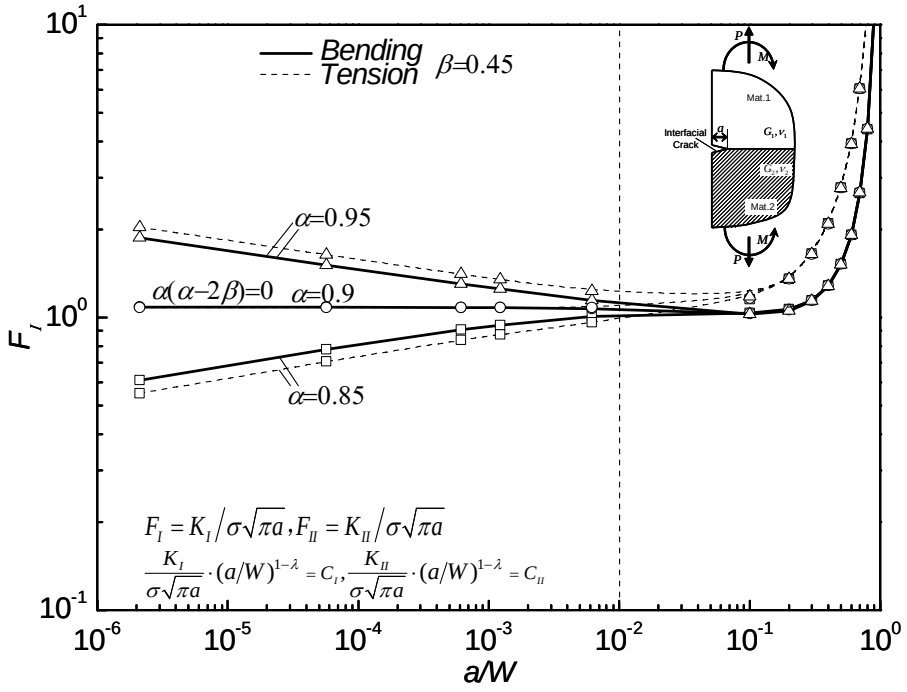

(a)

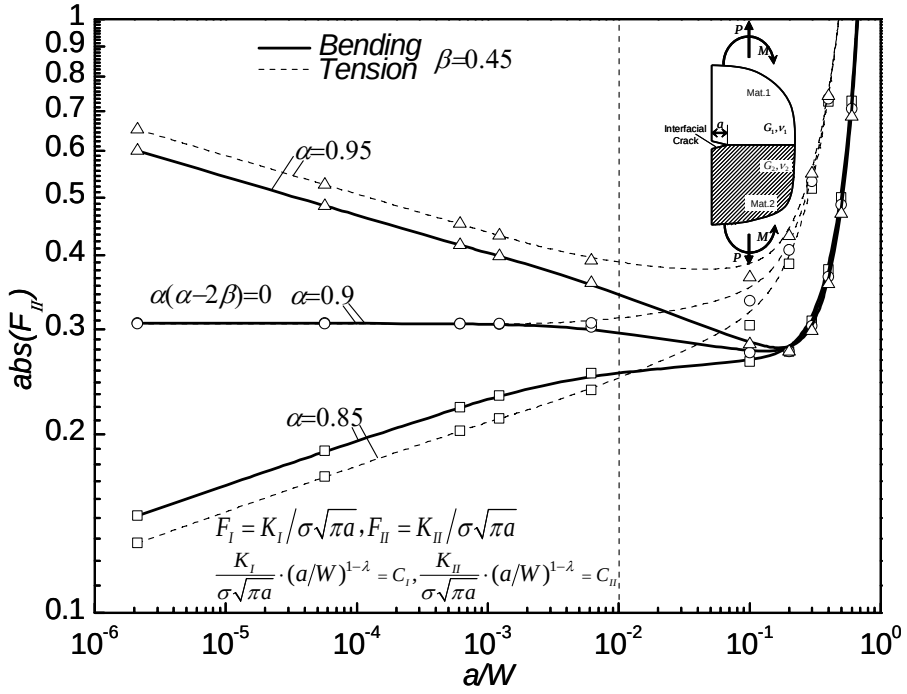

(b)

Fig. 3.11 Double logarithmic distributions of (a) F_I and (b) $abs(F_{II})$ for $\beta = 0.45$

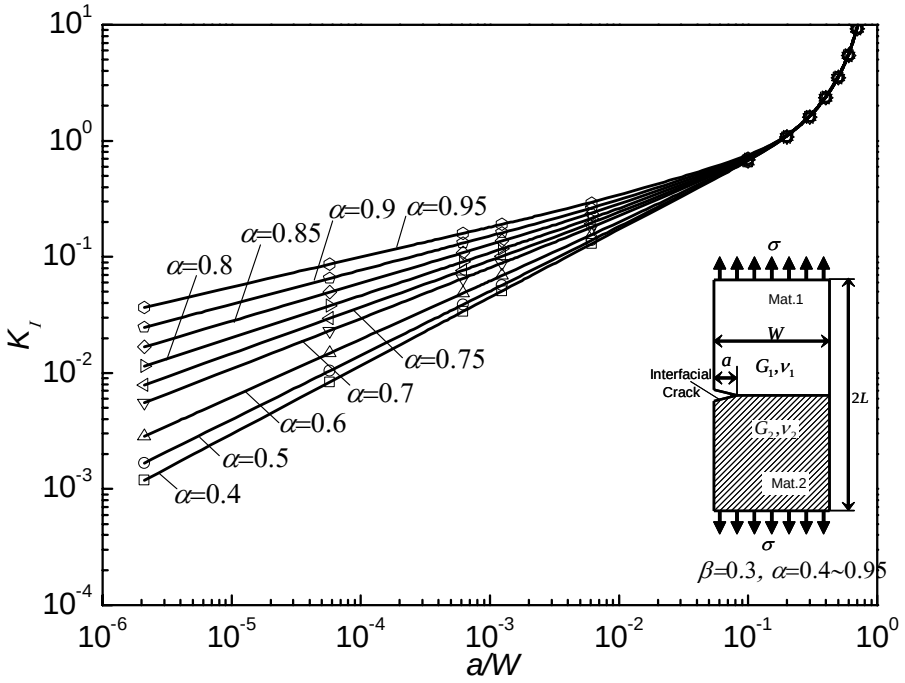

(a)

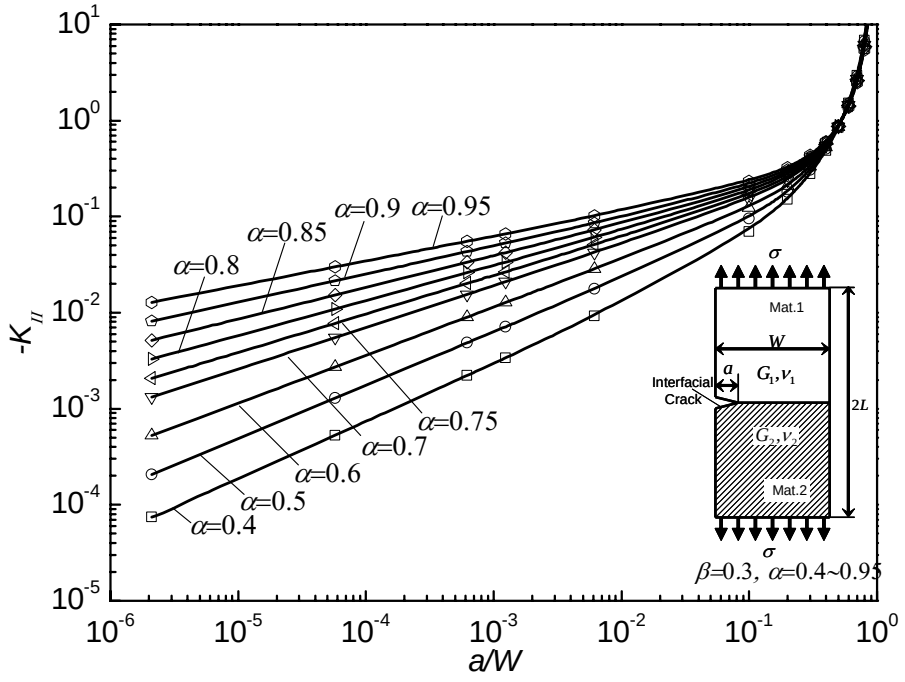

(b)

Fig. 3.12 The double logarithmic distributions of the general SIFs (a) K_I and (b) K_{II} at the crack tip for shallow edge interface cracks

3.4 Singular stress field at the end of a bonded plate

As shown in the Section 3.3, the SIFs of an edge interface crack may be affected by the singular stress field appearing at the interface corner of the bonded plate. It should be noted that more detailed investigation reveals that the slopes of the lines in Fig. 3.4-3.10 correspond to the singular index λ of the perfectly bonded plate without crack. It is known that the singularity at the end of bonded plate can be determined by the following relationships [6, 7].

$$\begin{aligned}
&\alpha(\alpha-2\beta)>0: \ \lambda<1, \quad \sigma_y=\sigma_{yy}\big|_{\theta=0}\to\infty \quad (r\to 0) \quad \text{Singularity exist}\\
&\alpha(\alpha-2\beta)=0: \ \lambda=1, \quad \sigma_y=\sigma_{yy}\big|_{\theta=0}\to \textit{finite} \quad (r\to 0) \quad \text{Singularity} = 0\\
&\alpha(\alpha-2\beta)<0: \ \lambda>1, \quad \sigma_y=\sigma_{yy}\big|_{\theta=0}\to 0 \quad (r\to 0) \quad \text{Singularity vanish}
\end{aligned} \tag{3.6}$$

Therefore the interface crack within this zone behaves in the following ways.

$$\begin{aligned}
&\alpha(\alpha-2\beta)>0: \ K_I/\sigma\sqrt{\pi a}\to\infty, K_{II}/\sigma\sqrt{\pi a}\to\infty,\\
&\alpha(\alpha-2\beta)=0: \ K_I/\sigma\sqrt{\pi a}, \ K_{II}/\sigma\sqrt{\pi a}\to \text{finite values}\\
&\alpha(\alpha-2\beta)<0: \ K_I/\sigma\sqrt{\pi a}\to 0, K_{II}/\sigma\sqrt{\pi a}\to 0.
\end{aligned} \tag{3.7}$$

In this section, the singular stress fields near the free-edge corner will be described in detail. Let's consider a perfectly dissimilar bonded plate without crack as shown in Fig. 3.13 with a cylindrical polar coordinate (r,θ) centered at the interface corner. The singular field around the bonded end can be expressed in the following form [8].

$$\sigma_\theta = Kr^{\lambda-1}f_{\theta\theta}(r,\theta), \quad \tau_{r\theta}=Kr^{\lambda-1}f_{r\theta}(r,\theta) \tag{3.8}$$

Here K is the intensity of stress singularity at the interface corner, r is the radial distance from the corner, and λ is the order of stress singularity. Also $f_{\theta\theta}(r,\theta), \ f_{r\theta}(r,\theta)$ are known functions of r,θ [8].

Many studies have considered the order of stress singularity for bonded corners with varying geometric configurations and material combinations [6-12]. For the bonded strip shown in Fig. 3.13, the angles which the traction-free surfaces make with the interface are $\pi/2$, then the values of λ can be obtained by solving the following equation

$$\begin{aligned} D(\alpha,\beta,\lambda) = &\left[\cos^2\left(\frac{\pi}{2}\lambda\right)-(1-\lambda)^2\right]^2\beta^2 + 2(1-\lambda)^2\left[\cos^2\left(\frac{\pi}{2}\lambda\right)-(1-\lambda)^2\right]\alpha\beta \\ &+(1-\lambda)^2\left[(1-\lambda)^2-1\right]\alpha^2 + \cos^2\left(\frac{\lambda\pi}{2}\right)\sin^2\left(\frac{\lambda\pi}{2}\right) = 0 \end{aligned} \tag{3.9}$$

Where, λ is the zero of $D(\alpha,\beta,\lambda)$ in $0<\mathrm{Re}(\lambda)<1$ that has the smallest real part. In general, $D(\alpha,\beta,\lambda)$ is expected to have several zeros in $0<\mathrm{Re}(\lambda)<1$. In all cases where more than one zero of $D(\alpha,\beta,\lambda)$ occurs only the smallest one will be exhibited [7]. The values of λ are computed for arbitrary material composite parameters (α,β), and the results are plotted and tabulated in Fig.3.14 and in Table 3.1, respectively. The contour plot of λ is also demonstrated in Fig.3.15. Here, it should be noticed that λ for any material combinations can be obtained from Table 3.1 since $\lambda(\alpha,\beta)=\lambda(-\alpha,-\beta)$.

Although the singular index has been discussed in many papers, the intensity of singular stress fields has just recently been obtained. Reedy and Guess [13] have determined the magnitude of intensity of stress singularity for a thin elastic layer sandwiched between two rigid substrates. Akisanya and Fleck [14] applied the contour integral to evaluate the singular stress field at the free-edge of a long bi-material strip subjected to uniform tension. Xu et al. [15] proposed numerical methods to determine the multiple stress singularities and the related stress intensity coefficients. Chen and Nisitani obtained the exact expression of the singular stress field for a bonded dissimilar strip [8]. From this paper, it is known that the root of Eq.(9) has a single real root $0<\lambda<1$ when $\alpha(\alpha-2\beta)>0$. In this research, in order to examine the stress field around the free-edge corner, K_σ is introduced to define the intensity of singular stress as

$$K_\sigma = \lim_{r \to 0}\left[r^{1-\lambda} \times \sigma_{\theta \mid \theta = \pi/2} \right] \tag{3.10}$$

The intensity of stress singularity K for an un-cracked bonded dissimilar strip can be obtained using [8].

$$K = K_\sigma / (4\lambda \cos(\lambda\pi/2)[(\lambda + 1 - \lambda\beta)\cos(\lambda\pi) + (\lambda+1)(2\lambda\beta - 1) - \lambda\beta + 2\lambda^2(\lambda+1)(\alpha-\beta)]) \tag{3.11}$$

The values of $K_\sigma/\sigma W^{1-\lambda}$ for $\lambda \le 1$ are calculated as a further work to the previous research [16]. And they are plotted in Fig. 3.16 and Fig. 3.17 against material composite parameters α, β. It should be noted that K_τ for the shear stress component also exists but is not demonstrated here since it is negligible in magnitude comparing with K_σ. The zone of free-edge singularity domains an extent of around 0.1 times the width of a bi-material strip. Therefore, the SIFs of very shallow edge interface cracks within the extent of singular zone will be mainly controlled by the free edge singularity.

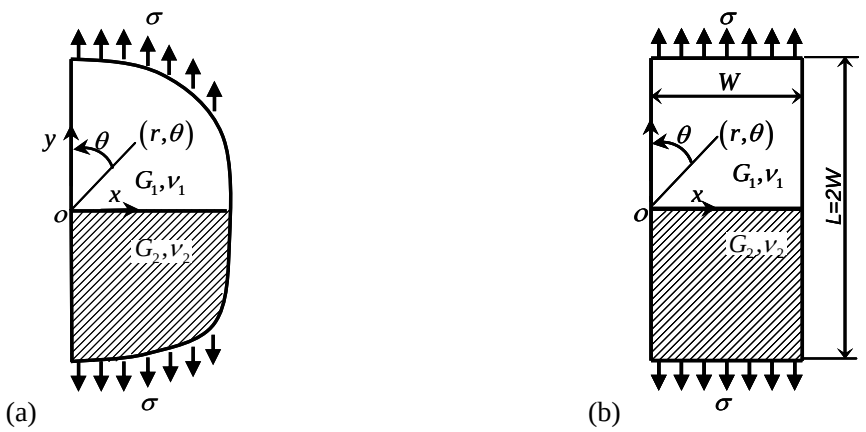

Fig. 3.13 (a) The bi-material bonded semi-infinite plate and (b) finite strip

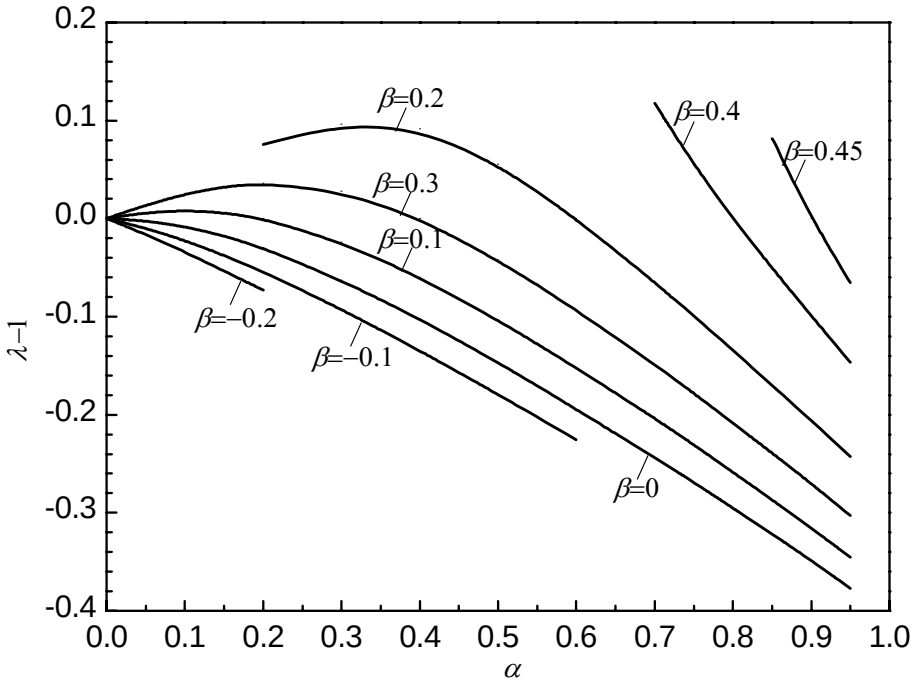

Fig. 3.14. Order of stress singularity $\lambda - 1$

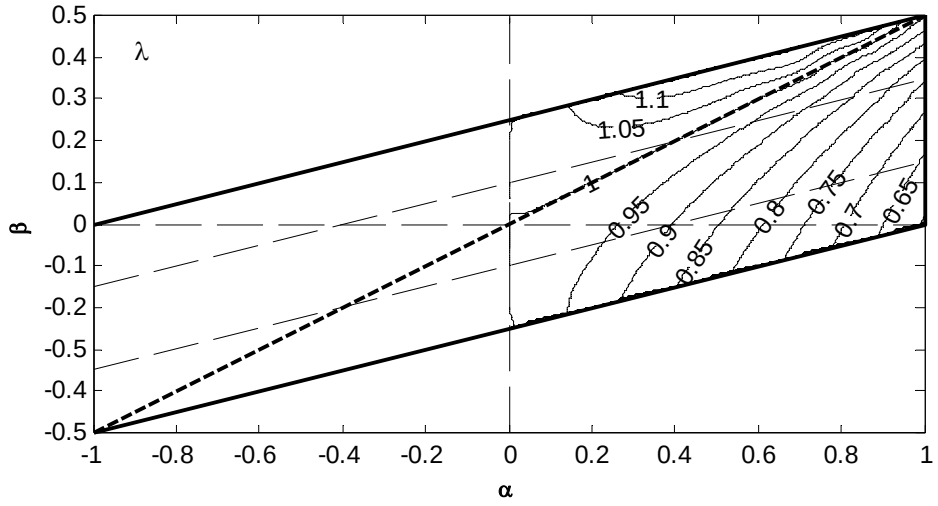

Fig.3.15 Contour plots of λ for bonded strips

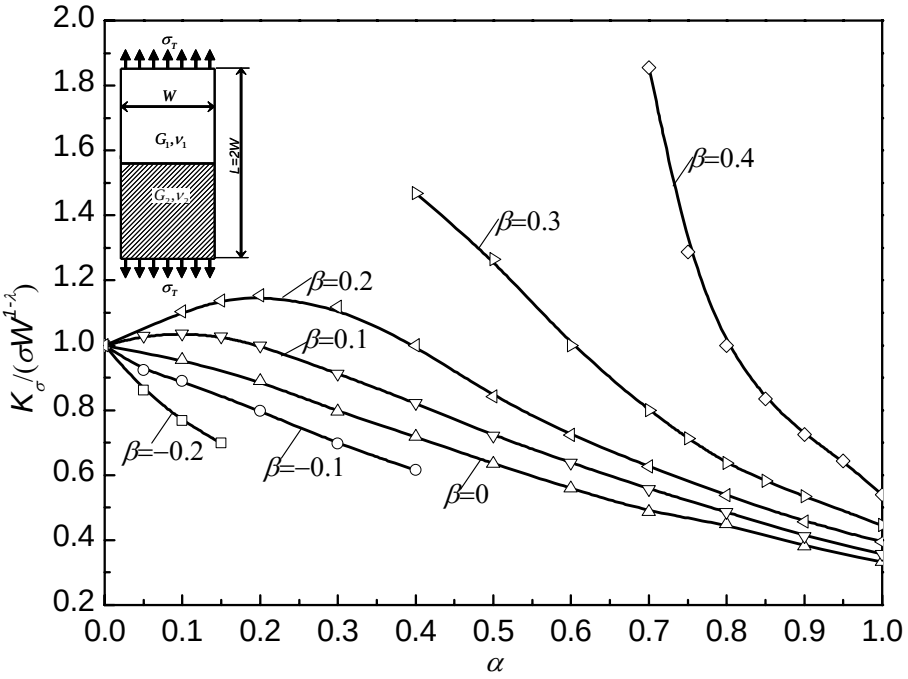

Fig. 3.16 Normalized intensity of stress singularity K_σ for various material combinations of the tensile loading case

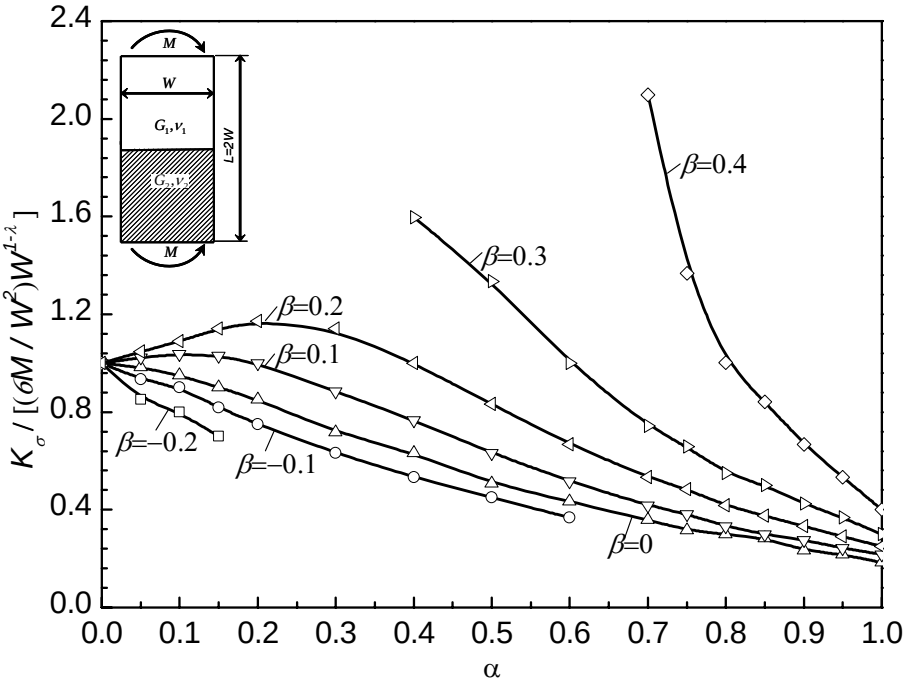

Fig. 3.17 Normalized intensity of stress singularity K_σ for various material combinations of the bending loading case

Table 3.1 Singular index λ for various combinations of materials

α	β =-0.2	β =-0.1	β =0	β =0.1	β =0.2	β =0.3	β =0.4	β =0.45
0	1	1	1	1	1			
0.05	0.98378	0.99035	0.99800	1.00613	1.01403			
0.1	0.96593	0.97774	0.99205	1.00831	1.02512			
0.15	0.94684	0.96269	0.98253	1.00626	1.03279			
0.2	0.92685	0.94571	0.96987	1	1.03604	1.07562		
0.3		0.90752	0.93713	0.97605	1.02764	1.09640		
0.4		0.86549	0.89741	0.94025	1	1.09130		
0.5		0.82096	0.85320	0.89662	0.95796	1.05584		
0.6		0.77459	0.80597	0.84801	0.90711	1		
0.7			0.75644	0.79606	0.85104	0.93477	1.11741	
0.75			0.73090	0.76909	0.82169	0.90048	1.05468	
0.8			0.70481	0.74151	0.79163	0.86554	1	
0.85			0.67824	0.71331	0.76091	0.83006	0.94923	1.08125
0.9			0.65105	0.68448	0.72953	0.79410	0.90075	1
0.95			0.62320	0.65496	0.69745	0.75761	0.85364	0.93488
1			0.59461	0.62466	0.66461	0.72053	0.80731	0.87624

3.5 Fitting functions for the stress intensity factors of edge interface cracks in the bonded half-planes

In Section 3.3 and 3.4, it has been proved that $K_I/\sigma\sqrt{\pi a}$ and $K_{II}/\sigma\sqrt{\pi a}$ have finite non-zero values only when $\alpha(\alpha-2\beta)=0$. Here, the normalized SIFs $F_I=K_I/\sigma\sqrt{\pi a}$ and $F_{II}=K_{II}/\sigma\sqrt{\pi a}$ for an edge interface crack in a bonded semi-infinite plate for $\alpha=2\beta$ are plotted in Fig. 3.18. From the figure, it is clear that F_I and F_{II} behave quadratic and linear relationship, respectively. The computed results for $\alpha=2\beta$ are also tabulated in Table 3.2. Then, the approximate expression as in Eq. (3.12) is given by fitting the computed results. Specifically, the result for the homogenous semi-infinite plate (when two materials are identical $\alpha=\beta=0$) computed in this research is $K_I/\sigma\sqrt{\pi a}=1.1208$, compared with the famous theoretical one $K_I/\sigma\sqrt{\pi a}=1.1215$, and it merely has an error of 0.062%.

$$\begin{aligned} K_I \big/ \sigma\sqrt{\pi a} &= 1.121 + 0.0159\beta - 0.221\beta^2 \\ K_{II} \big/ \sigma\sqrt{\pi a} &= -0.684\beta \end{aligned} \tag{3.12}$$

In conclusion, the solution of SIFs at the crack tip for a bonded dissimilar half-planes takes the form

$$\begin{cases} K_I \big/ \sigma\sqrt{\pi a} \to 0, K_{II} \big/ \sigma\sqrt{\pi a} \to 0 \quad when \quad \alpha(\alpha - 2\beta) < 0; \\ K_I \big/ \sigma\sqrt{\pi a} = 1.121 + 0.0159\beta - 0.221\beta^2, K_{II} \big/ \sigma\sqrt{\pi a} = -0.684\beta \quad when \quad \alpha(\alpha - 2\beta) = 0; \\ K_I \big/ \sigma\sqrt{\pi a} \to \infty, K_{II} \big/ \sigma\sqrt{\pi a} \to \infty \quad when \quad \alpha(\alpha - 2\beta) > 0. \end{cases} \tag{3.13}$$

Table 3.2 Results of the dimensionless SIFs for $\alpha = 2\beta$

β	$K_I \big/ \sigma\sqrt{\pi a}$	$K_{II} \big/ \sigma\sqrt{\pi a}$
0	1.121	0
0.1	1.120	-0.067
0.2	1.115	-0.135
0.3	1.106	-0.204
0.4	1.092	-0.273
0.45	1.083	-0.307

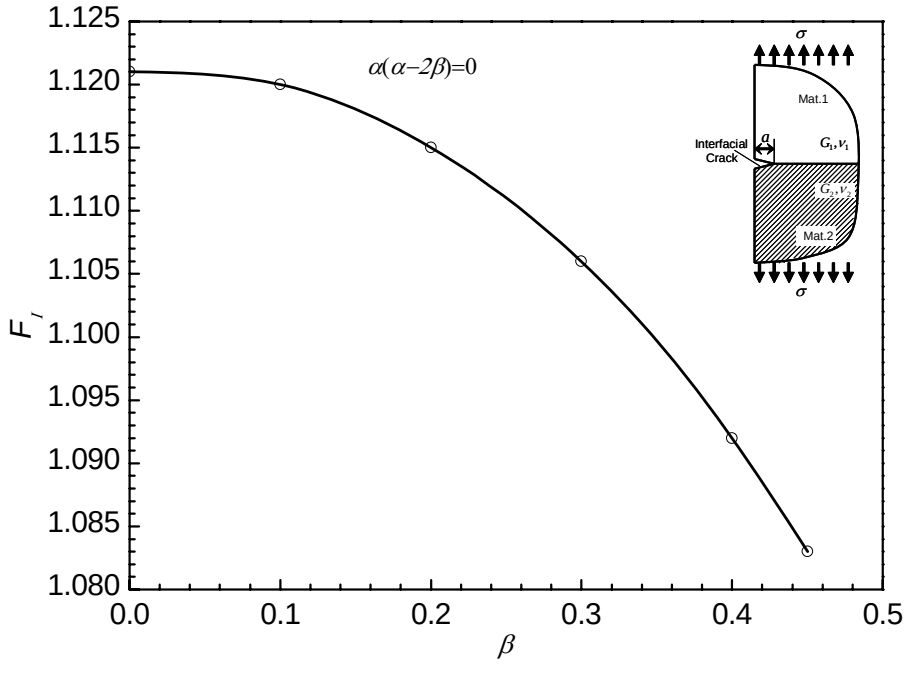

(a)

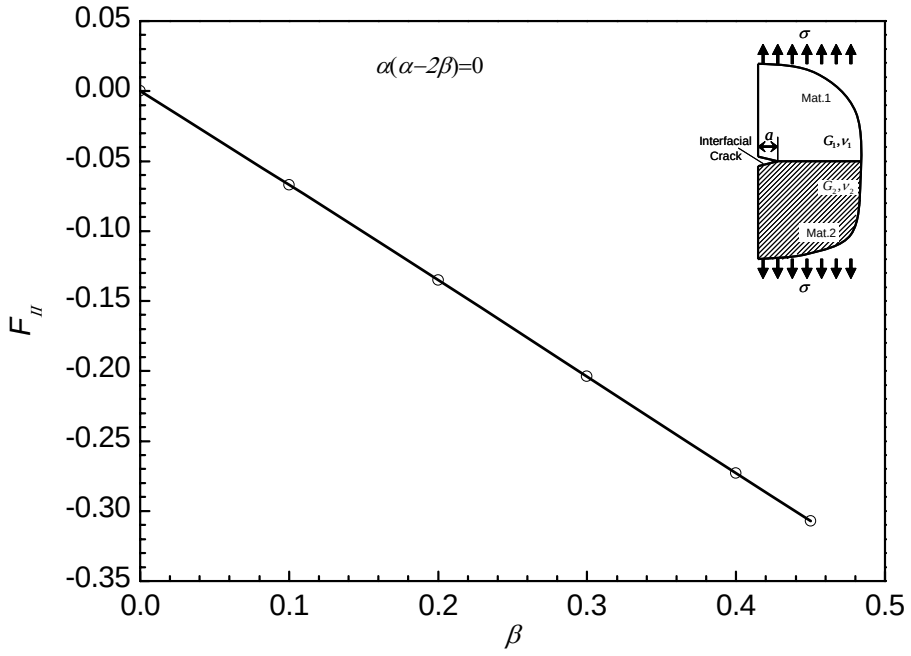

(b)

Fig. 3.18 Normalized SIFs (a) $F_I = K_I/\sigma\sqrt{\pi a}$ and (b) $F_{II} = K_{II}/\sigma\sqrt{\pi a}$ for $\alpha = 2\beta$ of an edge interface crack in a bonded semi-infinite plate

3.6 Conclusions

In this paper an edge interface crack in a bonded semi-infinite plate were analyzed asymptotically with varying the crack lengths and material combinations systematically. The limiting solutions were provided for the tensile and bending loading conditions. And the following achievements have been concluded as follows:

1. An empirical function of the SIFs for the single-edge cracked bonded dissimilar half-planes was proposed for arbitrary material combinations. The SIFs are expressed in the following form.

$$\begin{cases} K_1/\sigma\sqrt{\pi a}, K_2/\sigma\sqrt{\pi a} \to 0 \quad when \quad \alpha(\alpha-2\beta)<0; \\ K_1/\sigma\sqrt{\pi a} = 1.121+0.0159\beta-0.221\beta^2, K_2/\sigma\sqrt{\pi a} = -0.684\beta \quad when \quad \alpha(\alpha-2\beta)=0; \\ K_1/\sigma\sqrt{\pi a}, K_2/\sigma\sqrt{\pi a} \to \infty \quad when \quad \alpha(\alpha-2\beta)>0; \end{cases}$$

2. The singular stress field for a bonded strip without crack is investigated for various material combinations since the SIFs for the shallow interface edge crack are controlled by this singular stress field.

3.7 References of Chapter 3

[1] Noda, N.A., Zhang, Y., Takaishi, K.T.R., Lan, X., Stress Intensity Factors of an Interface Crack in a Bonded Plate under Uni-Axial Tension. J. Solid Mech Materials Engng, 2010; 4 (7):974-987.

[2] Zhang, Y., Noda, N.A., Takaishi, K., Lan, X., Stress intensity factors of a central interface crack in a bonded finite plate and periodic interface cracks under arbitrary material combinations, Engng Fract Mech., 2011;78: 1218-1232.

[3] Dundurs, J., 1969, Mathematical Theory of dislocations, American Society of Mech. Engineers, NY.

[4] Suga, T., Elssner, G. and Schmauder, S., Composite parameters and mechanical compatibility of material joints. Journal of composite materials, 1988;22:917-934.

[5] Yuuki, R., 1992. Mechanics of Interface, first ed. Baifuukann,Tokyo. (In Japanese)
[6] Bogy, D.B., Edge-Bonded Dissimilar Orthogonal Elastic Wedges under Normal and Shear Loading, Trans ASME, J Appl Mech, 1968;35: 460-466.
[7] Bogy, DB., Two edge-bonded elastic wedges of different materials and wedges angles under surface tractions. J. Appl Mech., 1971;38:377–86.
[8] Chen, D., and Nishitani, H., Intensity of Singular Stress Field near the Interface Edge Point of a Bonded Strip, Trans JSME, 1993;59: 2682-2686. (in Japanese)
[9] Bogy, D.B., Wang, K.C., Stress singularities at interface corners in bonded dissimilar isotropic elastic materials. Int J. Solids Struct., 1971;7:993–1005.
[10] Hein, V.L., Erdogan, F., Stress singularities in a two-material wedge. Int. J. Fract Mech. 1971;7:317–330.
[11] Dempsey, J.P., Sinclair, G.B., On the stress singularities in the plane elasticity of the composite wedge. J. Elast, 1979;9:373–91.
[12] Van Vroonhoven, J.C.W., Stress singularities in bi-material wedges with adhesion and delamination. Fatigue & Fracture of Engng Mater & Struct. 1992; 15:157-171.
[13] Reedy, Jr E.D. and Guess, T.R., Composite to metal tubular lap joints:strength and fatigue resistance. Int J Fract. 1993; 63: 351-367.
[14]Akisanya, A.R. and Fleck, N.A., Interfacial cracking from the free edge of a long bimaterial strip. Int. J. Solids Struct., 1977;34:1645-1665.
[15] Xu, J.Q., Liu, Y., Wang, X., Numerical methods for the determination of multiple stress singularities and related stress intensity coefficients. Eng. Fract. Mech., 1999;63: 775-790.
[16] Noda, N.A., Shirao, R., Li, J. and Sugimoto, J.S., Intensity of Singular Stress Fields Causing Interfacial Debonding at the End of Fiber under Pull-Out Force and Transverse Tension. Int J. Solids Structures, 2007;44(13):4472-4491.

4 CHAPTER Stress intensity factors of the single-edge-cracked bonded finite strip

4.1 Introductions

Multi-material systems are widely used in the designation of adhesive joints, bonded structures, thin film coating and composites. Failure of the multi-layer systems initiates at the corner where the interface intersects a traction-free edge as shown in Fig. 4.1 with a higher possibility, since a singular stress field develops at the interface corner. For a given interface crack, crack proporgation initiates as the SIFs increase to the critical values, and evently lead to the failure of the bonded structue. An exhaustive investigation on the variations of the SIFs of the bi-material strips for various crack lengths will contribute to a better understanding of the initiation and propagation of the interfacial cracks.

In this chapter we will calculate the SIFs of the bi-material bonded finite isotropic elastic strips as shown in Fig. 4.1 subjected to tensile and bending loading conditions. The discussion will be separated into cracks within and out of the zone of free-edge singularity. Fitting functions will be proposed to evaluate the SIFs of the shallow edge interface cracks within the singular zone. The SIFs for other relative crack lengths will be demonstrated in contour plots for the whole range of material combinations in the $\alpha - \beta$ space. And the combined effects of the relative crack lengths and material combinations to the SIFs of the bi-material strips will also be of special interests in this chapter.

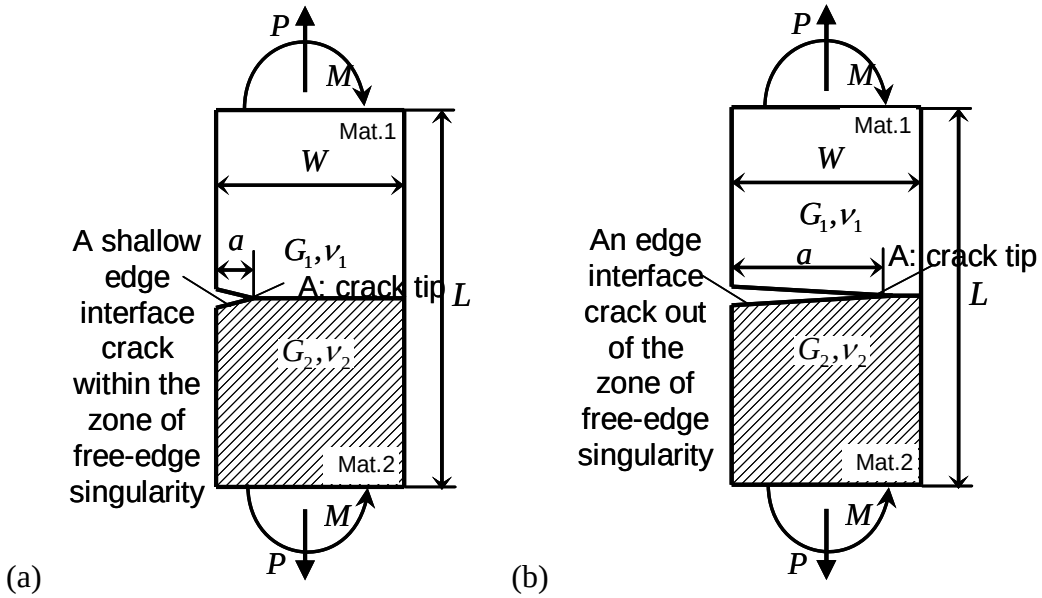

Fig. 4.1 The (a) shallow and (b) deep edge interface cracks in a bonded strip

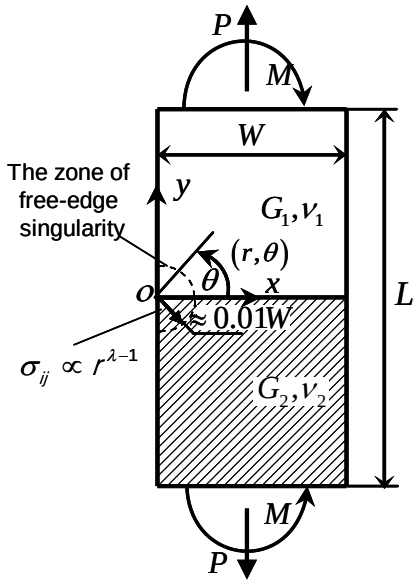

Fig. 4.2 Demonstration of the singular zone in a bi-material strip

4.2 The region of the zone of free-edge singularity

For the bi-material strip shown in Fig. 4.2, let (r,θ) be polar coordinates centered at the interface corner o. The extent of the region dominated by the free-edge singularity is demonstrated using a dashed curve. The stress components $\sigma_\theta, \tau_{r\theta}$ within the singular stress field near the interface corner are of the form

$$\sigma_\theta \propto r^{\lambda-1} f_{\theta\theta}(r,\theta), \tau_{r\theta} \propto r^{\lambda-1} f_{r\theta}(r,\theta) \tag{4.1}$$

Furthermore, it is found that the normal stress component σ_θ within the singularity zone reaches the maximum at the interface ($\theta = 0$). Discussions on the extent of the singularity zone have been published in several literatures. For example, Bogy [1] evaluated the extent of the singular zone along the interface ($\theta = 0$) for an infinitely long bi-material strip subjected to tension for elastic mismatch parameters $\alpha = -0.8, \beta = 0$. Reedy [2] calculated the region of singularity zone of the order of 0.6 times the interlayer thickness for a thin elastic layer sandwiched between two rigid substrates. Akisanya [3] determined the singularity zone size along the radial directions $\theta = 43°$ and $\theta = 1.6°$ for a long bi-material strip for $\alpha = 0.5$ and $\alpha = 0.8$, and for $\beta = 0$ and $\beta = \alpha/4$, by comparing the asymptotic and the finite element solutions for the normal stress component $\sigma_{\theta\theta}$. And the extent of the singularity zone is 0.1 times the strip width along $\theta = 43°$, and 0.03 times the strip width along $\theta = 1.6°$. It has been investigated in this research that the extent of the zone size in Fig. 4.2 varies with the radial direction θ and the Dundurs' material composite parameters (α,β).

Let's consider a shallow edge interface crack initiated within the zone of free-edge singularity shown in Fig. 4.1a, the stress state at the crack tip is dominated by the singular stress field for the bi-material strip shown in Fig. 4.2. As a result, the SIFs computed in this chapter will be discussed into two separate parts according to the relative crack length.

4.3 Stress intensity factors for edge interface cracks within the zone of free-edge singularity

The SIFs for the shallow edge interface cracks within the singular zone in a bi-material strip subjected to tensile and bending loading conditions as shown in Fig. 4.1a are investigated using the improved crack tip stress method. The results of $F_I \cdot (W/a)^{1-\lambda}$ and $F_{II} \cdot (W/a)^{1-\lambda}$ are plotted against logarithmic relative crack length a/W in Fig. 4.3a and b, respectively. The values for the tensile loads are plotted in dashed lines and those for the bending loads are plotted in solid lines. In addition, the material composite parameter β in Fig. 4.3 are restricted to $\beta = 0.3$, and similar phenomenon can be found from others material combinations of restricted β. As can be seen from these figures, the values for a given material combination approach constants with more than 3-digit when $a/W < 10^{-3}$, and differ only about 5% when $a/W < 10^{-3}$. That means the SIFs for the single-edge interface cracks within the singular zone have the same behavior due to the effect of free-edge singularity. Thus, we propose the following formula to calculate the SIFs at the crack tip for the very shallow edge interface cracks in a bi-material finite strip subjected to tension.

$$\begin{aligned} &\frac{K_I}{\sigma\sqrt{\pi a}} \cdot (a/W)^{1-\lambda} = C_I, \frac{K_{II}}{\sigma\sqrt{\pi a}} \cdot (a/W)^{1-\lambda} = C_{II} \\ &\sigma = P/W \quad \textit{for tensile loads} \\ &\sigma = 6M/W^2 \quad \textit{for bending loads} \end{aligned} \tag{4.2}$$

Where, coefficients C_I, C_{II} are constants depending upon the relative elastic properties of materials and the loading types. The values of the coefficients C_I, C_{II} are listed against material composite parameters in Table 4.1 and Table 4.2 as well as in Table 4.3 and Table 4.4 for the tensile and bending loads, respectively. And they are also plotted against (α, β) in Fig.4.4 with the tensile and bending loads in dashed and solid line, respectively. It is easy to be found that the coefficient curves C_I in Fig. 4.4a are similar to the theoretical

singularity order ones in Fig. 3.14 since the stress field near the interface corner is mainly dominated by the eigenvalue λ. Furthermore, the results of C_I, C_{II} for the tensile and bending loading conditions are compared for various material combinations. The SIFs agree quite well when $\alpha(\alpha - 2\beta) = 0$ for the two loading types.

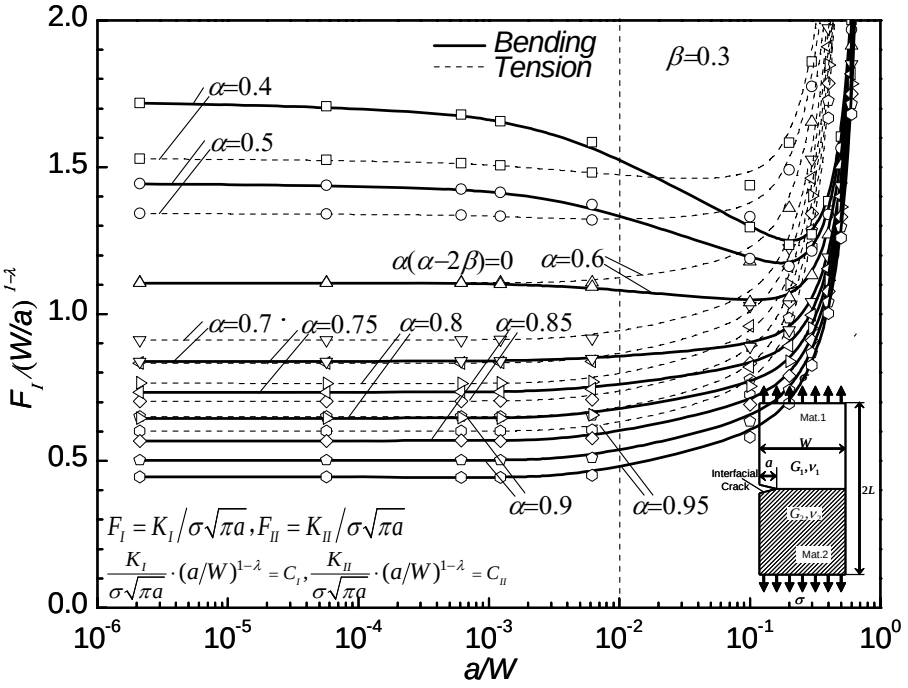

(a)

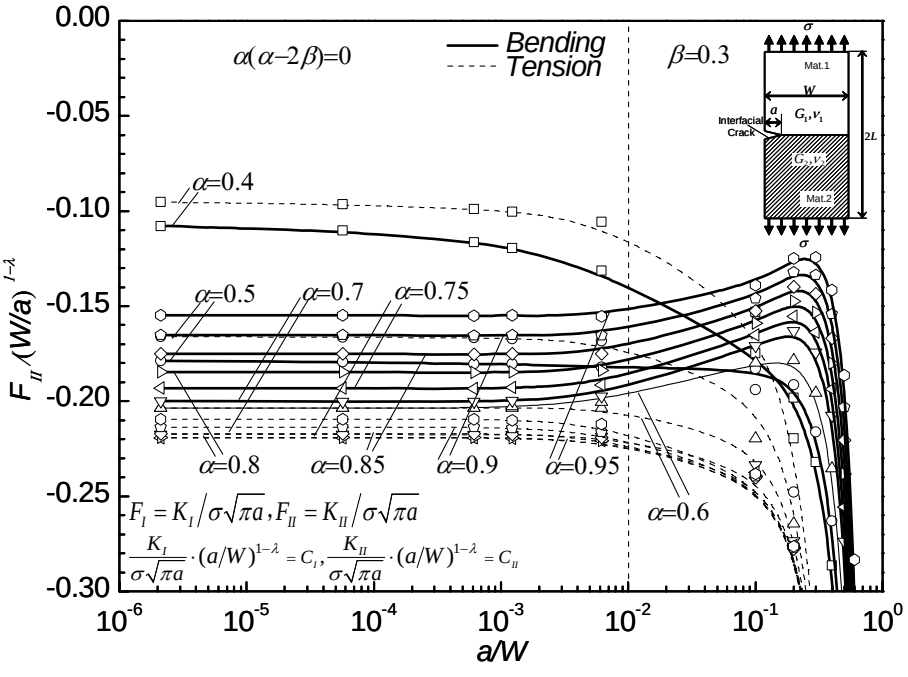

(b)

Fig.4.3 Variations of (a) $F_I \cdot (W/a)^{1-\lambda}$ and (b) $F_{II} \cdot (W/a)^{1-\lambda}$ for $\beta = 0.3$ and tension

Table 4.1 Tabulated values of C_I for tension

α	β =-0.2	β =-0.1	β =0	β =0.1	β =0.2	β =0.3	β =0.4	β =0.45
0.05	1.036	1.082	1.114	1.136				
0.1	0.979	1.043	1.094	1.146	1.187			
0.15	0.907	1.001	1.063	1.14	1.221			
0.2		0.958	1.025	1.12	1.24			
0.3		0.875	0.938	1.044	1.215			
0.4		0.798	0.852	0.947	1.115	1.528		
0.5		0.721	0.772	0.85	0.986	1.343		
0.6			0.7	0.763	0.863	1.106		
0.7			0.635	0.686	0.756	0.912	1.876	
0.75			0.604	0.651	0.709	0.833	1.356	
0.8			0.573	0.618	0.666	0.764	1.092	
0.85			0.542	0.586	0.626	0.704	0.925	1.589
0.9			0.508	0.556	0.588	0.65	0.806	1.083
0.95			0.46	0.527	0.553	0.602	0.715	0.867

Table 4.2 Tabulated values of C_{II} for tension

α	β =-0.2	β =-0.1	β =0	β =0.1	β =0.2	β =0.3	β =0.4	β =0.45
0.05	-0.083	-0.06	-0.026	0.014				
0.1	-0.093	-0.079	-0.052	-0.013	0.031			
0.15	-0.098	-0.094	-0.074	-0.041	0.006			
0.2		-0.106	-0.094	-0.067	-0.023			
0.3		-0.124	-0.123	-0.113	-0.084			
0.4		-0.133	-0.141	-0.144	-0.135	-0.095		
0.5		-0.137	-0.151	-0.162	-0.169	-0.166		
0.6			-0.156	-0.172	-0.187	-0.204		
0.7			-0.156	-0.176	-0.194	-0.218	-0.318	
0.75			-0.155	-0.176	-0.195	-0.219	-0.288	
0.8			-0.153	-0.175	-0.194	-0.219	-0.273	
0.85			-0.15	-0.173	-0.193	-0.217	-0.262	-0.379
0.9			-0.145	-0.171	-0.19	-0.214	-0.252	-0.307
0.95			-0.136	-0.168	-0.187	-0.209	-0.243	-0.278

Table 4.3 Tabulated values of C_I for bending

α	β =-0.2	β =-0.1	β =0	β =0.1	β =0.2	β =0.3	β =0.4	β =0.45
0.05	1.004	1.065	1.109	1.143	--			
0.1	0.925	1.009	1.081	1.157	1.219			
0.15	0.833	0.949	1.037	1.148	1.269			
0.2		0.888	0.982	1.120	1.295			
0.3		0.77	0.861	1.011	1.257			
0.4		0.664	0.742	0.875	1.115	1.718		
0.5		0.566	0.636	0.743	0.934	1.443		
0.6			0.542	0.627	0.766	1.106		
0.7			0.461	0.528	0.626	0.838	2.106	
0.75			0.423	0.485	0.566	0.734	1.45	
0.8			0.387	0.445	0.512	0.644	1.092	
0.85			0.351	0.408	0.463	0.568	0.867	1.72
0.9			0.312	0.373	0.419	0.502	0.711	1.083
0.95			0.262	0.341	0.379	0.445	0.594	0.799

Table 4.4 Tabulated values of C_{II} for bending

α	β =-0.2	β =-0.1	β =0	β =0.1	β =0.2	β =0.3	β =0.4	β =0.45
0.05	-0.080	-0.059	-0.026	0.013	--			
0.1	-0.087	-0.076	-0.051	-0.014	0.032			
0.15	-0.090	-0.089	-0.072	-0.041	0.006			
0.2		-0.098	-0.089	-0.067	-0.024			
0.3		-0.109	-0.113	-0.109	-0.087			
0.4		-0.111	-0.123	-0.133	-0.135	-0.108		
0.5		-0.107	-0.124	-0.142	-0.160	-0.179		
0.6			-0.120	-0.142	-0.166	-0.204		
0.7			-0.113	-0.135	-0.160	-0.200	-0.370	
0.75			-0.108	-0.131	-0.155	-0.193	-0.309	
0.8			-0.103	-0.126	-0.150	-0.185	-0.273	
0.85			-0.097	-0.121	-0.143	-0.175	-0.245	-0.420
0.9			-0.089	-0.115	-0.136	-0.165	-0.222	-0.307
0.95			-0.077	-0.109	-0.128	-0.155	-0.202	-0.256

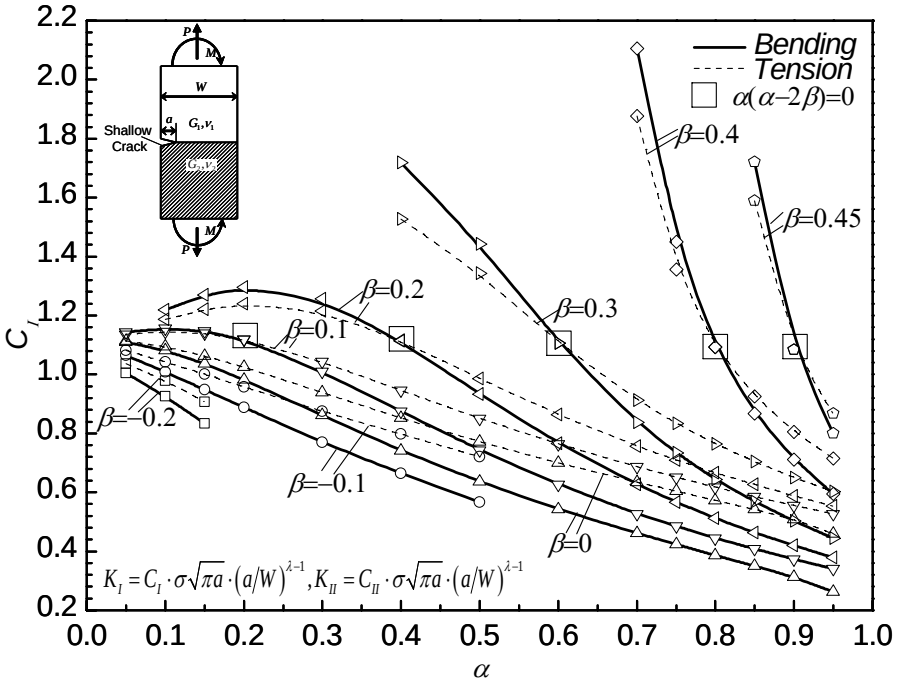

(a)

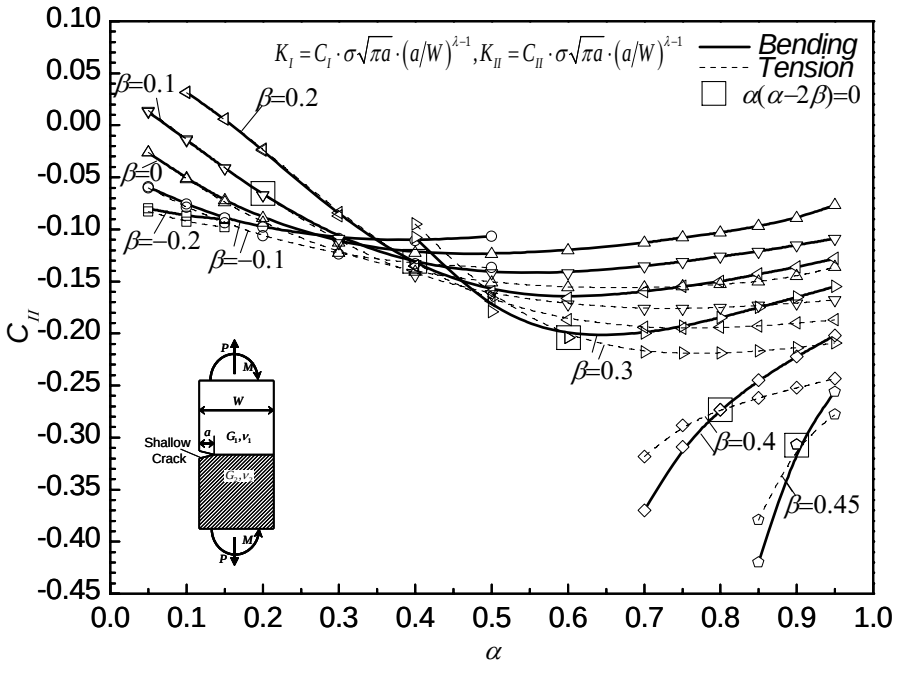

(b)

Fig. 4.4 Constants (a) C_I and (b) C_{II} for bending and tensile loading conditions

The examples of the normalized SIFs for the edge interface cracks $a/W = 0.001$ within the zone of free-edge singularity are computed and plotted against various Dundurs' material composite parameters. Fig. 4.5 and 4.6 show variations of F_I and F_{II} for bi-material bonded strips $a/W = 0.001$ subjected to tensile and bending loads, respectively. It should be noted that the SIF values behave the similar varying tendency within the singular zone for each loading type. This is due to the fact that the stress distributions of the shallow single-edge interface cracks are determined by the free-edge singularity near the interface corner.

The contour map variations of the SIFs can be obtained from the 3-dimensional plot as shown in Fig. 4.5 and 4.6. And it can be used to estimate the variation tendency for the whole range of material combinations for a fixed crack length. Say, Fig. 4.7 and 4.8 show the contour map variations for bi-material bonded strips $a/W = 0.001$ for tensile and bending loads, respectively. Similar variation tendencies can be easily observed from these figures. In addition, it can be seen from Fig. 4.7a and 4.8a that the variation tendencies of F_I can be distinguished into two groups according to $\alpha(\alpha - 2\beta)$. Say, F_I decreases radioactively outward the pole centered at around $(\alpha, \beta) = (1, 0.05)$ when $\alpha(\alpha - 2\beta) > 0$, and increases downwardly in the $\alpha - \beta$ space when $\alpha(\alpha - 2\beta) < 0$. However, different from the case of F_I, the values of F_{II} in Fig. 4.7b and 4.8b decrease radioactively and monotonously from the lower right corner to the upper left corner of the $\alpha - \beta$ space from the pole centered at around $(\alpha, \beta) = (1, 0.1)$.

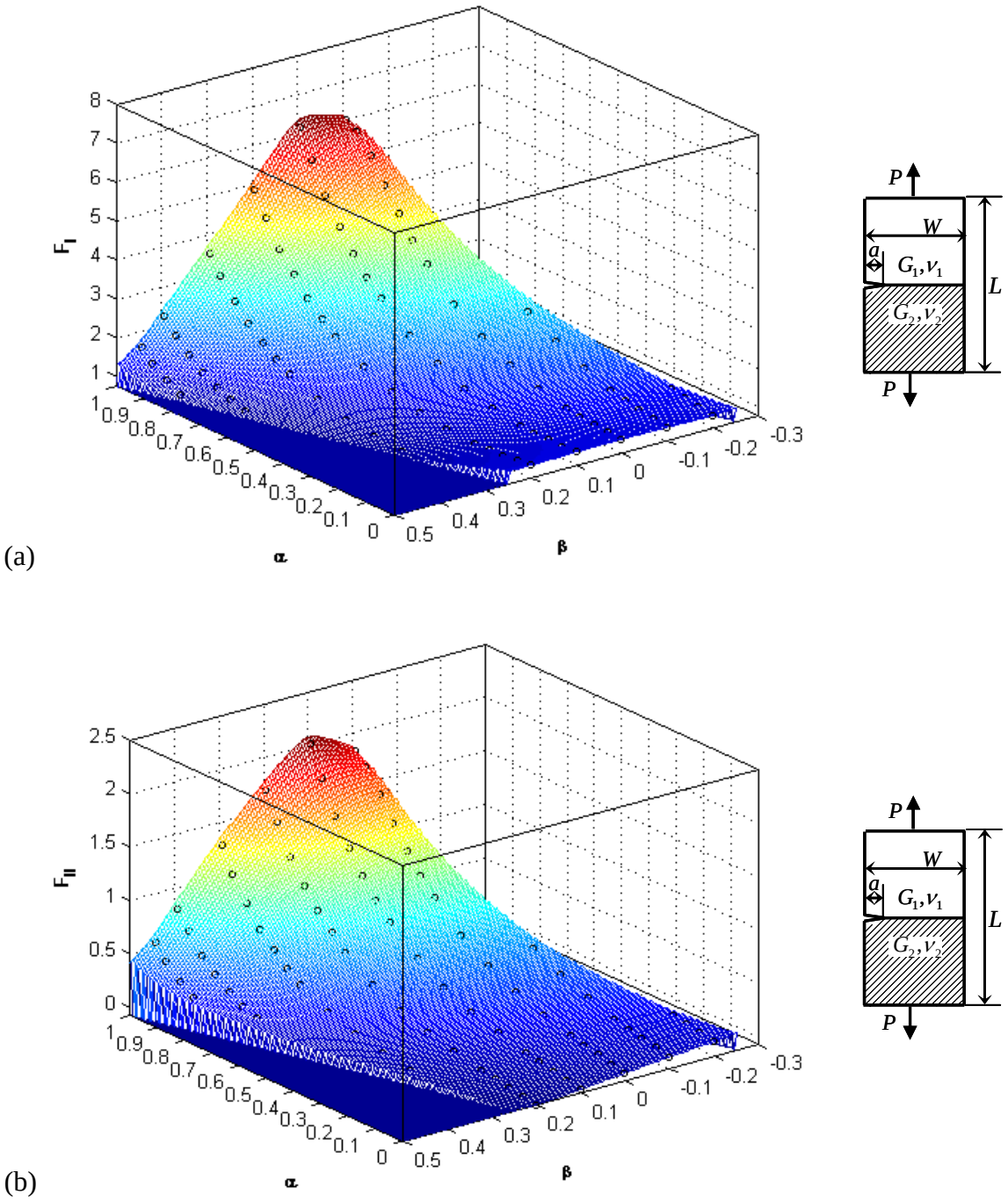

Fig. 4.5 3-dimensional variations of (a) F_I and (b) F_{II} for single edge interface crack $a/W = 0.001$ for tension

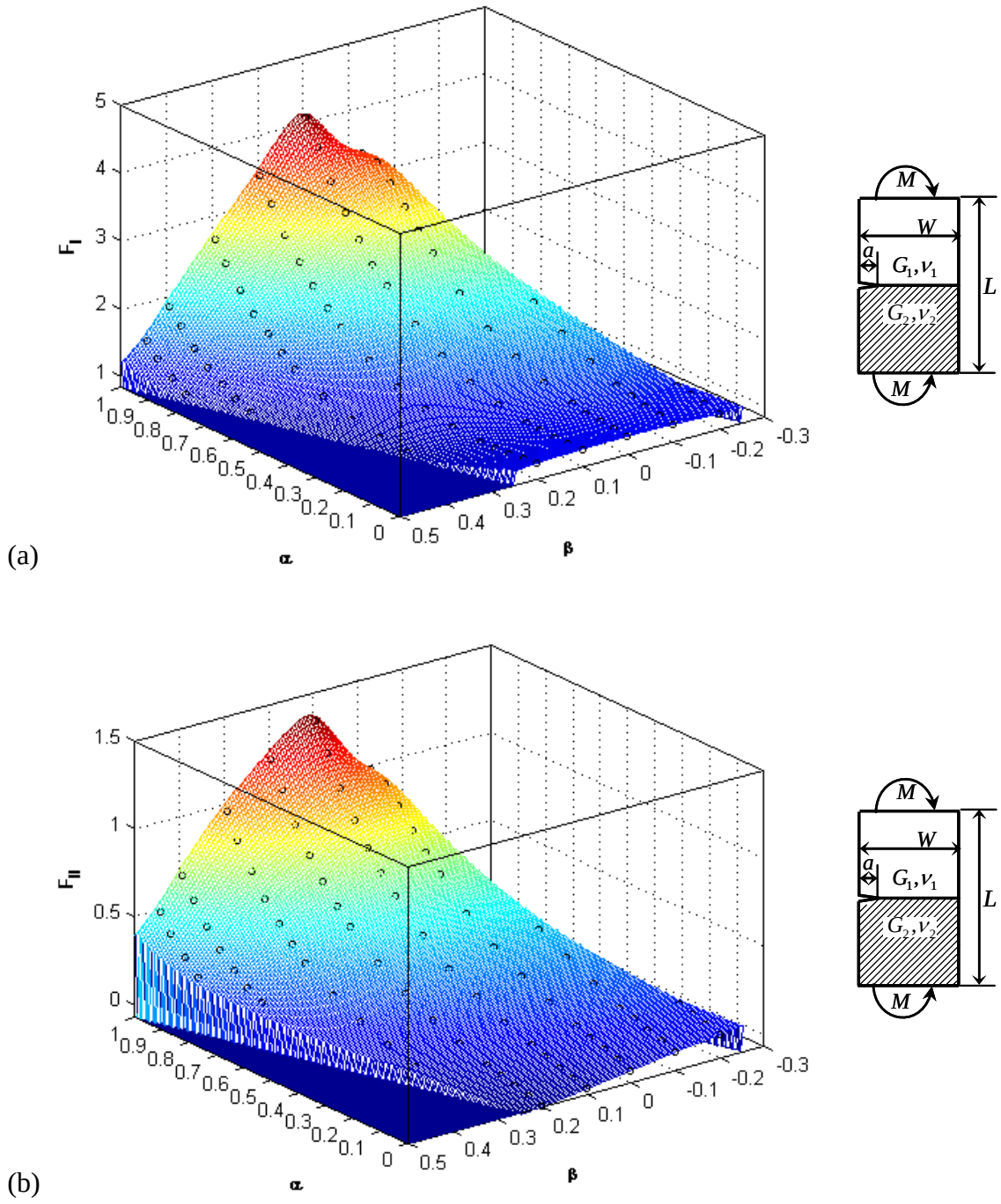

Fig. 4.6 3-dimensional variations of (a) F_I and (b) F_{II} of single edge interface crack $a/W = 0.001$ for the bending loads

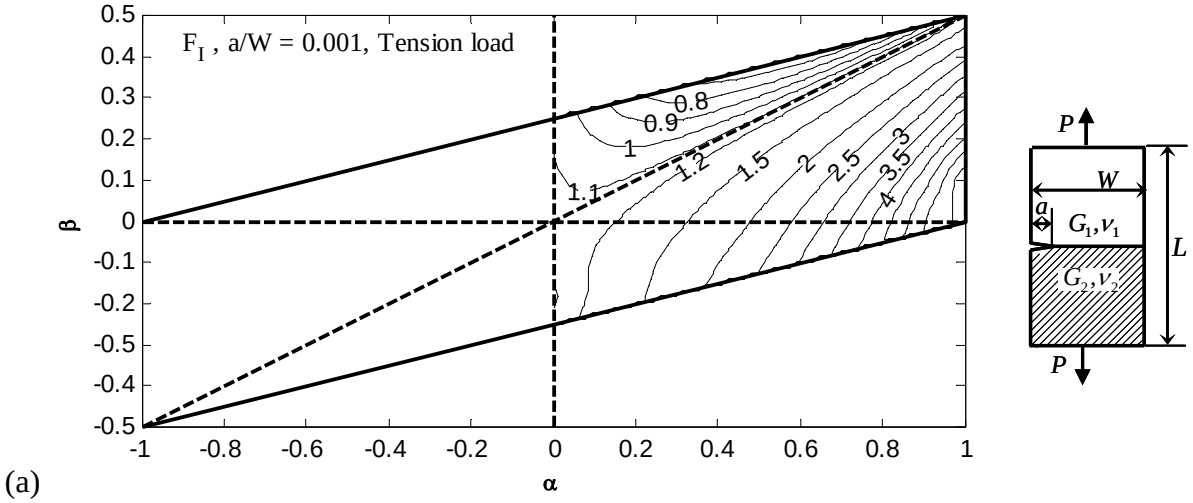

(a)

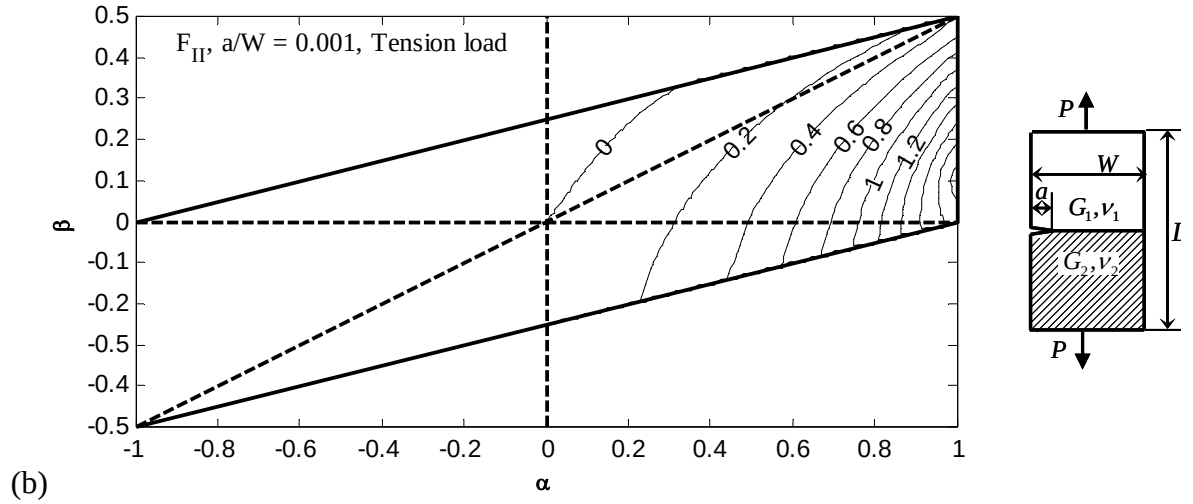

(b)

Fig. 4.7 Contour maps of (a) F_I and (b) F_{II} of $a/W = 0.001$ for the tensile case

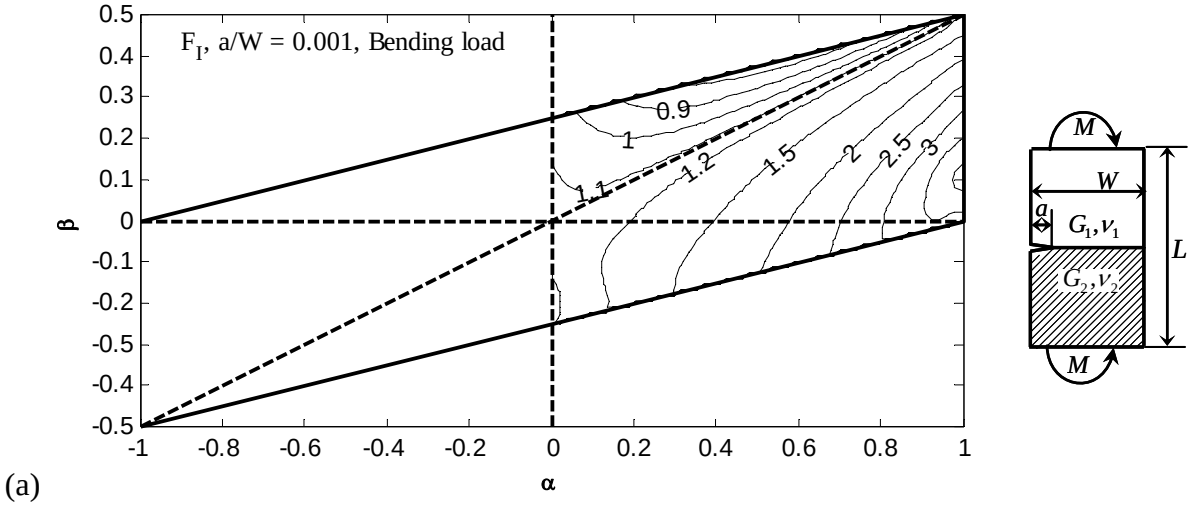

(a)

Fig. 4.8 Contour maps of (a) F_I and (b) F_{II} of $a/W = 0.001$ for the bending case (Continue)

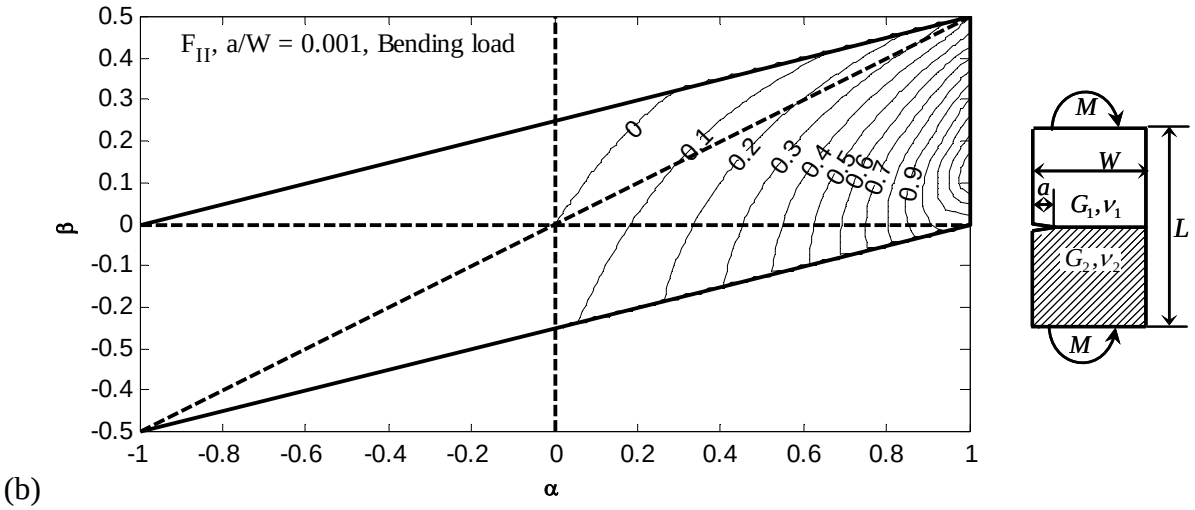

(b)

Fig. 4.8 Contour maps of (a) F_I and (b) F_{II} of $a/W = 0.001$ for the bending case

4.4 Stress intensity factors for edge interface cracks out of the zone of free-edge singularity

4.4.1 The tensile loading case

As depicted in Section 4.3, the SIFs of the shallow edge interface cracks within the singular zone can be well computed by using Eq.4.2. Here, the SIFs for crack lengths out of the zone of free-edge singularity ($0.1 \le a/W \le 0.9$) will be investigated.

The contour map variations of F_I and F_{II} for $0.1 \le a/W \le 0.9$ are plotted against Dundurs' material composite parameters in Fig. 4.9 – 4.17. It can be seen from Fig. 4.9 that the varying tendencies of F_I and F_{II} are similar to those in Fig. 4.7. This is due to the residual effect of the free-edge singularity since $a/W = 0.1$ is very close to the boundary of the singular zone. The contour plot of F_I for $a/W = 0.2, 0.3, 0.4$ in Fig. 4.10-4.12 are almost similar in trend. The values of F_I increase radioactively outward from the pole around $(\alpha, \beta) = (0.98, 0.45)$ in the $\alpha - \beta$ space. However, there are two radiation centers in the $\alpha - \beta$ space when $a/W \ge 0.5$ in Fig. 4.13-4.17, one is located around $(\alpha, \beta) = (0.98, 0.45)$, and the

other is at $(\alpha,\beta)=(1,0)$. The F_I values increase gradually outward from the two poles. Furthermore, the values of material combinations around the line $\beta=\alpha/4-0.1$ are clearly interfered by the two radiation centers. This is caused by the bending effect for the deep edge crack cases.

The contour lines of F_{II} in Fig. 4.9b-4.17b for $a/W \geq 0.2$ behave linearity in the $\alpha-\beta$ space. And all the lines in the $\alpha-\beta$ space for a fixed relative crack length are parallel to each other. The trend of the F_{II} lines rotate as the increase of the relative crack length. For example, the slope of the contour lines is -2.17326 for $a/W=0.2$ and then gradually increased to a positive value of 0.03378 for $a/W=0.2$.

The maximum and minimum values of F_I and F_{II} over $a/W=0.1\sim0.9$ with varying material composite parameters can be obtained from the contour plots. And they are tabulated in Table 4.5 and 4.6 together with the corresponding α,β in brackets, respectively. Specifically, over the whole range of $\alpha-\beta$ space, Table 5 shows that F_I peaks at the points in the $\beta=\alpha/4-0.25$ line when $a/W<0.4$, but peaks at around $\alpha=0,\beta=0$ when $a/W>0.4$. Furthermore, F_I bottoms out at around $\alpha=0.98,\beta=0.465$ for $a/W<0.4$ and $\alpha=1,\beta=0$ for $a/W>0.4$ in the whole $\alpha-\beta$ space. However, for the case of F_{II}, the maximum values are always located at $\alpha=1,\beta=0.5$ (the upper right corner of the $\alpha-\beta$ space) when $a/W>0.1$, and the minimum values are always located at $\alpha=0,\beta=-0.25$ (the lower left corner of the $\alpha-\beta$ space) when $a/W>0.2$.

The maximum and minimum values of F_I, F_{II} for typical engineering materials are listed in Table 4.6. As can be seen from this table, However, the lowest point of F_I for $a/W<0.4$ is not situated at one unique (α,β). But, F_I always peaks at $\alpha=1,\beta=0$ and bottoms out at $\alpha=1,\beta=0.35$ over the whole $\alpha-\beta$ space when $a/W>0.4$. Similarly, F_{II} always reach to its' maximum at $\alpha=1,\beta=0.35$ and minimum at $\alpha=0,\beta=-0.1$ when $a/W>0.1$.

Table 4.5 Maximum and minimum values of F_I and F_{II} of the tensile loading case for material combinations over the whole $\alpha-\beta$ space

Whole α - β space								
a/W	$F_{I\min}$	(α,β)	$F_{I\max}$	(α,β)	$F_{II\min}$	(α,β)	$F_{II\max}$	(α,β)
0.1	1.153	(0.7,0.425)	1.501	(1,0)	-0.030	(0,0.23)	0.471	(1,0.1)
0.2	1.350	(0.86,0.465)	1.493	(1,0)	-0.033	(0,-0.214)	0.452	(1,0.5)
0.3	1.639	(0.98,0.465)	1.709	(0.76,0.44)	-0.129	(0,-0.25)	0.589	(1,0.5)
0.4	2.077	(0.987,0.419)	2.146	(0.275,-0.184)	-0.271	(0,-0.25)	0.805	(1,0.5)
0.5	2.694	(1,0)	2.859	(0.034,0.259)	-0.492	(0,-0.25)	1.167	(1,0.5)
0.6	3.690	(1,0)	4.032	(0,0)	-0.877	(0,-0.25)	1.823	(1,0.5)
0.7	5.793	(1,0)	6.352	(0,0)	-1.660	(0,-0.25)	3.189	(1,0.5)
0.8	10.32	(1,0)	11.95	(0,0)	-3.708	(0,-0.25)	6.800	(1,0.5)
0.9	29.42	(1,0.5)	34.59	(0,0)	-13.08	(0,-0.25)	23.42	(1,0.5)

Table 4.6 Maximum and minimum values of F_I and F_{II} of the tensile loading case for material combinations of typical engineering materials.

Typical engineering materials								
a/W	$F_{I\min}$	(α,β)	$F_{I\max}$	(α,β)	$F_{II\min}$	(α,β)	$F_{II\max}$	(α,β)
0.1	1.185	(0.4,0.2)	1.385	(1,0.15)	-0.014	(0,0.1)	0.471	(1,0.1)
0.2	1.363	(0.56,0.39)	1.426	(1,0.15)	-0.016	(0,-0.1)	0.437	(1,0.35)
0.3	1.642	(0.98,0.495)	1.675	(1,0.15)	-0.058	(0,-0.1)	0.496	(1,0.35)
0.4	2.078	(0.987,0.346)	2.116	(0.114,-0.072)	-0.118	(0,-0.1)	0.610	(1,0.35)
0.5	2.769	(0.99,0.349)	2.825	(0,0.01)	-0.214	(0,-0.1)	0.820	(1,0.35)
0.6	3.935	(1,0.35)	4.032	(0,0)	-0.380	(0,-0.1)	1.194	(1,0.35)
0.7	6.158	(1,0.35)	6.352	(0,0)	-0.697	(0,-0.1)	2.010	(1,0.35)
0.8	11.44	(1,0.35)	11.95	(0,0)	-1.580	(0,-0.1)	4.192	(1,0.35)
0.9	32.14	(1,0.35)	34.59	(0,0)	-5.590	(0,-0.1)	14.52	(1,0.35)

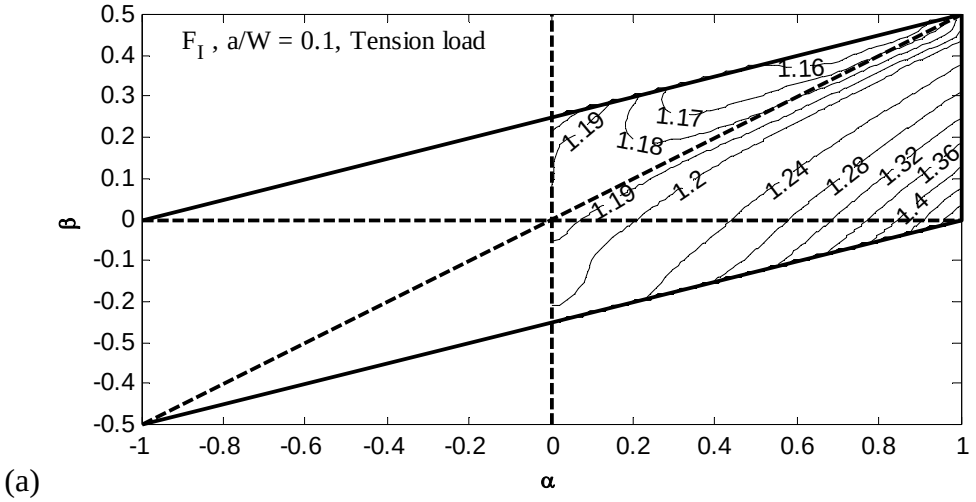

(a)

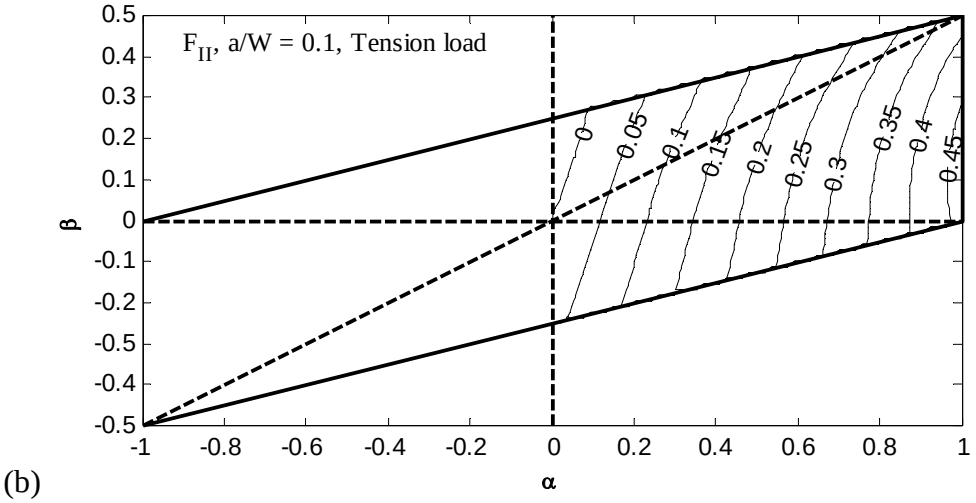

(b)

Fig. 4.9 Contour map of (a) F_I and (b) F_{II} of $a/W = 0.1$ for tension

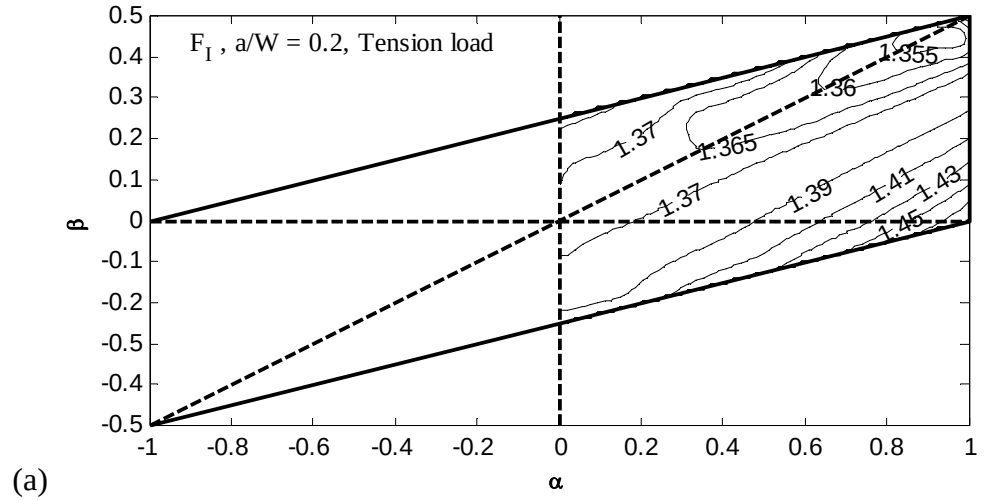

(a)

Fig. 4.10 Contour map of (a) F_I and (b) F_{II} of $a/W = 0.2$ for tension (Continue)

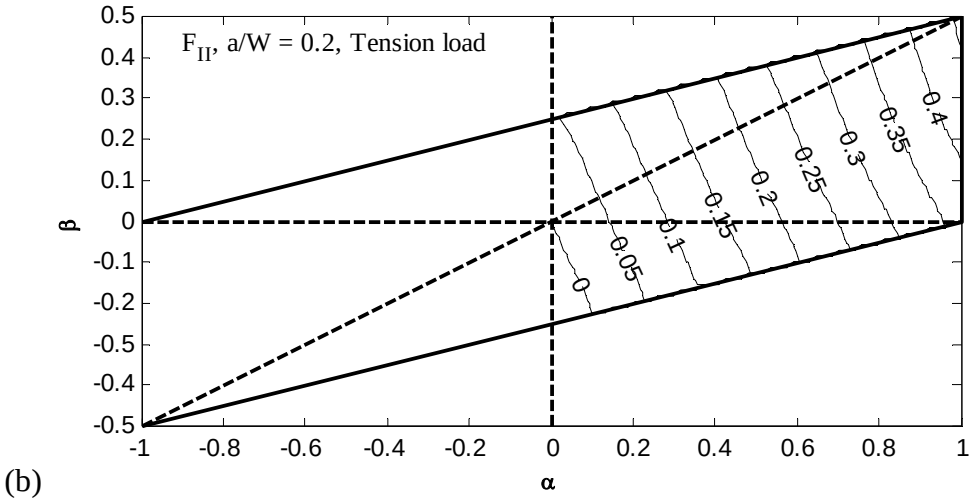

(b)

Fig. 4.10 Contour map of (a) F_I and (b) F_{II} of $a/W = 0.2$ for tension

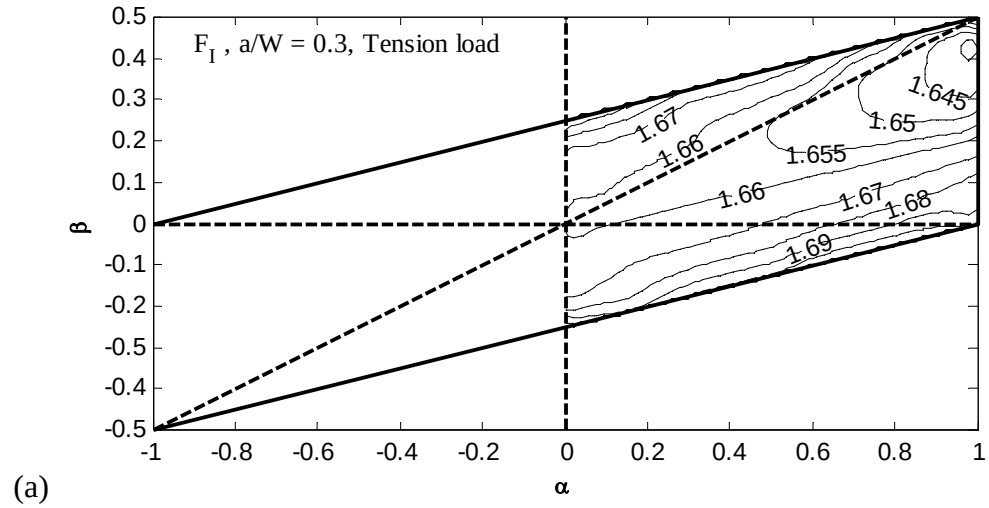

(a)

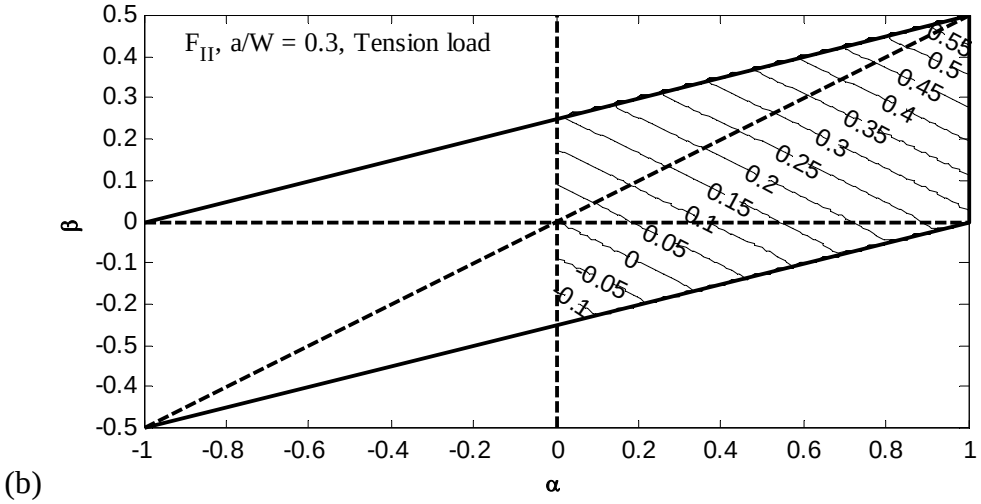

(b)

Fig. 4.11 Contour map of (a) F_I and (b) F_{II} of $a/W = 0.3$ for tension

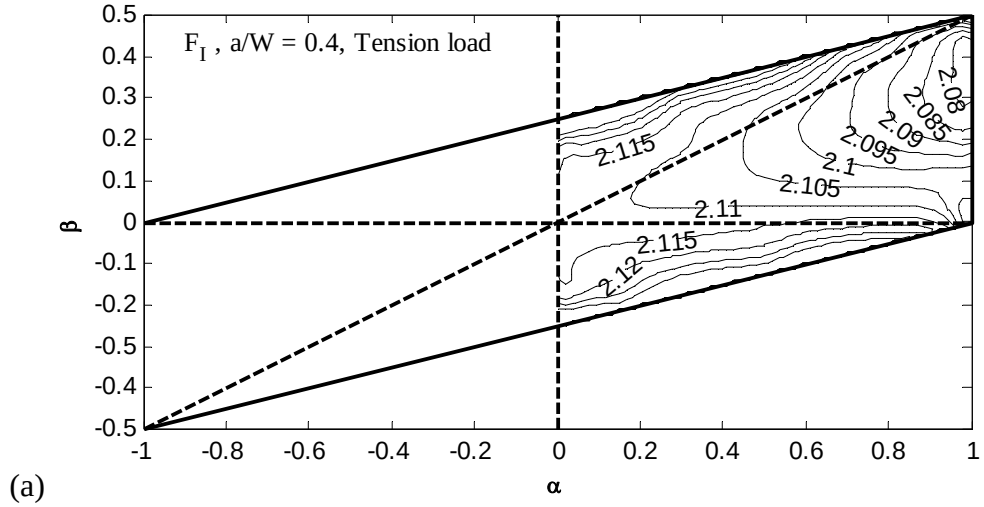

(a)

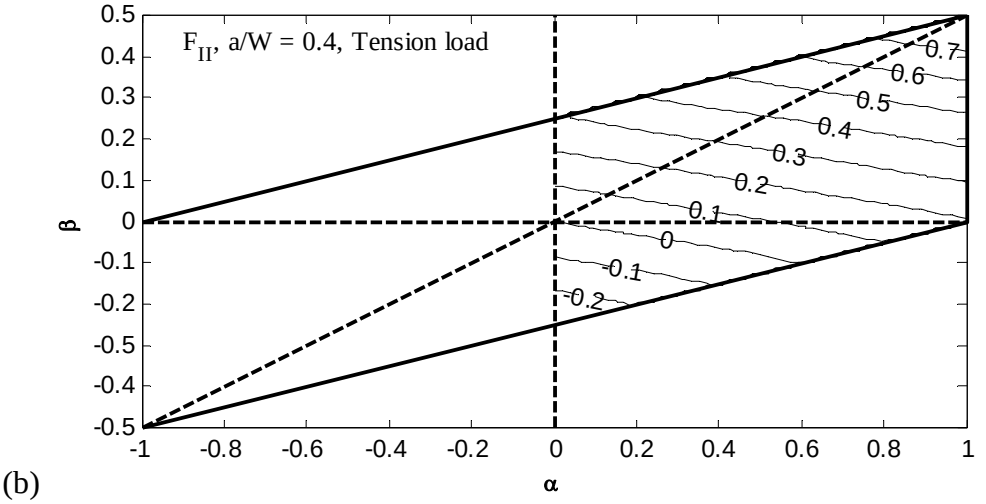

(b)

Fig. 4.12 Contour map of (a) F_I and (b) F_{II} of $a/W = 0.4$ for tension

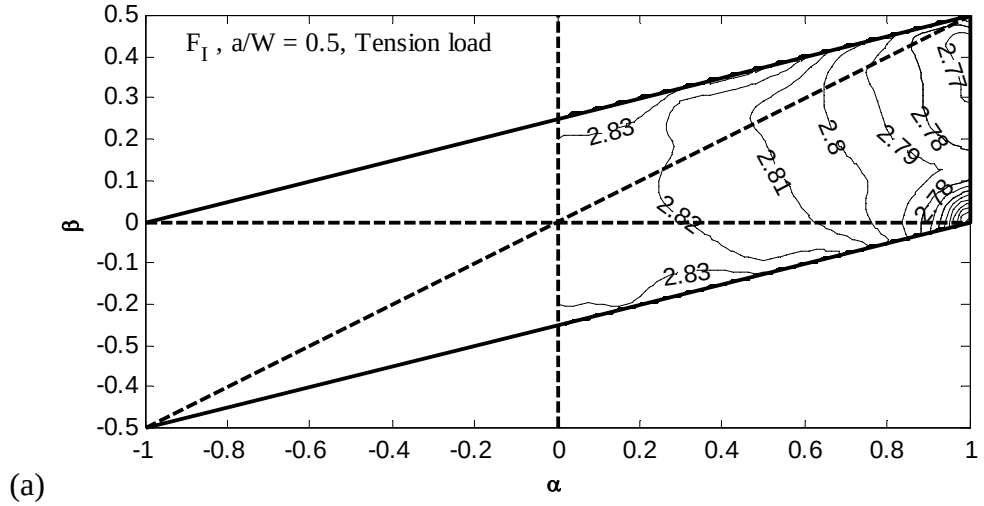

(a)

Fig. 4.13 Contour map of (a) F_I and (b) F_{II} of $a/W = 0.5$ for tension (Continue)

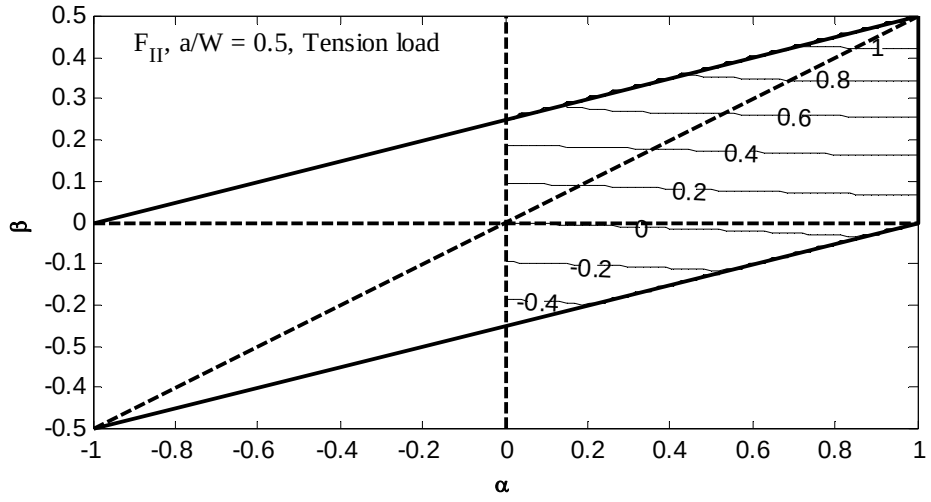

(b)

Fig. 4.13 Contour map of (a) F_I and (b) F_{II} of $a/W = 0.5$ for tension

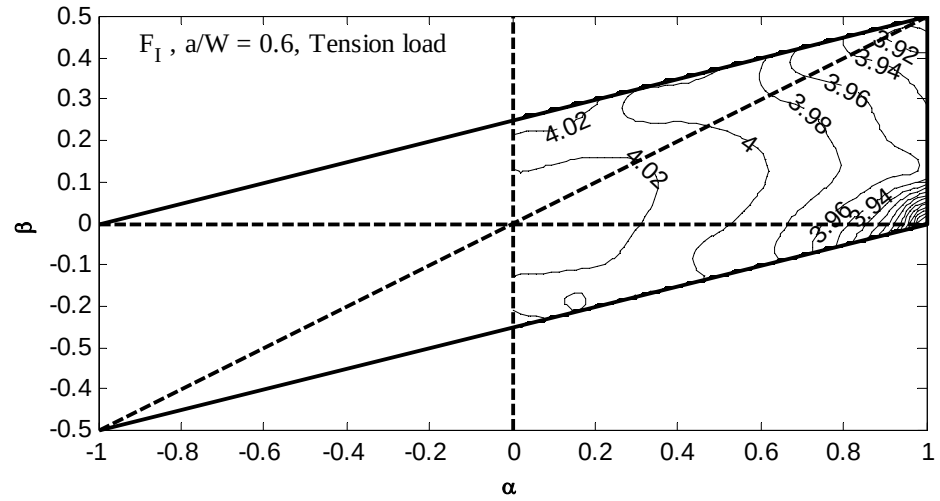

(a)

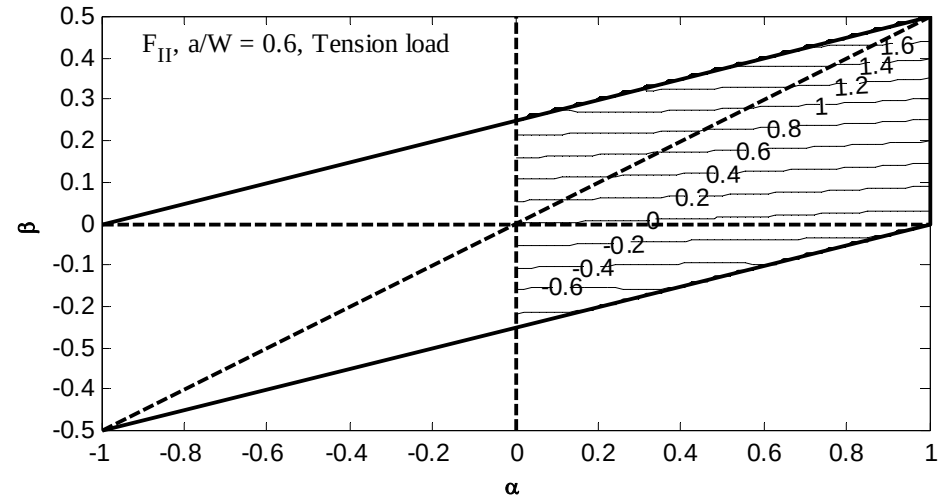

(b)

Fig. 4.14 Contour map of (a) F_I and (b) F_{II} of $a/W = 0.6$ for tension

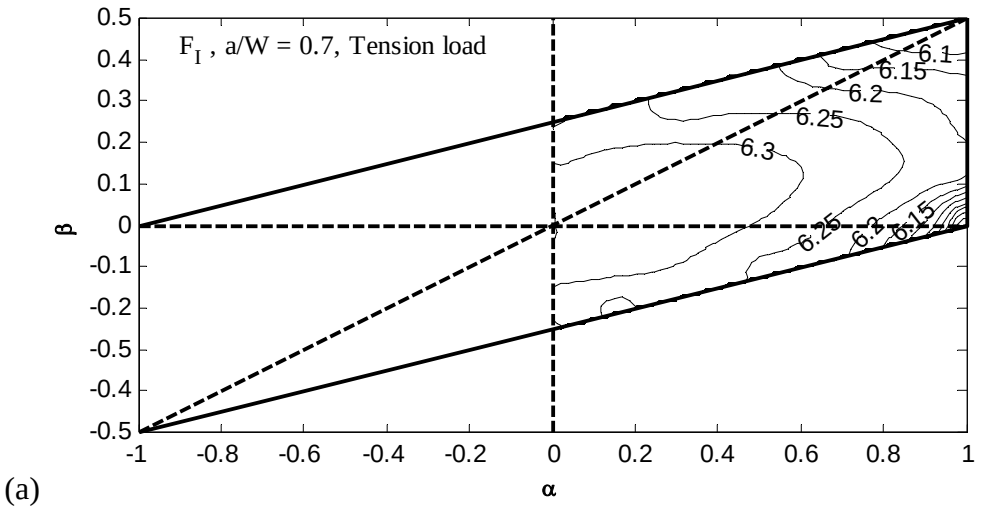

(a)

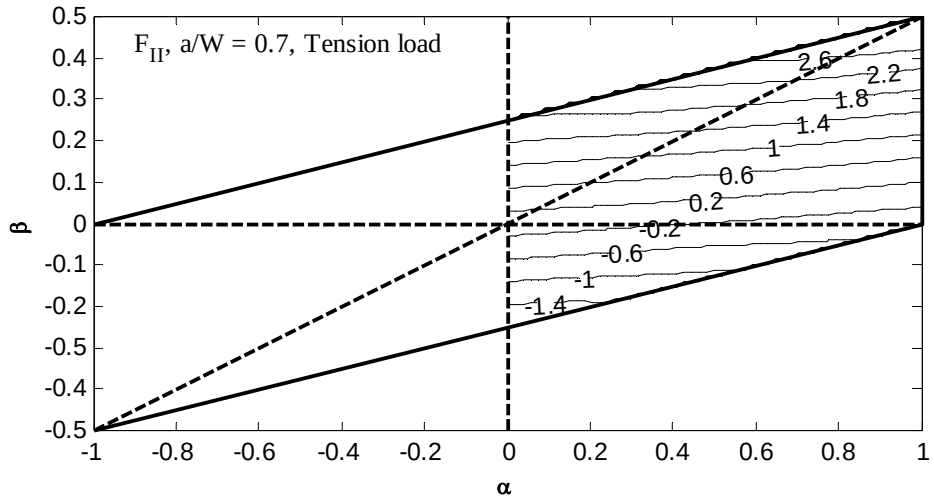

(b)

Fig. 4.15 Contour map of (a) F_I and (b) F_{II} of $a/W = 0.7$ for the tension case

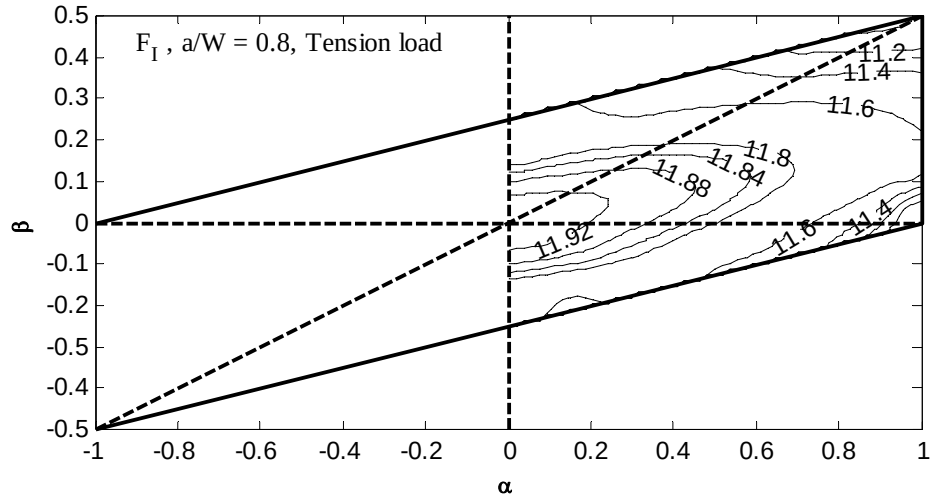

(a)

Fig. 4.16 Contour map of (a) F_I and (b) F_{II} of $a/W = 0.8$ for the tension case (Continue)

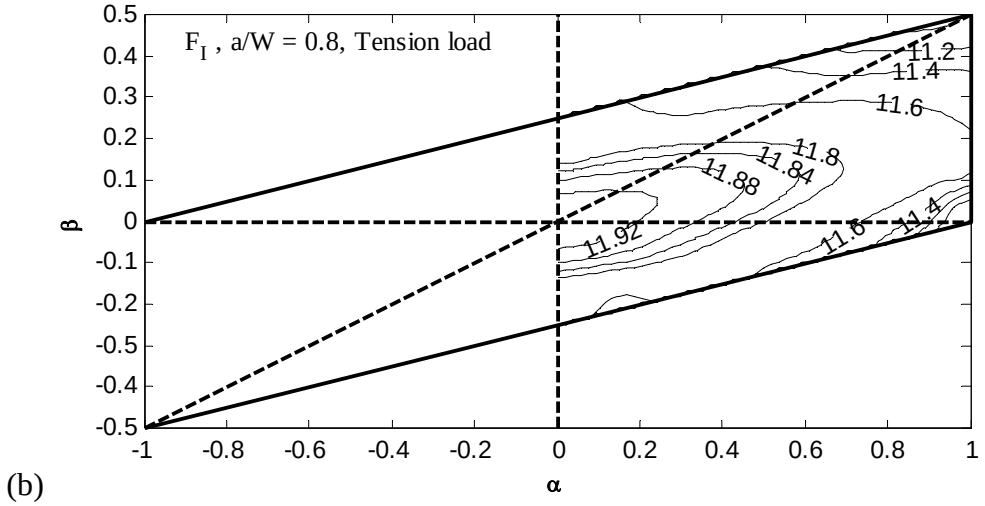

(b)

Fig. 4.16 Contour map of (a) F_I and (b) F_{II} of $a/W = 0.8$ for the tension case

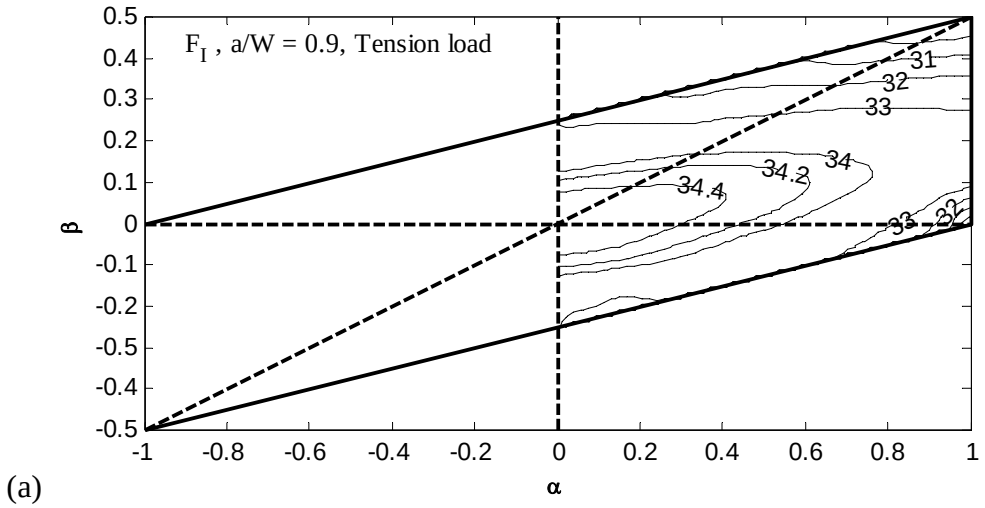

(a)

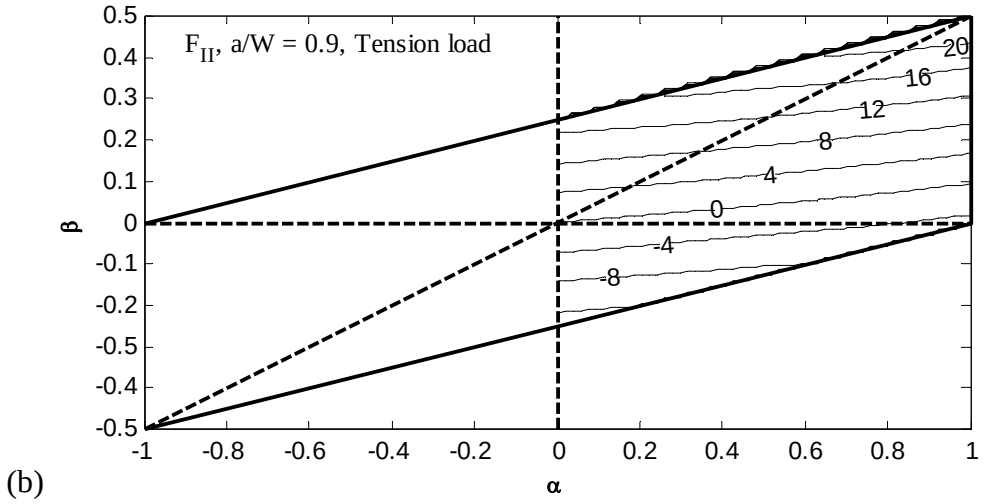

(b)

Fig. 4.17 Contour map of (a) F_I and (b) F_{II} of $a/W = 0.9$ for tension

4.4.2 The bending loading case

The contour map variations of F_I and F_{II} for the bending loading conditions are plotted against Dundurs' material composite parameters in Fig. 4.18–4.26. The contour plot of F_I for $a/W = 0.2, 0.3, 0.4$ in Fig. 4.18-4.21 are almost similar in trend. The values of F_I increase radioactively outward from the pole around $(\alpha, \beta) = (1 0)$ (the lower right corner in the $\alpha - \beta$ space). Similarly, there are two radiation centers in the $\alpha - \beta$ space when $a/W \geq 0.5$. However, this phenomenon is not as clear as that of the tensile loading case. This is maybe due to the enhanced bending effect for the bending loading case. The contour lines of F_{II} in Fig. 4.19b-4.26b for $a/W \geq 0.2$ behave linearity in the $\alpha - \beta$ space. And all the lines in the $\alpha - \beta$ space for a fixed relative crack length are parallel to each other. The maximum and minimum values of F_I and F_{II} over the whole range of material combinations can be obtained from the contour plots. And the maximum and minimum values of F_I, F_{II} are tabulated in Table 4.7, and the corresponding material composite parameters α, β are also tabulated in the brackets. Specifically, over the whole range of $\alpha - \beta$ space, Table 4.7 shows that F_I peaks at the points in the $\beta = \alpha/4 - 0.25$ line when $a/W < 0.2$, but peaks at around $\alpha = 1, \beta = 0.5$ when $0.4 < a/W < 0.7$ and then peaks at $\alpha = 0, \beta = 0$ when $a/W > 0.7$. Furthermore, F_I bottoms out at around $\alpha = 1, \beta = 0$ for almost the whole range of relative crack lengths in the whole $\alpha - \beta$ space. The maximum values of F_{II} are uniquely located at $\alpha = 1, \beta = 0.5$ (the upper right corner of the $\alpha - \beta$ space), and the minimum values are uniquely located at $\alpha = 0, \beta = -0.25$ (the lower left corner of the $\alpha - \beta$ space) when $a/W > 0.2$ for the whole range of material combinations and relative crack lengths.

The maximum and minimum values of F_I, F_{II} for typical engineering materials are listed in Table 4.8. As can be seen from this table, the lowest point of F_I locates at

$\alpha = 1, \beta = 0.15$ for each crack length when $0.3 < a/W < 0.8$, and changes to $\alpha = 1, \beta = 0.35$ when $a/W > 0.8$. However, the maximum point for F_I is not situated at one unique (α, β). In addition, F_{II} always reach to its' maximum at $\alpha = 1, \beta = 0.35$ and minimum at $\alpha = 0, \beta = -0.1$ when $a/W > 0.1$.

Table 4.7 Maximum and minimum values of F_I and F_{II} of the bending load case for material combinations over the whole $\alpha - \beta$ space

Whole α - β space								
a/W	$F_{I\min}$	(α, β)	$F_{I\max}$	(α, β)	$F_{II\min}$	(α, β)	$F_{II\max}$	(α, β)
0.1	0.754	(1,0)	1.061	(0,-0.25)	-0.047	(0,-0.25)	0.301	(1,0.5)
0.2	0.855	(1,0)	1.076	(1,-0.25)	-0.114	(0,-0.25)	0.299	(1,0.5)
0.3	0.982	(1,0)	1.159	(1,0.5)	-0.172	(0,-0.25)	0.329	(1,0.5)
0.4	1.154	(1,0)	1.305	(1,0.5)	-0.239	(0,-0.25)	0.396	(1,0.5)
0.5	1.323	(1,0)	1.543	(1,0.5)	-0.331	(0,-0.25)	0.523	(1,0.5)
0.6	1.645	(1,0)	1.944	(1,0.5)	-0.481	(0,-0.25)	0.762	(1,0.5)
0.7	2.398	(1,0)	2.724	(0,-0.015)	-0.774	(0,-0.25)	1.258	(1,0.5)
0.8	3.925	(1,0)	4.672	(0,0)	-1.515	(0,-0.25)	2.547	(1,0.5)
0.9	10.51	(1,0.5)	12.45	(0,0)	-4.786	(0,-0.25)	8.301	(1,0.5)

Table 4.8 Maximum and minimum values of F_I and F_{II} of the tensile loading case for material combinations of typical engineering materials

Typical engineering materials								
a/W	$F_{I\min}$	(α, β)	$F_{I\max}$	(α, β)	$F_{II\min}$	(α, β)	$F_{II\max}$	(α, β)
0.1	1.003	(1,0.22)	1.046	(0,-0.1)	0.021	(0,-0.1)	0.265	(1,0.35)
0.2	1.007	(1,0.195)	1.056	(0,-0.1) (0,0.1)	-0.049	(0,-0.1)	0.213	(1,0.35)
0.3	1.081	(1,0.15)	1.125	(0,-0.1) (0,0.1)	-0.073	(0,-0.1)	0.203	(1,0.35)
0.4	1.220	(1,0.15)	1.261	(0,0.1)	-0.101	(0,-0.1)	0.223	(1,0.35)
0.5	1.454	(1,0.15)	1.496	(1,0.35)	-0.140	(0,-0.1)	0.285	(1,0.35)
0.6	1.863	(1,0.15)	1.908	(1,0.35)	-0.203	(0,-0.1)	0.414	(1,0.35)
0.7	2.658	(1,0.15)	2.724	(0,-0.015)	-0.334	(0,-0.1)	0.701	(1,0.35)
0.8	4.542	(1,0.35)	4.672	(0,0)	-0.643	(0,-0.1)	1.475	(1,0.35)
0.9	11.66	(1,0.35)	12.45	(0,0)	-2.031	(0,-0.1)	5.036	(1,0.35)

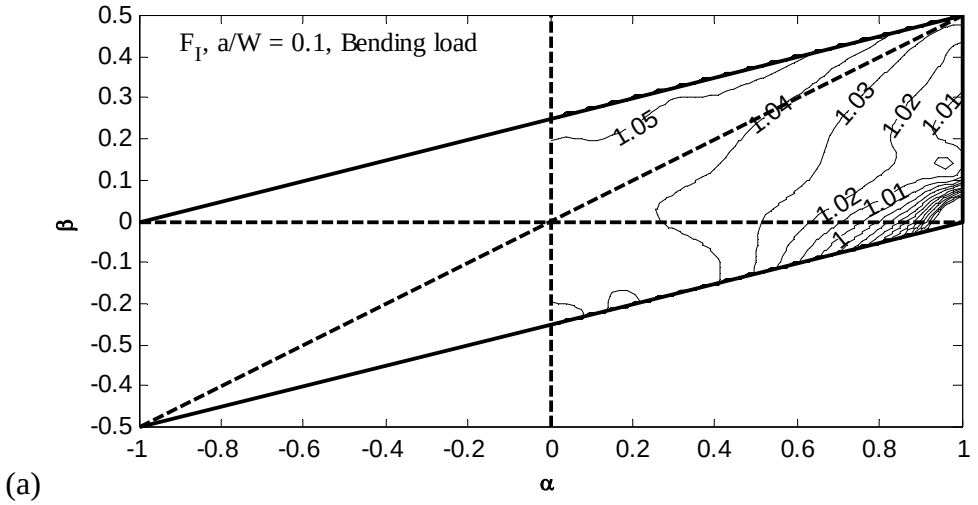

(a)

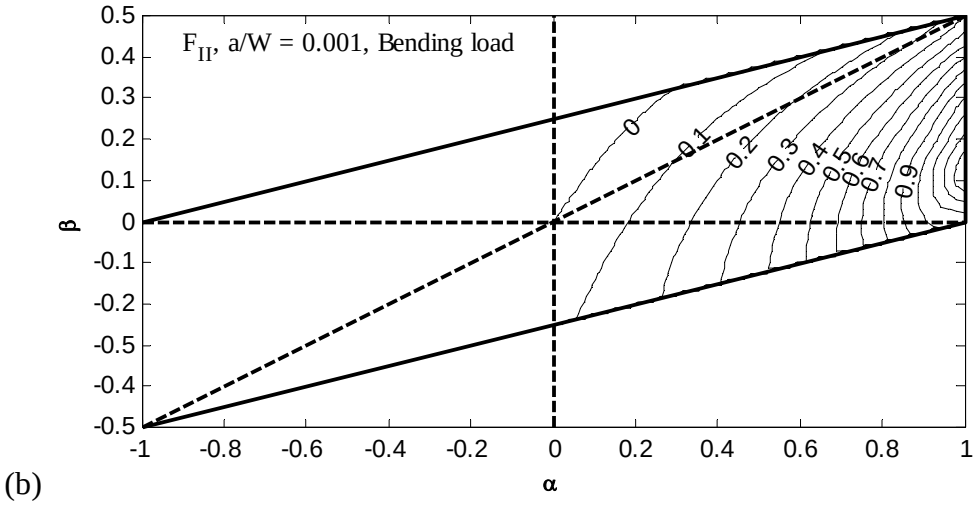

(b)

Fig. 4.18 Contour map of (a) F_I and (b) F_{II} of $a/W = 0.1$ for bending

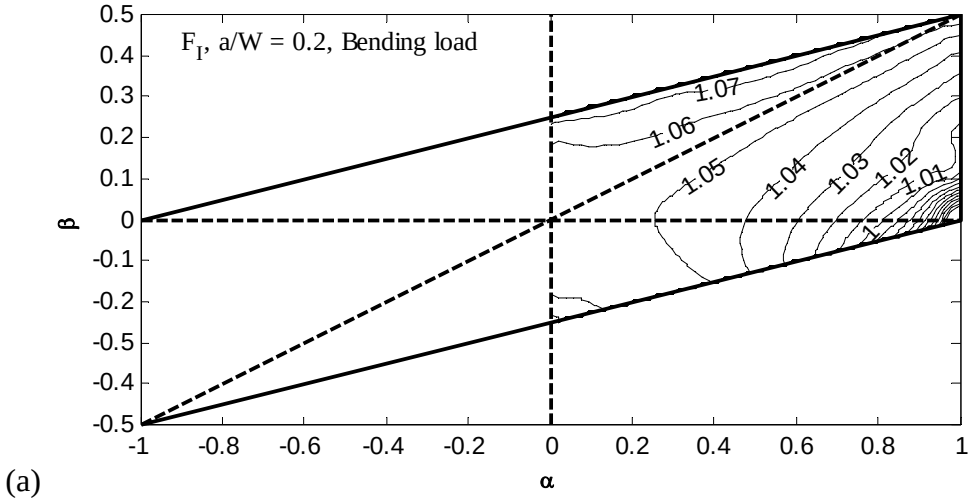

(a)

Fig. 4.19 Contour map of (a) F_I and (b) F_{II} of $a/W = 0.2$ for bending (Continue)

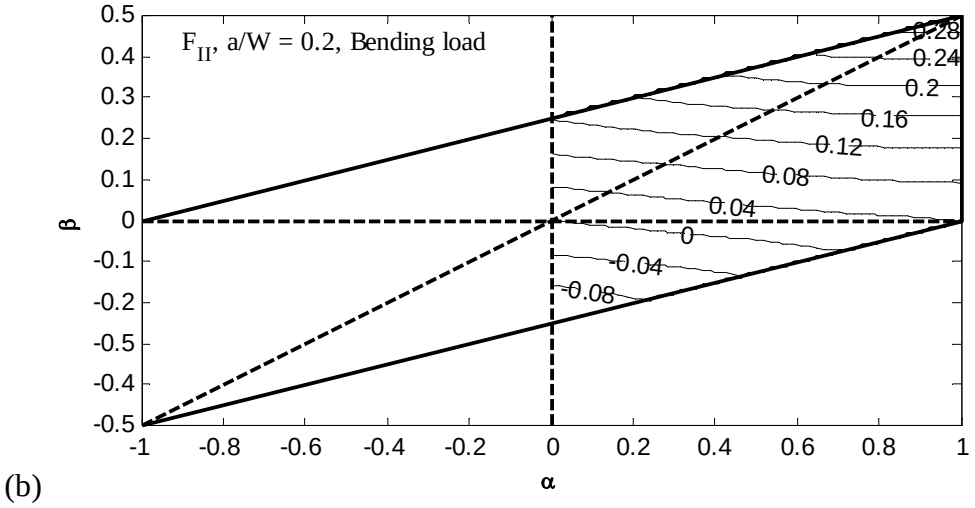

(b)

Fig. 4.19 Contour map of (a) F_I and (b) F_{II} of $a/W = 0.2$ for bending

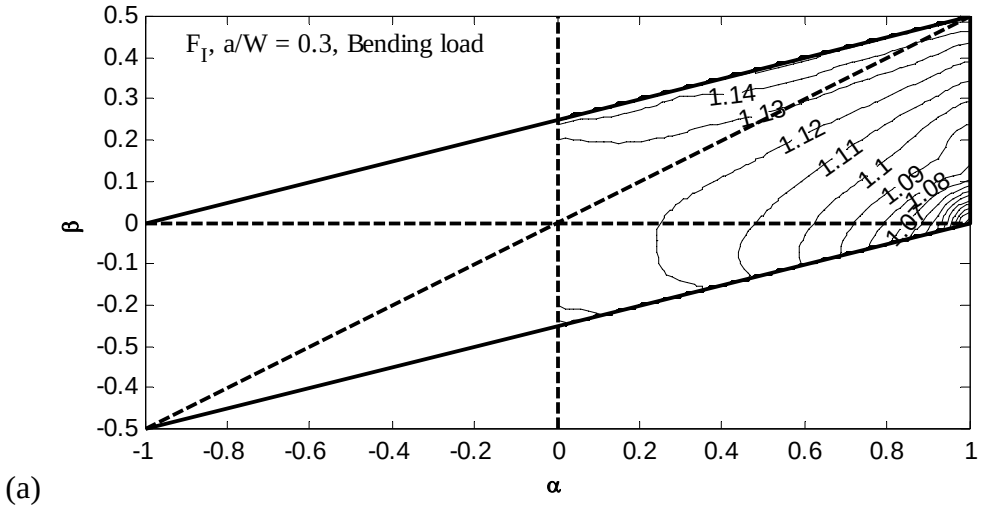

(a)

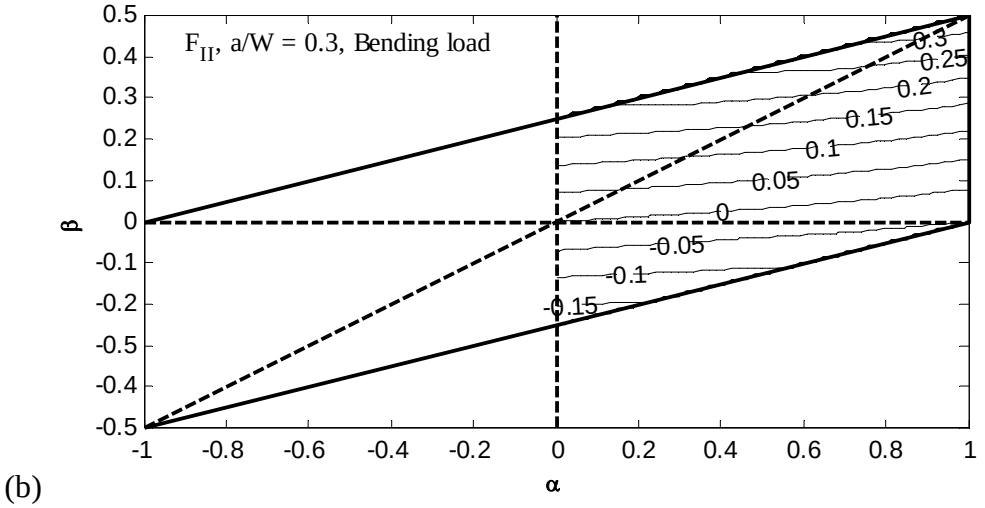

(b)

Fig. 4.20 Contour map of (a) F_I and (b) F_{II} of $a/W = 0.3$ for bending

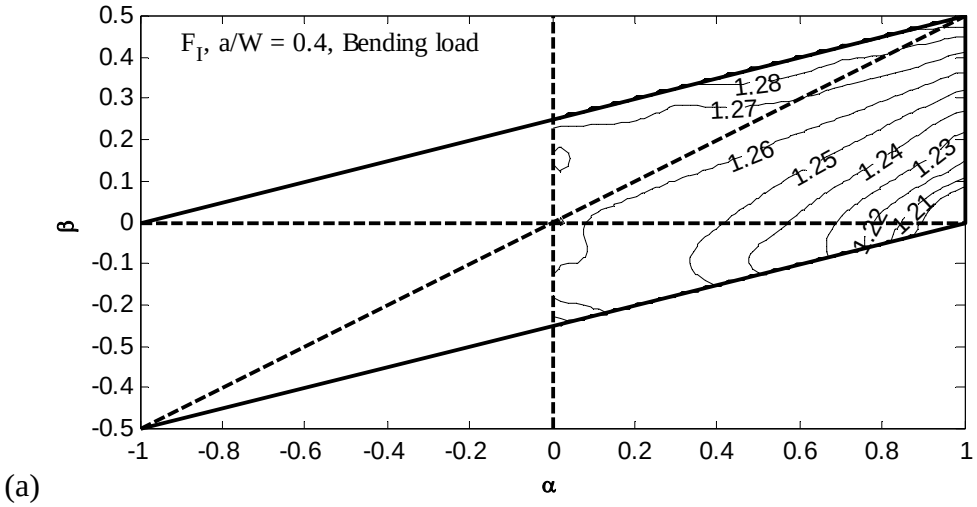

(a)

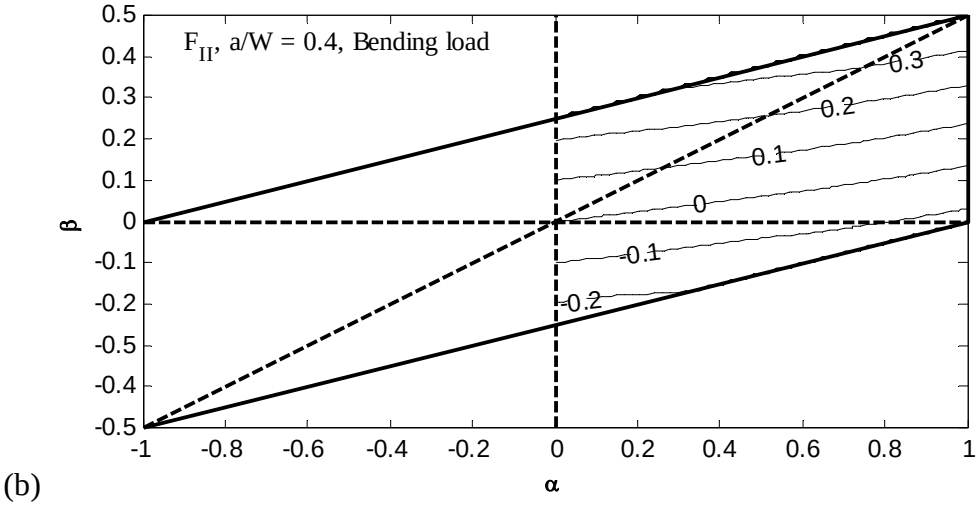

(b)

Fig. 4.21 Contour map of (a) F_I and (b) F_{II} of $a/W = 0.4$ for bending

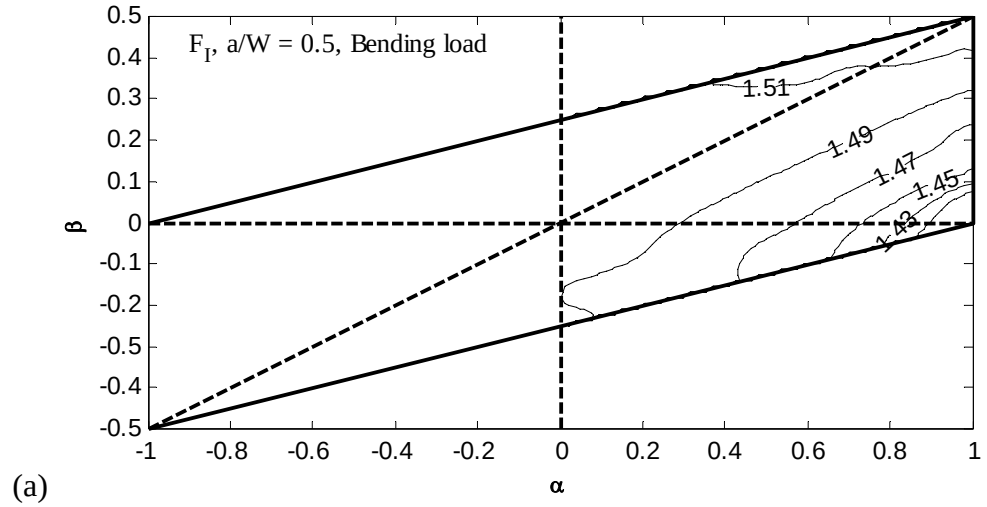

(a)

Fig. 4.22 Contour map of (a) F_I and (b) F_{II} of $a/W = 0.5$ for bending (Continue)

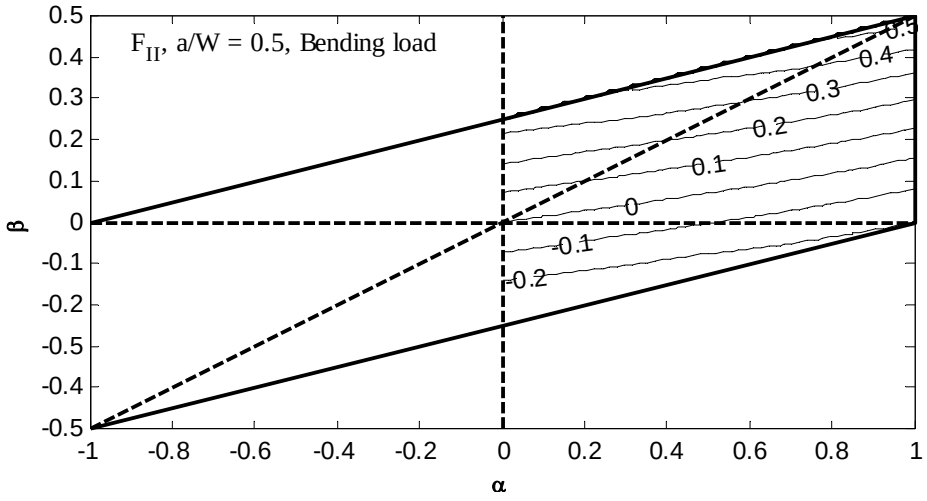

(b)

Fig. 4.22 Contour map of (a) F_I and (b) F_{II} of $a/W = 0.5$ for bending

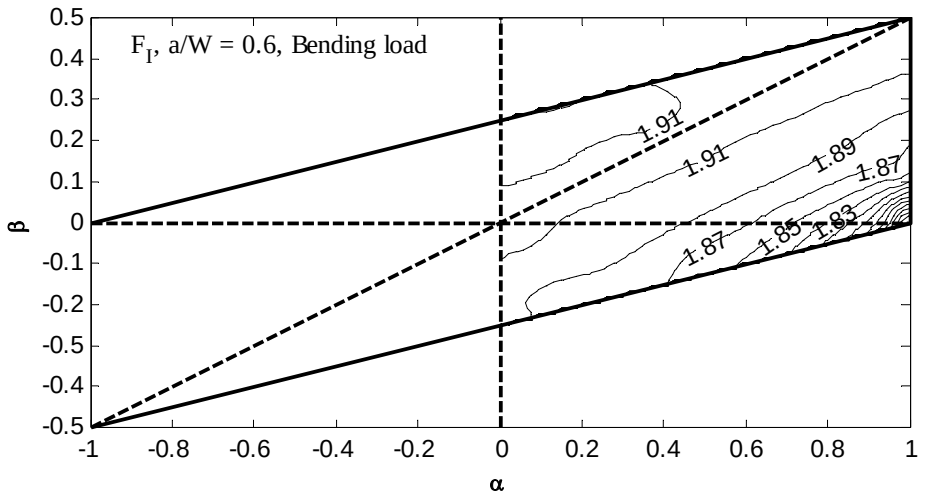

(a)

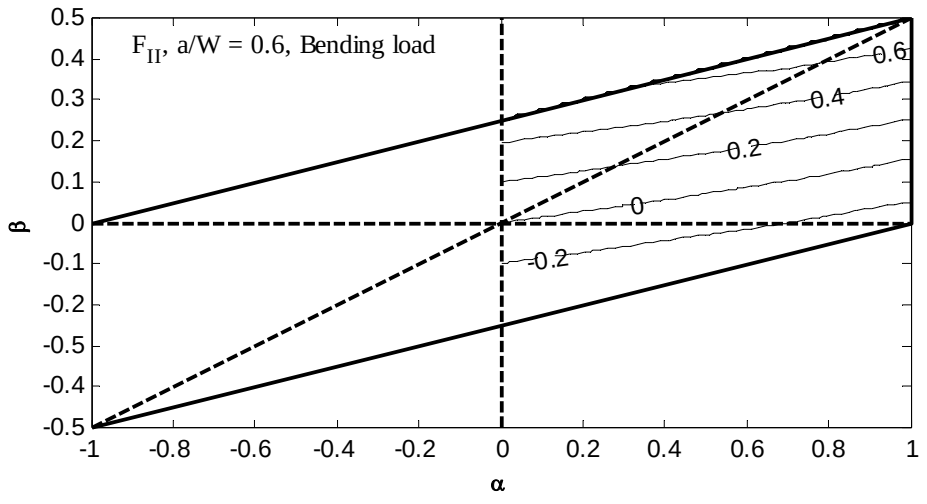

(b)

Fig. 4.23 Contour map of (a) F_I and (b) F_{II} of $a/W = 0.6$ for bending

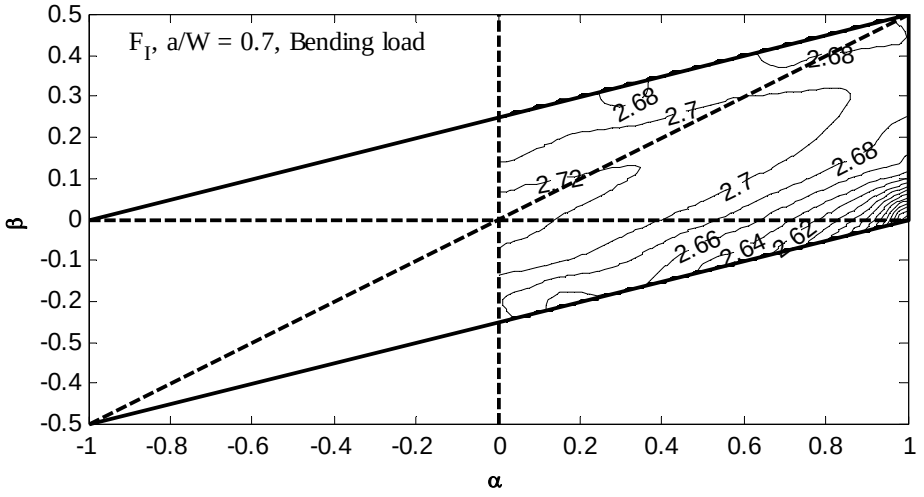

(a)

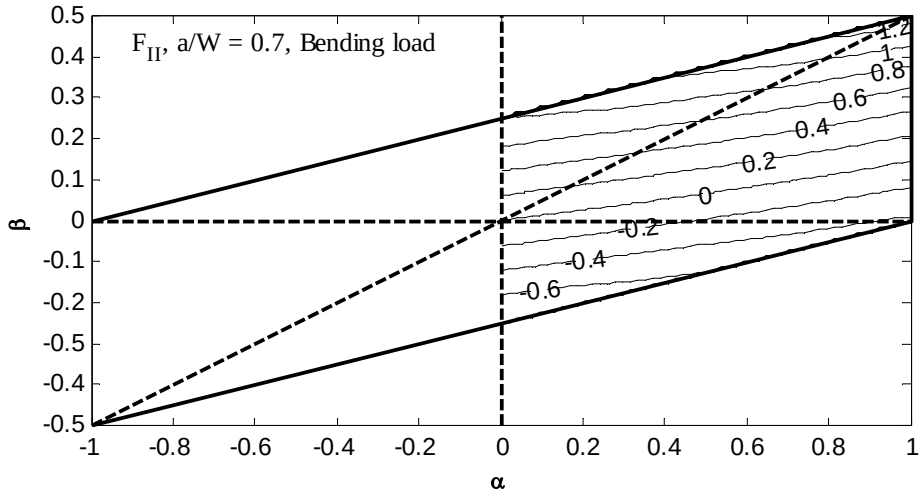

(b)

Fig. 4.24 Contour map of (a) F_I and (b) F_{II} of $a/W = 0.7$ for the bending case

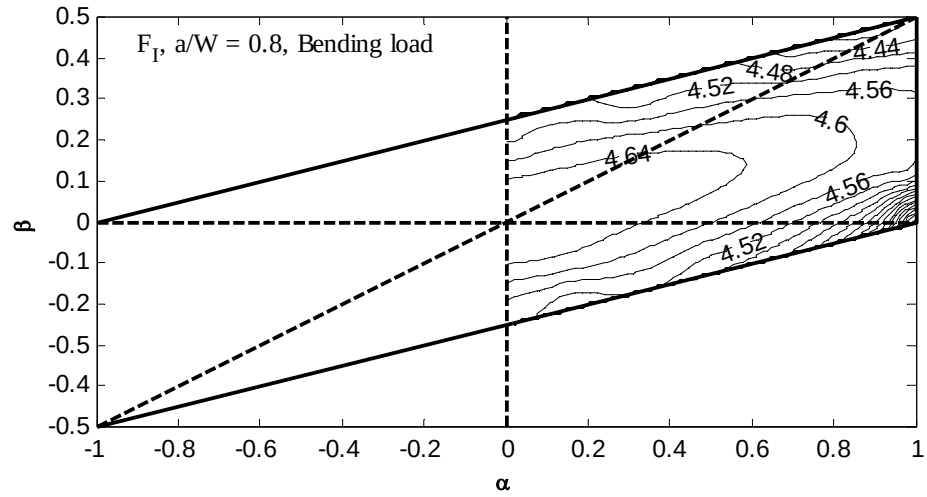

(a)

Fig. 4.25 Contour map of (a) F_I and (b) F_{II} of $a/W = 0.8$ for bending (Continue)

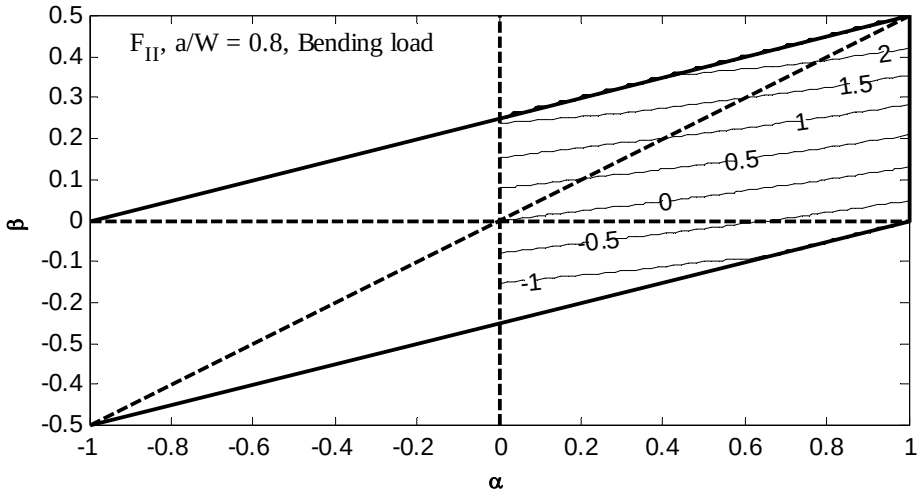

(b)

Fig. 4.25 Contour map of (a) F_I and (b) F_{II} of $a/W = 0.8$ for bending

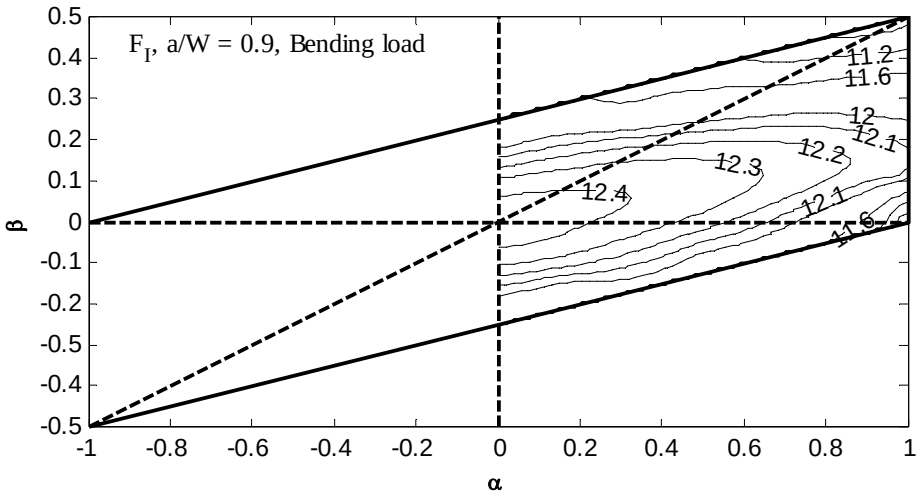

(a)

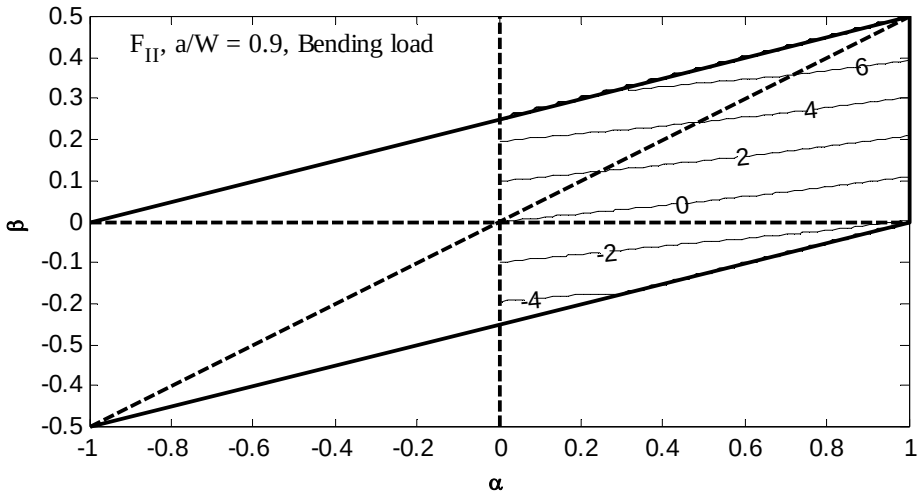

(b)

Fig. 4.26 Contour map of (a) F_I and (b) F_{II} of $a/W = 0.9$ for bending

4.5 Effects of relative crack lengths and material combinations to the stress intensity factors

In order to examine the effect of relative crack lengths and material combinations more clearly, the values of F_I are normalized using those of the homogenous plate [4,5]. Fig. 4.27-Fig. 4.29 show the variations of F_I, F_{II} with varying relative crack lengths for $\beta = -0.2, -0.1, 0, 0.1$ respectively. The values of the tensile loading are plotted in dashed lines and those of the bending loading are in solid lines. Fig. 4.27a-Fig. 4.29a clearly depict that there is an inflection point around $a/W = 0.4$ for arbitrary α, β regarding the tendency of $F_I/F_{I,\mathrm{homo}}$ for the tensile loading conditions. Specifically, $F_I/F_{I,\mathrm{homo}}$ increases with increasing α under fixed β before this point, but increases with decreasing α after this point. However, similar inflections points for $F_I/F_{I,\mathrm{homo}}$ can not be observed for the bending loading conditions, and $F_I/F_{I,\mathrm{homo}}$ grows with decreasing α by fixing β to a constant.

The variations of F_{II} are plotted in Fig. 4.27b-Fig. 4.29b. As can be seen from these figures, inflection points regarding the relative crack lengths can be observed for the two loading conditions. And the inflection points are located at around $a/W = 0.5$ for the tensile loading, and at $a/W = 0.25$ for the bending loading. In addition, F_{II} behave the similar varying tendencies for the two loading types. The values of F_{II} increase with decreasing α under fixed β before the inflection points, but grow with increasing α after these points.

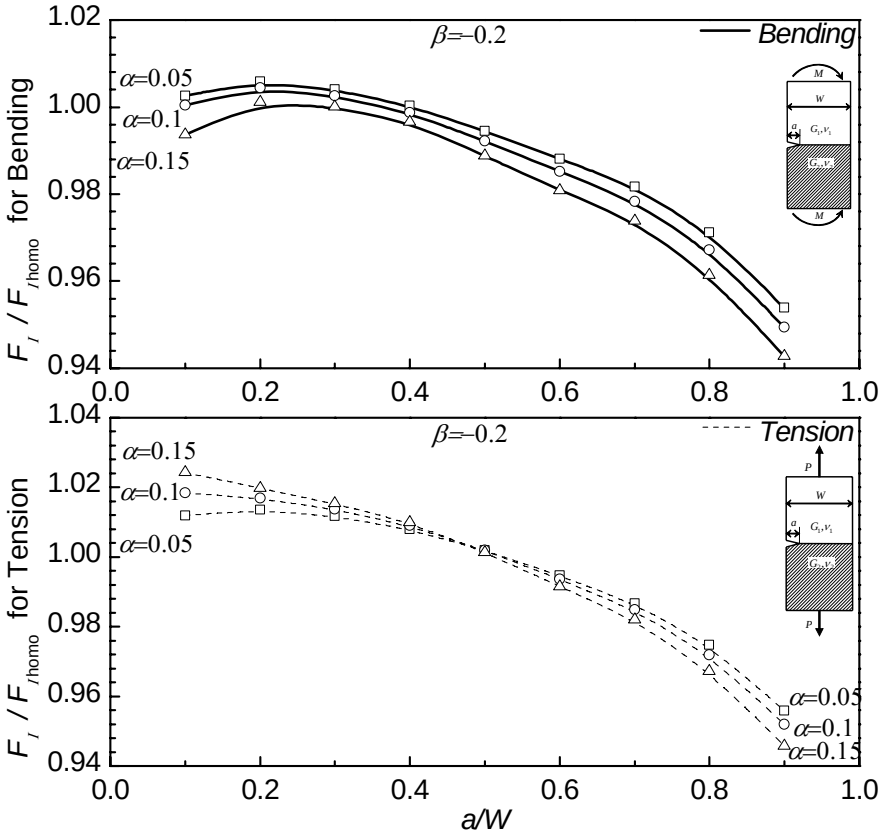

(a)

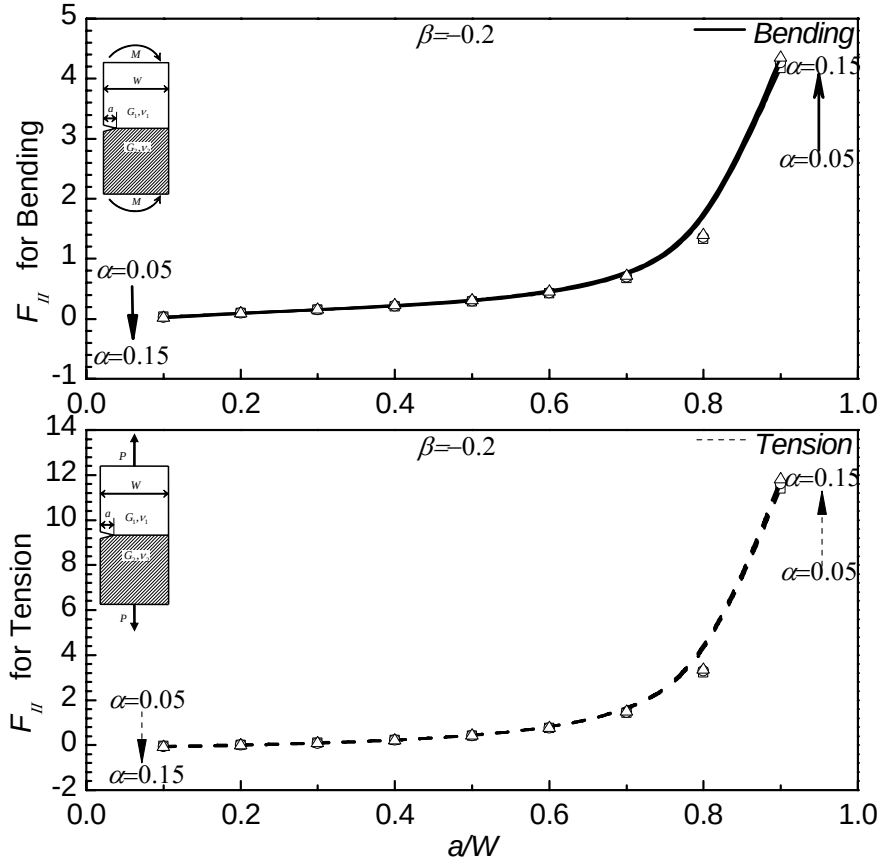

(b)

Fig. 4.27 Variations of SIFs of single edge interface crack with a/W for $\beta = -0.2$

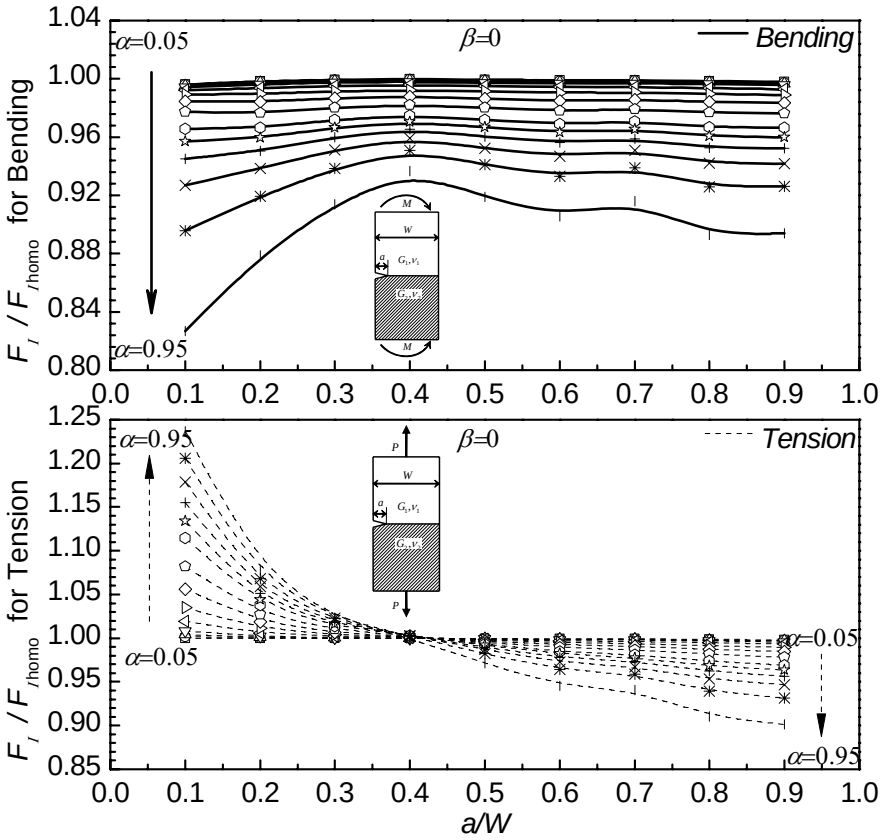

(a)

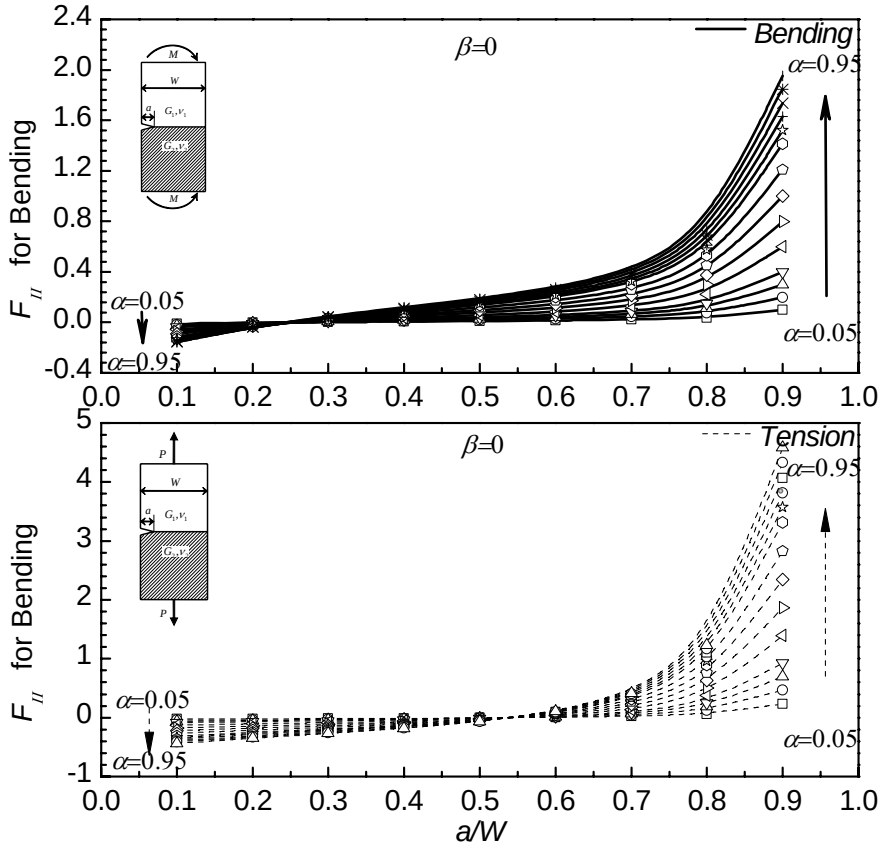

(b)

Fig. 4.28 Variations of SIFs of single edge interface crack with a/W for $\beta = 0$

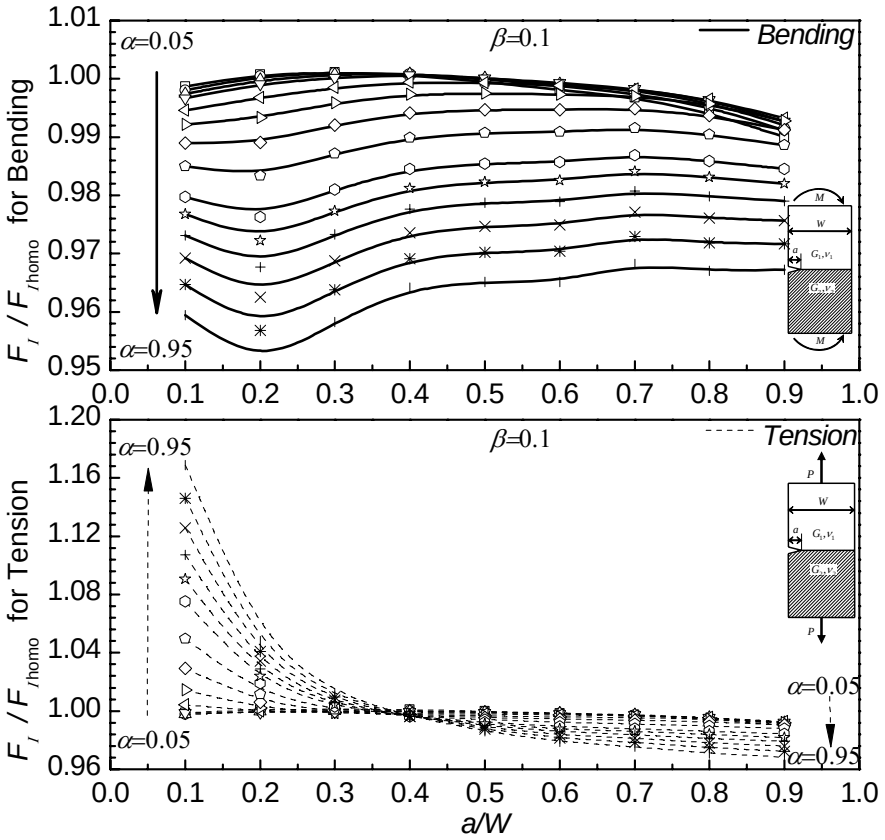

(a)

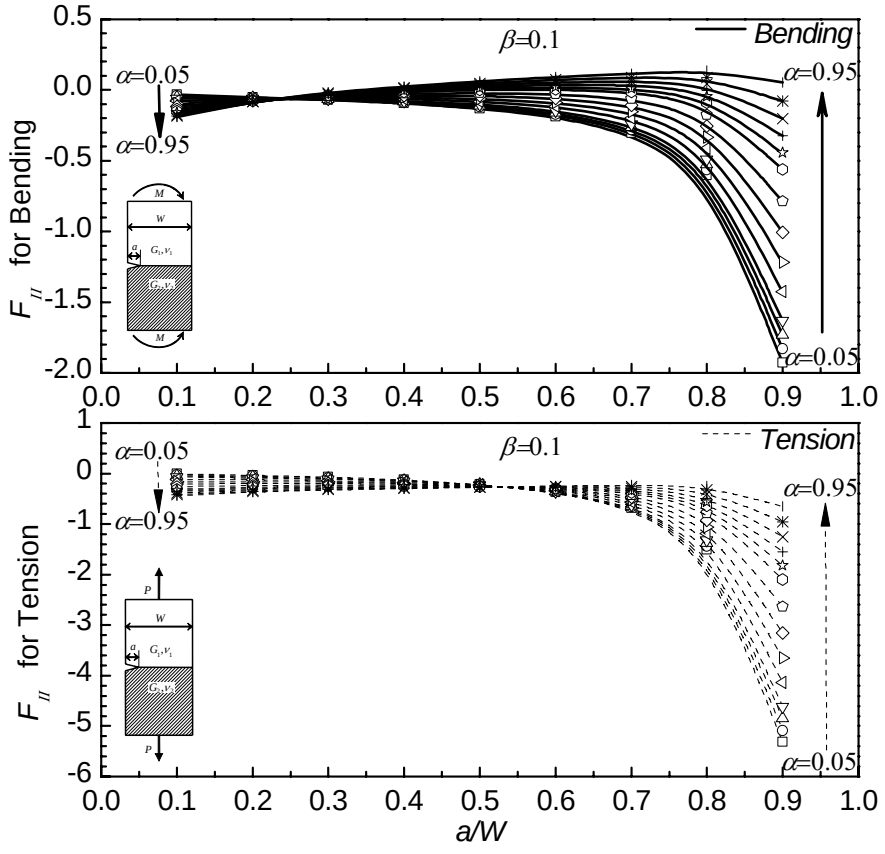

(b)

Fig. 4.29 Variations of SIFs of single edge interface crack with a/W for $\beta = 0.1$

4.6 Conclusions

In this chapter we calculated the SIFs of the bi-material bonded finite isotropic elastic strips subjected to tensile and bending loads. Fitting functions were proposed to calculate the SIFs for shallow edge interface cracks within the singular zone. Then the variations of SIFs were demonstrated in contour map plots for the $\alpha-\beta$ space. The maximum and minimum values of F_I, F_{II} for the whole $\alpha-\beta$ space and typical engineering materials were obtained, and their corresponding material combinations were also tabulated. Finally, the effects of the relative crack lengths and material combinations on the SIFs were also depicted.

4.7 References of Chapter 4

[1] Bogy, D.B.,The plane solution for joined dissimilar elastic semistrips under tension. J. Appl. Mech. 1975; 42(1):93-98.

[2] Reedy Jr., E.D., Asymptotic interface-corner solutions for butt tensile joints. Int. J. solids Struct. 1993;30:767-777.

[3] Akisanya, A.R., and Fleck, N.A., Interfacial cracking from the free-edge of a long bi-material strip. Int. J. Solids Struct, 1997; 34: 1645-1665.

[4] Kaya, A.C., Erdogan, F., On the solution of integral equations with singular kernels. Q. Appl. Math., 1987;1(45):105-122.

[5] Noda, N.A., Araki, K. and Erdogan, F., Stress intensity factor in two bonded elastic layers with a single edge crack. Trans JSME, series A, 1991; 57(537):82-89.

5 CHAPTER Stress intensity factors of the double edge interface cracks

5.1 Introduction

Composite materials and bonded structures are widely employed in the modern industrial context. The mechanical behavior of the bi-material interface is of great significance for the industrial application. Since the presence of cracks negatively affects a structure's performance and may result in damage, basic studies about the interface cracks win quite a number of attentions. High stress concentration at the bonding edge corner caused by differences in the elastic properties of its material components may lead to the initiation of micro-cracks and then to the propagation.

In the authors' previous research, Noda et al. investigated the SIFs of an edge interface crack in a bonded dissimilar semi-infinite plane [1]. And Lan et al. discussed the effect of the material combinations and the relative crack lengths to the SIFs of a single edge cracked bonded strip [2].The SIFs of the single-edge cracked bi-material strip have been examined for various material combinations in Chapter 4. As a further research of the author's previous work, the study object is extended to the double-edge interface crack of a bonded strip. In this chapter, therefore, the SIFs will be investigated for a bi-material bonded finite strip as shown in Fig. 5.1b by applying the finite element method with varying not only the material combinations but also the relative crack sizes. The SIFs will be computed and listed by varying various material combinations and relative crack

lengths. The material combinations (α,β) vary $0 \le \alpha \le 1, -0.25 \le \beta \le 0.5$ in the $\alpha - \beta$ space, and the relative crack size a/W varies from the very shallow crack to the very deep crack. Furthermore, we will show that the SIFs for the double-edge interface crack also behave a good double logarithmic linearity to the crack length within the zone of dominance of the free edge singularity. Then, a formula will be proposed to determine the SIFs for the shallow edge interface cracks under arbitrary combination of materials and relative crack size, by fitting the computed results. The effect of the relative crack lengths and material mismatch parameters are also discussed in this chapter. The SIF values for the single and double edge interface cracks will be compared for the whole range of combination of materials ($0 \le \alpha \le 0.95, -0.2 \le \beta \le 0.45$) and relative crack lengths ($0 \le a/W \le 0.9$). For the single and double edge cracked homogenous strips shown in Fig. 5.2, it is well known that the SIFs for the single crack are always no less than those of the double crack. However, this law should not be always true for the interfacial cracks. It will be shown that the SIFs of a double edge interface crack may be possibly larger than those of a single edge interface crack for some specific combination of materials and relative crack lengths. In addition, the SIFs should be compared in three different zones of relative crack lengths.

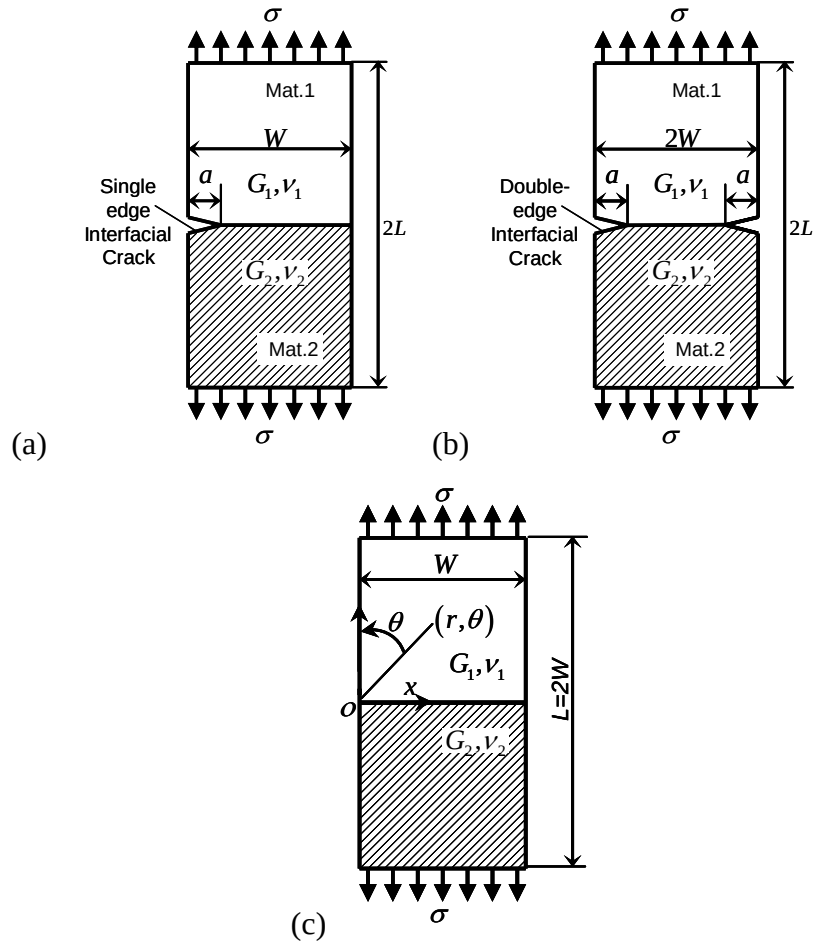

Fig. 5.1 (a) Single edge interface crack and (b) double edge interface crack in a bonded strip (c) bi-material bonded strip without crack

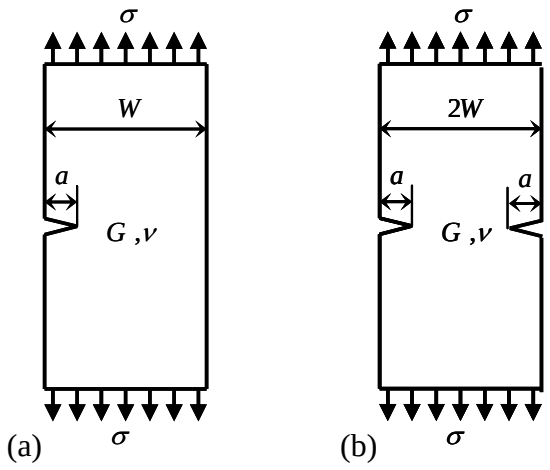

Fig. 5.2 (a) Single and (b) double edge cracks in homogenous strips

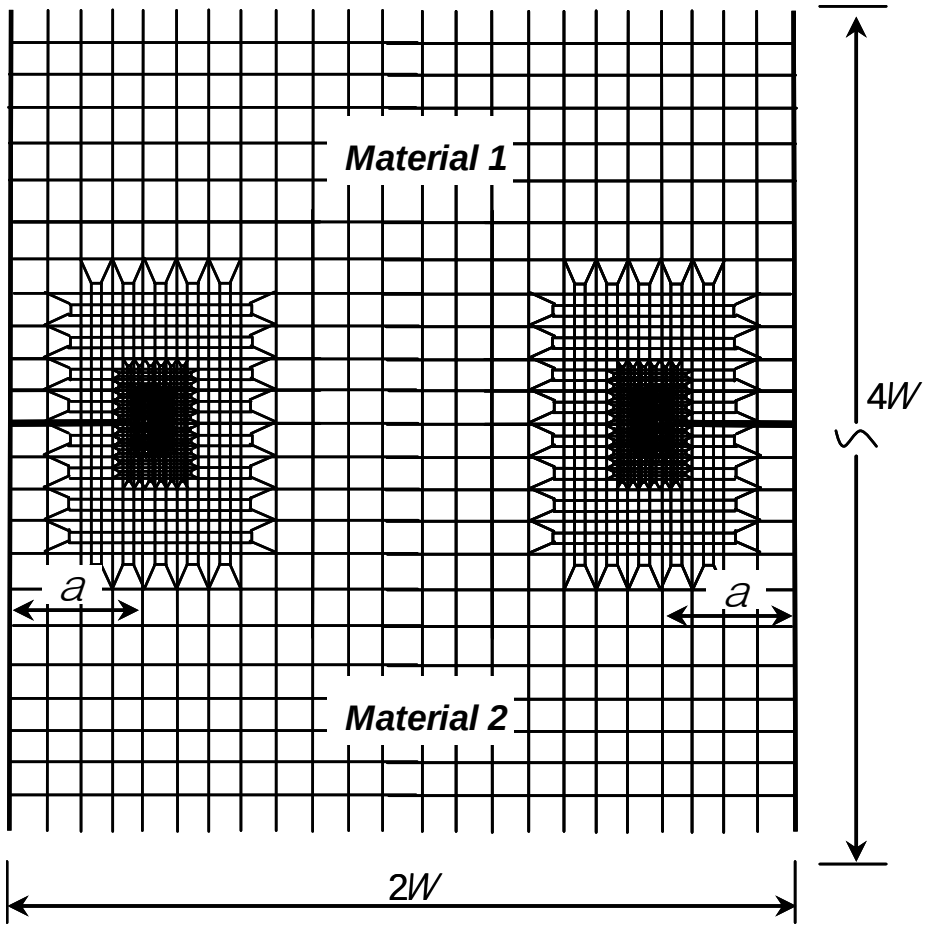

Fig. 5.3 FE mesh type and geometric configurations for a double-edge interface crack

5.2 Numerical verification for the double edge crack problems

The robustness and accuracy of the current method in treating double-edge cracked problems are investigated. The FE model for the double-edge cracked bi-material strip is created in a self-similar manner as depicted in Chapter 2. Fig. 5.3 shows the mesh type and geometric configurations for the double-edge cracked bonded strip. It is supposed that two edge interface cracks initiate at the left and right corner of the strip. And the crack lengths are kept the same and fixed to a=10mm which is the same as the half crack length of the reference problem. Then we vary the width of the bonded strip $2W$ to make $0 < a/W < 1$,

and keep the length two times the size of the width in the FE model. Furthermore, the minimum element size e of the FE models are kept the same for each pair of reference and given unknown problems.

The SIFs for the extremely deep crack cases ($a/W = 0.8$) of a double edge cracked homogenous strip ($\alpha = \beta = 0$, two materials are identical) are plotted against the minimum element size of the FE model in Fig. 5.4. As can be seen from this figure, accurate result can be obtained using linear extrapolation. The values for other relative crack lengths are tabulated and compared to those predicted by Nisitani [3] in Table 5.1. It can be seen from the table that the extrapolated results in this research and those of Nisitani [3] are in very good agreement.

Fig. 5.5a and b show the variations of the normalized SIFs F_I, F_{II} for a double edge cracked dissimilar bonded strips $a/W = 0.8$, respectively. Similar to the discussion in Chapter 2, the elastic parameters are restricted to $G_2/G_1 = 4, \nu_2 = \nu_1 = 0.3$ and plane stress condition is assumed in the analysis. As can be seen from Fig. 5.5a, a linear relationship can be observed for the case of F_I. However, different from the case of single edge cracked bi-material strip, Fig. 5.5b shows that the values of F_{II} converge from $e < a/243$. This is maybe because less bending effects due to the symmetry of the double-edge interface cracks. Therefore, the post-processing technique of linear extrapolation is only employed to compute F_I. And accurate results of F_{II} can be obtained directly by using the minimum element size $e < a/243$. The extrapolated values for a double edge cracked bonded strip shown in Fig. 5.1b are tabulated in Table 5.2. It should be noted that those results in Table 5.2 appear to be new and there are no published data available to be compared with. As shown in the previous examples and discussions in Chapter 2, the current method is proved to produce accurate numerical results for mode I crack problems, and therefore it can be assumed that the results in Table 5.2 are also valid and reliable.

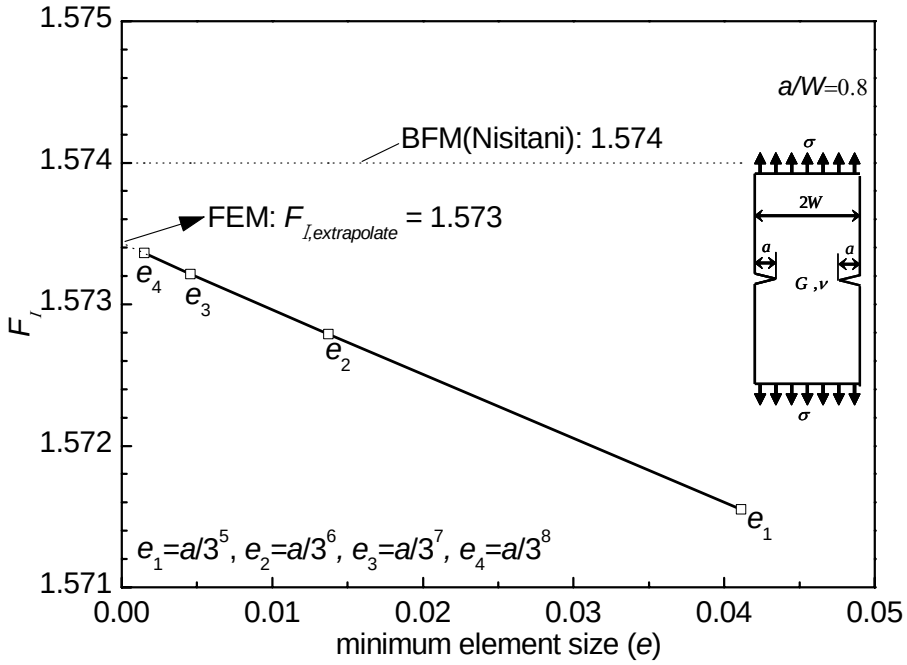

Fig. 5.4 Variations of the normalized stress intensity factors F_I with the minimum element size e for a double-edge cracked homogenous strip $a/W = 0.8$ subjected to uniform tension

Table 5.1 Normalized stress intensity factors F_I for the single and double edge cracked homogenous strips

a/W	Present	Ref. [3]
0.1	1.117	1.117
0.2	1.112	1.112
0.3	1.115	1.115
0.4	1.132	1.132
0.5	1.169	1.169
0.6	1.236	1.236
0.7	1.353	1.353
0.8	1.573	1.574
0.9	2.115	2.116

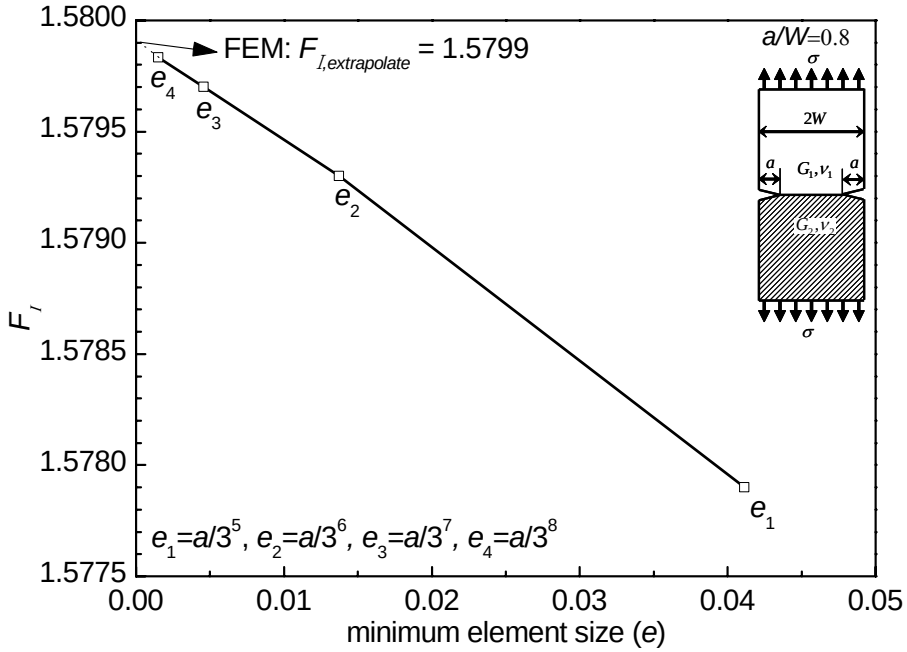

(a)

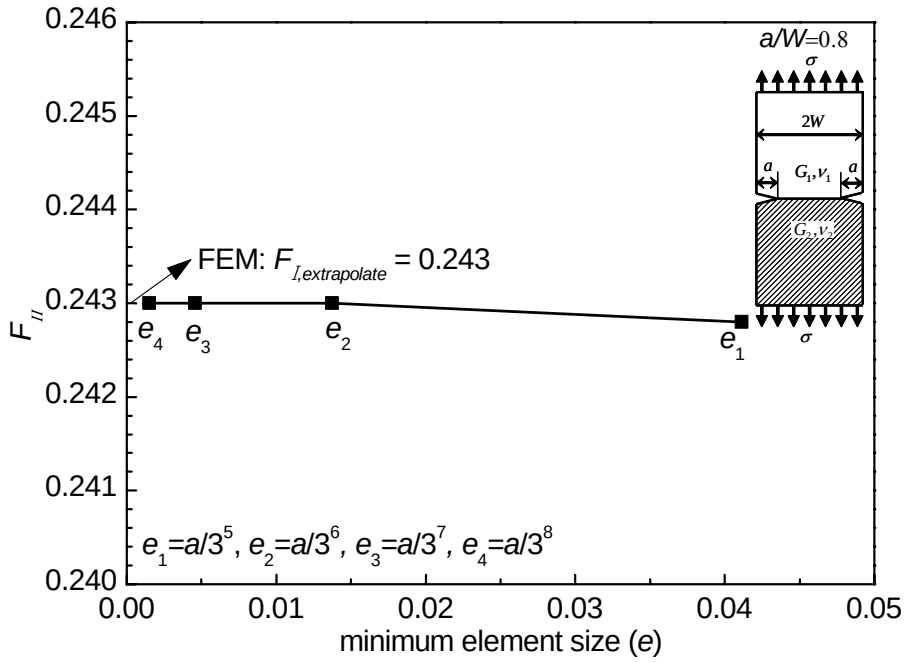

(b)

Fig. 5.5 Variations of the normalized stress intensity factors (a) F_I and (b) F_{II} with the minimum element size e for a double-edge cracked bi-material strip $a/W = 0.8$ subjected to uniform tension

Table 5.2 Normalized stress intensity factors for a double edge cracked bonded strip shown in Fig. 1b ($\nu_1 = \nu_2 = 0.3$, plane stress)

a/W	$E_2/E_1 = 2$		$E_2/E_1 = 4$		$E_2/E_1 = 10$		$E_2/E_1 = 100$	
	F_I	F_{II}	F_I	F_{II}	F_I	F_{II}	F_I	F_{II}
0.1	1.131	-0.128	1.164	-0.241	1.212	-0.350	1.264	-0.447
0.2	1.115	-0.119	1.122	-0.219	1.132	-0.309	1.142	-0.382
0.3	1.115	-0.112	1.113	-0.204	1.112	-0.284	1.1109	-0.347
0.4	1.131	-0.106	1.128	-0.193	1.124	-0.268	1.120	-0.325
0.5	1.168	-0.103	1.166	-0.188	1.163	-0.259	1.159	-0.315
0.6	1.236	-0.104	1.235	-0.189	1.235	-0.261	1.234	-0.318
0.7	1.354	-0.111	1.356	-0.202	1.358	-0.280	1.361	-0.342
0.8	1.575	-0.133	1.580	-0.243	1.586	-0.338	1.591	-0.414
0.9	2.118	-0.207	2.122	-0.380	2.128	-0.531	2.133	-0.652

5.3 Stress intensity factors of the double-edge interface cracks within the singular zone

In chapter 4, it has been confirmed that the normalized SIFs within the zone of free-edge singularity for a single-edge cracked bi-material strip behave a double logarithmic linearity to the relative crack length a/W [1,2]. Here, the double edge interface crack is the main interest. The SIFs will be investigated by varying the relative crack length a/W, as well as the material composite parameters α and β. Then the SIFs for the two interfacial cracks will be compared systematically. In this chapter, we restrict our discussion to the material combinations with $\beta = 0.3$. The double logarithmic distributions of the normalized SIFs F_I and F_{II} are plotted against a/W as shown in Fig. 5.6a and b, respectively. By the way, the SIFs for the single-edge interface cracks are also plotted in Fig. 5.6 to be compared with. F_I, F_{II} for the double-edge interface cracks are plotted in solid curves and those for the single-edge interface cracks are plotted in dashed ones. From

Fig. 5.6, it can be found that, similar double logarithmic linearity of F_I, F_{II} can be observed when $a/W < 0.01$. Furthermore, the slopes corresponding to the same material composite parameters of the two types of cracks are totally the same, and they are equal to the singular index $\lambda - 1$ of the perfectly bonded strip without crack as shown in Fig. 5.1c.

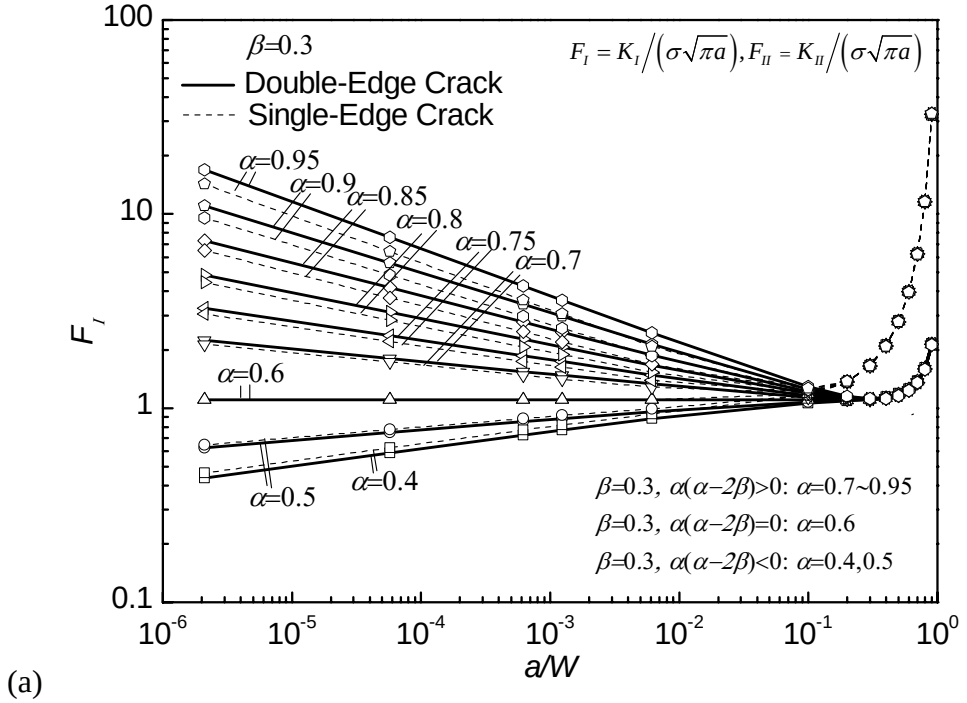

(a)

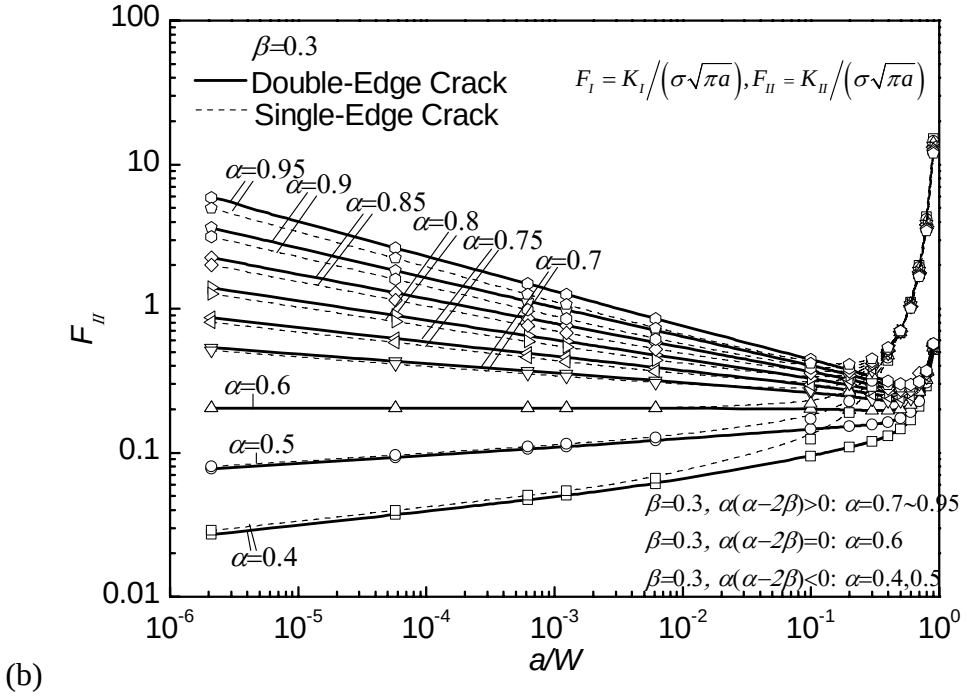

(b)

Fig. 5.6 Double logarithmic distributions of (a) F_I and (b) F_{II} for the single and double edge interface cracks

Table 5.3 Tabulated values of C_I

α	$\beta = -0.2$	$\beta = -0.1$	$\beta = 0$	$\beta = 0.1$	$\beta = 0.2$	$\beta = 0.3$	$\beta = 0.4$	$\beta = 0.45$
0.05	1.05	1.089	1.116	1.131				
0.1	1.002	1.059	1.1	1.139	1.166			
0.15	0.945	1.027	1.076	1.135	1.193			
0.2		0.994	1.046	1.12	1.209			
0.3		0.932	0.98	1.061	1.191			
0.4		0.875	0.914	0.987	1.115	1.434		
0.5		0.819	0.854	0.913	1.015	1.29		
0.6			0.8	0.847	0.92	1.106		
0.7			0.75	0.789	0.838	0.954	1.734	
0.75			0.729	0.762	0.802	0.892	1.302	
0.8			0.7	0.737	0.769	0.838	1.092	
0.85			0.674	0.713	0.738	0.791	0.959	1.505
0.9			0.645	0.69	0.709	0.749	0.864	1.083
0.95			0.6	0.667	0.681	0.711	0.791	0.907

Table 5.4 Tabulated values of C_{II}

α	$\beta = -0.2$	$\beta = -0.1$	$\beta = 0$	$\beta = 0.1$	$\beta = 0.2$	$\beta = 0.3$	$\beta = 0.4$	$\beta = 0.45$
0.05	-0.084	-0.061	-0.027	0.013				
0.1	-0.095	-0.08	-0.052	-0.013	0.031			
0.15	-0.102	-0.097	-0.075	-0.041	0.006			
0.2		-0.11	-0.096	-0.067	-0.022			
0.3		-0.132	-0.128	-0.114	-0.082			
0.4		-0.146	-0.151	-0.15	-0.135	-0.09		
0.5		-0.155	-0.167	-0.174	-0.174	-0.16		
0.6			-0.178	-0.191	-0.199	-0.204		
0.7			-0.184	-0.202	-0.215	-0.227	-0.29	
0.75			-0.186	-0.206	-0.22	-0.235	-0.277	
0.8			-0.186	-0.209	-0.224	-0.24	-0.273	
0.85			-0.187	-0.211	-0.227	-0.244	-0.271	-0.358
0.9			-0.183	-0.212	-0.229	-0.246	-0.27	-0.307
0.95			-0.175	-0.213	-0.23	-0.248	-0.269	-0.291

The double logarithmic discussions about the single-edge interface crack in Chapter 3 [1] are also applicable to the double edge interface cracks. It has been proved that the empirical function Eq.(5.1) is also suitable for the double-edge cracks case by merely modifying the constants C_I, C_{II}. Here, what should be noticed is that F_I, F_{II} are the same

within the singular zone for the two types of cracks when $\alpha(\alpha-2\beta)=0$. See, the curves of $\alpha=0.6,\beta=0.3$ are coincide when $a/W<0.01$ in Fig. 5.6 . The detailed information about Eq.(5.1) can be referred in Chapter 3 [1,2].

$$F_I \cdot (a/W)^{1-\lambda} = C_I, F_{II} \cdot (a/W)^{1-\lambda} = C_{II} \tag{5.1}$$

The constants C_I, C_{II} in Eq. (5.1) for the double edge crack case are computed for various material composite parameters. The values of C_I, C_{II} are plotted and tabulated against (α,β) in Fig. 5.7a and b as well as in Table 5.3 and Table 5.4, respectively. The parameters C_I, C_{II} for the single-edge interface cracks are also plotted against (α,β) in dashed lines in Fig. 5.7 to be compared with. It has been seen that they have the same values when $\alpha(\alpha-2\beta)=0$ despite the crack differences. In addition, the detailed information about the corresponding intensity of stress singularity can be found in Chapter 3 [4,5].

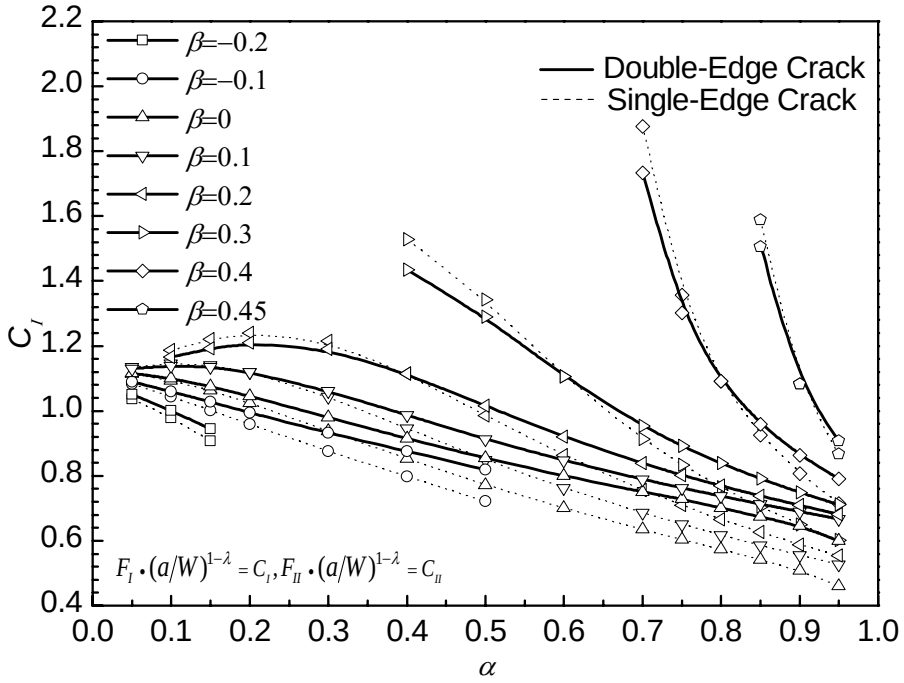

(a)

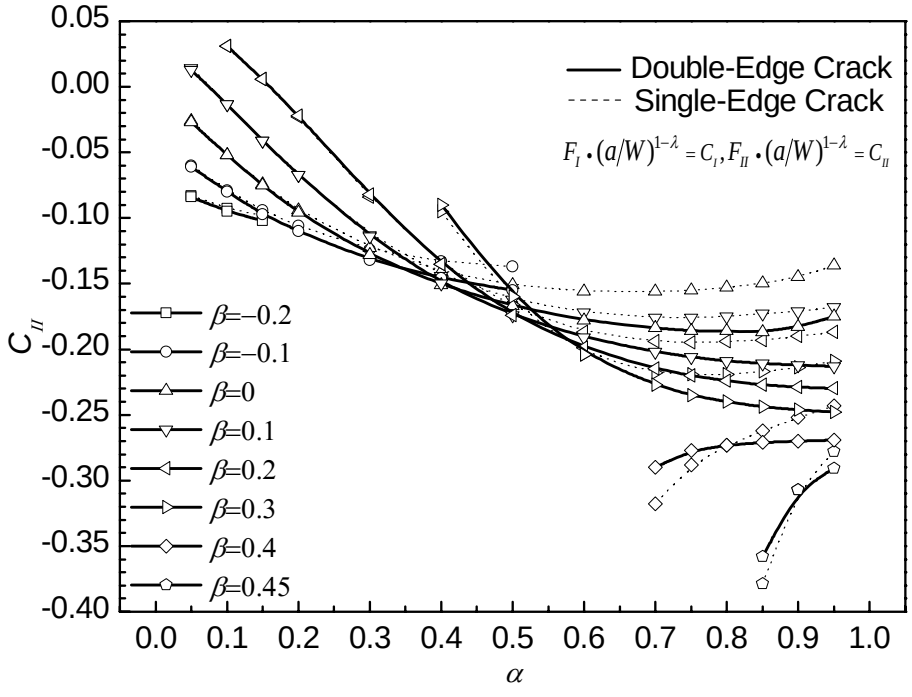

(b)

Fig. 5.7 Values of C_I, C_{II} of Eq.(16) for single and double edge interface cracks

Recall Eq. (5.1) and Fig. 5.7, the SIFs at the crack tip for the two types of cracks of the same relative crack length a/W within the singular zone (shallow crack, $a/W < 0.01$) have the following relationships.

$$\begin{aligned} &F_{I,Dbl} > F_{I,Sgl}, F_{II,Dbl} > F_{II,Sgl}, \text{ when } \alpha(\alpha - 2\beta) > 0; \\ &F_{I,Dbl} = F_{I,Sgl}, F_{II,Dbl} = F_{II,Sgl}, \text{ when } \alpha(\alpha - 2\beta) = 0; \\ &F_{I,Dbl} < F_{I,Sgl}, F_{II,Dbl} < F_{II,Sgl}, \text{ when } \alpha(\alpha - 2\beta) < 0. \end{aligned} \tag{5.2}$$

Where, $F_{I,Dbl}, F_{II,Dbl}$ denote the normalized SIFs for a double edge interface crack, and $F_{I,Sgl}, F_{II,Sgl}$ denote those for a single edge interface crack.

The size of the zone of dominance of free-edge singularity can be determined in a manner as given below. The lines for the single and double edge interface cracks under the same material parameters should be parallel (the line slopes are equal to the order of stress singularity $1-\lambda$). Then, by examining the agreement of the slopes of the lines with the theoretical values of $1-\lambda$, the size of the singular zone can be determined. Take $\beta = 0.3$ as an example, extremely good agreement for the two slopes can be found for $a/W < 0.001$ and an error within 5% for $a/W < 0.01$. So, the size of singular zone can be roughly decided as $a/W < 0.01$. More computations of the SIFs for $0.001 < a/W < 0.01$ are needed to determine the size of the singular zone accurately. It should be noted that the singular zone varies with the bi-elastic material combinations and the radial directions which is centered at the interface corner.

5.4 Comparison of the stress intensity factors for the double and single edge interface cracks

In this section, the SIFs at the crack tip for the double-edge and single-edge interface cracks are systematically investigated and compared for various material combinations and crack lengths. For the case of the single-edge and double-edge cracked homogenous strips

shown in Fig. 5.2, it is well known that the SIFs for the single crack are always no less than those of the double crack. However, this law should not be always true for the case of interfacial cracks. So, the SIFs for the single and double edge interface cracks will be compared for arbitrary combination of materials in the following section.

The normalized SIF curves of three typical material combinations (good pair, equal pair and bad pair) shown in Fig. 5.6 are chosen and plotted in Fig. 5.8. As can be seen from the figure, the whole transverse region of the perfectly bonded strip shown in Fig. 5.1c can be separated into three different zones according to the dominance effect of the free-edge singularity. Namely, they are denoted as zone 1, 2 and 3 as shown in Fig. 5.8 for notational convenient. The boundaries of zone 1 and 2 as well as zone 2 and 3 are roughly defined as $0.01W$ and $0.1W$ respectively. Zone 1 is termed the zone of dominance of free-edge singularity, and it has been discussed in Section 5.3. Exact double logarithmic linearity exists within this zone and the SIFs can be obtained by Eq.(5.1) if the interface cracks initiate within zone 1 ($a/W \le 0.01$). Zone 2 is regarded as the transitional zone between zone 1 and 3. The SIFs are also affected by the free-edge singularity, since Zone 2 is close to the very vicinity of Zone 1. However, the double logarithmic distributions don't behave exact linearity any more in Zone 2. Furthermore, Zone 3 is totally no affected by the free-edge singularity since it is too far away from Zone 1. As can be seen from Fig. 5.8, the SIFs of a single edge interface crack within zone 3 are always bigger than those of a double edge interface crack. This phenomenon is caused by the counterbalance effect due to symmetry of the double edge interface crack. However, when the crack is located in zone 2 (say, $0.01 \le a/W \le 0.1$), the relationships of the SIFs for the two types of cracks become complexity, and no unique or clear regular pattern can be followed. In this case, the SIFs are determined by the combined effect of the free-edge singularity and the counterbalance of symmetry. Generally, the left part of zone 2 is largely affected by the free-edge singularity

and the right part is largely dominated by the counterbalance effect. Specifically, F_I, F_{II} for $a/W = 0.1$ (crack locates in zone 2) are plotted against various combination of materials in Fig. 5.9a and b respectively. It can be seen clearly seen that the SIFs for a double-edge interface crack can still be bigger than those of a single-edge crack for specific combination of materials. Fig. 5.10a and b show the variations of F_I, F_{II} for $a/W = 0.2$ (crack locates in zone 3) for various combination of materials respectively. Fig. 5.10a and b show that the absolute values of F_I, F_{II} for a single edge crack are always bigger than those of a double edge crack. In addition, the SIFs of the double-edge cracks equal those of the single-edge crack within the singular zone for $\alpha(\alpha - 2\beta) = 0$, and are always smaller than those of the single-edge crack within zone 3.

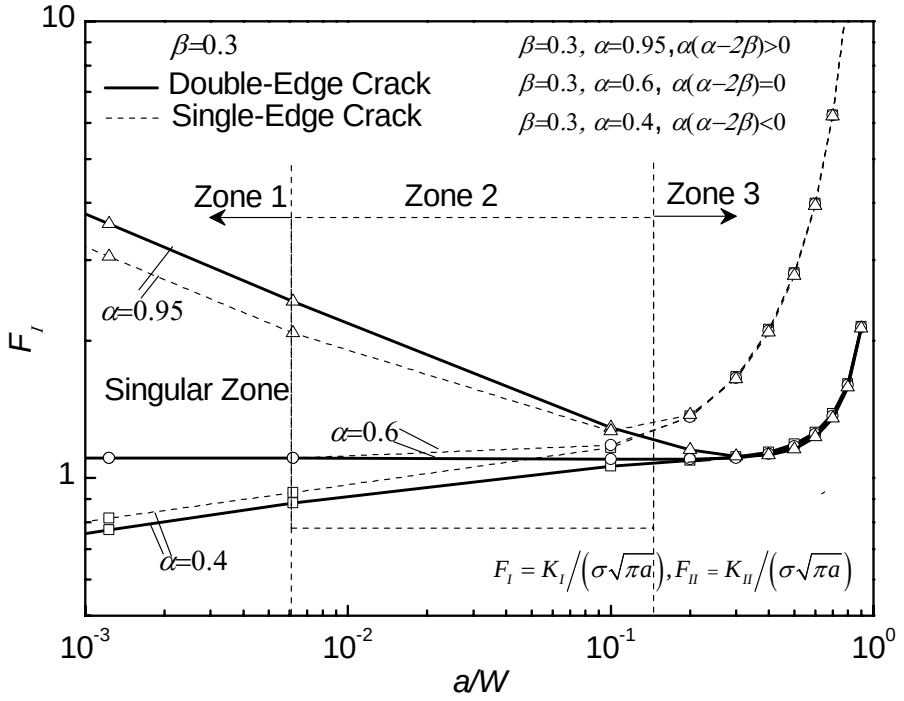

(a)

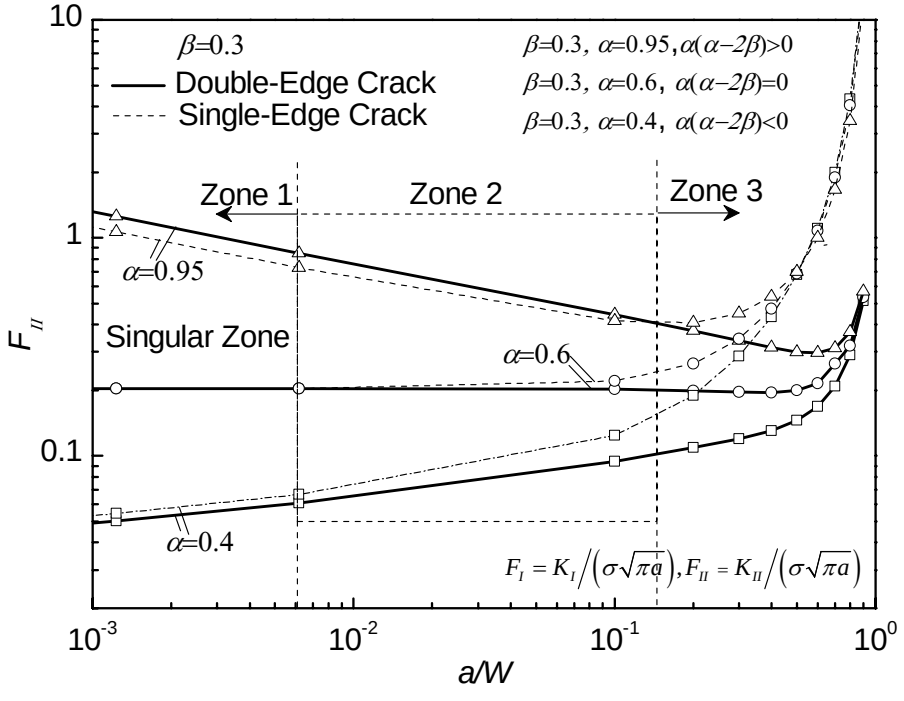

(b)

Fig. 5.8 Three different zones for a dissimilar bonded strip

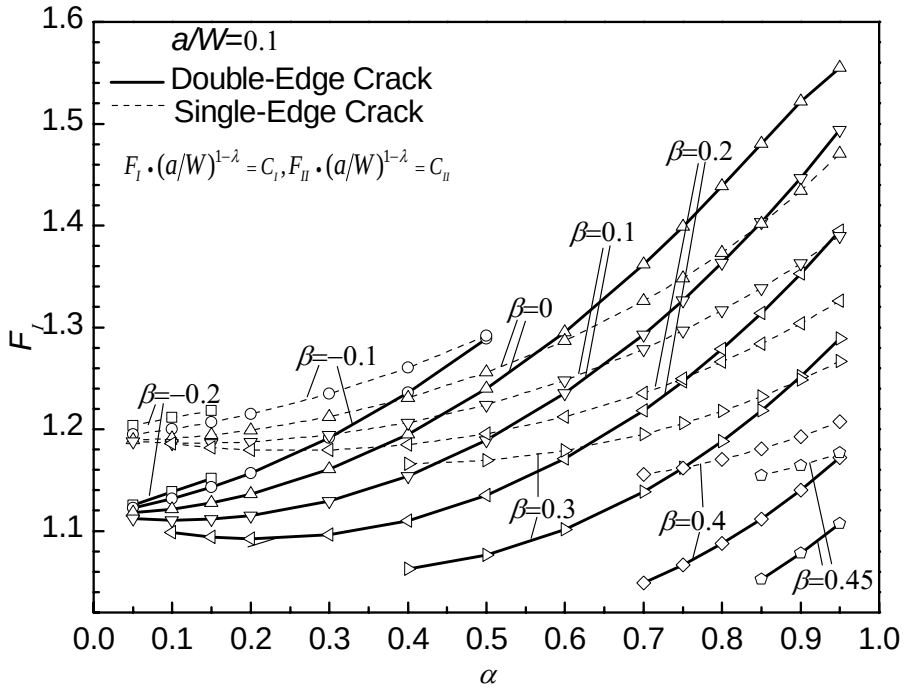

(a)

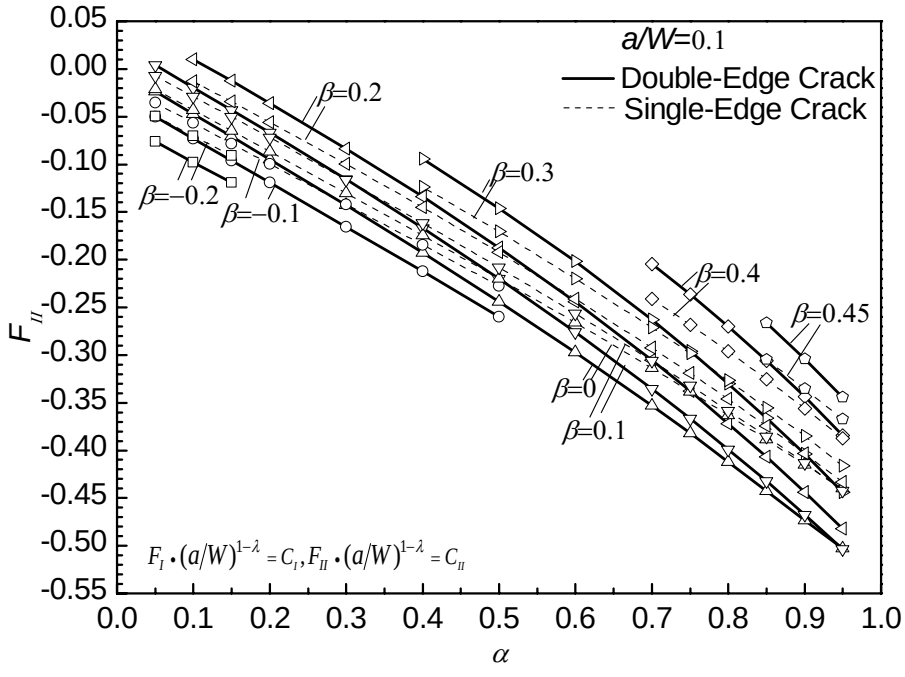

(b)

Fig 5.9. (a) F_I and (b) F_{II} for a single and a double edge interface cracks $a/W = 0.1$

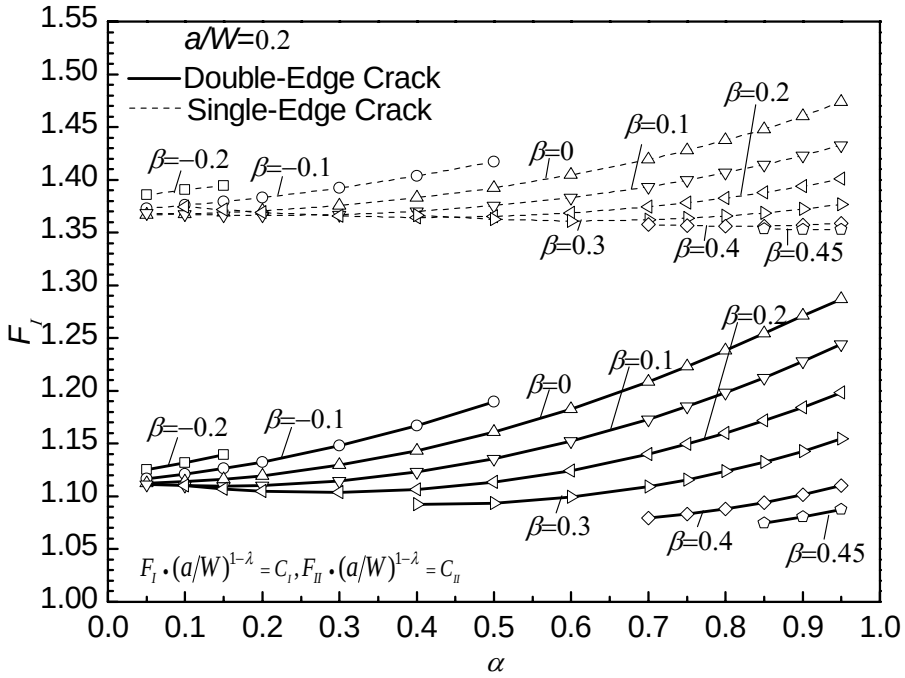

(a)

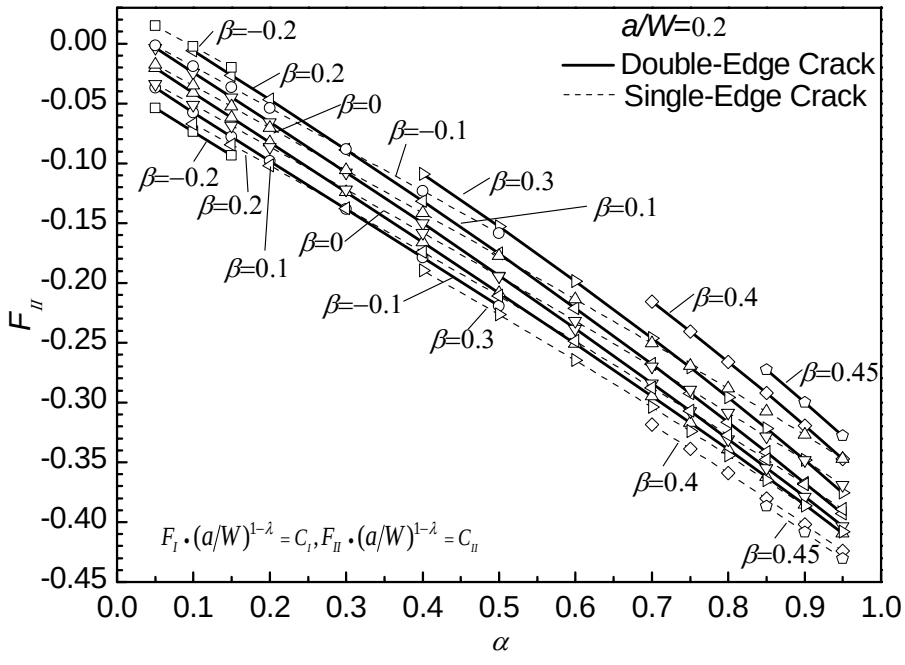

(b)

Fig. 5.10 (a) F_I and (b) F_{II} for a single and a double edge interface cracks $a/W = 0.2$

5.5 Conclusions

In this chapter, variations of the normalized SIFs F_I, F_{II} at the crack tip of the double edge interface cracks in a bi-material strip were investigated and indicated for various material combinations and relative crack lengths a/W. Then, the SIFs of the single-edge and double-edge interface cracks were systematically compared with the following conclusions listed.

1. The normalized SIFs for the single and double edge cracked bi-material strips behave similar linear double logarithmic relationships within the zone of free-edge singularity. Especially, the slopes for the two types of cracks are the same for the same material combinations when $\alpha(\alpha - 2\beta) = 0$.

2. The empirical function Eq. (4.2) is also available to the double-edge interface cracks by merely re-computing the constants C_I, C_{II}. And the new results of C_I, C_{II} for the double-edge interface cracks are computed and listed for various material combinations.

3. The SIF values for the single-edge and double-edge interface cracks were compared for the whole range of combination of materials and relative crack lengths. The SIFs of a double-edge interface crack may be possibly larger than those of a single-edge interface crack for some specific combination of materials and relative crack lengths.

4. The extent of the bonded strip can be divided into three different zones according to the dominance of the effect of free-edge singularity and counterbalance of bending.

5.6 References of Chapter 5

[1] Noda, N.A., Lan, X., Michinaka, K., Zhang, Y. and Oda K., Stress intensity factor of an edge interface crack in a bonded semi-infinite plate. Trans JSME, Series A, 2010, 76(770):1270-77.

[2] Lan,X., Noda,N.A., Michinaka,K., Zhang,Y., The effect of material combinations and relative crack size to the stress intensity factors at the crack tip of a bi-material bonded strip. Engineering Fracture Mechanics. 2011, 78: 2572-2584.

[3] Nisitani, H., Chen, D.H. and Samimoto, A., Versatile program of two-dimensional stress analysis based on body fore method. Tyoko: Baifukan, 1994. (in Japanese)

[4] Chen, D.H. and Nishitani, H., Intensity of singular stress field near the interface edge point of a bonded strip, Trans JSME, Series A, 1993, 59:2682-2686.

[5] Reedy, Jr., Asymptotic interface-corner solutions for butt tensile joints. Int J Solids Struct, 1993; 30: 767-777.

6 CHAPTER

Stress intensity factors for adhesively bonded joints

6.1 Introductions

The increasing demands of electronics nowadays request not only thin, short and small geometric configurations but also high reliable performances. There is an increasing concern that the Chip Scale Packaging (CSP) assemblies may not meet the critical mechanical and thermal cycling reliability requirements. Reliability evaluations of adhesive strength on the interface problems are important for IC packaging designation and CSP materials selection. It is not easy to get the real adhesive strengths using the traditional experimental manners. Generally, this is due to three reasons. Firstly, the adhesive strengths are largely dependent on the specifications and geometric configurations of the specimens. Secondly, singular stress field exists around the bonding corner which leads to non-uniform stress distribution. And thirdly, the conventional adhesion tests give merely the apparent adhesion strengths including the effect of residual stress and the results can not be used for design. Therefore, new testing manners and failure criteria based on fracture mechanics win quite a lot of attentions till recently [1-10]. Fig 6.1a shows the quasi-static fracture testing of Double Cantilever Beam (DCM) type specimen [4-8]. And Fig.6.1b shows the three-point bending tests of End Notch Flexure (ENF) specimens [9, 10] composed of an IC molding compound and Fe-42Ni lead frame material. Specifically, constant adhesion strengths without effects of residual stress were

obtained independently of specimen dimensions [10].

Little research has considered the SIFs of the adhesively bonded joints for arbitrary material combinations till recently. In this chapter, the SIFs of three-layered joints/ adhesive joints will be computed for arbitrary material combinations and compared for tensile and bending loads. In addition, the effects of adhesive layer thickness on the SIFs for the three-layered joints which are wildly seen in the modern chip packaging technology will also be studied and demonstrated. Furthermore, the adhesion strength evaluation based on SIFs will be discussed in Appendix B. This chapter is to contribute the structural design and material selection of IC plastic packages.

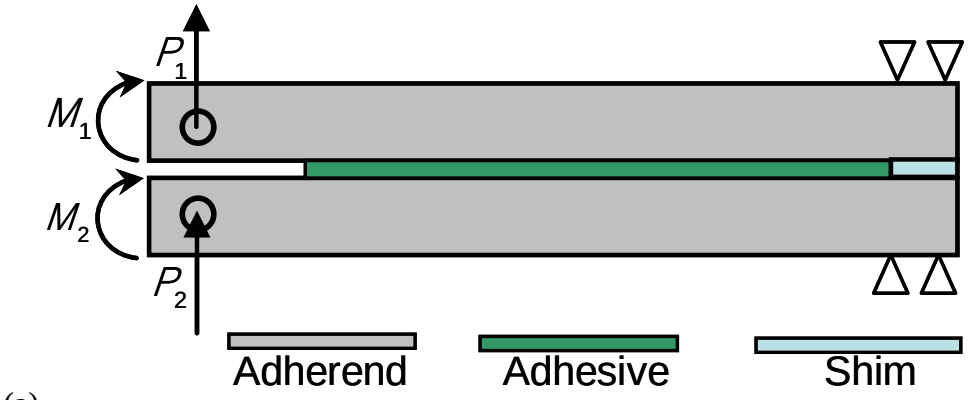

(a)

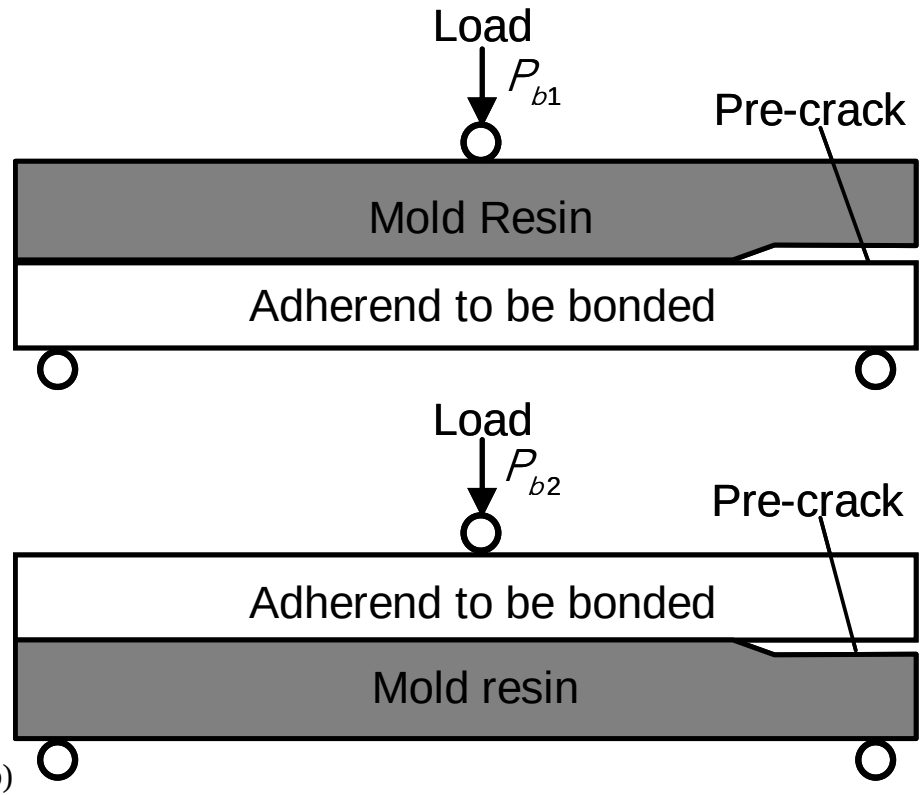

(b)

Fig. 6.1 (a) Double cantilever beam test and (b) testing manner of adhesive strength for IC mold resin

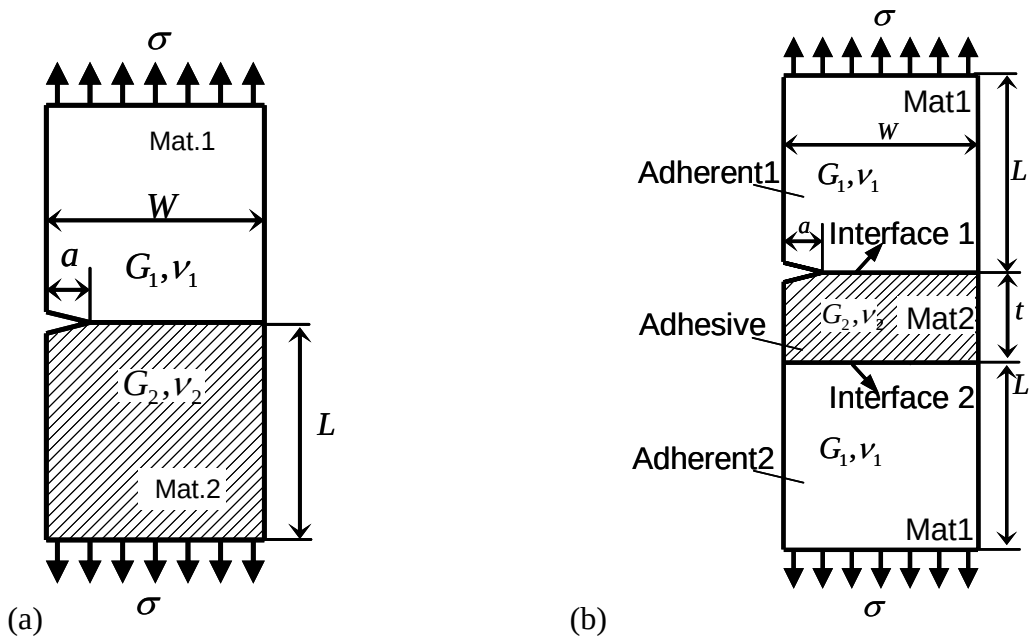

Fig. 6.2 (a) bi-material butt joints and (b) adhesive joints

6.2 Numerical verification for the single-edge cracked adhesively bonded strips

The robustness and accuracy of the improved crack tip stress method in treating several edge interface crack problems have been investigated in the previous chapters. In order to achieve high accuracy, the exactly same mesh patterns for the reference and target unknown problems are employed in the FE models. However, it is difficult to keep exactly same mesh patterns due to the existence of the adhesive layer for the adhesively bonded strips. Therefore the FE modeling techniques on the adhesive layers will be discussed in this section and the numerical data will be compared to show the accuracy.

The adhesively bonded strip with a single-edge interface crack initiated on Interface I shown in Fig. 6.2b is investigated. The geometric specifications are $a/W = 0.1$ and $t/W = 0.1$, and the crack length is fixed to $a = 10mm$. The same central cracked dissimilar bonded planes depicted in Chapter 2 is chosen as the reference problem, and its crack length is

$2a = 20mm$. The mesh patterns around the central crack for the reference problem are shown in Fig.6.3. For the convenience of understanding, the meshes with different materials in Fig. 6.3 are distinguished using different colors. In order to find a reliable modeling technique for the adhesively bonded strip, we presumed a comparison with two different types of models.

Generally, there are two manners to create the FE models for the adhesively bonded strips. Fig. 6.4a and b show the two different meshing techniques manner 1 and manner 2, respectively. Specifically, as shown in Fig. 6.4a, manner 1 keeps the FE meshes around the crack exactly the same with those of the reference problem shown in Fig. 6.3. The adhesive layer is introduced by merely assigning the new material (material 2 in Fig. 6.4a) to the corresponding elements of the desired adhesive layer thickness. However, in Fig. 6.4b, manner 2 keeps the meshes of the most upper and lower layers (material 1) the same with those of the reference problem shown in Fig. 6.3. Then the adhesive layer is created by adding the new elements in cyan color shown in Fig. 6.4b. It should be noted that creating FE model in manner 1 doesn't always turn to be success for arbitrary adhesive layer thickness, because exact line boundaries don't exist in the model all the time. And manner 1 in Fig. 6.4a has the best mesh similarity with the reference problem and the worst robustness in creating the Model, and vice versa for manner 2. Then we pursued the analysis for several material combinations of $G_2/G_1 = 1,2,3,4,10,100$ by fixing $\upsilon_1 = \upsilon_2 = 0.3$ in plane stress conditions. The values obtained using different FE models in Fig. 6.4a and b are tabulated in Table 6.1. The FE stress components for the reference and target unknown problems are also included in this table. As can be seen from this table, the stress components computed by the FE models shown in Fig. 6.4a and b have 3-4 digits coincidence, and their corresponding SIFs have 4-5 digits coincidence. Therefore, the mesh pattern for the adhesive layer does not affect the computational accuracy too much. And

considering the flexibility and robustness in creating the model successfully, manner 2 in Fig. 6.4b is suggested and employed to creating the FE models in this chapter.

Table 6.1 SIFs computed by using FE models in Fig.6.4a and b for an single-edge cracked adhesively bonded strips

			Reference T		Reference S		Unknown Problem		Final Results			
E_2/E_1	α	β	σ y	τ xy	σ y	τ xy	σ y	τ xy	ε	τ ∞	F_I	F_{II}
FE model in Fig.6.4a												
1	0	0	20.6855	6.0E-10	0	11.7483	24.5812	0	0	0	1.1883	0
2	-0.3333	-0.1167	20.0492	-2.5977	4.8652	11.4294	26.4685	-2.5466	0.0373	0.0562	1.2970	0.1704
3	-0.5	-0.175	19.2508	-3.8644	7.2250	11.0285	27.0141	-3.9934	0.0563	0.0842	1.3474	0.2677
4	-0.6	-0.21	18.6162	-4.6060	8.5995	10.7092	27.1759	-4.9252	0.06786	0.1004	1.3761	0.3294
10	-0.8182	-0.2864	16.8208	-6.1570	11.447	9.8026	26.7761	-7.1430	0.0938	0.1299	1.4269	0.4643
100	-0.9802	-0.3431	15.1168	-7.2287	13.383	8.9378	23.5538	-8.6220	0.1138	0.1225	1.3665	0.4922
FE model in Fig. 6.4b												
1	0	0	20.6855	6.0E-10	0	11.7483	24.5823	0	0	0	1.1884	0
2	-0.3333	-0.1167	20.0492	-2.5977	4.8652	11.4294	26.47	-2.5454	0.0373	0.0563	1.2970	0.1705
3	-0.5	-0.175	19.2508	-3.8644	7.2250	11.0285	27.0157	-3.9924	0.0563	0.0843	1.3474	0.2678
4	-0.6	-0.21	18.6162	-4.6060	8.5995	10.7092	27.1775	-4.9243	0.0679	0.1005	1.3761	0.3296
10	-0.8182	-0.2864	16.8208	-6.1567	11.447	9.8026	26.7771	-7.1425	0.0938	0.1299	1.4270	0.4643
100	-0.9802	-0.3431	15.1168	-7.2287	13.383	8.9378	23.5537	-8.6219	0.1138	0.1225	1.3665	0.4922

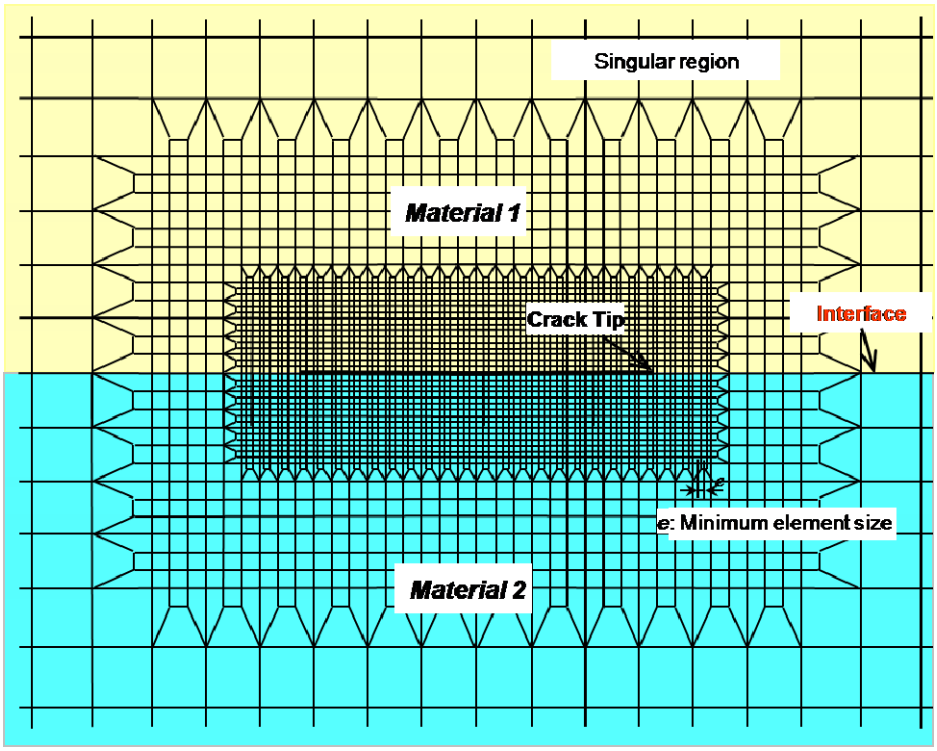

Fig. 6.3 FE mesh pattern for the reference problem (central cracked dissimilar infinite plate)

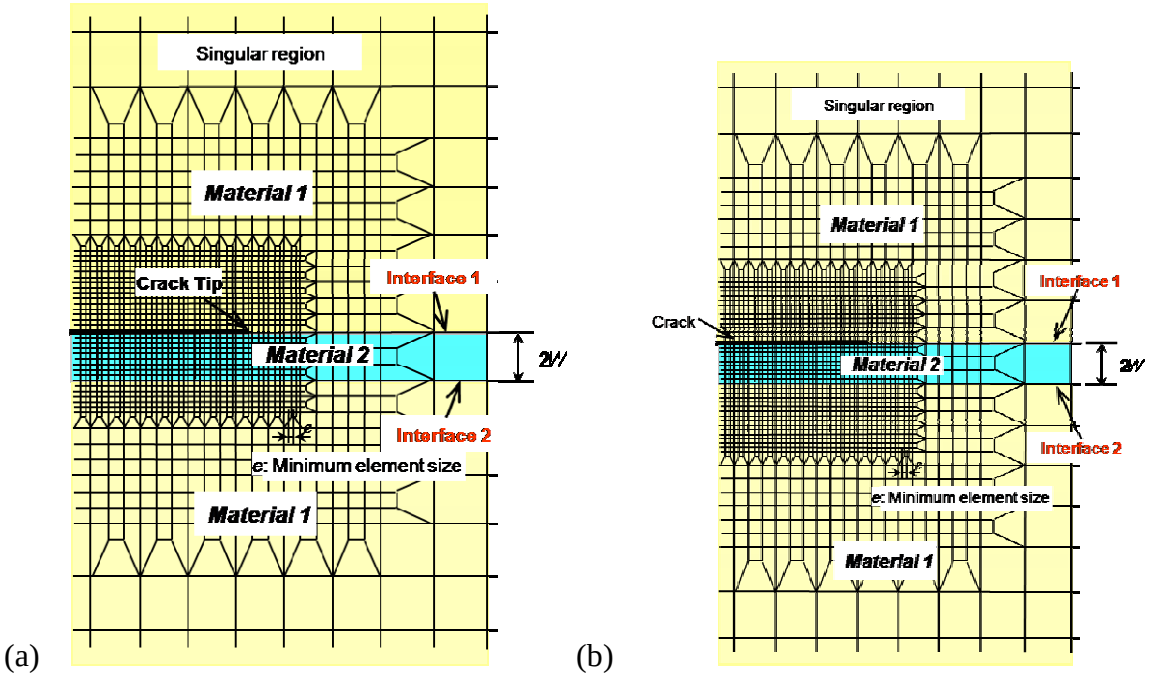

Fig. 6.4 The meshing techniques for the adhesively bonded strips: (a) manner 1 and (b) manner 2

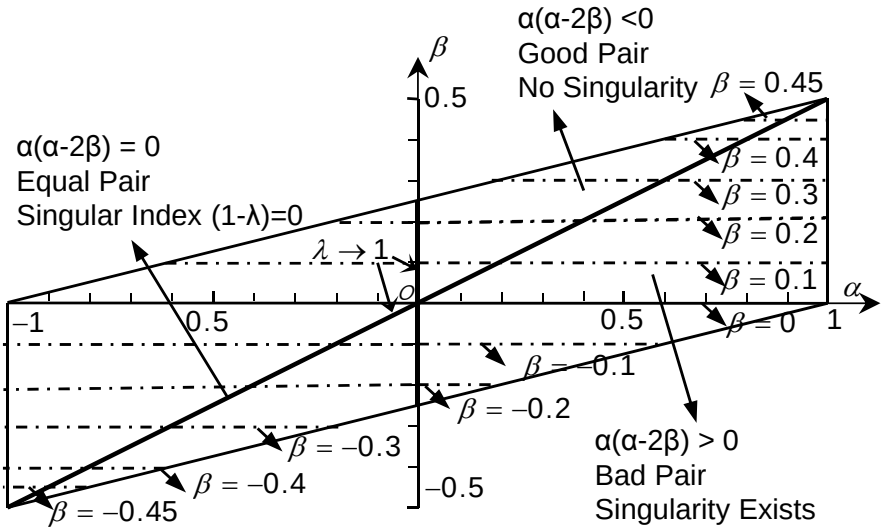

Fig. 6.5 The whole Dundurs' parameters $\alpha-\beta$ space

6.3 Stress intensity factors for bi-material adhesive joints

The single edge cracked bonded strip shown in Fig. 6.2a has been well investigated in Chapter 4. And the discussions here will concentrate into the adhesively bonded joints shown in Fig. 6.2b. Fig. 6.2b shows the geometric configurations. The adhesive joint consists of two identical adherents which are adhesively bonded together by the adhesive layer. The width of the strip is W, and the heights of the adherents and adhesive are L and t, respectively. An edge interface crack of length a is assumed to initiate on interface 1. For the adhesive joints shown in Fig. 6.2b, the SIFs are also uniquely determined by the Dundurs' material composite parameters. However, different from the case of bi-material joints shown in Fig. 6.2a, the SIFs for combinations in the left ($\alpha<0$) and right region ($\alpha>0$) in the $\alpha-\beta$ space are not point symmetry. Thus, the SIFs for various material combinations should be computed for the whole $\alpha-\beta$ space as shown in Fig. 6.5.

The shallow edge interface cracks within the singular zone as $a/W=0.001$ are

investigated for the adhesive joints for the whole range of material combinations in the $\alpha-\beta$ space ($\alpha\in[-1,1],\beta\in[-0.5,0.5]$). In addition, the SIFs for various thicknesses of adhesive layers are also calculated. Fig. 6.6-6.10 show the SIFs for the adhesive joints shown in Fig. 6.4b with the adhesive layer thickness of $t/W=2,1,0.1,0.01,0.001$ respectively. As can be seen from Fig. 6.6, the values of F_I for $t/W=2$ are strictly mirror symmetric about $\alpha=0$ and those for F_{II} are reflection symmetric about $\alpha=0,\beta=0$ in the $\alpha-\beta$ space. In addition, the SIF values are identical with those of the bi-material joints shown in Fig. 6.4a. However, the values for $t/W=1$ are not strictly symmetric although similar varying tendency can be observed in Fig. 6.7. This means the SIFs of adhesive joints is not affected by adherent 2 when the thickness of adhesive layer is long enough comparing with the strip width. Symmetries are not observed for $t/W=0.1,0.01,0.001$ as shown in Fig. 6.8-6.10. This is due to the interference of the two singular fields around the adjacent interface corners. The values for material combinations in the left $\alpha-\beta$ space ($\alpha<0$) have bigger varying magnitude than those in the right $\alpha-\beta$ space ($\alpha>0$). For $t/W=0.01,0.001$ in Fig. 6.9a and 6.10a, F_I grows monotonously with the decrease of α for a fixed β. The amplitude of the variation for F_{II} decreases as the decrease of the thickness of adhesive layer. The SIFs for the bending loads are demonstrated in Fig. 6.11-6.15. Similar conclusions can be found for the bending loading conditions. Furthermore, the contour plot SIF distributions for Fig. 6.6-6.15 are given in Appendix C.

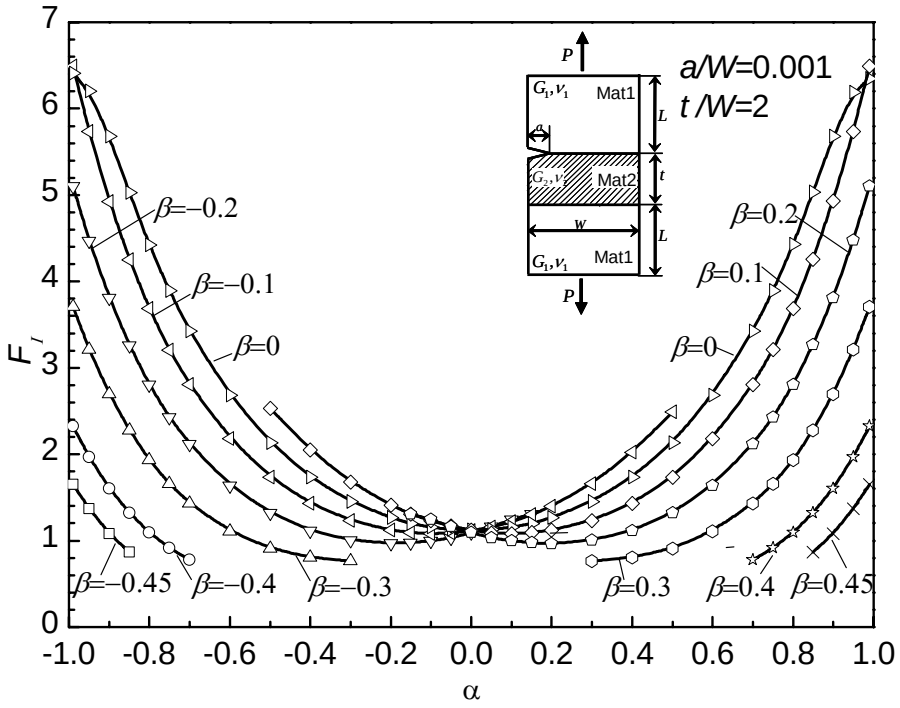

(a)

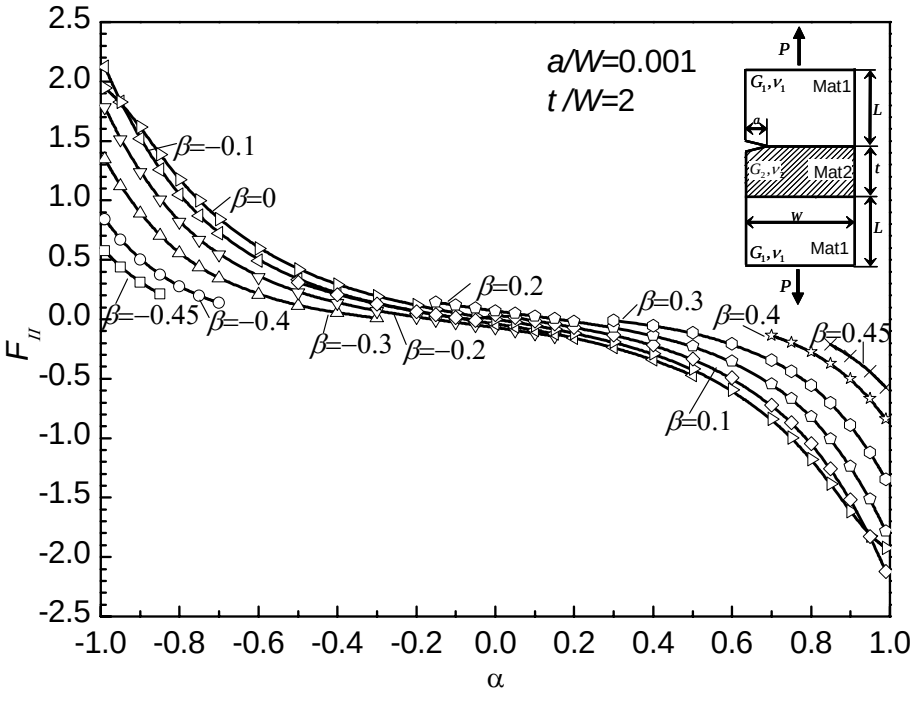

(b)

Fig. 6.6 Stress intensity factors (a) F_I and (b) F_{II} of adhesive joints $a/W = 0.001, t/W = 2$ for the tensile loading case

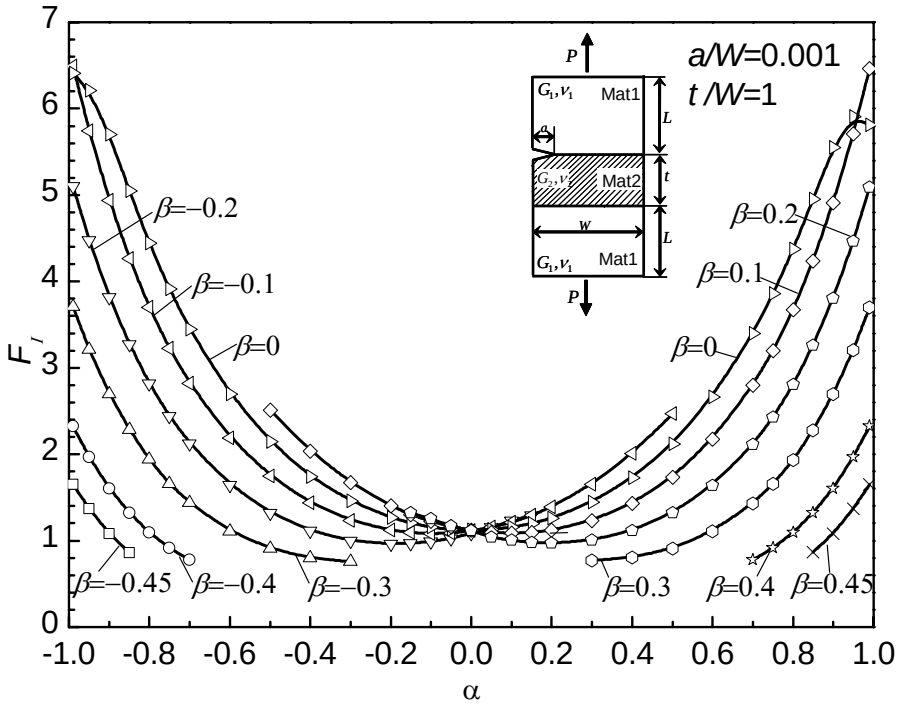

(a)

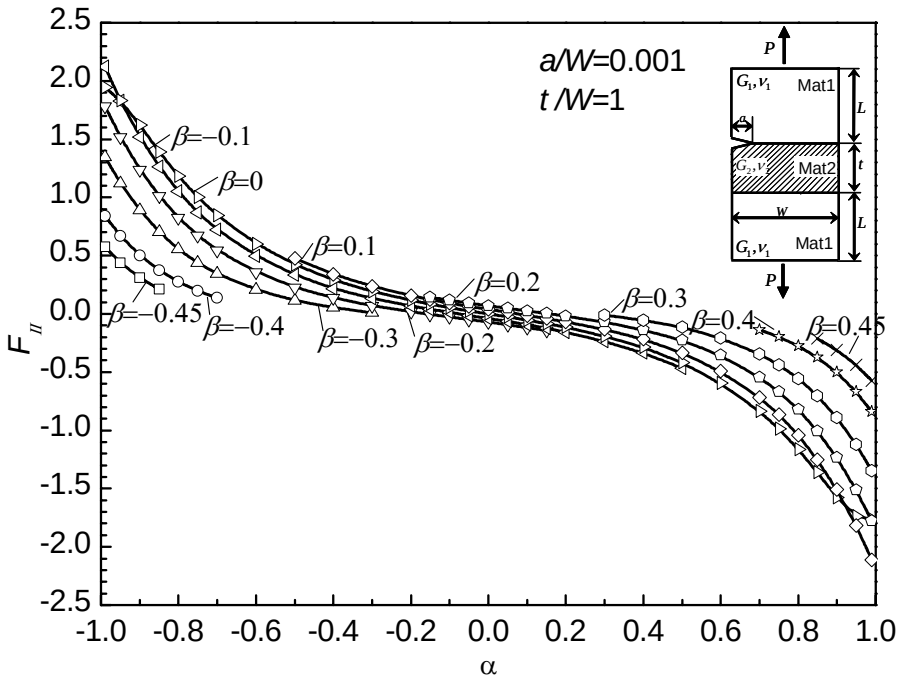

(b)

Fig. 6.7 Stress intensity factors (a) F_I and (b) F_{II} of adhesive joints $a/W = 0.001, t/W = 1$ for the tensile loading case

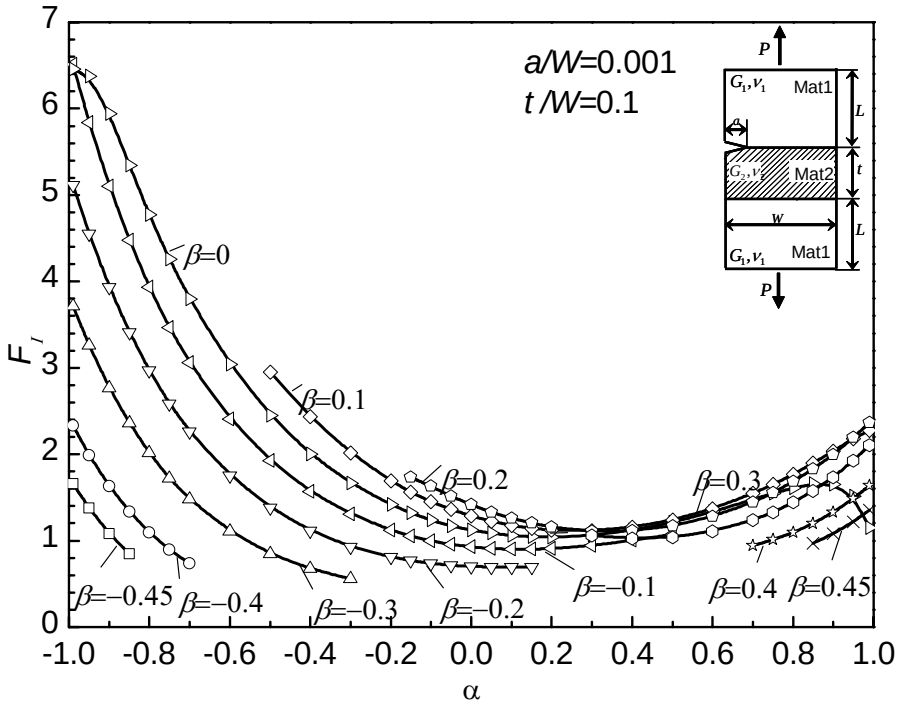

(a)

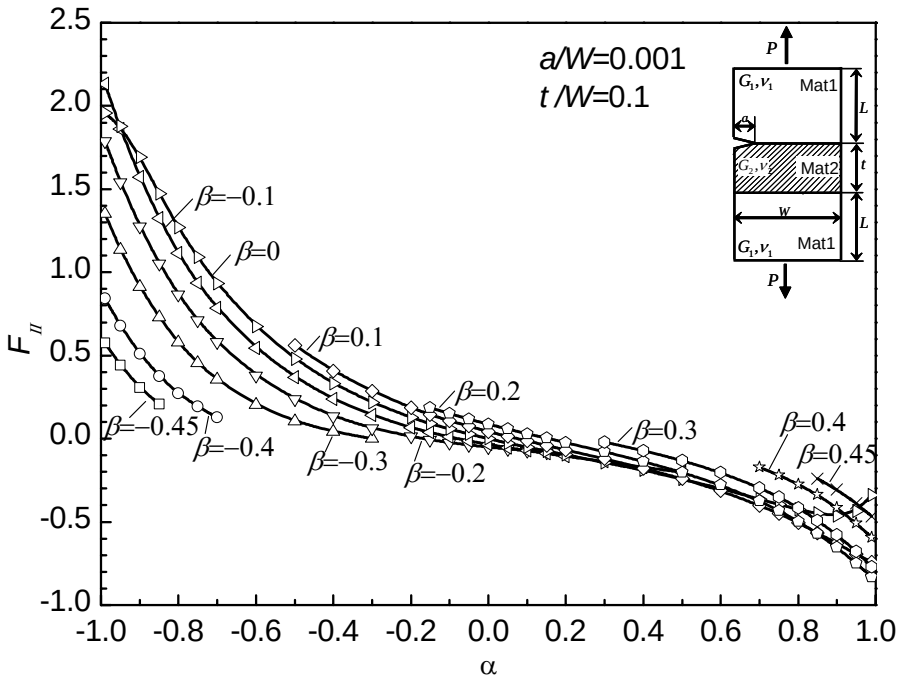

(b)

Fig. 6.8 Stress intensity factors (a) F_I and (b) F_{II} of adhesive joints $a/W = 0.001, t/W = 0.1$ for the tensile loading case

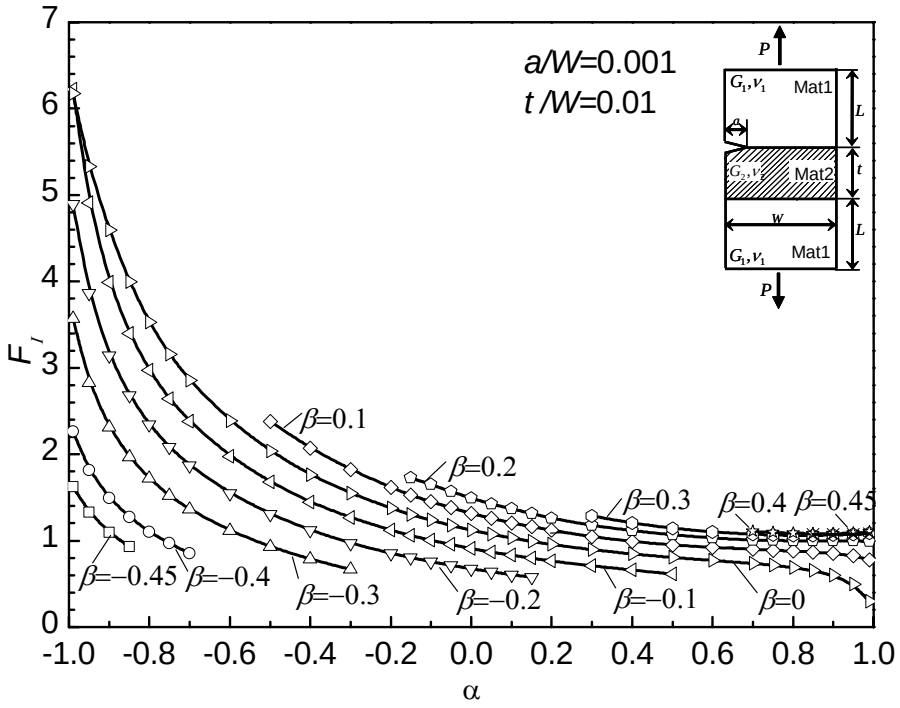

(a)

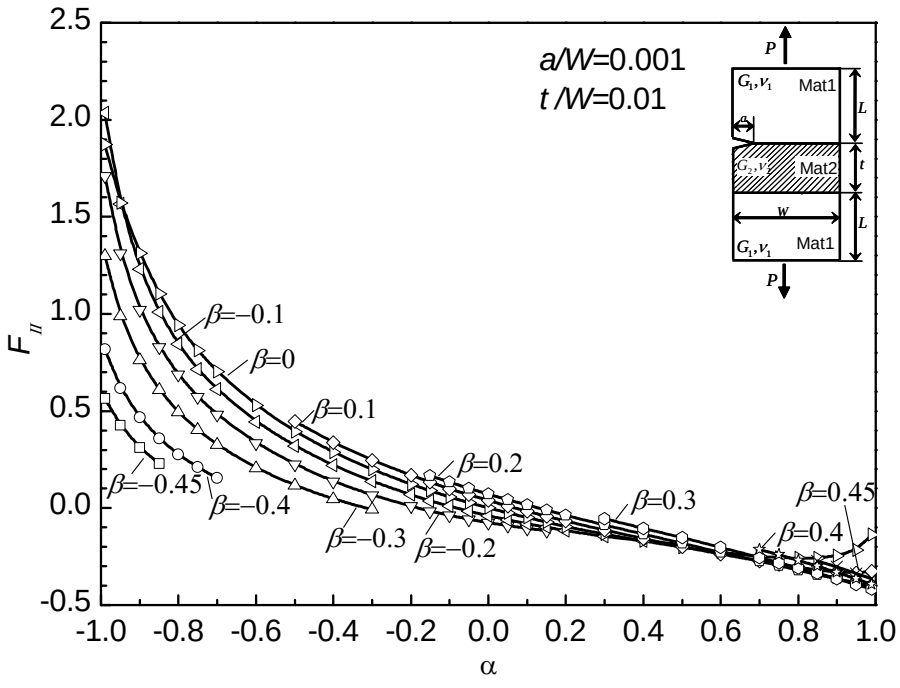

(b)

Fig.6.9 Stress intensity factors (a) F_I and (b) F_{II} of adhesive joints $a/W = 0.001, t/W = 0.01$ for the tensile loading case

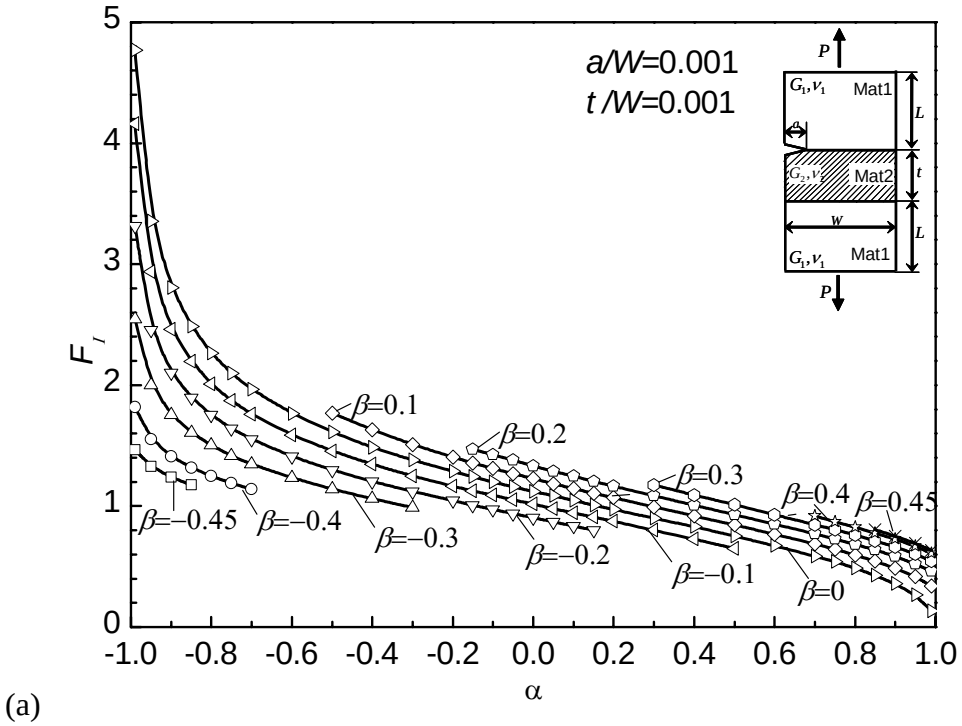

(a)

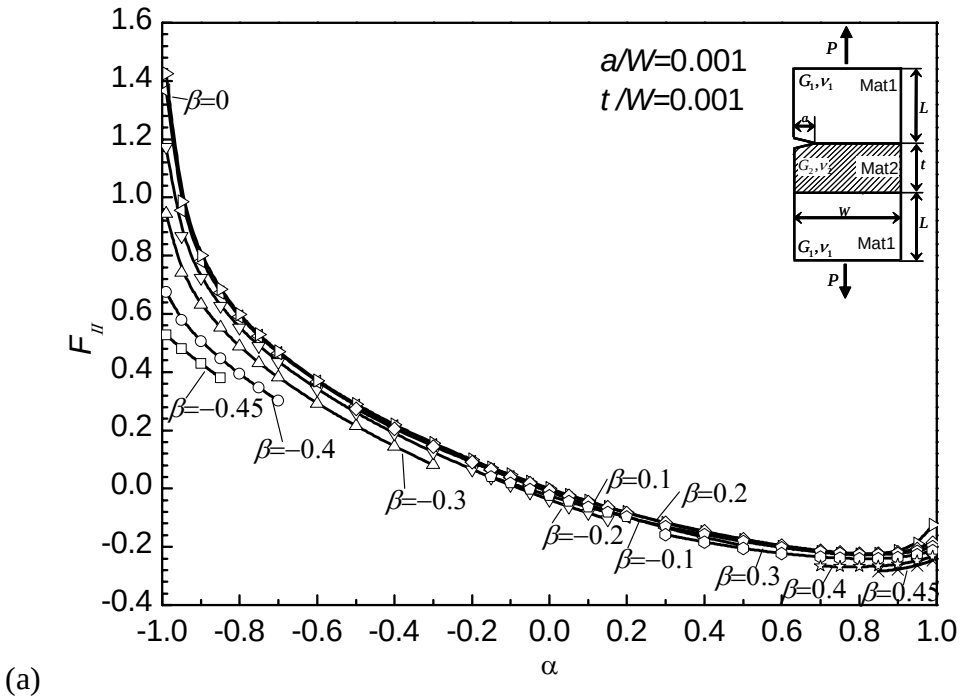

(a)

Fig. 6.10 Stress intensity factors (a) F_I and (b) F_{II} of adhesive joints $a/W = 0.001, t/W = 0.001$ for the tensile loading case

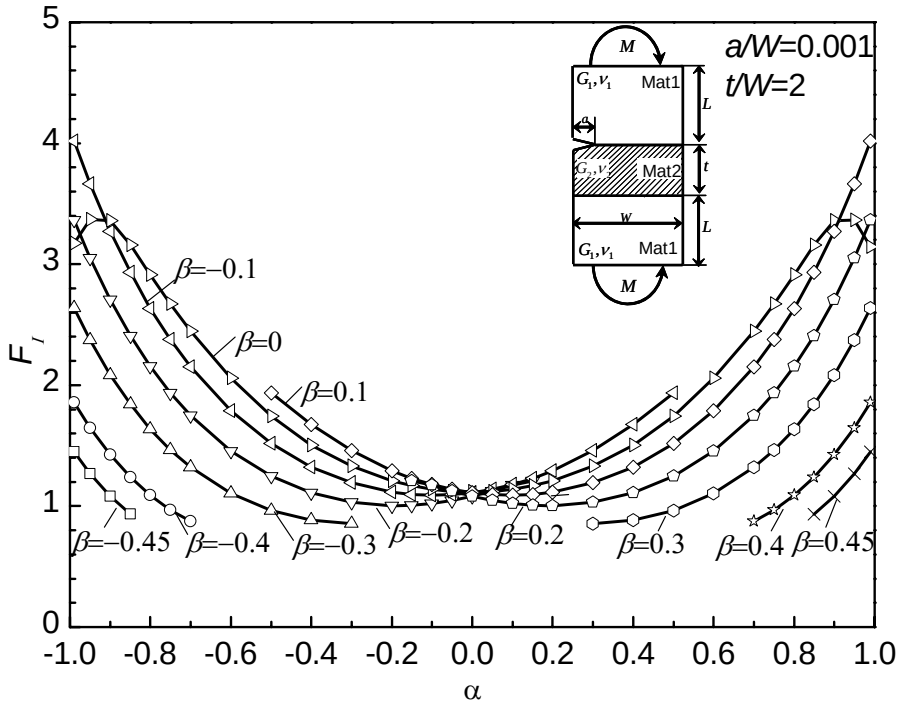

(a)

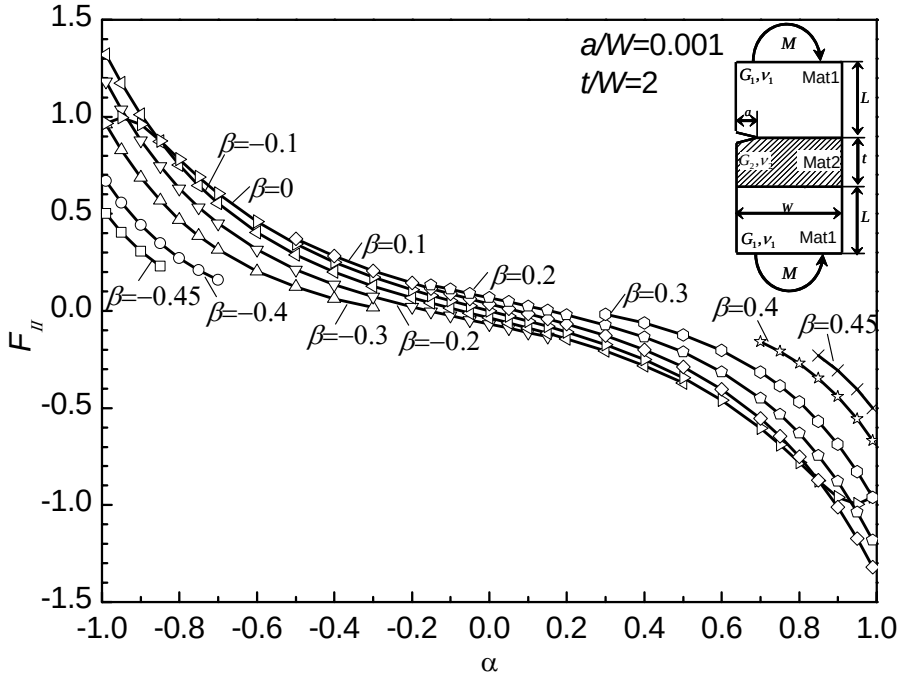

(b)

Fig. 6.11 Stress intensity factors (a) F_I and (b) F_{II} of adhesive joints $a/W = 0.001, t/W = 2$ for the bending loading case

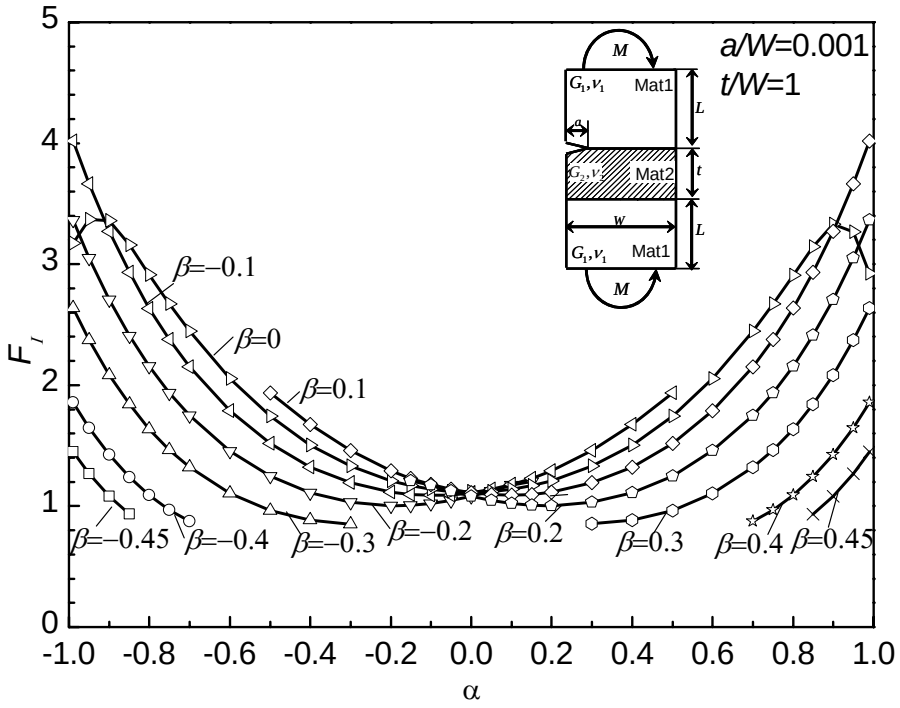

(a)

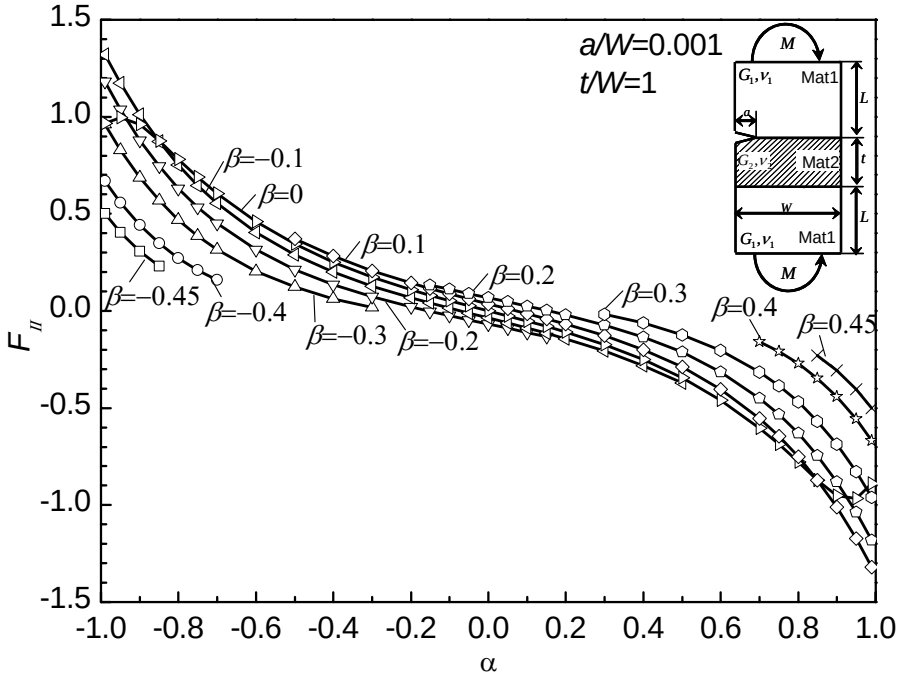

(b)

Fig. 6.12 Stress intensity factors (a) F_I and (b) F_{II} of adhesive joints $a/W = 0.001, t/W = 1$ for the bending loading case

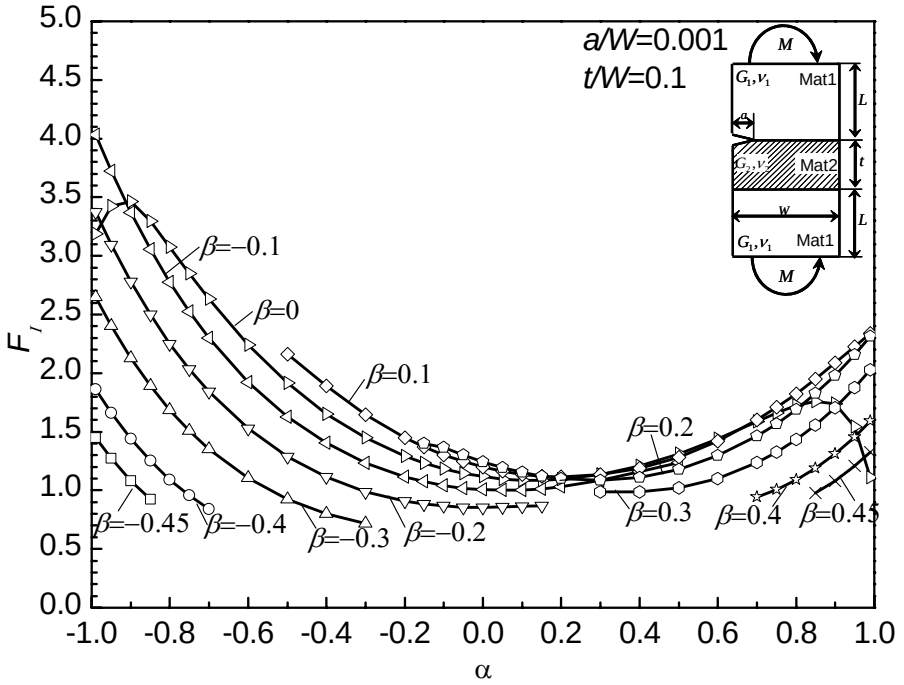

(a)

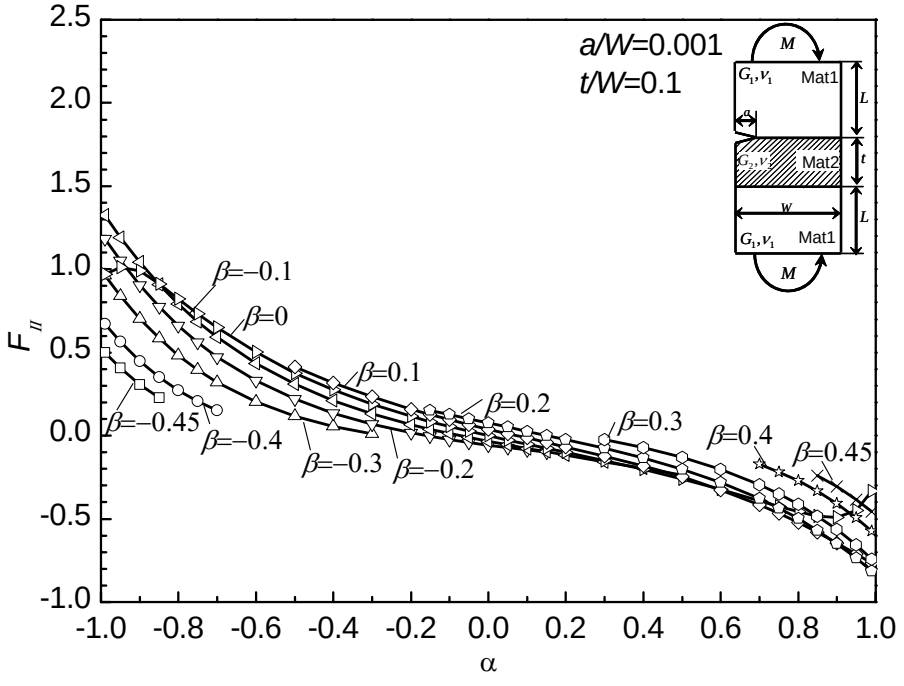

(b)

Fig. 6.13 Stress intensity factors (a) F_I and (b) F_{II} of adhesive joints $a/W = 0.001, t/W = 0.1$ for the bending loading case

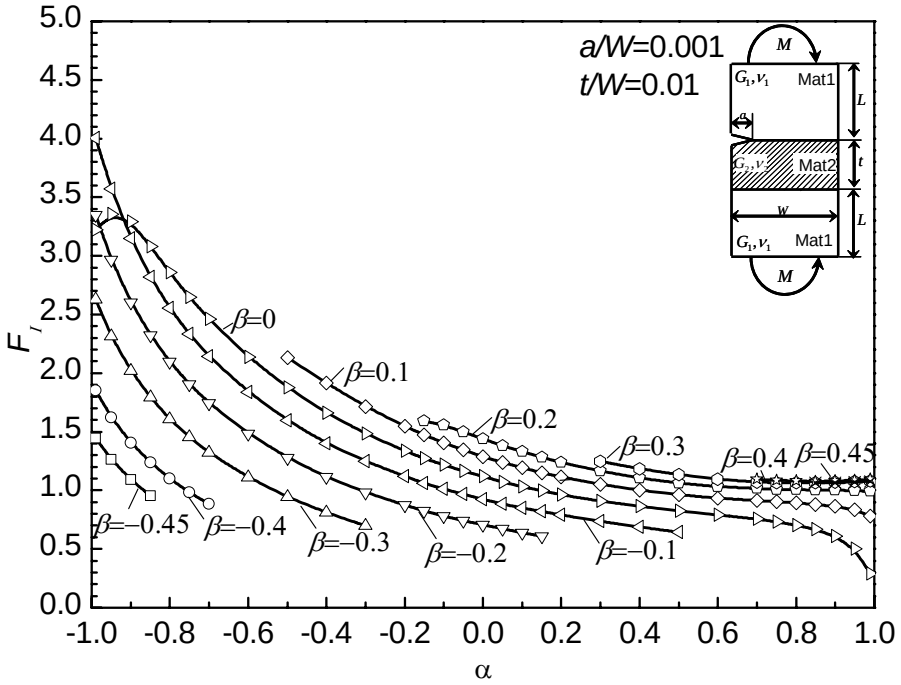

(a)

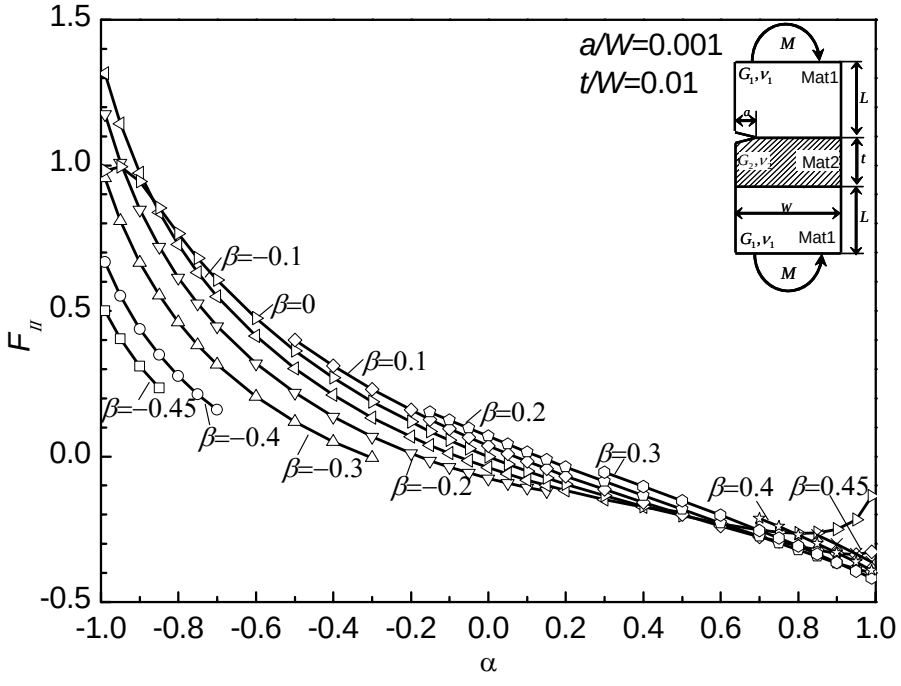

(b)

Fig.6.14 Stress intensity factors (a) F_I and (b) F_{II} of adhesive joints $a/W = 0.001, t/W = 0.01$ for the bending loading case

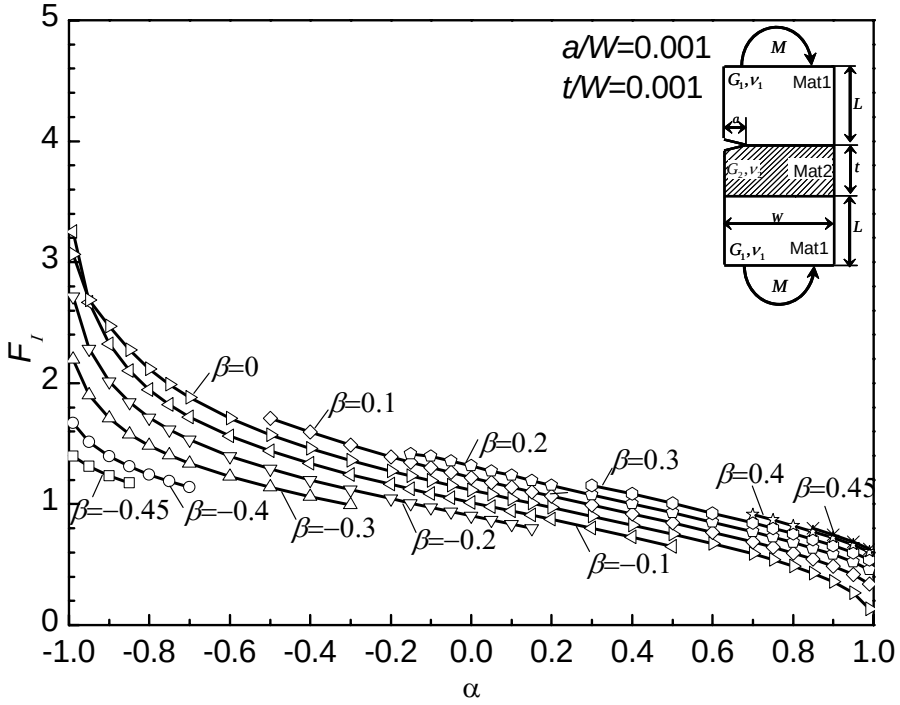

(a)

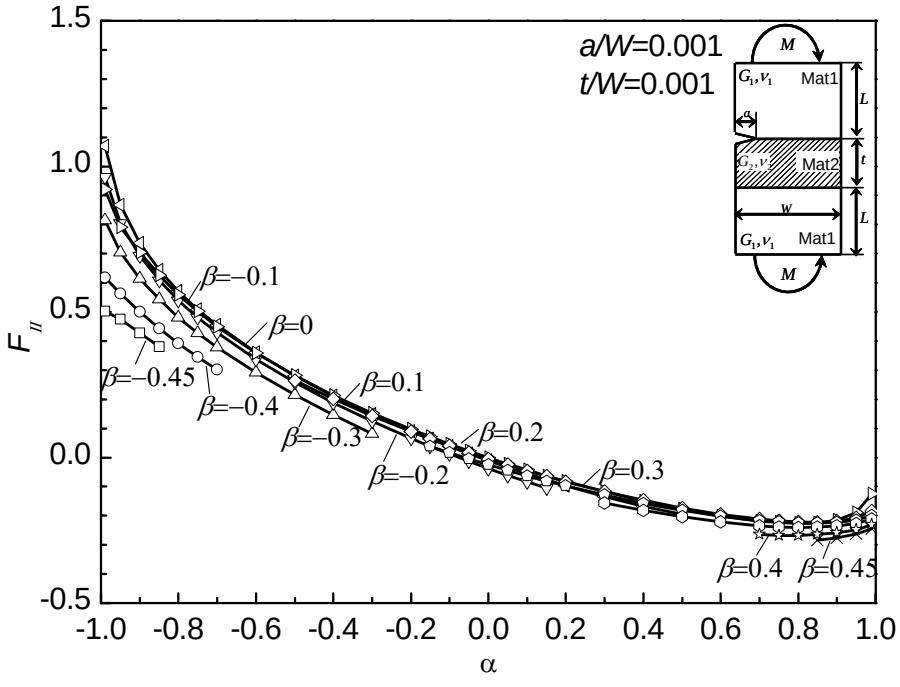

(b)

Fig. 6.15 Stress intensity factors (a) F_I and (b) F_{II} of adhesive joints $a/W = 0.001, t/W = 0.001$ for the bending loading case

6.4 The effect of interlayer thickness on the stress intensity factors for three-layered joints in CSP

Two-dimensional plane-strain problems of the single-edge cracked three-layered joints in CSP shown in Fig. 6.16 are analyzed for various crack lengths and interlayer thicknesses. It is supposed that a crack of length a has initiated at the interface 1 and 2 of the three-layered strips. The geometric configurations of the analytical models are demonstrated in Fig. 6.16a and b, respectively. Eight-node quadrilateral elements in plane strain are used for both the reference and the target unknown problems. The three-layered strips are composed of Si (IC chip), resin and FR-4.5(substrate) which are widely observed in the chip size packaging technology of electronic devices. The elastic parameters are tabulated in Table 6.2 [11]. The post-processing technique is also employed for this problem. The normalized SIFs of the problems shown in Fig. 6.16a and b predicted by the current method for different crack lengths and interlayer thicknesses are tabulated in Table 6.3 and 6.4 as well as in Table 6.5 and 6.6, respectively. The SIFs for the dissimilar bonded strips in Fig. 6.16c and d are tabulated in brackets in the last row of each table. As can be seen from the tables, the SIFs of Fig. 6.16c and d are in good agreement with those of Fig. 6.16a and b when $t/W > 1$, respectively. It should be noted that these results appear to be new and that there are no published data with which to compare them. Furthermore, the SIF values are also plotted in Fig. 6.17 and 6.18 for the edge interface cracks in interface 1 and 2, respectively. The SIFs of the tensile loads are plotted in solid lines and those for the bending loads are plotted in dashed lines. The figures show that the SIF values increase monotonically as the increase of the thickness of interlayer for a fixed crack length, and they reach to upper limit values asymptotically when the thickness of interlayer is bigger than the width of the strip ($t/W > 1$).

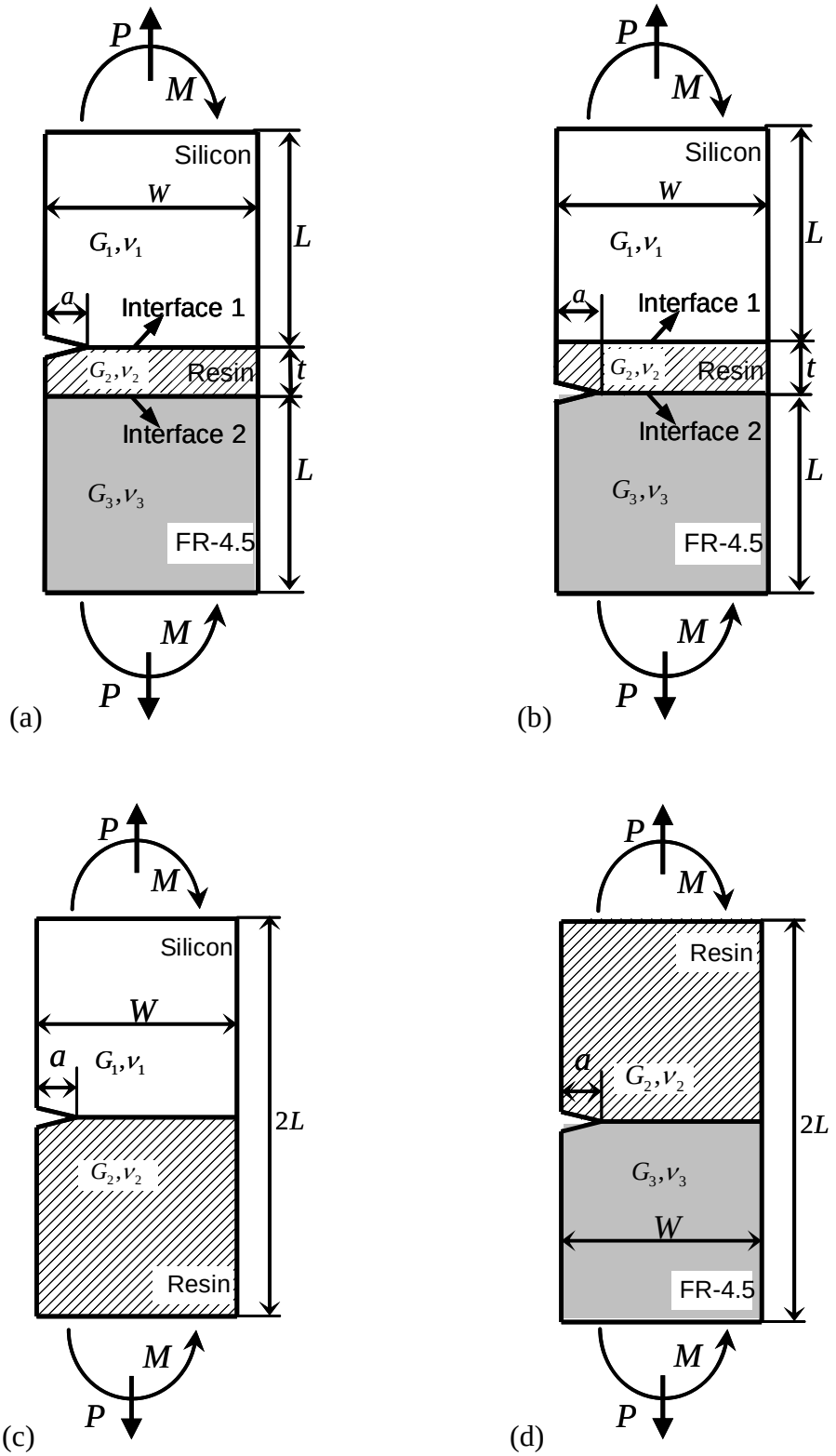

Fig.6.16 Single-edge interface crack on (a) interface 1 and (b) interface 2 of an adhesively bonded strip

Table 6.2 Material properties for adhesively bonded joint (CSP in the electronic device) (Koguchi and Nakajima 2010)

Material Property	Silicon	Resin	FR-4.5
Young's modulus (GPa)	166	2.74	15.34
Poisson's ratio	0.26	0.38	0.15

Table 6.3 Normalized SIFs of cracks on interface I in Fig.8a for tensile loads

	$a/W = 0.001$		$a/W = 0.01$		$a/W = 0.1$		$a/W = 0.2$		$a/W = 0.3$	
t/W	F_I	F_{II}	F_I	F_{II}	F_I	F_{II}	F_I	F_{II}	F_I	F_{II}
0.001	0.998	-0.206	0.661	-0.027	0.568	0.060	0.656	0.099	0.830	0.141
0.01	1.566	-0.203	0.782	-0.154	0.605	-0.009	0.677	0.018	0.821	0.036
0.04	2.180	-0.216	0.991	-0.176	0.684	-0.060	0.758	-0.030	0.921	-0.022
0.1	2.769	-0.258	1.529	-0.207	0.794	-0.126	0.880	-0.079	1.076	-0.067
0.2	3.454	-0.317	1.875	-0.211	0.929	-0.166	1.034	-0.135	1.280	-0.108
0.4	4.412	-0.404	2.100	-0.213	1.169	-0.168	1.253	-0.140	1.491	-0.098
1	5.146	-0.473	2.473	-0.239	1.399	-0.125	1.450	-0.064	1.696	0.005
2	5.148	-0.474	2.476	-0.240	1.409	-0.118	1.460	-0.053	1.705	0.017
4	5.148	-0.474	2.476	-0.240	1.409	-0.118	1.460	-0.053	1.705	0.017
Fig.6.14c	(5.148)	(-0.474)	(2.476)	(-0.240)	(1.409)	(-0.118)	(1.460)	(-0.053)	(1.705)	(0.017)

Table 6.4 Normalized SIFs of cracks on interface I in Fig.8a for bending loads

	$a/W = 0.001$		$a/W = 0.01$		$a/W = 0.1$		$a/W = 0.2$		$a/W = 0.3$	
t/W	F_I	F_{II}	F_I	F_{II}	F_I	F_{II}	F_I	F_{II}	F_I	F_{II}
0.001	0.872	-0.176	0.589	-0.014	0.478	0.073	0.492	0.106	0.549	0.135
0.01	1.368	-0.179	0.706	-0.120	0.513	0.022	0.509	0.048	0.546	0.062
0.04	1.957	-0.195	0.913	-0.147	0.588	-0.009	0.572	0.021	0.612	0.031
0.1	2.522	-0.237	1.250	-0.153	0.688	-0.045	0.673	0.004	0.722	0.021
0.2	3.011	-0.280	1.505	-0.154	0.830	-0.042	0.806	0.007	0.867	0.039
0.4	3.368	-0.313	1.641	-0.155	0.982	0.002	0.953	0.070	0.994	0.107
1	3.435	-0.320	1.680	-0.156	1.030	0.025	1.011	0.115	1.074	0.178
2	3.434	-0.320	1.680	-0.156	1.030	0.025	1.011	0.115	1.074	0.178
4	3.434	-0.320	1.680	-0.156	1.030	0.025	1.011	0.115	1.074	0.178
Fig.6.14c	(3.434)	(-0.320)	(1.680)	(-0.156)	(1.030)	(0.025)	(1.011)	(0.115)	(1.074)	(0.178)

Table 6.5 Normalized SIFs of cracks on interface II in Fig.8b for tensile loads

	$a/W = 0.001$		$a/W = 0.01$		$a/W = 0.1$		$a/W = 0.2$		$a/W = 0.3$	
t/W	F_I	F_{II}	F_I	F_{II}	F_I	F_{II}	F_I	F_{II}	F_I	F_{II}
0.001	0.942	0.101	0.583	0.181	0.415	0.303	0.444	0.405	0.563	0.571
0.01	0.945	0.168	0.743	0.094	0.533	0.182	0.574	0.254	0.681	0.340
0.04	1.128	0.171	0.792	0.147	0.722	0.140	0.698	0.186	0.840	0.253
0.1	1.384	0.194	1.054	0.192	0.767	0.137	0.842	0.162	1.027	0.211
0.2	1.702	0.232	1.266	0.203	0.879	0.167	1.005	0.173	1.248	0.194
0.4	2.184	0.295	1.407	0.207	1.064	0.184	1.207	0.175	1.465	0.162
1	2.628	0.356	1.711	0.239	1.277	0.158	1.395	0.116	1.668	0.072
2	2.641	0.358	1.722	0.240	1.292	0.152	1.409	0.105	1.679	0.060
4	2.641	0.358	1.722	0.240	1.292	0.152	1.409	0.105	1.679	0.060
Fig.6.14d	(2.641)	(0.358)	(1.722)	(0.240)	(1.292)	(0.152)	(1.409)	(0.105)	(1.679)	(0.060)

Table 6.6 Normalized SIFs of cracks on interface II in Fig.8b for bending loads

	$a/W = 0.001$		$a/W = 0.01$		$a/W = 0.1$		$a/W = 0.2$		$a/W = 0.3$	
t/W	F_I	F_{II}	F_I	F_{II}	F_I	F_{II}	F_I	F_{II}	F_I	F_{II}
0.001	0.826	0.096	0.517	0.170	0.338	0.273	0.316	0.328	0.352	0.409
0.01	0.898	0.159	0.680	0.105	0.444	0.176	0.421	0.216	0.439	0.254
0.04	1.175	0.174	0.803	0.145	0.553	0.131	0.521	0.161	0.549	0.189
0.1	1.494	0.207	1.020	0.165	0.513	0.813	0.647	0.124	0.689	0.143
0.2	1.787	0.244	1.215	0.173	0.832	0.094	0.802	0.086	0.859	0.087
0.4	2.019	0.275	1.335	0.177	0.986	0.054	0.967	0.010	1.009	-0.007
1	2.072	0.283	1.376	0.180	1.038	0.033	1.034	-0.036	1.101	-0.083
2	2.072	0.283	1.375	0.180	1.039	0.033	1.035	-0.037	1.102	-0.083
4	2.072	0.283	1.375	0.180	1.039	0.033	1.035	-0.037	1.102	-0.083
Fig.6.14d	(2.072)	(0.283)	(1.375)	(0.180)	(1.039)	(0.033)	(1.035)	(-0.037)	(1.102)	(-0.083)

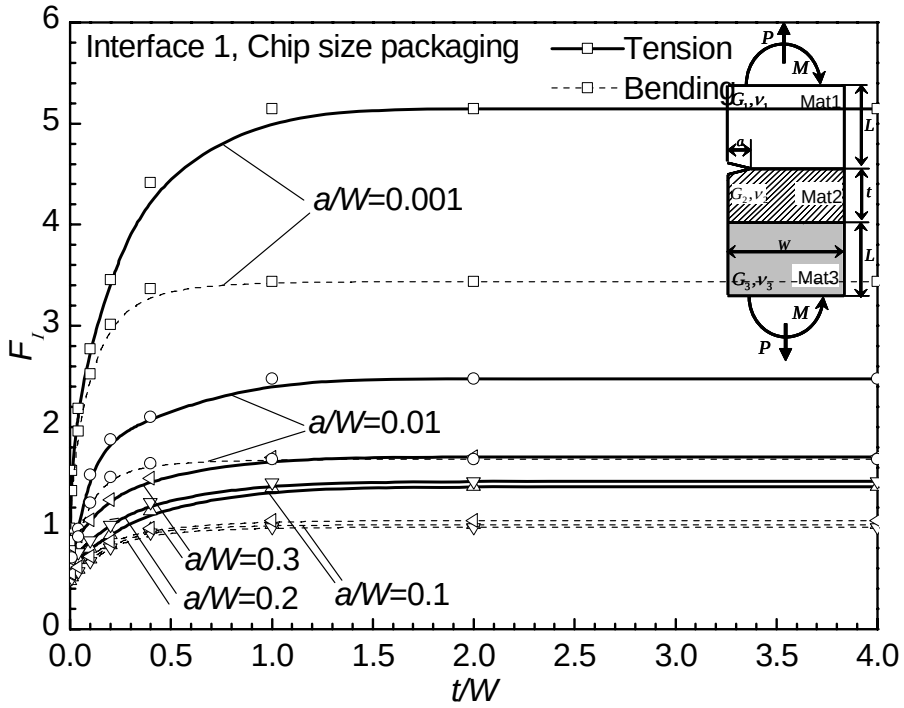

(a)

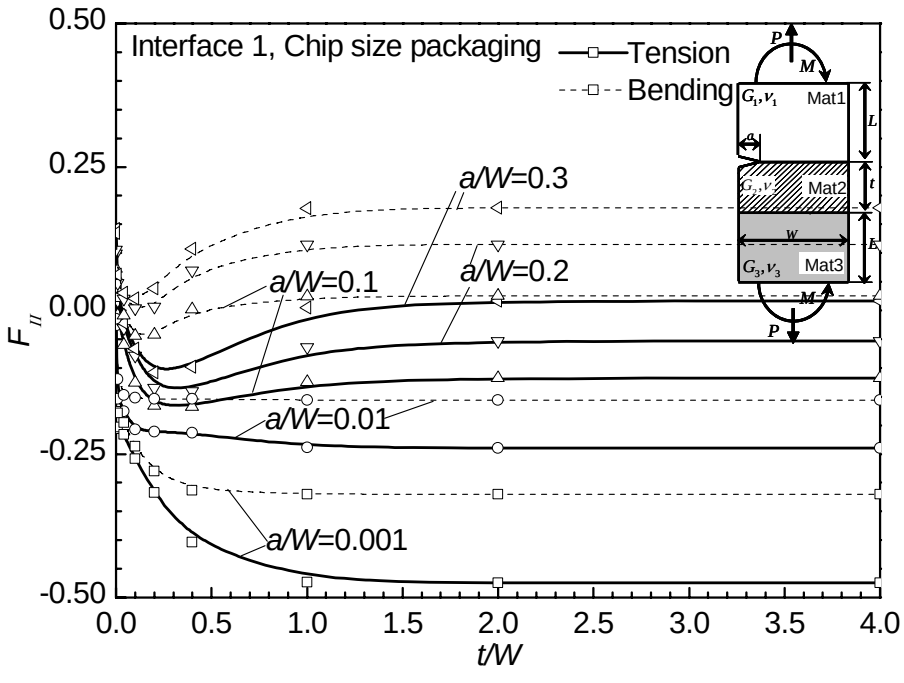

(b)

Fig.6.17 Variation of SIFs for edge interface cracks in interface 1 for various crack lengths and thicknesses of adhesive layer

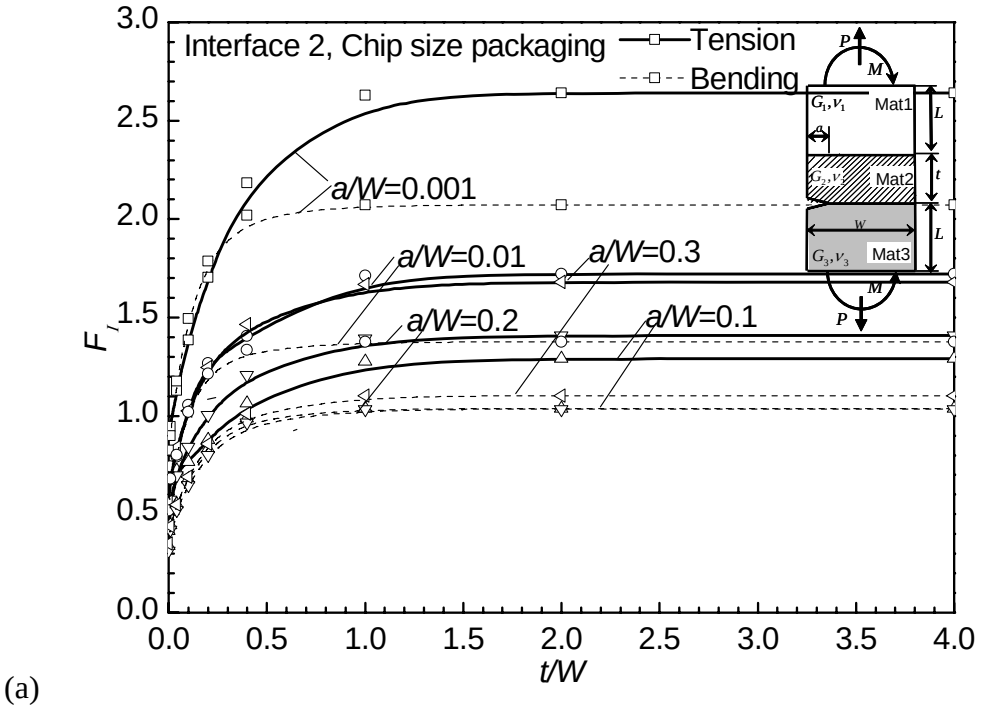

(a)

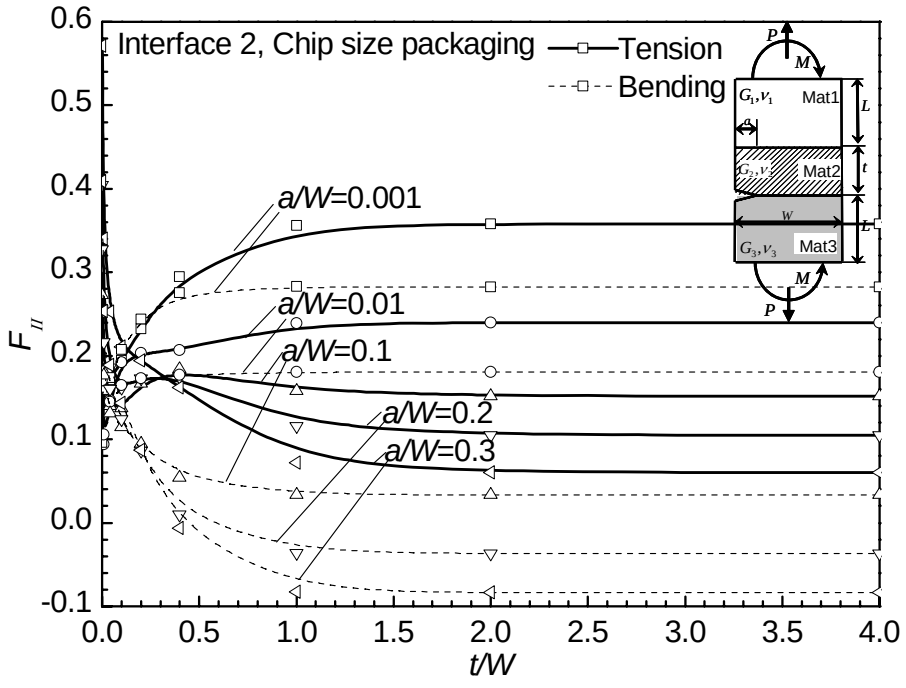

(b)

Fig. 6.18 Variation of SIFs for edge interface cracks in interface 2 for various crack lengths and thicknesses of adhesive layer

6.5 Conclusions

In this chapter, the SIFs of three-layered joints/ adhesive joints were computed for arbitrary material combinations. The effects of adhesive layer thickness on the SIFs for the three-layered joints in CSP were studied and demonstrated. Furthermore, the adhesion strength evaluation based on SIFs were discussed in Appendix B. The following conclusions have been made as follows.

1. The SIFs of an adhesive joint which two identical adherents bonded by adhesive agent are uniquely determined by the Dundurs' material composite parameters. And the values of F_I are strictly mirror symmetric about $\alpha = 0$ and those for F_{II} are reflection symmetric about $\alpha = 0, \beta = 0$ in the $\alpha - \beta$ space when adhesive thickness is long enough (say, $t/W = 2$).

2. The three-layered strips in CSP which are composed of Si (IC chip), resin and FR-4.5(substrate) were investigated. The SIF values of edge interface cracks in CSP increase monotonically as the increase of the thickness of interlayer for a fixed crack length, and they reach to upper limit values asymptotically when the thickness of interlayer is bigger than the width of the strip ($t/W > 1$).

6.6 References of Chapter 6

[1] Hattori, T.O., Sakata, S.J., Hatsuda, T.O. and Murakami, G., A stress singularity parameters approach for evaluating adhesive strength. Trans JSME. Series A, 1988;54(499):597-602. (In Japanese)

[2] Hattori, T.O. and Watanabe, T.S., Standardizing of strength evaluation methods using stress singularity parameters. Trans JSME. Series A, 2001;67(661):1486-1492. (In Japanese)

[3] Shibutani, T.H., Evaluation of Crack Initiation at Interfacial Edge on the Basis of Fracture Mechanics Concept and Application to Electronics Devices (Tutorial Series : Foundations for Reliability Analysis), Trans JIEP, 2004;7(7):639-644.

[4] Fernlund, G., Spelt, J.K., Mixed-mode fracture characterization of adhesive joints. Comp. Sci. Technol., 1994;50: 441-9.

[5] Pang, H.L.J., Seetoh, C.W., A compact mixed-mode (CMM) fracture specimen for adhesive bonded joints. Engng. Frac. Mech., 1997;57:57-65.

[6] Choupani, N., Mixed-mode cohesive fracture of adhesive joints: experimental and numerical studies. Engng. Frac. Mech., 2008; 75:4363-82.

[7] Marannano, G.V., Mistretta, L., Cirello, A., Pasta, S., Crack growth analysis at adhesive-adherent interface in bonded joints under mixed-mode I/II. Eng. Frac. Mech., 2008;75:5122-33.

[8] Hafiz ,T.A., Abdel Wahab, M.M.., Crocombe, A.D. and Smith, P.A., Mixed-mode fracture of adhesively bonded metallic joints under quasi-static loading. Engng Frac. Mech., 2010; 77: 3434-3445.

[9] Otsuka, K., Interface mechanics – foundations for IC packaging and materials. Baifukan, Tokyo, First Ed. 1994. (In Japanese)

[10] Nishimura, A.O., Hirose, I. and Tanaka, N.T., A new method for measuring adhesion strength of IC molding compounds. Trans JSME. Series A, 1993;59(559):620-626. (In Japanese)

[11] Koguchi, H., Nakajima, M., Influence of interlayer thickness on the intensity of singular stress field in 3D three-Layered Joints under an external load. J Solid Mech Mat Engng., 2010;4:1027-1039.

7

CHAPTER

Conclusions

Composite materials and bonded structures are widely employed in the modern industrial context. The mechanical behavior of the bi-material interface is of great significance for the industrial application. Singular stress fields exist around the areas of the edge interface corners for two materials bonded together. High stress concentration at the edge interface corner caused by differences in the elastic properties may lead to the initiation of micro-cracks and then to the propagation. Therefore basic studies about the interface cracks win quite a number of attentions. Little research was found regarding the SIFs for arbitrary material combinations. And this paper was devoted to the SIFs for edge interface cracks.

Several types of edge interface cracks were treated in this paper. The SIFs were calculated using the numerical method proposed by Oda, the method is denoted as “Crack tip stress method” which is based on Nisitani’s concept. The effects of material combinations and relative crack lengths were investigated in this paper.

The following conclusions have been obtained as follows.

(1) In Chapter 2: The computational accuracy of the extended “crack tip stress method” proposed by Oda were reexamined by pursuing a convergence study. The limitations of the method were demonstrated and investigated. Then, a post-processing technique of linear extrapolation was proposed to improve the computational accuracy. The

accuracy and efficiency of the improved crack tip stress method were demonstrated by comparing the SIF results of several numerical examples with published data. It was certified that the new technique could determine the SIFs of interface cracks more accurately with less computational coat.

(2)In Chapter 3: The asymptotic solutions of the SIFs at the crack tip of a bi-material bonded semi-infinite plate were pursued for under arbitrary combination of materials. It was found that the double logarithmic distributions of the SIFs against relative crack lengths behave good linearity within the singular zone. In addition, an approximate formula calculating the SIFs for the bonded dissimilar half-planes under arbitrary combination of materials was proposed by fitting the computed results.

(3)In Chapter 4: The SIFs of the dissimilar bonded finite strips subjected to tensile and bending loading conditions were investigated. Relationships as $\frac{K_I}{\sigma\sqrt{\pi a}}\cdot(a/W)^{1-\lambda}=C_I$ and $\frac{K_{II}}{\sigma\sqrt{\pi a}}\cdot(a/W)^{1-\lambda}=C_{II}$ exist for the very shallow edge interface cracks in bi-material butt joints subjected to tensile and bending loads. And the coefficients C_I, C_{II} are merely determined upon the relative elastic properties of materials and the loading types. In addition, the effects of material combinations and relative crack lengths to the SIFs were also investigated. Furthermore, the contour map variations of the SIFs for the whole $\alpha-\beta$ space were demonstrated.

(4)In Chapter 5: The SIFs for the single and double edge interface cracks were compared for the whole range of combination of materials ($0\le\alpha\le 0.95, -0.2\le\beta\le 0.45$) and relative crack lengths ($0\le a/W\le 0.9$). It was found that the SIFs of a double edge interface crack may be possibly larger than those of a single edge interface crack for some specific combination of materials and relative crack lengths. In addition, the SIFs should be compared in three different zones of relative crack lengths.

(6)In Chapter 6: The SIFs of the adhesive joints for various material combinations

were calculated. In this chapter the SIFs are computed for the whole region of the $\alpha - \beta$ space since no symmetry of the SIFs exists any more for the adhesive joints. The variations of the SIFs for various thicknesses of adhesive layer were also demonstrated. The SIFs for the three-layered adhesive joints composed of Si (IC chip), resin and FR-4.5(substrate) which are used in CSP were also investigated for various interlayer thicknesses. It was found that the SIFs reach to constants for the adhesive joints when the interlayer thickness is bigger that the joint width.

A APPENDIX

Dundurs' composite parameters for engineering materials

Till recently, several studies have considered the Dundurs' composite parameters of typical engineering materials. Suga, (1988) investigated the parameters and mechanical compatibility of various material joints. Yuuki (1993) showed the variations of the parameters in the $\alpha-\beta$ space for the materials combinations among metal, ceramics, resin, and glass. The results are tabulated in Table A1 and re-plotted in Fig.A1. Consider the symmetry of $\alpha-\beta$ space for the bi-material joints, only the right part ($\alpha>0$) is given in Fig.A1. The origin $\alpha=\beta=0$ represents combinations of identical materials, and the $\alpha-\beta$ space is located within the parallelogram region which is composed by the lines $\beta=1/4(\alpha\pm1),\alpha=0,\alpha=1$. Material combinations of $\alpha=2\beta$ are plotted in the dashed line. Uniform stress distributions can be observed for $\alpha=2\beta$. And the $\alpha-\beta$ space can be divided into two regions by the line $\alpha=2\beta$. Each pair of (α,β) above the line has no singularity and is denoted as good pair ($\alpha(\alpha-2\beta)<0$). And the one below the line is denoted as bad pair ($\alpha(\alpha-2\beta)>0$) since stress singularity exists near the interface corner.

As can been seen from Fig. A.1, most material combinations are located in the so called "bad pair" region. However, metal-to-glass joints distribute along the line $\alpha=2\beta$, and a considerable number of metal-to-glass joints can be found in the "good pair" region. In addition, metal/metal, ceramics/ceramics and glass/glass joints are also found to have "good pair" material combinations.

Table A1. Elastic properties of several engineering materials (Yuuki, 1993)

	Material	Young's Modulus (GPa)	Poisson's Ratio
Metal	Fe	206	0.30
	Al	70.3	0.345
	Ti	115.7	0.321
	Cu	129.8	0.343
	Zn	108.4	0.249
	Si	200	0.30
Ceramics	Al_2O_3	359	0.20
	SiC	440	0.16
	Si_3N_4	304	0.27
	MgO	303	0.175
Resin	Epoxy Resin	4.93	0.33
	Polyester	3.0	0.38
Glass	Crystal	73.1	0.17
	LF5	59.0	0.226
	SF53	58.0	0.236
	BaSF64	105.0	0.262
	BK7	81.5	0.208
	CaNa	70.3	0.240

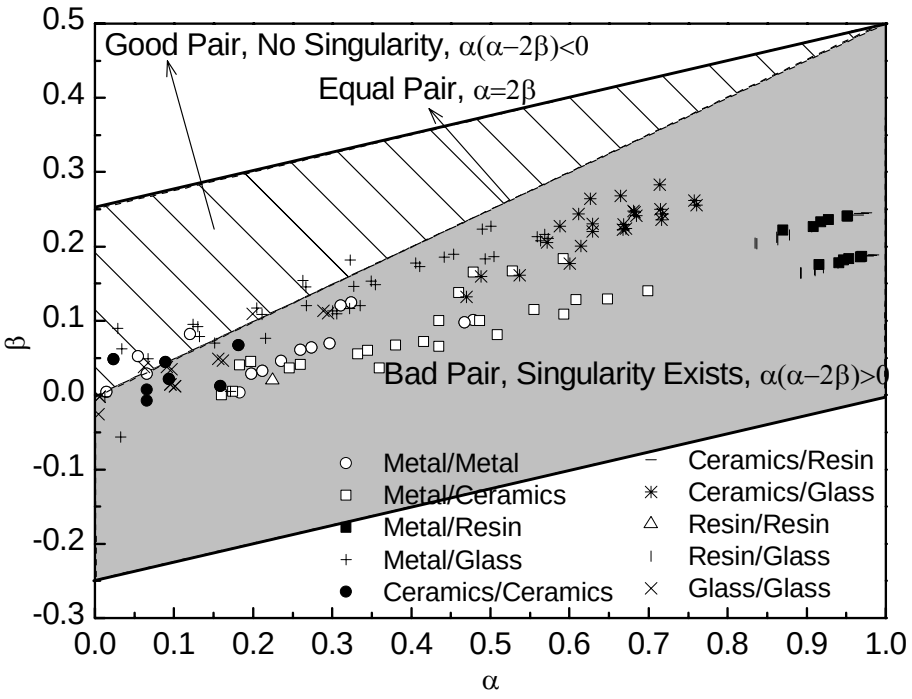

Fig. A.1 Material combinations for typical engineering materials

B APPENDIX

De-bonding strength evaluation based on the stress intensity factors for adhesive joints

B.1 Introduction

Bonded structures are widely used in industrial fields. It has been certified that the adhesive strength increases with decreasing the adhesive thickness. The previous studies suggested that this is because more defects and cavities appear in the thick adhesive layer when large amount of adhesive agents are used. Suzuki [1] evaluated the de-bonding strength experimentally using bonded tensile specimen as shown in Fig.1a; He pointed out that the adhesive strength is affected by the adhesive thickness for the adhesive joint which S35C JIS medium carbon steel plates bonded by epoxy resin Epikote 871.

In this appendix, de-bonding criterions will be considered in terms of the intensities of the singular stress and stress intensity factors on the basis of two types of models. One is the perfectly-bonded model as shown in Fig. B.1b, and the other is the partially-debonded model shown in Fig. B.1c. Then the critical de-bonding conditions will be discussed.

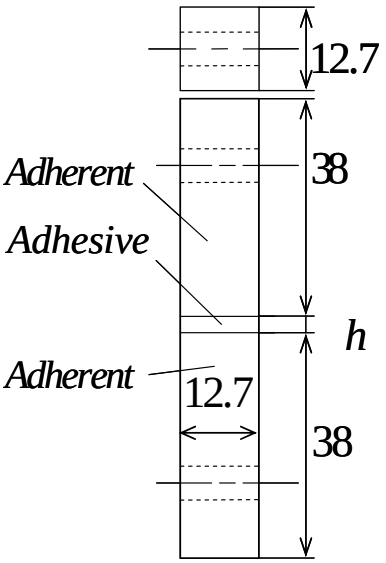

(a)

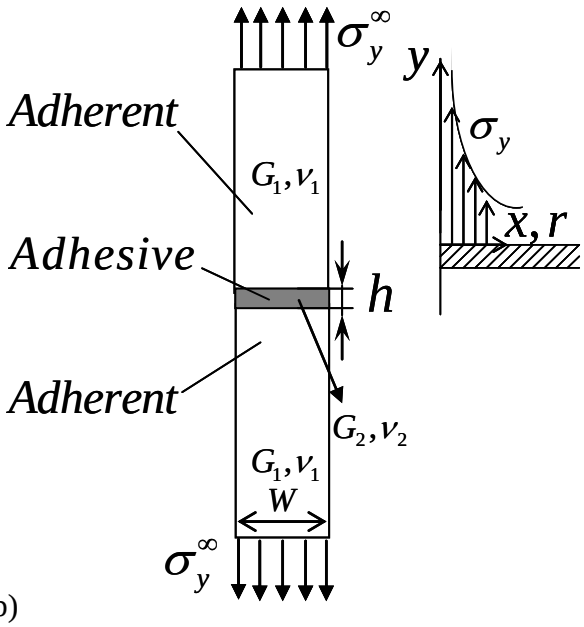

(b)

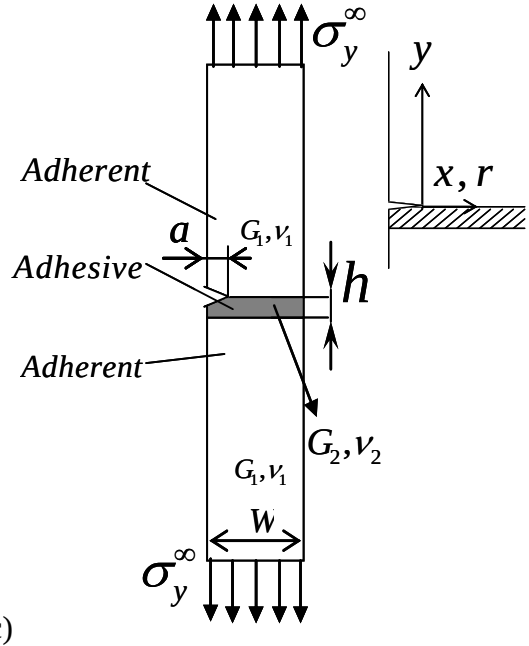

(c)

$$\sigma_y \to \frac{K_\sigma}{r^{1-\lambda}}$$

$$\sigma_y + i\tau_{xy} \to \frac{K_I + iK_{II}}{\sqrt{2\pi r}} \left(\frac{r}{W} \right)^{i\varepsilon} \quad (r \to 0)$$

(a) Experimental specimen (b) Perfectly-bonded model (c) Partially-debonded model
Fig. B1 Models used in this study

B.2 Experimental data used in the study

In this appendix, the specimen used in Suzuki [1] which the adherents S35C are bonded with adhesive epoxy resin Epikote 871 as shown in Fig. B.1a is analyzed. The elastic parameters of the adherent and adhesives are tabulated in Table B.1. The experimental results of the adhesion strengths and their standard deviations obtained by Suzuki [1] are tabulated in Table B.2 against various adhesive thicknesses. In Table B.2, the adhesion strengths are computed using the mean values of the experimental results, and the relative standard deviations are given behind.

Table B.1 Material property of adherent and adhesives

β	Elastic modulus E (GPa)	Poisson's ratio ν	λ	α	β
Adherent: Medium carbon steel S35C	210	0.3	—	—	—
Adhesive A: Epikote828	3.14	0.37	0.69	0.97	0.20
Adhesive B: Epikote871	2.16	0.38	0.67	0.98	0.19

Table B.2 The experimental adhesive strength $\sigma_y(Average)$ obtained by Suzuki [1]

		Material A	Material B
h	h/W	σ_y^∞ (Average)	σ_y^∞ (Average)
0.05	0.0039	57.2±7.34	76.8±2.96
0.1	0.0078	53.5±6.52	71.4±0.981
0.3	0.024	32.5±2.72	49.7±3.03
0.6	0.047	25.9±2.71	41.2±1.94
1.0	0.079	22.6±1.18	25.3±3.09
2.0	0.16	18.4±2.08	19.7±1.31
5.0	0.39	13.4±1.76	13.4±1.71

B.3Failure criterion using the perfectly-bonded model

For the perfectly-bonded model shown in Fig. B.1b, the singular stress can be expressed as $\sigma_y = K_\sigma / r^{1-\lambda} = F_\sigma \sigma_y^\infty (W/r)^{1-\lambda}$. The values of F_σ for various adhesive thicknesses were computed by Zhang et al. [2]. Then, the intensity of singular stress field $K_{\sigma c}$ can be obtained using Eq. (B.1). The values of F_σ and $K_{\sigma c}$ are tabulated in Table B.3. The values of $K_{\sigma c}$ for perfectly bonded model are plotted in Fig. B.2 against various adhesive thicknesses. Fig. B.2 indicates that the critical values of the intensity of singular

stress field $K_{\sigma c}$ are almost constant with varying the adhesive thickness h/W. The mean values of the intensity of singular stress field and their standard deviations are $8.04 \pm 1.42 [MPa \cdot m^{0.315}]$ for adhesive A, and are $9.79 \pm 1.33 [MPa \cdot m^{0.326}]$ for adhesive B.

The critical intensity of the singular stress fields $K_{\sigma c}$ of the perfectly-bonded strip shown in Fig. B.1b was computed for various thicknesses of adhesive layer h/W, by using the values of tensile adhesive strength σ_y from experiment. It is found that the average values of $K_{\sigma c}$ =9.79±1.33 $[MPa \cdot m^{0.326}]$. It can be clearly seen that the standard deviations are within 17.6%. The mean values of $K_{\sigma c}$ and its deviation are tabulated in Table B.3 for Adhesives A and B. It can be seen from this table that $K_{\sigma c}$ and its deviation are $8.04 \pm 1.42 \left(MPa \cdot m^{0.315} \right)$ for adhesive A, and $9.79 \pm 1.33 \left(MPa \cdot m^{0.326} \right)$ for adhesive B. Failure condition as $K_{\sigma c} = const$ is available for the estimation of de-bonding for perfectly bonded models.

$$K_{\sigma c} = F_\sigma \sigma_y^\infty W^{1-\lambda} \tag{B.1}$$

Table B.3 Debonding stress σ_y and critical value of $K_{\sigma c}$ using perfectly-bonded model for (a) Adhesive A and (b) Adhesive B (Experimental results, [6] $K_{\sigma c} = F_\sigma \sigma_y W^{1-\lambda}$)

	Adhesive A			Adhesive B		
h/W	σ_y^∞ (Average)	F_σ	$K_{\sigma c}$	σ_y^∞ (Average)	F_σ	$K_{\sigma c}$
0.001	—	0.048	—	—	0.048	—
0.0039	57.2	0.054	6.89 ± 1.45	76.8	0.054	8.10 ± 1.72
0.0078	53.5	0.062	7.34 ± 1.13	71.4	0.062	8.79 ± 0.10
0.01	—	0.066	—	—	0.066	—
0.024	32.5	0.092	6.70 ± 1.45	49.7	0.092	9.79 ± 0.60
0.047	25.9	0.132	7.63 ± 0.89	41.2	0.132	11.8 ± 2.08
0.079	22.6	0.171	8.60 ± 0.72	25.3	0.171	9.76 ± 1.19
0.1	—	0.192	—	—	0.192	—
0.16	18.4	0.231	9.46 ± 1.78	19.7	0.231	10.3 ± 0.855
0.39	13.4	0.323	9.64 ± 2.05	13.4	0.323	10.0 ± 1.27
0.5	—	0.343	—	—	0.343	—
$K_{\sigma c,ave}$			8.04 ± 1.42			9.79 ± 1.33

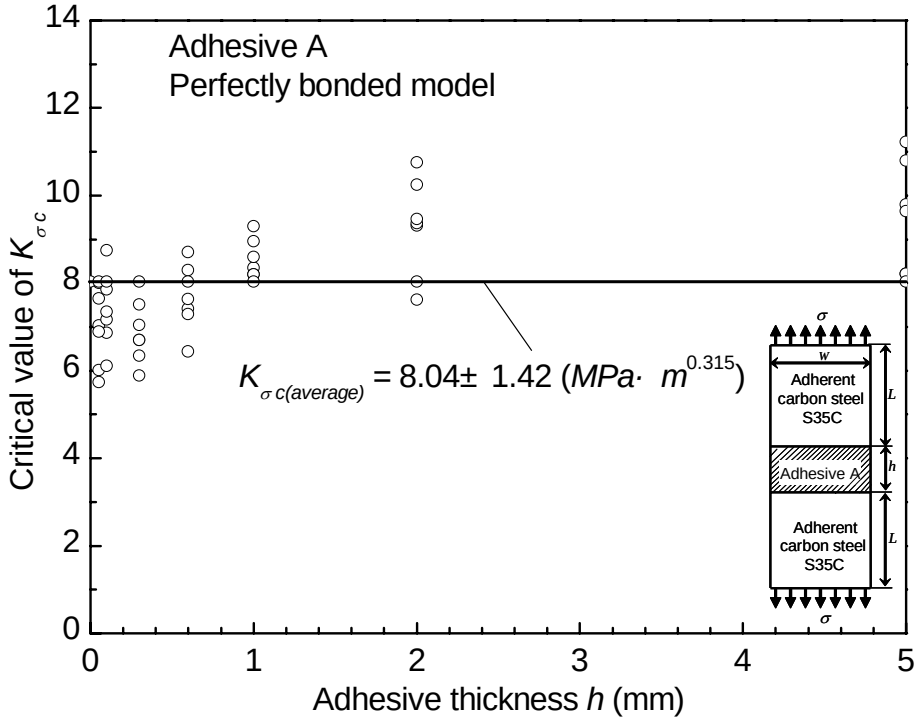

(a)

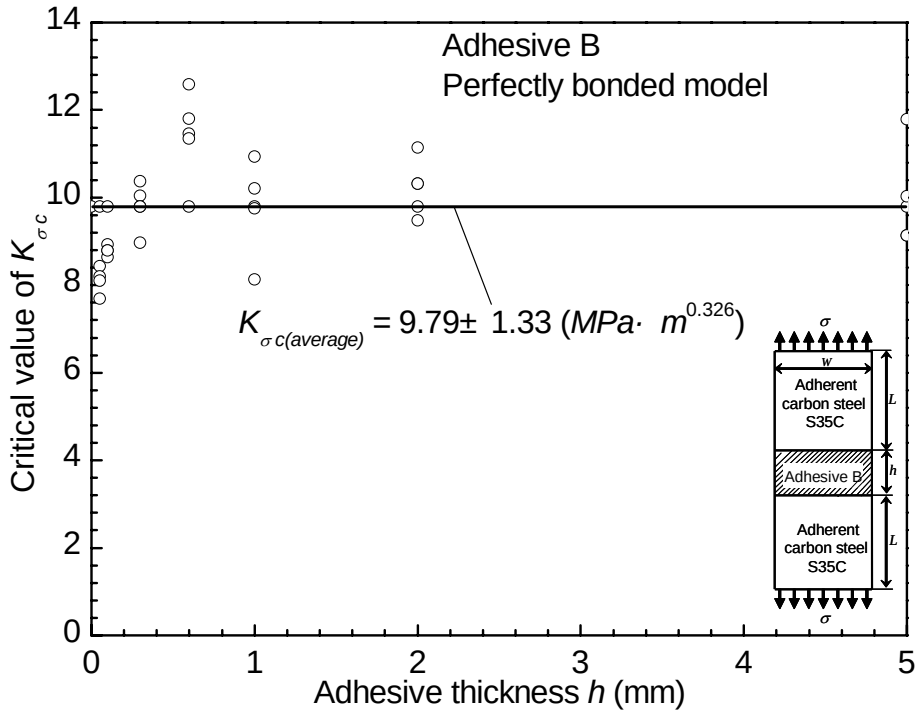

(b)

Fig. B.2 Relationship between of $K_{\sigma c}$ and h for adhesives A and B

B.4 Failure criterion using the partially-debonded model

Two different partially-debonded models with relative crack lengths $a/W = 0.01, 0.1$ are used to evaluate the bondng strength. For the partially-debonded moadel, the singular stress can be expressed in Eq. (B.2). The values of τ_{xy} and K_{II} are ignored due to tiny value magnitude compared with σ_y and K_I. The dimensionless SIFs F_I are calculated as shown in Reference [3,4]. Then the critical SIFs can be obtained using Eq. B.3. Fig. B.3 and B.4 indicate that the critical values of the stress intensity factors K_{Ic} are almost constant with varying the adhesive thickness h/W (see Eq. (B.2)).

$$\sigma_y + i\tau_{xy} = K_I + iK_{II}\left(r/W\right)^{i\varepsilon} / \sqrt{2\pi r}\,(r \to 0) \tag{B.2}$$

$$K_{Ic} = F_I \sigma_y^{\infty} \sqrt{\pi a} \tag{B.3}$$

The critical stress intensity factors K_{Ic} were computed for adhesives A and B with varying the interlayer thicknesses, using the partially-debonded model of $a/W = 0.01$ and $a/W = 0.1$. The values are tabulated in Table B.4. As can be seen from this table, the average values of $K_{\sigma c}$ and their standard deviations are $4.04 \pm 0.537\left(MPa \cdot m^{0.5}\right)$ of model $a/W = 0.01$ and $4.98 \pm 0.622\left(MPa \cdot m^{0.5}\right)$ of model $a/W = 0.1$ for adhesive A, as well as $7.69 \pm 1.13\left(MPa \cdot m^{0.5}\right)$ of model $a/W = 0.01$ and $9.36 \pm 1.09\left(MPa \cdot m^{0.5}\right)$ of model $a/W = 0.1$ for adhesive B, respectively . In addition, the errors of the standard deviations are within 20%, therefore, the failure condition as $K_{Ic} = const$ is also available for the estimation of the de-bonding for partially-bonded models.

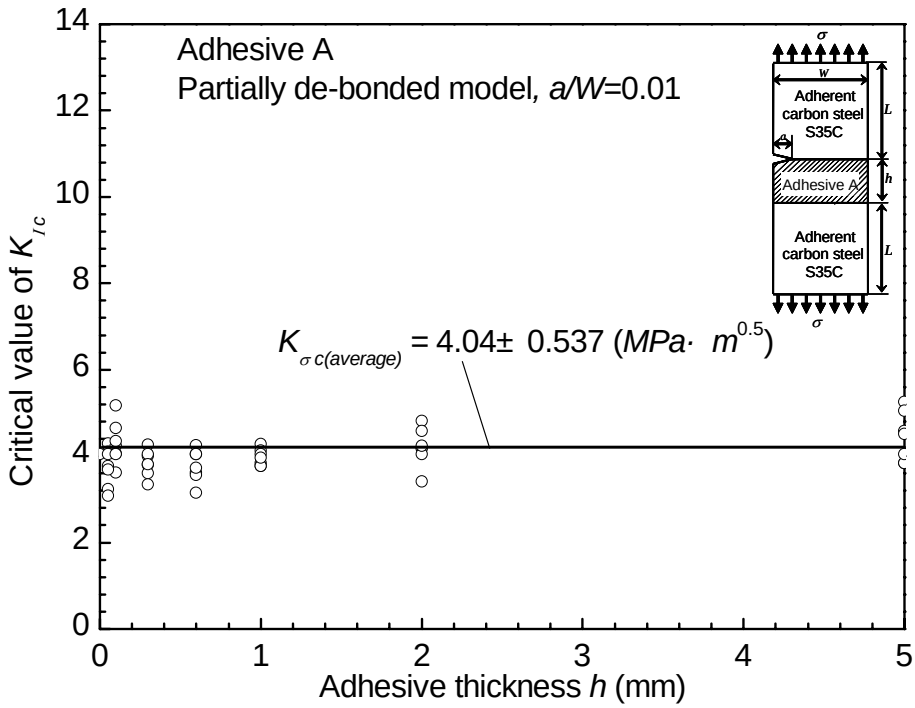

(a)

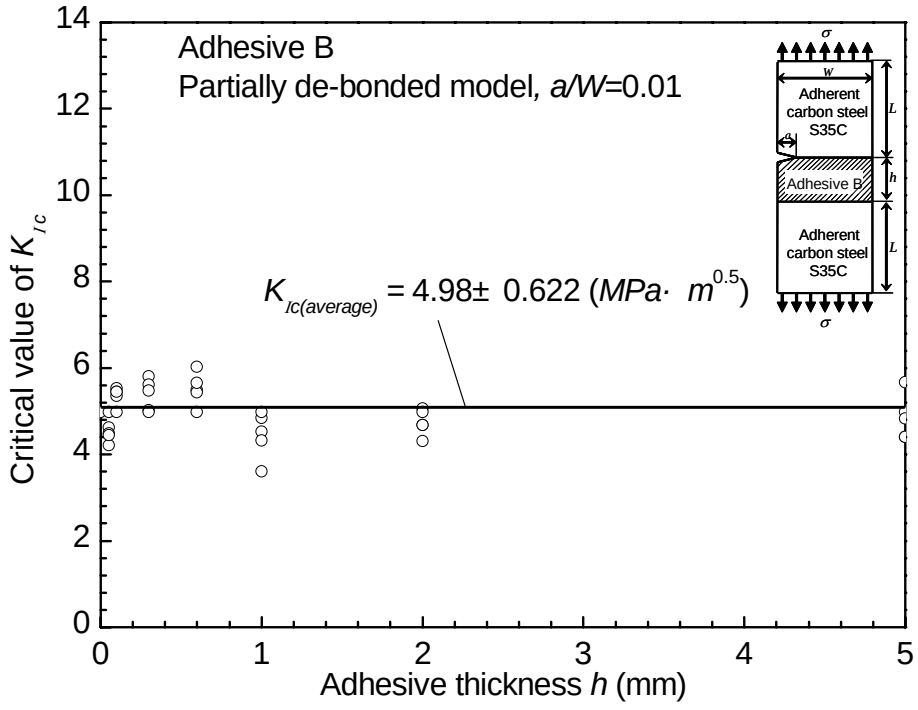

(b)

Fig. B.3 Relationship between of K_{Ic} and h ($a/W = 0.01$) for adhesives A and B

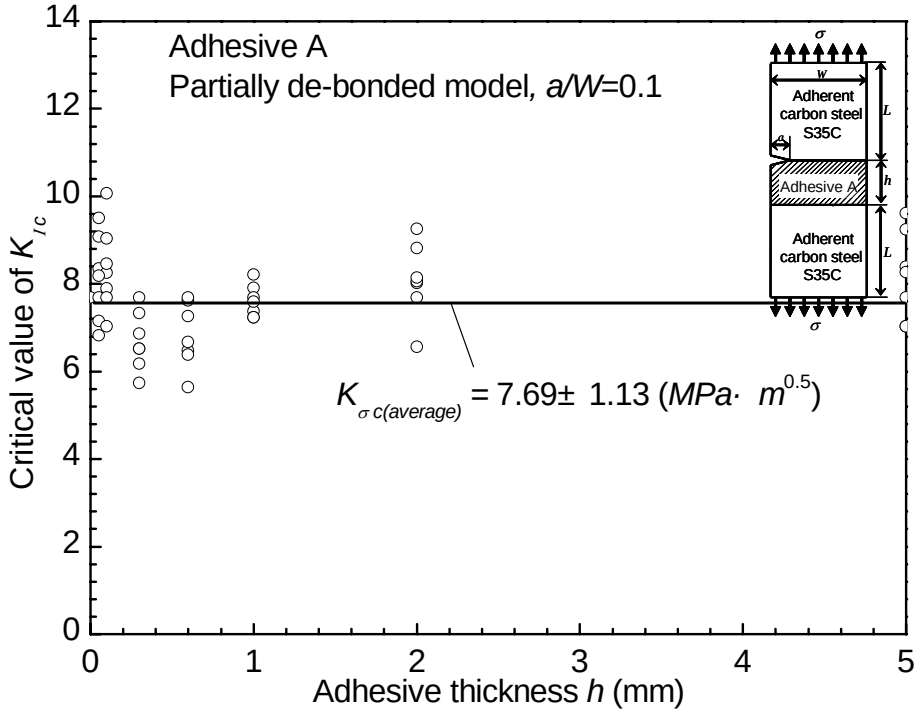

(a)

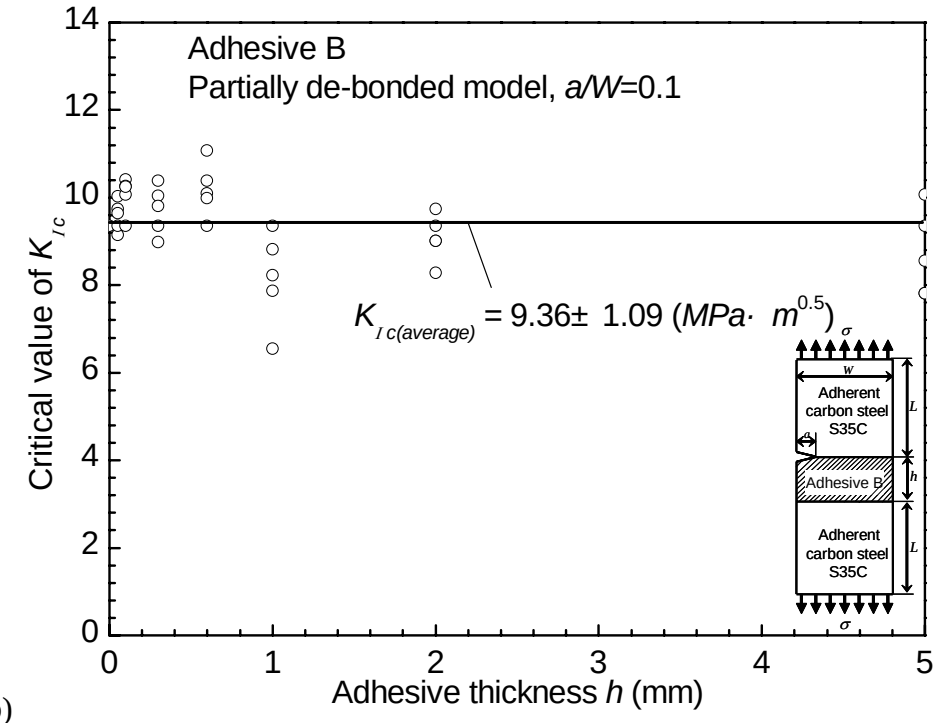

(b)

Fig. B.4 Relationship between of K_{Ic} and $h\,(a/W = 0.1)$ for adhesives A and B

Table B.4 Debonding stress σ_y and fracture toughness $K_{\sigma c}$ assuming partially-debonded model $a/W = 0.01, 0.1$ (Experimental results, $K_{Ic} = F_I \sigma_y \sqrt{\pi a}$)

	Material A					Material B				
		$a/W = 0.01$		$a/W = 0.1$			$a/W = 0.01$		$a/W = 0.1$	
h/W	σ_y^∞	F_I	K_{Ic}	F_I	K_{Ic}	σ_y^∞	F_I	K_{Ic}	F_I	K_{Ic}
0.001	—	0.266	—	0.231	—	—	0.266	—	0.231	—
0.0039	57.2	0.364	3.69 ± 0.588	0.255	8.18 ± 1.16	76.8	0.364	4.44 ± 0.566	0.255	9.64 ± 0.465
0.0078	53.5	0.460	4.35 ± 0.615	0.283	8.46 ± 1.29	71.4	0.460	5.44 ± 0.475	0.283	10.3 ± 0.903
0.01	—	0.509	—	0.300	—	—	0.509	—	0.300	—
0.024	32.5	0.660	3.84 ± 0.395	0.358	6.53 ± 1.29	49.7	0.660	5.48 ± 0.602	0.358	9.80 ± 0.742
0.047	25.9	0.810	3.72 ± 0.500	0.459	6.67 ± 1.23	41.2	0.810	5.65 ± 0.723	0.459	10.4 ± 1.14
0.079	22.6	0.990	3.96 ± 0.222	0.600	7.59 ± 0.41	25.3	0.990	4.32 ± 0.841	0.600	7.87 ± 1.77
0.1	—	1.09	—	0.663	—	—	1.09	—	0.663	—
0.16	18.4	1.30	4.24 ± 0.517	0.790	8.14 ± 1.02	19.7	1.30	4.68 ± 0.429	0.790	9.01 ± 0.691
0.39	13.4	1.90	4.51 ± 0.758	1.10	8.26 ± 1.23	13.4	1.90	4.82 ± 0.621	1.10	8.56 ± 1.33
0.5	—	2.10	—	1.19	—	—	2.10	—	1.19	—
$K_{\sigma c,ave}$			4.04 ± 0.537		7.69 ± 1.13			4.98 ± 0.622		9.36 ± 1.09

B.5 Discussions on the adhesion strength

In this section, the critical intensity of singular stress $K_{\sigma c}$ and critical SIF K_{Ic} obtained in Section B.3 and B.4 will be re-examined. The adhesion strength σ_y^∞ for the perfectly-bonded model can be obtained using Eq. (B.4), and that for the partially-debonded model $a/W = 0.01, a/W = 0.001$ can be computed using Eq. (B5).

$$\sigma_y^\infty = \frac{K_{\sigma c(average)}}{F_\sigma W^{1-\lambda}} \tag{B.4}$$

$$\sigma_y^\infty = \frac{K_{Ic(average)}}{F_I \sqrt{\pi a}} \tag{B.5}$$

Where $K_{\sigma c(average)}, K_{Ic(average)}$ are the mean critical values of the intensity of singular stress and SIF respectively. The estimated values of the adhesion strength calculated from different models for the two adhesive materials A and B are plotted in Fig. B.5 together with the experimental results. As can be seen from Fig. B.5, the errors are within $12\% - 20\%$ for those models.

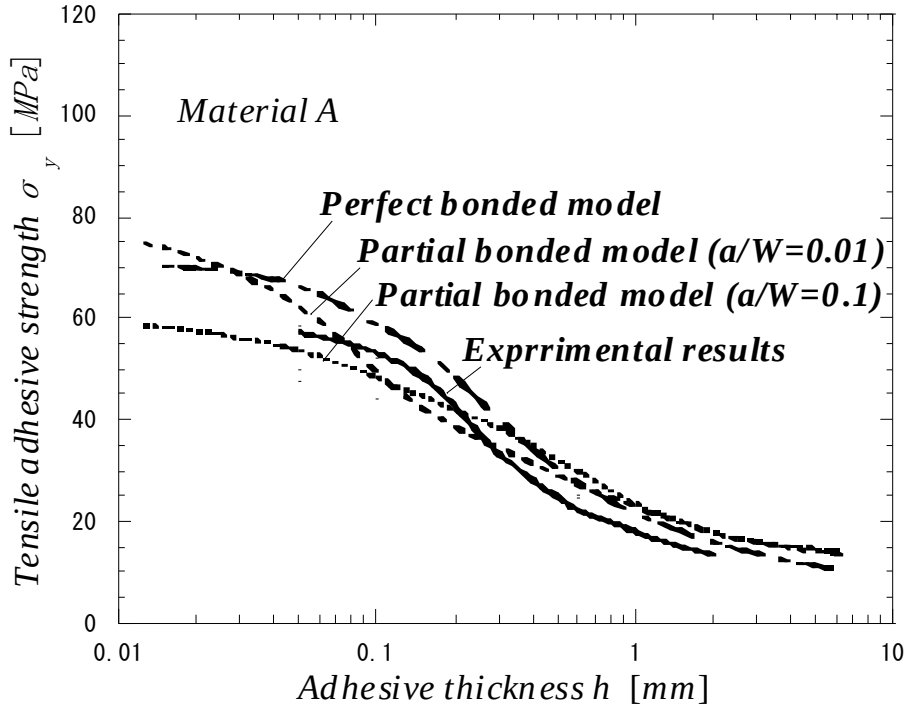

(a)

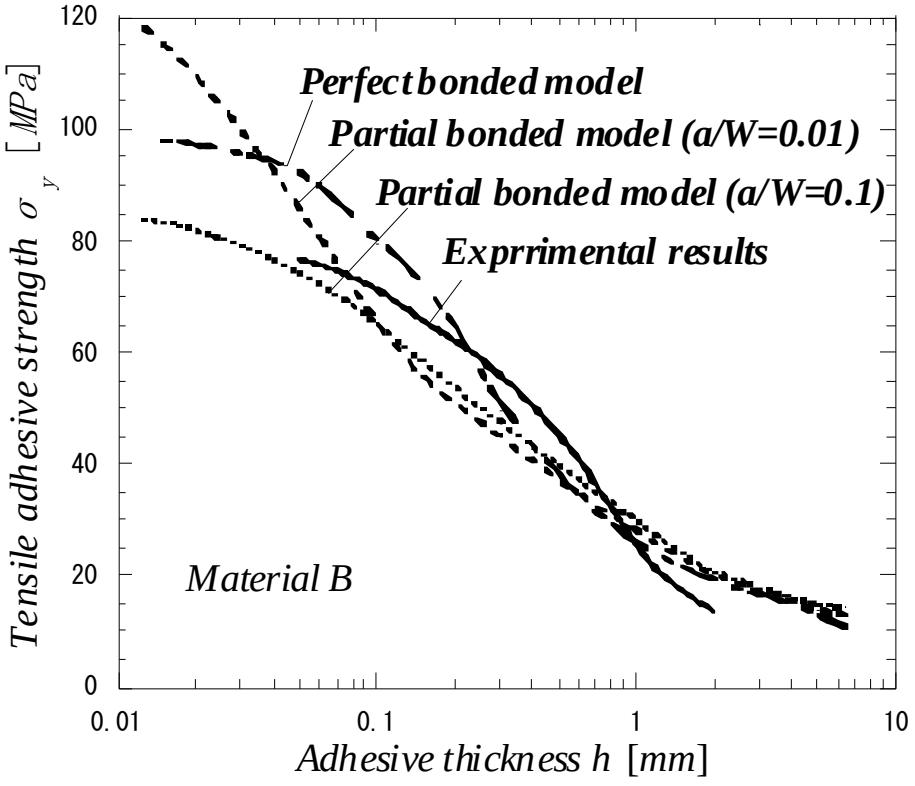

(b)

Fig. B.5 Relationship between σ_y and h for adhesives A and B

B.6 References of Appendix B

[1] Suzuki, Y., Adhesive tensile strengths of scarf and butt joints of steel plates (relation between adhesive layer thicknesses and adhesive strengths of joints. The Japan Society of Mechanical Engineers, 1987;30 (265):1042-1051.

[2] Zhang, Y., Noda, N.A., Takaishi, K.T., Lan, X., Effect of adhesive thickness on the interface of singular stress at the adhesive dissimilar joint. Trans JSME, Series A, 2011;77 (774):360-372.

[3] Noda, N.A., Lan, X., Michinaka, K., Zhang, Y. and Oda, K., Stress intensity factor of an edge interface crack in a bonded semi-infinite plate. Trans JSME, Series A, 2010;76(770):1270-77. (in Japanese)

[4] Lan, X., Michinaka, K., Zhang, Y., Noda, N.A., Stress intensity factor of an edge interface crack in a bonded finite plate under tension. Journal of the Society of Materials Science, 2011;60(8):748-755.

C
APPENDIX

Contour plot of the stress intensity factors for various adhesive joints

C.1 Tensile Loading Case

In this appendix, the contour plots of the SIFs of the adhesive joints subjected to tension as shown in Fig. C.1 for various material combinations and interlayer thicknesses will be demonstrated. Here, all the relative crack lengths of the adhesive joints are fixed to $a/W = 0.001$, then by varying the thickness of the adhesive layers, the SIFs are computed for the whole range of material combinations. Fig. C.2 ~ Fig. C.6 show the contour plots of the SIFs for the adhesive joints $a/W = 0.001$ with the adhesive layer thickness as $t/W = 2, 1, 0.1, 0.01, 0.001$ respectively.

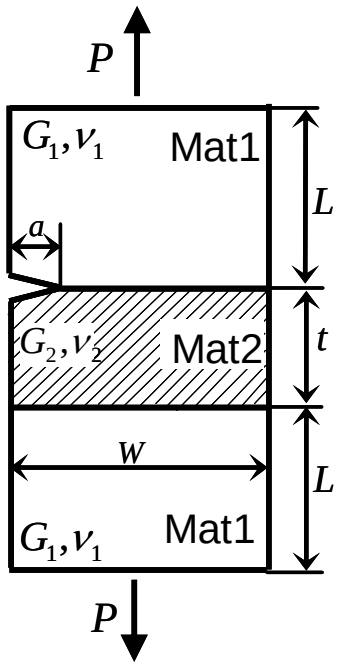

Fig. C.1 Adhesively bonded strip subjected to tension

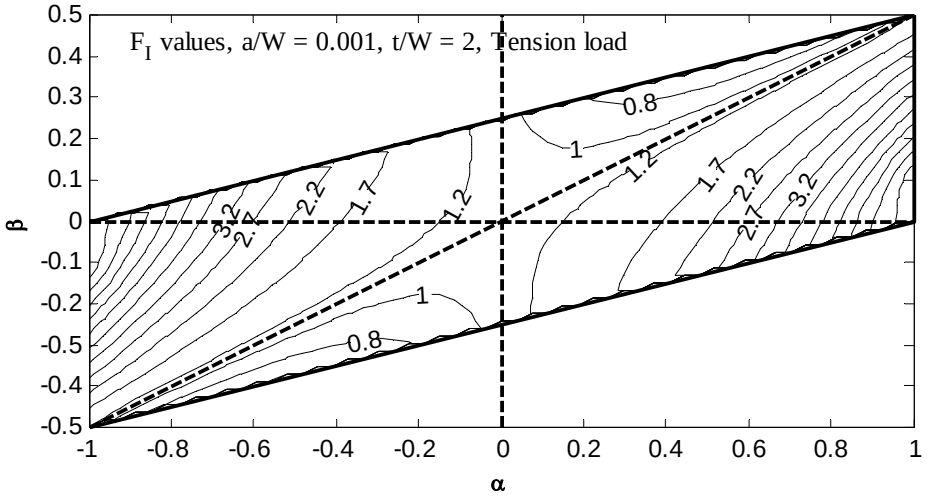

(a)

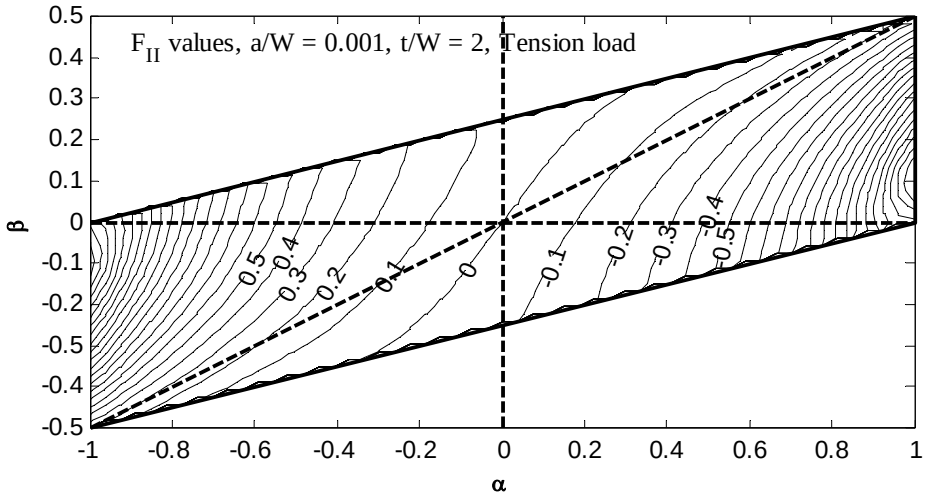

(b)

Fig. C.2 Contour map of (a) F_I and (b) F_{II} of $a/W = 0.001, t/W = 2$ for tension

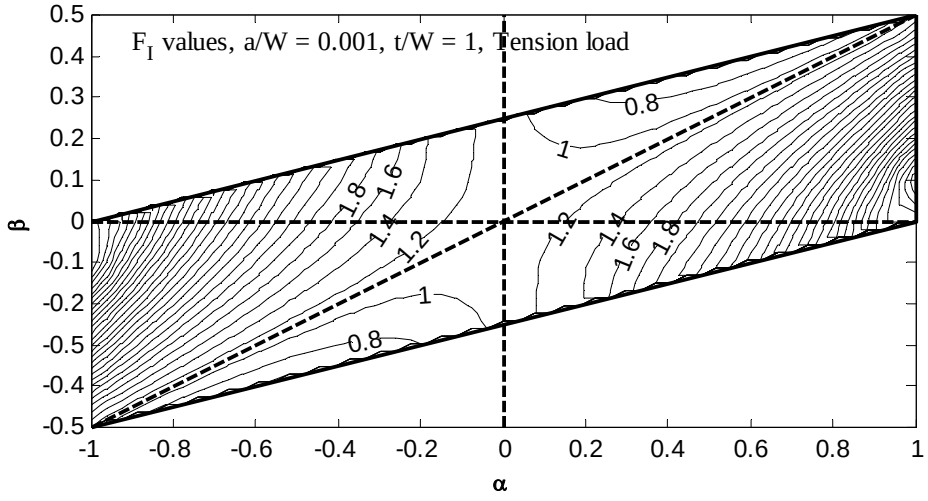

(a)

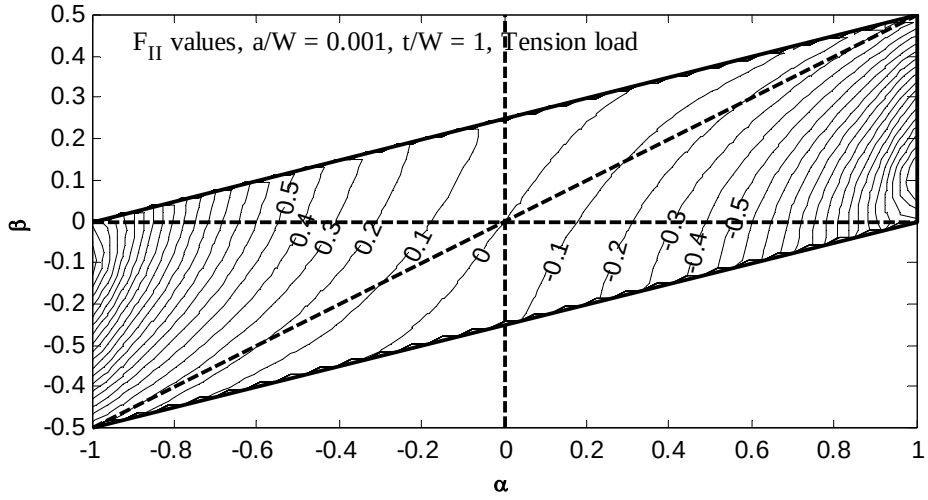

(b)

Fig. C.3 Contour map of (a) F_I and (b) F_{II} of $a/W = 0.001, t/W = 1$ for tension

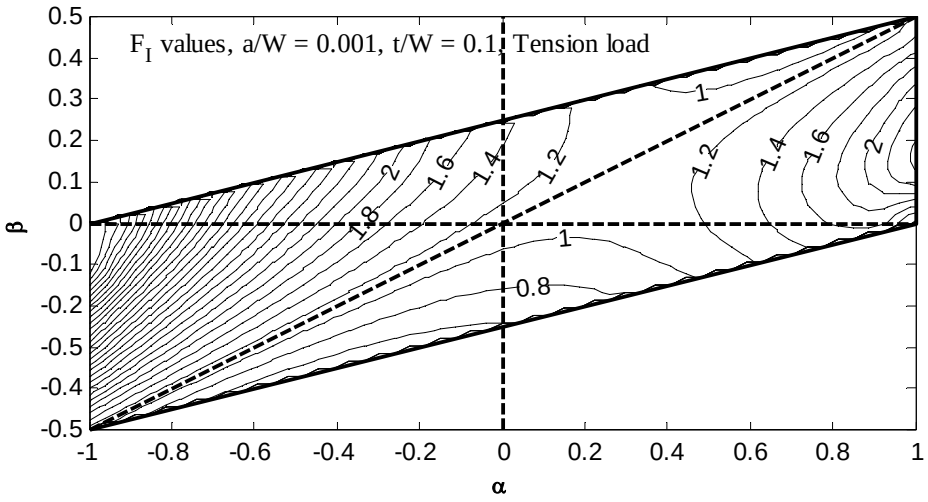

(a)

Fig. C.4 Contour map of (a) F_I and (b) F_{II} of $a/W = 0.001, t/W = 0.1$ for tension (Continue)

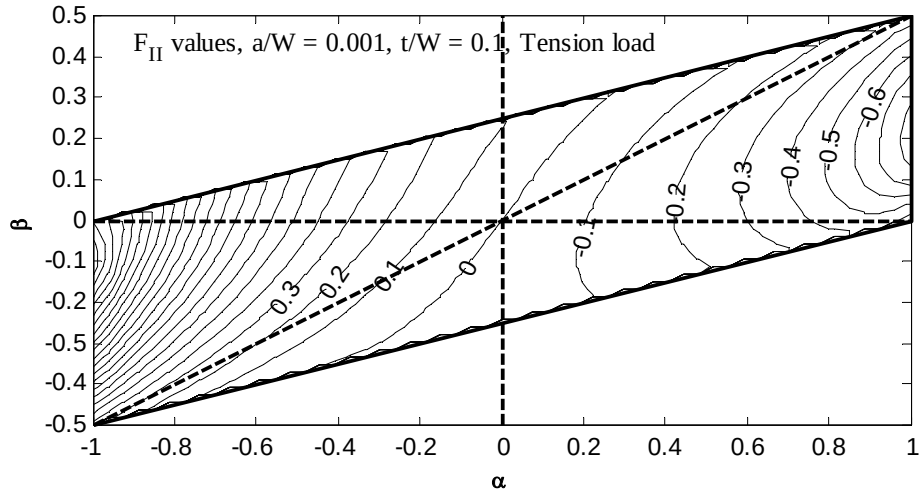

(b)

Fig. C.4 Contour map of (a) F_I and (b) F_{II} of $a/W = 0.001, t/W = 0.1$ for tension

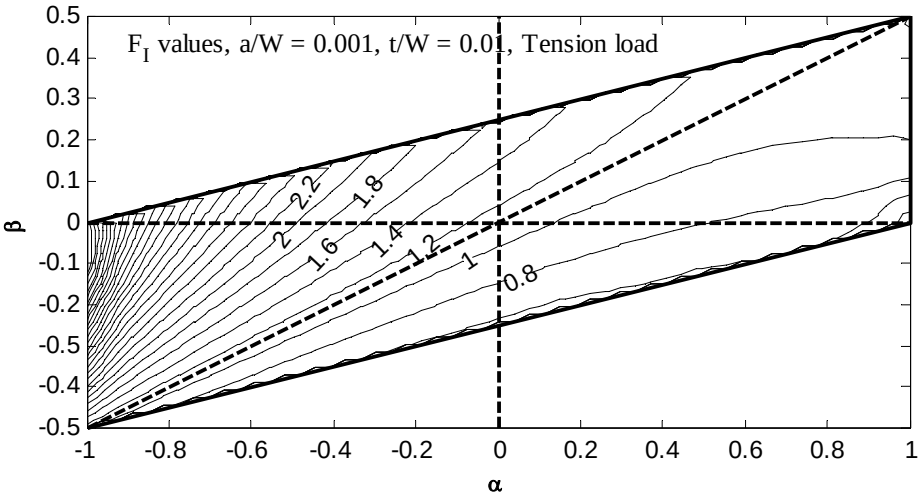

(a)

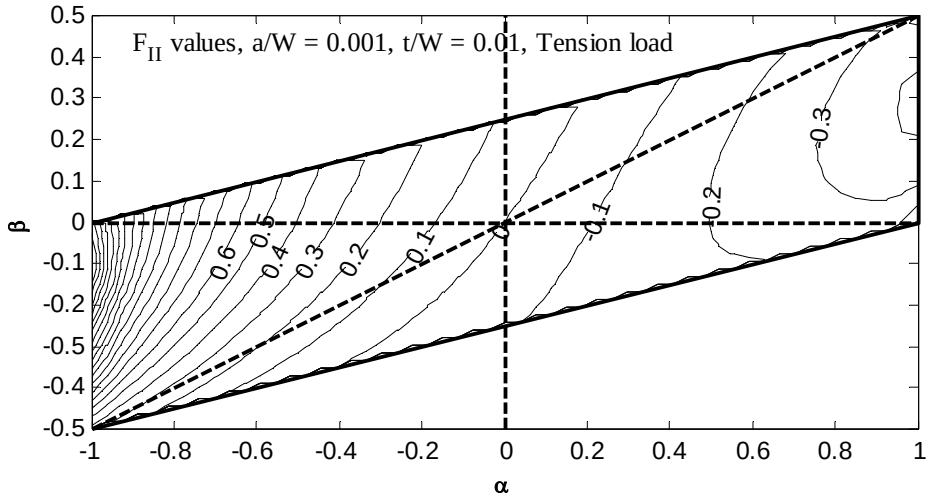

(b)

Fig. C.5 Contour map of (a) F_I and (b) F_{II} of $a/W = 0.001, t/W = 0.01$ for tension

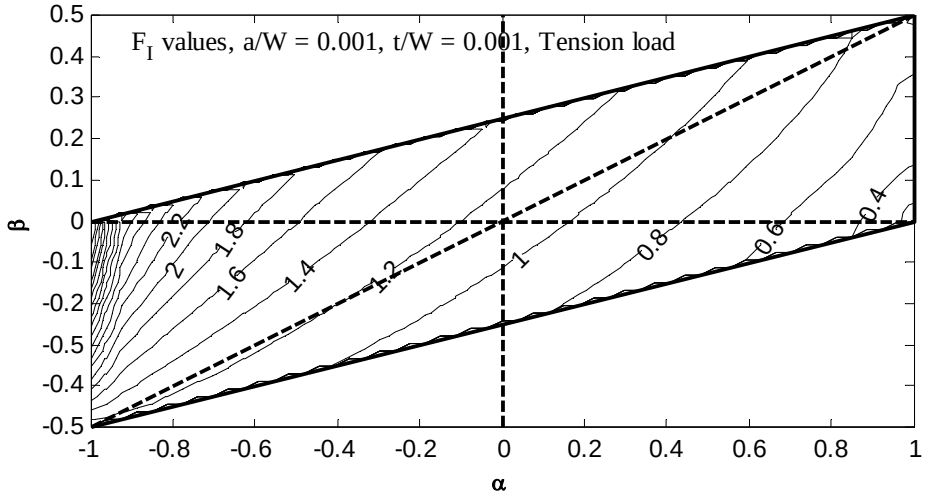

(a)

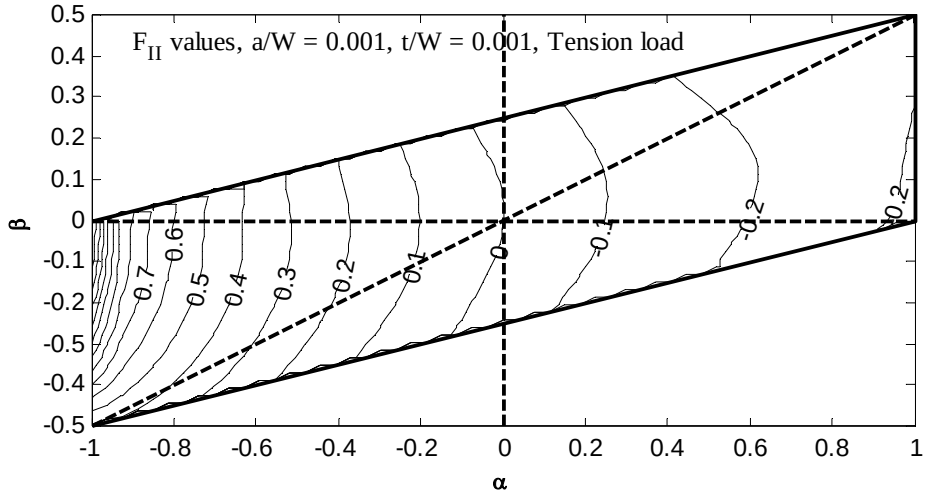

(b)

Fig. C.6 Contour map of (a) F_I and (b) F_{II} of $a/W = 0.001, t/W = 0.001$ for tension

C.2 Bending Loading Case

In this section, the contour plots of the SIFs of the adhesive joints subjected to bending loads as shown in Fig. C.7 are demonstrated. Similarly, all the relative crack lengths of the adhesive joints are fixed to $a/W = 0.001$, then the SIFs are computed for the whole α-β space by varying the thickness of the adhesive layers. Fig. C.8 ~ Fig. C.12 show the contour plots of the SIFs for the adhesive joints $a/W = 0.001$ with the adhesive layer thickness of $t/W = 2, 1, 0.1, 0.01, 0.001$ respectively.

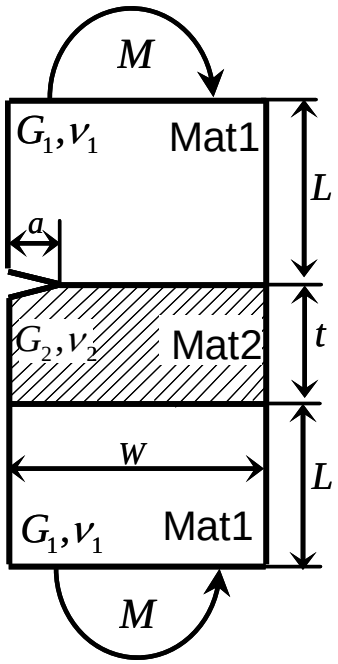

Fig. C.7 Adhesively bonded strip subjected to bending moment

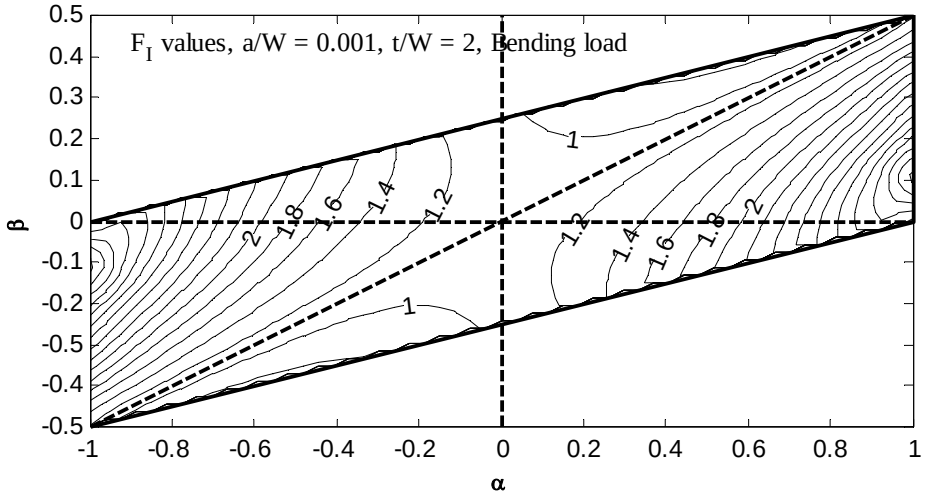

(a)

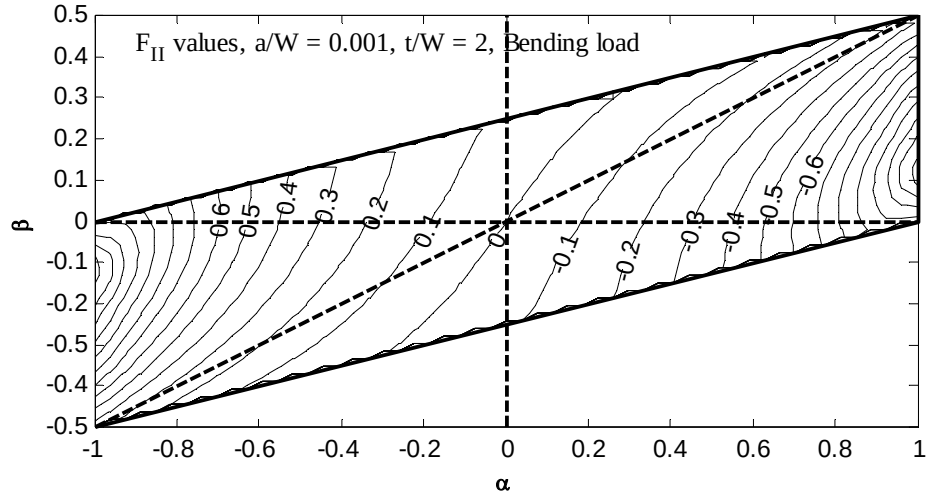

(b)

Fig. C.8 Contour map of (a) F_I and (b) F_{II} of $a/W = 0.001, t/W = 2$ for bending loads

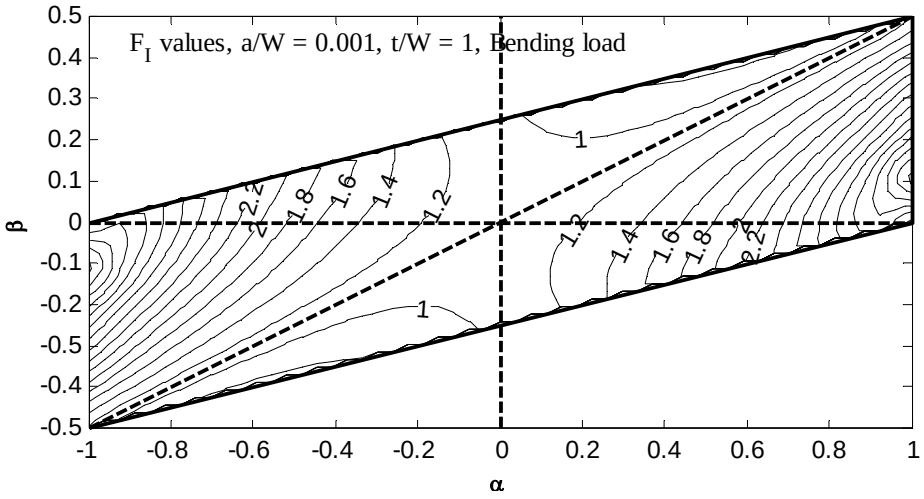

(a)

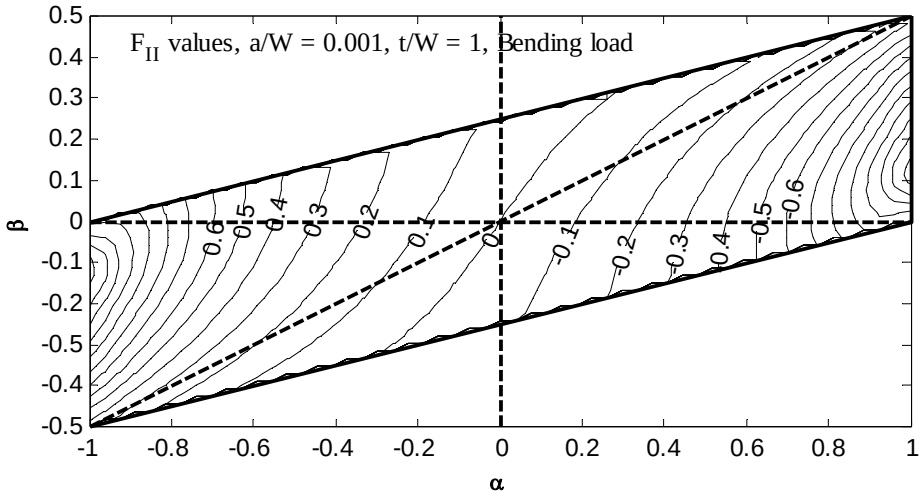

(b)

Fig. C.9 Contour map of (a) F_I and (b) F_{II} of $a/W = 0.001, t/W = 1$ for bending loads

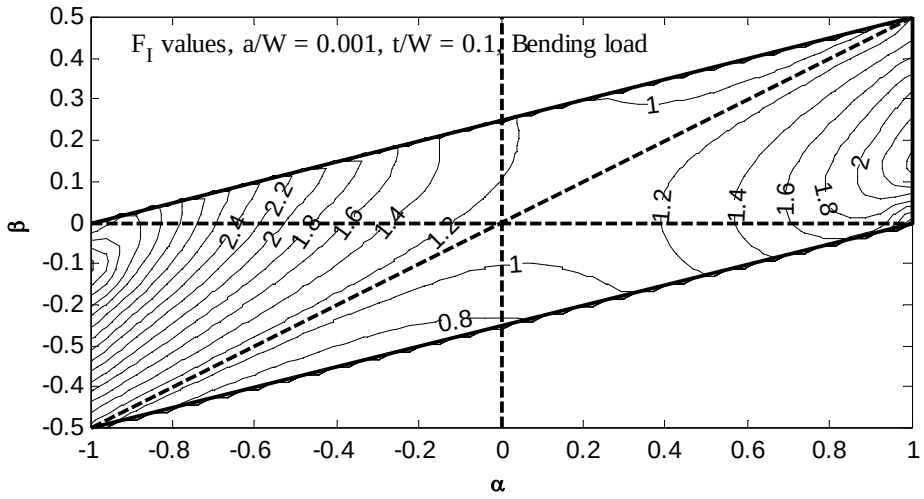

(a)

Fig. C.10 Contour map of (a) F_I and (b) F_{II} of $a/W = 0.001, t/W = 0.1$ for bending loads (Continue)

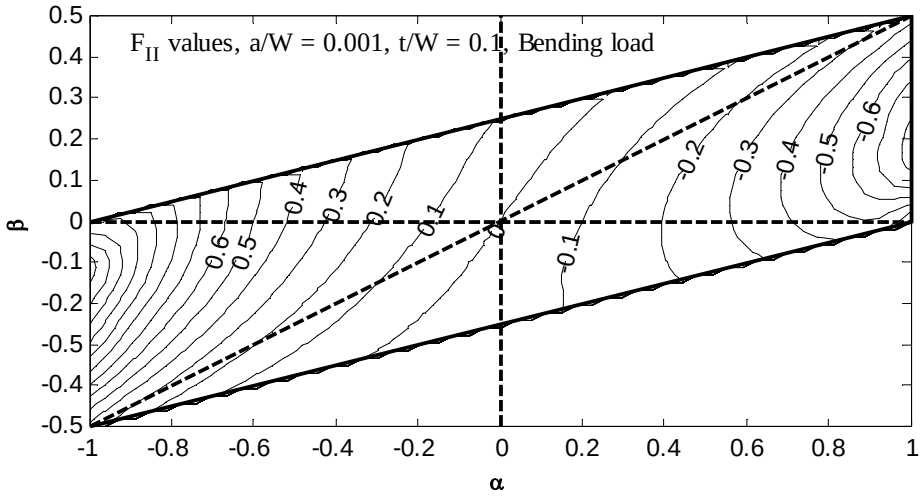

(b)

Fig. C.10 Contour map of (a) F_I and (b) F_{II} of $a/W = 0.001, t/W = 0.1$ for bending loads

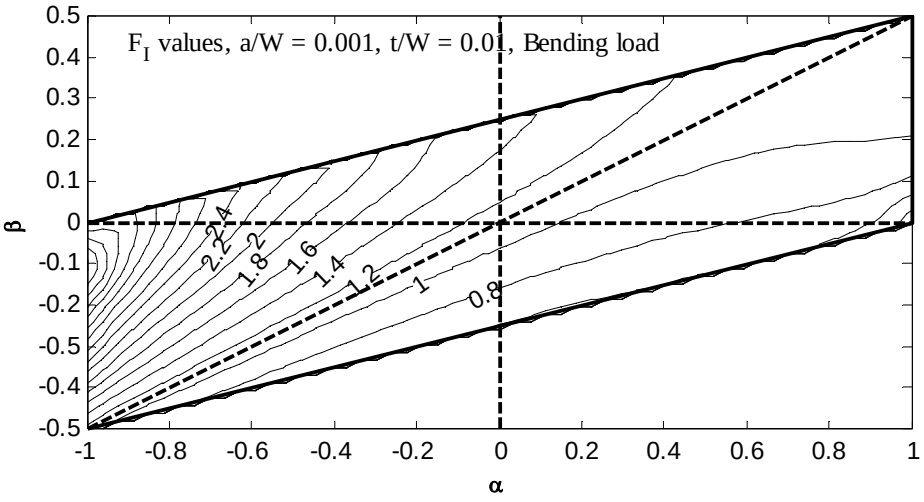

(a)

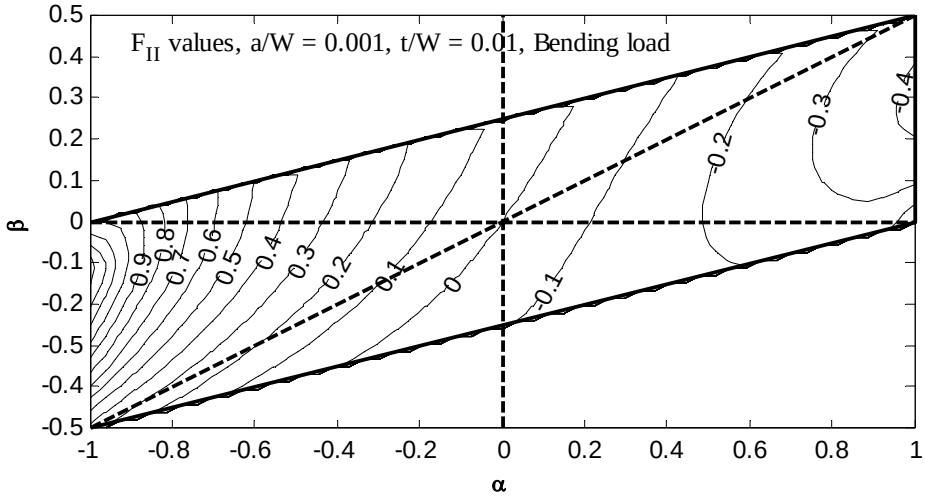

(b)

Fig. C.11 Contour map of (a) F_I and (b) F_{II} of $a/W = 0.001, t/W = 0.01$ for bending loads

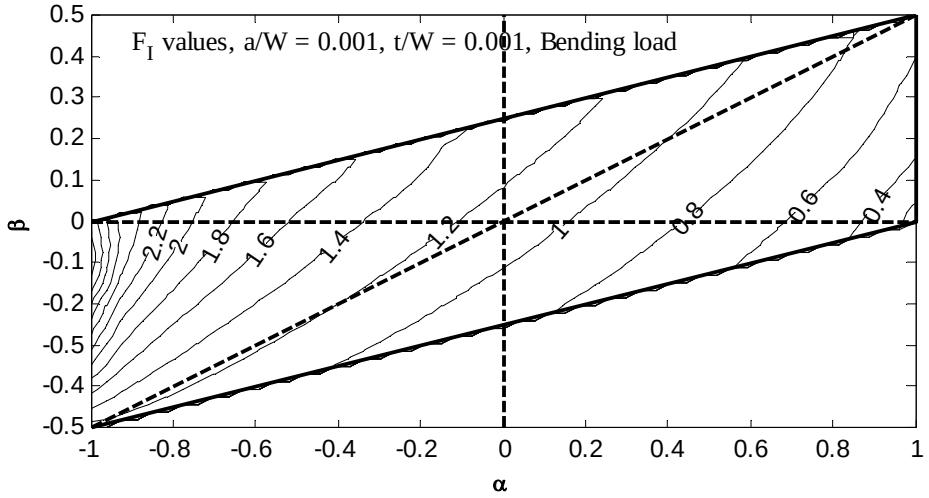

(a)

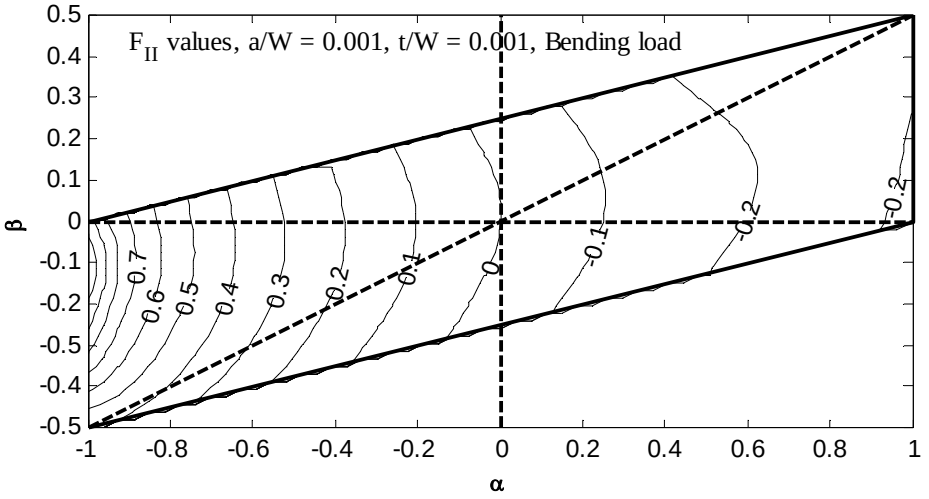

(b)

Fig. C.12 Contour map of (a) F_I and (b) F_{II} of $a/W = 0.001, t/W = 0.001$ for bending loads